WILEY-VCH

Edited by Bradley Ladewig, San Ping Jiang, and Yushan Yan

Materials for Low-Temperature Fuel Cells

Series Editor: G.Q. Max Lu

Materials for Sustainable Energy and Development

Edited by
Bradley Ladewig
San P. Jiang
Yushan Yan

Materials for Low-Temperature Fuel Cells

Related Titles

Fricke, J., Borst, W.L.

Essentials of Energy Technology

Sources, Transport, Storage, Conservation

2013
Print ISBN: 978-3-527-33416-2; also available in digital formats

Jiang, S. P. / Yan, Y. (eds.)

Materials for High-Temperature Fuel Cells

Series: Materials for Sustainable Energy and Development
Series editor: Lu, G. Q. M. (ed.)

2013
Print ISBN: 978-3-527-33041-6; also available in digital formats

García-Martínez, J. (ed.)

Nanotechnology for the Energy Challenge

Second Edition
2013
Print ISBN: 978-3-527-33380-6; also available in digital formats

Stolten, D., Scherer, V. (eds.)

Transition to Renewable Energy Systems

2013
Print ISBN: 978-3-527-33239-7; also available in digital formats

Stolten, D. / Emonts, B. (eds.)

Fuel Cell Science and Engineering

Materials, Processes, Systems and Technology

2012
Print ISBN: 978-3-527-33012-6; also available in digital formats

Stolten, D. (ed.)

Hydrogen and Fuel Cells

Fundamentals, Technologies and Applications

2010
Print ISBN: 978-3-527-32711-9

Edited by Bradley Ladewig, San P. Jiang,
and Yushan Yan

Materials for Low-Temperature Fuel Cells

WILEY-VCH
Verlag GmbH & Co. KGaA

Editors

Dr. Bradley Ladewig
Monash University
Department of Chemical Engin.
Building 36, Clayton Campus
Victoria 3800
Australia

Prof. San P. Jiang
Curtin University
Department of Chemical Engineering &
Fuels and Energy Technology Institute
1, Turner Avenue
6845 Perth, WA
Australia

Prof. Yushan Yan
University of Delaware
Department of Chemical and Biomolecular Engineering
150 Academy Street
DE 19716
United States

Series Editor

G. Q. Max Lu
Univ. of Queensland
ARC Centre Funct.Nanomat.
AIBN Bldg. Level 5 West
4072 Brisbane Queensland
Australia

Library of Congress Card No.: applied for

British Library Cataloguing-in-Publication Data
A catalogue record for this book is available from the British Library.

Bibliographic information published by the Deutsche Nationalbibliothek
The Deutsche Nationalbibliothek lists this publication in the Deutsche Nationalbibliografie; detailed bibliographic data are available on the Internet at http://dnb.d-nb.de.

Print ISBN: 978-3-527-33042-3
ePDF ISBN: 978-3-527-64432-2
ePub ISBN: 978-3-527-64431-5
Mobi ISBN: 978-3-527-64433-9
oBook ISBN: 978-3-527-64430-8

Cover Design Formgeber, Mannheim, Germany
Typesetting Thomson Digital, Noida, India
Printing and Binding Markono Print Media Pte Ltd, Singapore

Printed on acid-free paper

Editorial Board

Members of the Advisory Board of the "Materials for Sustainable Energy and Development" Series

Contents

Series Editor's Preface

The Wiley Series on New Materials for Sustainable Energy and Development

Sustainable energy and development is attracting increasing attention from the scientific research communities and industries alike, with an international race to develop technologies for clean fossil energy, hydrogen and renewable energy as well as water reuse and recycling. According to the REN21 (Renewables Global Status Report 2012 p. 17) total investment in renewable energy reached $257 billion in 2011, up from $211 billion in 2010. The top countries for investment in 2011 were China, Germany, the United States, Italy, and Brazil. In addressing the challenging issues of energy security, oil price rise, and climate change, innovative materials are essential enablers.

In this context, there is a need for an authoritative source of information, presented in a systematic manner, on the latest scientific breakthroughs and knowledge advancement in materials science and engineering as they pertain to energy and the environment. The aim of the *Wiley Series on New Materials for Sustainable Energy and Development* is to serve the community in this respect. This has been an ambitious publication project on materials science for energy applications. Each volume of the series will include high-quality contributions from top international researchers, and is expected to become the standard reference for many years to come.

This book series covers advances in materials science and innovation for renewable energy, clean use of fossil energy, and greenhouse gas mitigation and associated environmental technologies. Current volumes in the series are:

Supercapacitors. Materials, Systems, and Applications
Functional Nanostructured Materials and Membranes for Water Treatment
Materials for High-Temperature Fuel Cells
Materials for Low-Temperature Fuel Cells
Advanced Thermoelectric Materials. Fundamentals and Applications
Advanced Lithium-Ion Batteries. Recent Trends and Perspectives
Photocatalysis and Water Purification. From Fundamentals to Recent Applications

In presenting this volume on Materials for Low-Temperature Fuel Cells, I would like to thank the authors and editors of this important book, for their tremendous effort and hard work in completing the manuscript in a timely manner. The quality of the chapters reflects well the caliber of the contributing authors to this book, and will no doubt be recognized and valued by readers.

Finally, I would like to thank the editorial board members. I am grateful to their excellent advice and help in terms of examining coverage of topics and suggesting authors, and evaluating book proposals.

I would also like to thank the editors from the publisher Wiley-VCH with whom I have worked since 2008, Dr Esther Levy, Dr Gudrun Walter, Dr Bente Flier, and Dr Martin Graf-Utzmann for their professional assistance and strong support during this project.

I hope you will find this book interesting, informative and valuable as a reference in your work. We will endeavour to bring to you further volumes in this series or update you on the future book plans in this growing field.

Brisbane, Australia *G.Q. Max Lu*
31 July 2012

About the Series Editor

Professor Max Lu
Editor, New Materials for Sustainable Energy and Development Series

Professor Lu's research expertise is in the areas of materials chemistry and nanotechnology. He is known for his work on nanoparticles and nanoporous materials for clean energy and environmental technologies. With over 500 journal publications in high-impact journals, including Nature, *Journal of the American Chemical Society, Angewandte Chemie, and Advanced Materials*, he is also coinventor of 20 international patents. Professor Lu is an Institute for Scientific Information (ISI) Highly Cited Author in Materials Science with over 17 500 citations (h-index of 63). He has received numerous prestigious awards nationally and internationally, including the Chinese Academy of Sciences International Cooperation Award (2011), the Orica Award, the RK Murphy Medal, the Le Fevre Prize, the ExxonMobil Award, the Chemeca Medal, the Top 100 Most Influential Engineers in Australia (2004, 2010, and 2012), and the Top 50 Most Influential Chinese in the World (2006). He won the Australian Research Council Federation Fellowship twice (2003 and 2008). He is an elected Fellow of the Australian Academy of Technological Sciences and Engineering (ATSE) and Fellow of Institution of Chemical Engineers (IChemE). He is editor and editorial board member of 12 major international journals including *Journal of Colloid and Interface Science and Carbon*.

Max Lu has been Deputy Vice-Chancellor and Vice-President (Research) since 2009. He previously held positions of acting Senior Deputy Vice-Chancellor (2012), acting Deputy Vice-Chancellor (Research), and Pro-Vice-Chancellor

(Research Linkages) from October 2008 to June 2009. He was also the Foundation Director of the ARC Centre of Excellence for Functional Nanomaterials from 2003 to 2009.

Professor Lu had formerly served on many government committees and advisory groups including the Prime Minister's Science, Engineering and Innovation Council (2004, 2005, and 2009) and the ARC College of Experts (2002–2004). He is the past Chairman of the IChemE Australia Board and former Director of the Board of ATSE. His other previous board memberships include Uniseed Pty Ltd., ARC Nanotechnology Network, and Queensland China Council. He is currently Board member of the Australian Synchrotron, National eResearch Collaboration Tools and Resources, and Research Data Storage Infrastructure. He also holds a ministerial appointment as member of the National Emerging Technologies Forum.

About the Volume Editors

Associate Professor Bradley Ladewig is an academic in the Department of Chemical Engineering at Monash University, Australia, where he leads a research group developing membrane materials and technologies for clean energy applications. He has a wide range of experience as a chemical engineering researcher, including in membrane development for direct methanol fuel cells, testing and modeling of combined heat and power PEM fuel cell systems, and desalination membrane development. Recently he has worked on several collaborative projects in the field of direct carbon fuel cells, metal organic framework materials as gas sorbents and membrane components, and low-cost microfluidic sensors based on paper and thread substrates. He is a Fellow of the Institution of Chemical Engineers.

Professor San Ping Jiang is a professor at the Department of Chemical Engineering, the Deputy Director of Fuels and Energy Technology Institute, Curtin University, Australia and Adjunct Professor of the University of the Sunshine Coast, Australia. He also holds Visiting/Guest Professorships at the Southwest University, Central South University, Harbin Institute of Technology, Guangzhou University, Huazhong University of Science and Technology, Wuhan University of Technology, University of Science and Technology of China (USTC), Sichung University, and Shandong University. Dr. Jiang has broad experience in both academia and industry, having held positions at Nanyang Technological University, the CSIRO Manufacturing Science and Technology Division in Australia, and Ceramic Fuel Cells Ltd (CFCL). His research interests encompass solid oxide fuel cells, proton exchange and direct methanol fuel cells, direct alcohol fuel cells, and electrolysis. With an h-index of 50, he has published over 270 journal papers, which have accrued ~8,500 citations.

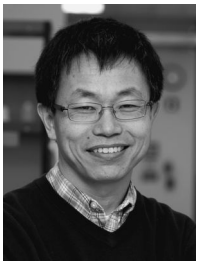

Professor Yushan Yan is Distinguished Engineering Professor in the Department of Chemical and Biomolecular Engineering at the University of Delaware. His previous positions include Presidential Chair, University Scholar, and Department Chair at the University of California Riverside and Senior Staff Engineer at AlliedSignal Inc. He was instrumental to the formation of technology startups such as NanoH_2O, Full Cycle Energy, Zeolite Solution Materials, and OH-Energy. His research focuses on zeolite thin films and electrochemical devices including fuel cells, electrolyzers, solar hydrogen and redox flow batteries. He has published 160+ journal papers and has a h-index of 52. He was recognized by the Donald Breck Award from the International Zeolite Association and is a Fellow of the American Association for the Advancement of Science.

List of Contributors

Benjamin M. Asquith
Monash University
Department of Chemical Engineering
Clayton Campus
Melbourne, VIC 3800
Australia

and

Leibniz-Institut für Polymerforschung Dresden e.V.
Hohe Strasse 6
01069 Dresden
Germany

Daniel J.L. Brett
University College of London
Department of Chemical Engineering
Electrochemical Innovation Lab
Torrington Place
London WC1E 7JE
UK

Yanzhen Fan
Oregon State University
Department of Biological and Ecological Engineering
116 Gilmore Hall
Corvallis, OR 97331
USA

Shuang Gu
University of Delaware
Department of Chemical and Biomolecular Engineering
150 Academy Street
Newark, DE 19716
USA

Falk Harnisch
The University of Queensland
Advanced Water Management Centre
Brisbane, QLD 4072
Australia

and

TU Braunschweig
Institute of Environmental and Sustainable Chemistry
38106 Braunschweig
Germany

Rhodri Jervis
University College of London
Department of Chemical Engineering
Electrochemical Innovation Lab
Torrington Place
London WC1E 7JE
UK

Luhua Jiang
Chinese Academy of Sciences
Dalian Institute of Chemical Physics
Dalian National Laboratory for
Clean Energy
Division of Fuel Cell & Battery
457 Zhongshan Road
Dalian 116023
China

Robert B. Kaspar
University of Delaware
Department of Chemical and
Biomolecular Engineering
150 Academy Street
Newark, DE 19716
USA

Bradley P. Ladewig
Monash University
Department of Chemical
Engineering
Clayton Campus
Melbourne, VIC 3800
Australia

Wenzhen Li
Michigan Technological University
Chemical Engineering Department
1400 Townsend Drive
Houghton, MI 49931
USA

Hong Liu
Oregon State University
Department of Biological and
Ecological Engineering
116 Gilmore Hall
Corvallis, OR 97331
USA

Jochen Meier-Haack
Leibniz-Institut für
Polymerforschung Dresden e.V.
Hohe Strasse 6
01069 Dresden
Germany

Nam-Trung Nguyen
Nanyang Technological University
School of Mechanical Aerospace
Engineering
Nanyang Avenue 50
Singapore 639798
Singapore

Korneel Rabaey
The University of Queensland
Advanced Water Management
Centre
Brisbane, QLD 4072
Australia

and

Ghent University
Laboratory of Microbial Ecology
and Technology (LabMET)
Coupure Links 653
9000 Ghent
Belgium

Seyed Ali Mousavi Shaegh
Nanyang Technological University
School of Mechanical Aerospace
Engineering
Nanyang Avenue 50
Singapore 639798
Singapore

Gongquan Sun
Chinese Academy of Sciences
Dalian Institute of Chemical Physics
Dalian National Laboratory for
Clean Energy
Division of Fuel Cell & Battery
457 Zhongshan Road
Dalian 116023
China

Junhua Wang
University of Delaware
Department of Chemical and
Biomolecular Engineering
150 Academy Street
Newark, DE 19716
USA

Shuangyin Wang
Nanyang Technological University
School of Chemical and
Biomedicinal Engineering
Nanyang Avenue 50
Singapore 639798
Singapore

Xin Wang
Nanyang Technological University
School of Chemical and
Biomedicinal Engineering
Nanyang Avenue 50
Singapore 639798
Singapore

Yushan Yan
University of Delaware
Department of Chemical and
Biomolecular Engineering
150 Academy Street
Newark, DE 19716
USA

Bingzi Zhang
University of Delaware
Department of Chemical and
Biomolecular Engineering
150 Academy Street
Newark, DE 19716
USA

1
Key Materials for Low-Temperature Fuel Cells: An Introduction

Bradley P. Ladewig, Benjamin M. Asquith, and Jochen Meier-Haack

The promise of lower temperature fuel cells as versatile, efficient power sources has been made many times, both in academia and in the corporate world. Their potential as devices capable of converting chemical energy into electrical energy at high efficiency has been known for many years; however, despite an enormous worldwide research effort, they have not achieved mainstream commercial success.

One of the key impediments that is universally recognized is that there remain a series of key materials challenges that must be overcome before low-temperature fuel cells can achieve their full potential. In this book, we present a snapshot of the current state of the art, critically reviewed, as it relates to the materials challenges facing low-temperature fuel cells. In terms of what actually constitutes a low-temperature fuel cell, since there is no universal definition, we adopt here the convention of a fuel cell operating below 200 °C. In most cases, low-temperature fuel cells operate well below 100 °C; however, given the advances that have been made with high-performance polymer membranes (in particular, based on polybenzimidazole, as highlighted in Chapter 5), there now exists the potential to operate some systems with a vapor-phase feed. Clearly, this takes advantage of the superior reaction kinetics at elevated temperatures and allows for greater power density devices.

This book does not seek to be an all-encompassing encyclopedia that addresses every materials aspect of low-temperature fuel cells. Readers seeking a comprehensive reference work should consult the excellent handbook edited by Wolf Vielstich [1]. Rather, we have sought to highlight the key, contemporary challenges of interest to the fuel cell researcher (and those working in industry). We have intentionally sought to focus on the emerging areas of interest, with a particular focus on alkaline exchange (or hydroxide exchange) membrane fuel cells. These fuel cells are a radical departure from the thousands of research works published over the past decades that focused exclusively on proton exchange or cation exchange membrane low-temperature fuel cells (most obviously because the earlier high-performance membranes, from the chloralkali industry, were cation exchange membranes). There are critical materials challenges in advancing alkaline exchange membrane fuel cells, not least of which is the development of a new suite of polymer membranes that selectively transport

Materials for Low-Temperature Fuel Cells, First Edition. Edited by Bradley Ladewig, San P. Jiang, and Yushan Yan.

hydroxide ions. There are also more subtle catalyst selection issues, and these are covered in quite some detail in this book.

Two other specific areas must be mentioned in this introduction: the emerging fields of microbial fuel cells and microfluidic fuel cells. In some ways these two new fields can be considered embodiments of low-temperature fuel cells operating at the extreme size scales – microbial fuel cells have their genesis in the exploration of wastewater treatment in electrochemical and bioelectrochemical systems. These proposed applications are by their nature enormous in size, with reactor volumes measured in the tens of cubic meters (many orders of magnitude larger than the conventional low-temperature fuel cells).

In contrast, microfluidic fuel cells are at the opposite end of the size spectrum, and have come into the realm of fuel cell research in the past decade as the general field of microfluidics has exploded with interest. This has been driven not only through the widespread availability of the tools for fabrication of microfluidic devices but also by the possible application of microfluidic fuel cells in functional devices such as sensors and health care products.

The following chapters address a broad spectrum of topics, and it is hoped that the reader will recognize and appreciate the underlying theme of this book, which is to highlight the key materials challenges facing the field of low-temperature fuel cells, and expertly and concisely review the current state of the art.

Reference

1 Vielstich, W. (2009) *Handbook of Fuel Cells, 6 Volume Set*, John Wiley & Sons, Inc., Hoboken, NJ.

2
Alkaline Anion Exchange Membrane Fuel Cells

Rhodri Jervis and Daniel J.L. Brett

2.1
Fuel Cells

Fuel cells represent a potentially integral technology in a greener electricity-based energy economy. Converting chemical energy directly into electricity with no moving parts and no particulate or greenhouse gas emissions at point of operation, they can offer higher efficiencies than combustion and greater energy storage and reduced "charge" times compared with batteries. While they retain few of the disadvantages of existing electricity generation technologies, a major barrier to commercialization and widespread use at present is cost. The key working part of a fuel cell, the membrane electrode assembly (MEA), comprises a catalyst, usually containing platinum, and an ionic polymer membrane, both of which contribute significantly to the overall cost of a fuel cell. This chapter will concentrate on the potential for alkaline anion exchange membrane (AAEM) fuel cells to provide a route to reduced costs and help realize commercial ubiquity of fuel cells in various energy sectors. We will first discuss the basic principles of the more common acidic PEM fuel cells and the thermodynamics and kinetics of the electrochemical reactions governing their operation, before explaining the key differences in AAEM fuel cells and how they might provide an advantage over the more established technology.

This basic idea of the fuel cell goes back to as far as 1839 when Swansea-born physicist Sir William Gove realized that reverse electrolysis of water was possible. However, development from this concept was slow and it was not until the 1960s and the Apollo Space Programme that fuel cells became practicable, in the form of aqueous alkaline electrolyte fuel cells. Aqueous electrolyte-based fuel cells have many disadvantages for portability causing recent focus to shift toward solid electrolytes, in particular toward polymer electrolyte membrane (PEM) fuel cells. These employ an ionomer, which is a polymer containing an ionic functional group in the monomer, as the electrolyte in order to allow hydrogen ion transport through a nonaqueous medium. Recent improvements in membrane technology, and in particular the performance of the industry standard Nafion membranes, have made PEM fuel cells a major focus of research. The alkaline

Materials for Low-Temperature Fuel Cells, First Edition. Edited by Bradley Ladewig, San P. Jiang, and Yushan Yan.

analog of the more common PEM fuel cell uses a hydroxide-conducting membrane in an attempt to exploit the superior cathode kinetics of alkaline systems and ultimately reduce the catalyst's contribution to the cost of fuel cells.

2.2 PEM Fuel Cell Principles

The main elemental principle of a fuel cell is the direct electrochemical redox reaction that produces the electrical current. In the hydrogen/oxygen fuel cell, the redox reaction is composed of two electrochemical half equations – the hydrogen oxidation reaction (HOR) at the anode:

$$H_2 \rightleftharpoons 2H^+ + 2e^- \tag{2.1}$$

and the oxygen reduction reaction (ORR) at the cathode:

$$\frac{1}{2}O_2 + 2H^+ + 2e^- \rightleftharpoons H_2O \tag{2.2}$$

These combine to give the overall redox reaction:

$$H_2 + \frac{1}{2}O_2 \rightleftharpoons H_2O \tag{2.3}$$

Hydrogen is fed into the anode and air/oxygen into the cathode through flowfields and diffuses through a gas diffusion layer (GDL) to the catalyst layer where the gas, catalyst, and electrolyte meet in what is called a triple-phase boundary. It is here where the HOR and ORR occur on the anode and the cathode, respectively, separated by the polymer electrolyte membrane. The protons generated by the HOR diffuse through the electrolyte to react at the cathode and the electrons generated, impeded by the insulating polymer, travel through the external circuit creating a current (Figure 2.1).

2.2.1 Equilibrium Kinetics

The HOR and ORR reactions occurring at the electrodes of fuel cells are linked only through the conservation of charge; the electrons and protons produced at the anode must be consumed at the cathode. Though the current is identical at both electrodes, the activation polarization required to generate this current for each reaction is not. As current is a rate of charge and electrons are produced and consumed in electrochemical half reactions, the current is a direct measure of the rate of an electrochemical reaction. If reaction of 1 mol of reactant yields n mol of electrons, the current i is given by

$$i = nF\frac{dN}{dt}, \tag{2.4}$$

where dN/dt is the rate of reaction in mol s^{-1}. As these reactions occur at interfaces, the current is generally normalized to area such that $j = i/A$ and the

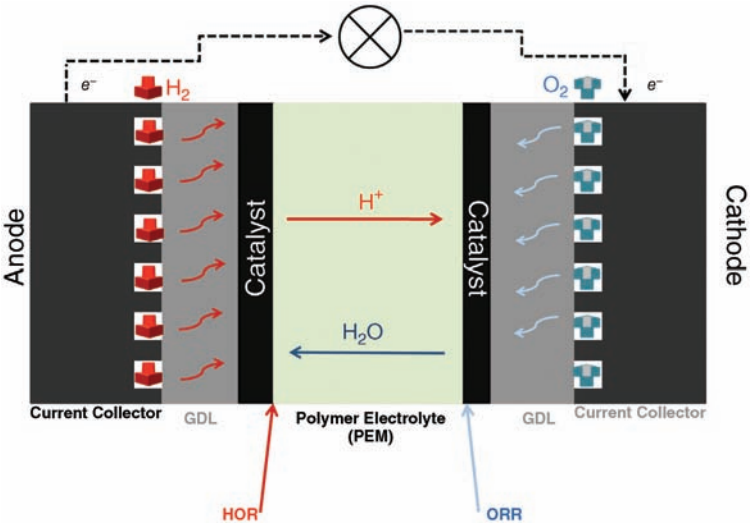

Figure 2.1 Schematic of an acidic PEM fuel cell.

reaction rate per unit area is ν, where j is called the current density (this also helps in comparison between different fuel cells of different geometric areas). Rearranging Equation 2.4 for rate, we get

$$\nu = \frac{j}{nF}. \tag{2.5}$$

Reaction rate is a product of the surface concentration and a reaction rate constant, such that

$$\nu_1 = C_r k_1. \tag{2.6}$$

From statistical mechanics, it can also be shown that the rate constant is a function of the Gibbs free energy of the transition state because the reactants must be in the transition state in order to have a probability of reacting. This rate constant is given by

$$k_1 = \frac{k_B T}{h} e^{-(\Delta G_1/RT)}, \tag{2.7}$$

where, k_B is the Boltzmann constant, T is the temperature (in Kelvin), h is the Planck's constant, R is the molar gas constant, and ΔG_1 is the activation energy for the forward reaction given by the difference in free energy between the reactants' free energy and the transition-state free energy, as shown in Figure 2.2.

However, ν_1 is just the rate of the forward reaction of the electrochemical half reaction. The rate of the reverse reaction, ν_2, is given by substituting ΔG_1 for ΔG_2, the difference in free energy between the products and the activation

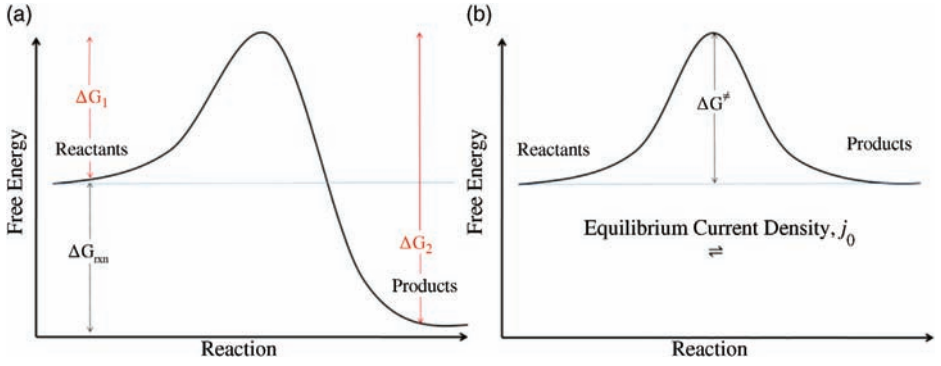

Figure 2.2 Activation energies for reaction. (a) The products have a lower free energy than the reactants and the forward reaction is favored. (b) On the buildup of the charge double layer the potential is equalized and results in electrochemical equilibrium.

energy. Then, the overall reaction rate ν is given by $\nu_1 - \nu_2$ and therefore the net current is

$$j = nF(\nu_1 - \nu_2). \tag{2.8}$$

At equilibrium, the rate of the forward reaction and that of reverse reaction are equal and j, the overall current density, is 0. However, j is composed of the forward current density, $j_1 = nF\nu_1$, and the reverse current density, $j_2 = nF\nu_1$, both of which at equilibrium are equal to what is known as the exchange current density j_0. From Figure 2.2b, at equilibrium both the forward and reverse reactions have the same activation energy $\Delta G^{\neq}$. Thus, the exchange current density is given by

$$j_0 = nFC_r f e^{-\left(\Delta G^{\neq}/RT\right)}, \tag{2.9}$$

where the pre-exponential term of Equation 2.7 has been compressed to f. The forward and reverse activation energies $\Delta G^{\neq}$ are the same in this example by virtue of the transition state being symmetrical. This is not always the case however and so a symmetry factor β is used for the general case. β is a measure of the asymmetry of a transition state in that it measures the fraction of a change in potential of the electrode that promotes the forward reaction. β takes a value between 0 and 1 and the fraction of the potential that would promote the reverse reaction is given by $(1 - \beta)$. If, as shown in Figure 2.2, the transition state is symmetrical, then β is 0.5 and the forward and reverse reactions are promoted equally by an increase in electrode potential. This is the case with most catalysts as they promote the oxidation and reduction directions of a half reaction equally by lowering the activation energy (due to a lowering of the transition state). So it is a reasonably safe assumption that β is 0.5, except that this applies to only a single-electron transfer reaction. If there are multiple and sequential electron transfer reactions in a mechanism, β may still be 0.5 if one step is significantly slower and thus the rate-determining step; however, this is not always the case.

Because of this, β is often replaced by an experimental parameter called the charge transfer coefficient α, which does not necessarily sum to 1 for the forward and reverse coefficients, unlike for the symmetry factor β. For this reason, the experimental value αn is often quoted instead of $\alpha 2$.

Since, from thermodynamics, $E = -\Delta G/nF$ and including the charge transfer coefficient, our expression for the exchange current density becomes

$$j_0 = nFC_{\mathrm{r}} f_1 \mathrm{e}^{((\alpha_1 nFE_0)/RT)} = nFC_{\mathrm{p}} f_2 \mathrm{e}^{((-\alpha_2 nFE_0)/RT)}, \tag{2.10}$$

where α_1 and α_2 are the charge transfer coefficients for the forward and reverse reactions, respectively, and E_0 is the reversible equilibrium potential for the given half reaction. By rearranging Equation 2.10 and taking the natural logarithm, it is shown that

$$E_0 = \frac{RT}{nF} \ln\left(\frac{f_1}{f_2}\right) - \frac{RT}{nF} \ln\left(\frac{C_{\mathrm{r}}}{C_{\mathrm{p}}}\right), \tag{2.11}$$

which is the Nernst equation. This is expected as any kinetic theory should reduce to a thermodynamic one when at equilibrium.

2.2.2 Butler–Volmer Kinetics

At dynamic equilibrium there is no net current flowing; hence, in order to generate a useful current (or charge transfer rate), the forward, electron-producing reaction must once again be more favored than the reverse reaction. To do this, the situation must be forced from the equalized potential created by the charge double layer to a state where the potential of the products is lower than that of the reactants (as shown in Figure 2.2). This is achieved by sacrificing some of the electrode potential to drive a potential difference between the reactants and products, and hence a current. This is the source of the activation overpotential (η_{act}), the voltage sacrificed to overcome the equalizing effect of the charge double layer and induce net charge transfer from a state of dynamic equilibrium. If we consider applying an overpotential of η to an electrochemical half reaction such that the resulting potential is

$$E = \eta + E_0, \tag{2.12}$$

the overall net current density is

$$j = j_1 - j_2 = nFC_r f_1 \mathrm{e}^{((\alpha_1 nF(\eta + E_0))/RT)} - nFC_p f_2 \mathrm{e}^{((-\alpha_2 nF(\eta + E_0))/RT)}. \tag{2.13}$$

From Equation 2.10 we can see that our two definitions of exchange current density occur in Equation 2.13, meaning it simplifies to yield

$$j = j_0 \left[\mathrm{e}^{((\alpha_1 nF\eta)/RT)} - \mathrm{e}^{((-\alpha_2 nF\eta)/RT)}\right]. \tag{2.14}$$

This is the Butler–Volmer (BV) equation and is widely used to model fuel cell reactions. It should be noted that all of the above derivations refer to just one

half reaction at just one of the electrodes and the BV equation should be applied to each electrode individually. The HOR at the anode and the ORR at the cathode will have different exchange current densities, charge transfer coefficients, and activation overpotentials, but are linked through the conservation of charge, meaning that the total cell current is the same as the cathode current as well as the anode current: $i_{\text{cell}} = i_{\text{c}} = i_{\text{a}}$. Because of this, we can equate the two BV equations at each electrode:

$$j_{0,a}\left[e^{\left((\alpha_{,a1}nF\eta_a)/RT\right)} - e^{\left((-\alpha_{2,a}nF\eta_a)/RT\right)}\right] = j_{0,c}\left[e^{\left((\alpha_{1,c}nF\eta_c)/RT\right)} - e^{\left((-\alpha_{2,c}nF\eta_c)/RT\right)}\right]. \tag{2.15}$$

In this way the overpotential of both the cathode and the anode will adjust to drive the desired current density from the fuel cell, with the negative polarization of the cathode and the positive polarization of the anode sacrificing more and more of the reversible potential of the cell until no more is left and the limiting current is reached.

2.2.3 Exchange Current Density

The exchange current density is an extremely important parameter that has a dominating influence on the kinetics of electrochemical reactions. It reflects the rate of charge transfer, and thus a high j_0 is desired for facile electrode kinetics and therefore minimized activation potential losses. The definition of exchange current density given in Equation 2.10 is a rather simplistic one, given that it does not account for changes in the reactant and product concentrations during reaction and does not explicitly show the effect of temperature on j_0. The surface area and loading of the catalyst can also be accounted for to give a definition of j_0 as follows:

$$j_0 = j_0^0 a\left(\frac{C_{\text{r}}}{C_{\text{r}}^0}\right)e^{\left[-(E_0/RT)(1-(T/T_0))\right]}, \tag{2.16}$$

where j_0^0 is a reference exchange current density measured at a reference temperature T_0 and a reference concentration C_{r}^0. The parameter a is a roughness factor given as the ratio between the actual electrochemical surface area of the catalyst and the geometric surface area of the electrode. From Equation 2.16 we can see that the exchange current density is an exponentially increasing function of temperature, and though the BV Equation 2.14 suggests ostensibly that there should be higher activation losses with higher temperature, in fact the effect of increasing temperature is to greatly increase j_0 and so significantly decrease kinetic losses, in a highly nonlinear way. Thus, fuel cells operating at higher temperatures will tend to have greatly reduced activation losses.

Though the exchange current density is not an intrinsic property of the catalyst, it is strongly related to the catalyst type. Increasing the j_0 of a catalyst/

reaction is highly desirable for good fuel cell performance and can be achieved in the following ways:

- Increase the reactant concentration
- Decrease the activation energy E_0
- Increase the temperature
- Increase the roughness factor a

Increasing the reactant concentration has a minor effect on the thermodynamics of the reaction (due to the logarithmic form of the Nernst equation), but it can have a significant benefit on the kinetics of a reaction (linear). For this reason, fuel cells are often operated on pure oxygen as the partial pressure of oxygen in air is only 0.2, and so the exchange current density is reduced when operating with air.

Decreasing the activation energy represents the catalyst's influence on j_0. The catalyst can do this by offering a favorable surface for reaction and stabilizing the transition state, giving a lower activation barrier. The strength of bonds between the catalyst and the adsorbed species is an important consideration when looking for a suitable catalyst. The bond strength needs to be "just right," in that it is strong enough to hold the reactant species to the catalyst in the first place, giving greater chance of reaction, but not so strong that it is difficult to break and form products, which would mean lots of immovable adsorbed reactants and a reduction in the number of available sites for reaction. This is often shown by a so-called volcano plot, with platinum group metals generally having the optimum intermediate strength bonds (Figure 2.3).

In general, the activation energy is also affected by the complexity of the reaction, with more complex mechanisms incurring much greater activation losses than for more simplistic ones. For this reason, the ORR is much slower than the very facile HOR and usually contributes the majority of the activation losses in an acidic PEM fuel cell (Figure 2.4).

The HOR in acid solution is considered to proceed through either the Tafel–Volmer or Heyrovsky–Volmer mechanisms, depending on the nature of the adsorption step. If it is a purely chemical process, the mechanism is Tafel–Volmer and if it is a combined chemical and electrochemical process, it is Heyrovsky–Volmer [3].

$$H_2 + M_{cat} \rightleftharpoons 2M_{cat}H_{chem} \text{ (Tafel)} \tag{2.17}$$

$$M_{cat}H_{chem} \rightleftharpoons M_{cat} + H^+ + e^- \text{ (Volmer)} \tag{2.18}$$

$$H_2 + M_{cat} \rightleftharpoons M_{cat}H_{chem} + H^+ + e^- \text{ (Heyrovsky)} \tag{2.19}$$

As already discussed, increasing the temperature will increase the exchange current density. The physical reason for this is that a higher proportion of the reactant molecules will have sufficient energy to react to give products.

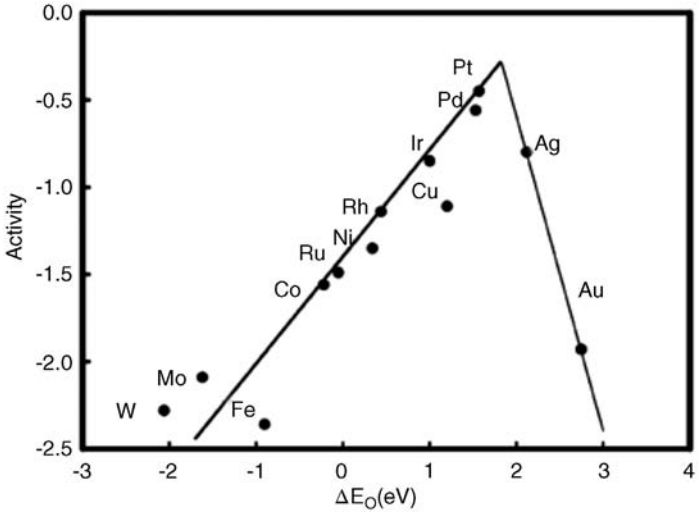

Figure 2.3 Volcano plot of activity of various transition metals for the ORR as a function of binding energy of the O atom to the catalyst. From Ref. [1].

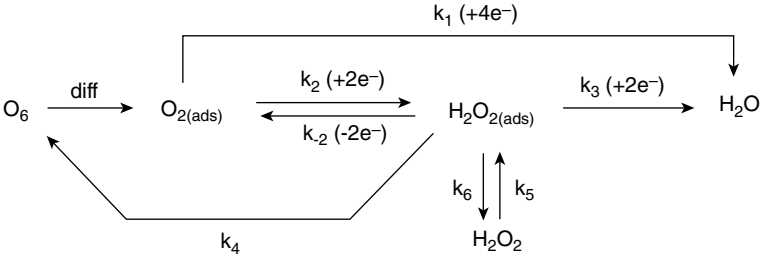

Figure 2.4 The possible reaction mechanistic pathways for oxygen reduction. The direct four-electron pathway (k_1) is desired as it is more efficient and does not generate the potentially damaging peroxide intermediate. Reproduced from Ref. [2].

Increasing the roughness factor a is the equivalent of increasing the electrochemical surface area of the catalyst, that is, increasing the number of surface sites available for reaction. This will obviously increase the exchange current density as more reactions can take place per second. Roughness factors for carbon-supported platinum electrodes (a widely used fuel cell catalyst) vary between 600 and 2000 [4].

2.2.4
The Fuel Cell Polarization Curve

The activation overpotential described in the Butler–Volmer equation can be thought of as a reduction in the voltage of a fuel cell from its theoretical thermodynamic voltage that must be incurred in order to operate at a useful current

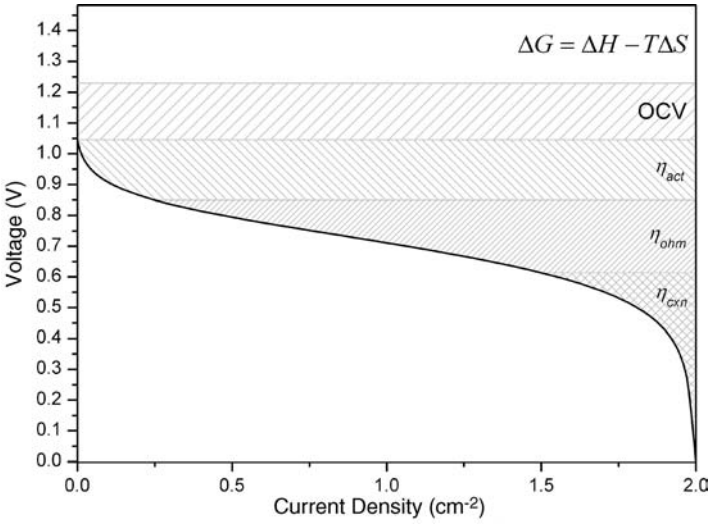

Figure 2.5 An example polar curve, modeled from the preceding treatment of fuel cell behavior, showing regions where the decrease in voltage from the value given by the enthalpy of formation of H_2 have most influence; entropy, internal currents, kinetic losses, resistive losses, and mass transport losses, respectively.

density. It is not the only loss of voltage that occurs during operation of a fuel cell; there are also losses due to ohmic resistances, mass transport limitations, and open-circuit losses. The origins of these overpotentials will be described in more detail elsewhere in the book, but with all the various overpotentials and voltage losses accounted for, a description of how a fuel cell's voltage changes with current density can be formulated, resulting in a fuel cell polarization (or "polar") curve. The total cell voltage is given by

$$E_{\text{cell}} = E_{\text{thermo}} - \eta_{\text{act}} - \eta_{\text{ohm}} - \eta_{\text{conc}} - \eta_{\text{OCV}}, \tag{2.20}$$

where E_{thermo} is the thermodynamically predicted potential at the given temperature and pressure and η_{act}, η_{ohm}, η_{conc}, and η_{OCV} refer to the losses due to activation, ohmic resistance, mass transport, and internal currents, respectively, as described in the previous sections. A typical polar curve is shown in Figure 2.5. It should be noted that although the curve can be roughly segregated into domains where each of the losses is most influential, losses that are a function of operating current (η_{act}, η_{ohm}, and η_{conc}) have an influence across the full range of the polar curve.

2.3 Alkaline Fuel Cells

Most of the discussion so far has pertained to acidic PEM fuel cells as they have been the main focus of low-temperature fuel cell research for the last 20 years

or so. They have many advantages warranting this focus, but also some disadvantages, the major one being the sluggish kinetics of the ORR in acid media. As the kinetics of the ORR are more facile in alkaline media [5–10], the alkaline fuel cell (AFC) is seen as a potential way to utilize cheaper, nonprecious metal cathode catalysts such as Ag [11,12], Au (both unstable in highly acidic media) [13], or Ni [14,15], or to simply allow lower cathode loading of Pt.

2.3.1 The ORR Mechanism

The key step in the reduction of oxygen at a catalytic surface is the breaking of the O−O bond that requires four coupled proton and electron transfers, opening up the possibility of many side reactions and products (see Figure 2.4) [6]. The complexity of the ORR and its numerous potential side products means that it is still relatively poorly understood, although the consensus is that it proceeds either via a direct four-electron reduction pathway or via a peroxide intermediate in a 2 + 2 "serial" four-electron pathway [16–18].

The direct four-electron pathway (Equation 2.21) requires breaking of the O−O bond before the first electron transfer can occur (considering the rate-determining step [12]), and as the dislocation energy of O_2 is large, this is only energetically favorable with a strong Cat–O bond to repay the energy required to break the initial bond (and incurring a significant overpotential). The energetically favored pathway is therefore the so-called serial four-electron pathway (Equations 2.22 and 2.23): a two-electron reduction to peroxide and then a further two-electron reduction of the peroxide to water (as the dislocation energies of the O_2^- and O_2^{2-} anions are lower than that of O_2) [11].

Studies by Markovic *et al.* suggested that the ORR on Pt surfaces in acid proceeds via the series pathway, but the presence of adsorbed anions and underpotentially deposited hydrogen can prevent the second two-electron reduction of peroxide from occurring properly, meaning a certain percentage of the reaction stops at the peroxide intermediate [19–21]. The strongly adsorbed anion reduces the number of adjacent Pt sites available for O_2 adsorption and O−O bond breaking [18] and manifests itself in the analysis as n being less than 4 (i.e., some percentage of reactant does not proceed fully to four-electron reduction into water). These multiple steps and the possibility of desorption of peroxide intermediates mean that the ORR has poor kinetics, with only Pt offering reasonable catalysis.

It is often stated in the literature that the ORR kinetics are more facile in alkaline media [10,22–25], but it is not fully explained why this might be the case and is often attributed to anion adsorption effects stemming from electrolyte choice and experiments in aqueous electrolytes [11,26,27]. As the polymer electrolytes employed in fuel cells do not have mobile anions, these sorts of fundamental ORR studies may not be so applicable to a working fuel cell environment [27], although Srinivasan *et al.* suggest that the kinetics in AFCs are still faster than in acidic PEM fuel cells [28]. The morphology and type of Pt catalyst (single crystal, polycrystalline, or Pt/C) can also have a large effect on the kinetics and reported

exchange current densities for the ORR [27,29–31], with Pt bulk surfaces showing higher activity for ORR than Pt nanoparticles [32,33]. Nevertheless, although some studies show a similar activity for Pt in acid and alkaline [34] and suggest that Pt or Pt/C are still the best catalysts for ORR in alkaline [35], there is potential for utilization of cheaper cathode catalysts in alkaline fuel cells [5–9].

Blizanac *et al.* [11,12] studied the pH effect of ORR on silver single crystals with a rotating ring disk electrode (RRDE) allowing the detection of intermediate species and found that in alkaline electrolyte, the ORR proceeds almost entirely through a four-electron pathway with very little peroxide intermediate detected. In contrast, acidic electrolyte required high overpotentials to prevent the two-electron pathway (producing peroxide) from dominating, and the onset potential for the ORR was also higher than in alkaline. ORR on gold is also known to be significantly better in alkaline solution than acid, with the Au_{100} surface showing selectivity for the four-electron pathway [36]. In alkaline, the direct pathway is given by

$$O_2 + 2H_2O + 4e^- \rightarrow 4OH^- \tag{2.21}$$

and the serial pathway by

$$O_2 + H_2O + 2e^- \rightarrow HO_2^- + OH^- \tag{2.22}$$

followed by

$$HO_2^- + H_2O + 2e^- \rightarrow 3OH^- \tag{2.23}$$

Carbon-supported catalysts (e.g., those employed in fuel cell electrodes) can show potentially very different behavior for the ORR than that of the bulk metal. Yang *et al.* [37] showed that Pd/C catalysts in alkaline had high activity for ORR, and that the carbon support itself is active for the two-electron reduction of O_2 to peroxide (which can then migrate to the Pd particles for subsequent two-electron reduction to water). It is shown that all carbon materials have some ORR activity in alkaline solution (but none in acid), normally for the two-electron reduction to peroxide, although some oxidized carbon surfaces can complete the serial reduction to water at higher overpotentials [24,38–40].

Thus, the alkaline fuel cell is seen as a way to utilizing much cheaper cathode catalysts and thereby reducing the cost of fuel cells for commercialization.

2.3.2 The HOR in Alkaline

The kinetics of the hydrogen oxidation reaction in acidic PEM fuel cells above room temperature are often so fast that they contribute a negligible voltage to the overall activation overpotential, which is therefore often assumed to be wholly attributable to the ORR [41]. This allows catalyst loadings on the anode to be as low as $0.05\,mg_{Pt}\,cm^{-2}$ without affecting overall fuel cell performance significantly [42] and means that catalyst development is mainly focused on the cathode. However, in alkaline media, the HOR on polycrystalline Pt has been

suggested to have an exchange current density two orders of magnitude lower than that in acid [43], and so the activation polarization at the anode in alkaline fuel cells cannot be negated so easily [28]. In fact, in order to take advantage of the ability to use cheaper cathode catalysts in AFCs, anode HOR catalysis is a vitally important and oft-neglected area of required improvement [34,44].

The mechanism of HOR is thought to follow a similar Tafel–Volmer or Heyrovsky–Volmer mechanism, as discussed in Section 1.2.3, except with OH^--mediated reactions:

$$H_2 + M_{cat} \rightleftharpoons 2M_{cat}H_{chem} \text{ (Tafel)} \tag{2.24}$$

$$M_{cat}H_{chem} + OH^- \rightleftharpoons M_{cat} + H_2O + e^- \text{ (Volmer)} \tag{2.25}$$

$$H_2 + M_{cat} + OH^- \rightleftharpoons M_{cat}H_{chem} + H_2O + e^- \text{ (Heyrovsky)} \tag{2.26}$$

Single-crystal Pt studies of HOR in alkaline have suggested that the Tafel or Heyrovsky steps are rate determining [45,46]. It is said that there are two states of adsorbed H atoms on electrode surfaces: a strongly bound underpotentially deposited hydrogen H_{UPD}, and the weakly adsorbed reactive intermediate, overpotentially adsorbed hydrogen H_{OPD} [47]. The reason for the slower HOR in alkaline has been attributed to the adsorption of OH species that serves to block H_2 adsorption sites and hinder reaction [18,45] and is even suggested to alter the energetics of the H_{OPD} layer [46].

Sheng *et al.* [34] recently compared the rotating disk electrode (RDE) studies of the HOR in acid and alkaline and those for the carbon-supported Pt (Pt/C) for the first time. RDE studies are used to separate the current into its kinetic- and diffusion-based constituents, as shown by the Levich–Koutecky equation:

$$\frac{1}{i} = \frac{1}{i_k} + \frac{1}{i_d} = \frac{1}{i_k} + \frac{1}{Bc_0\omega^{1/2}} \tag{2.27}$$

where B is a constant given by $0.62nFD^{2/3}\nu^{-1/6}$, in which D is the diffusion coefficient and ν is the kinematic viscosity of the electrolyte, c_0 is the solubility of the reactant, and ω is the rotation rate of the disk electrode in rad^{-1}. In this way, varying the rotation rate of the electrode and plotting the inverse of the current versus $\omega^{-1/2}$ can give an intercept of the inverse of the kinetically controlled current and, therefore, deconvolute the diffusion-controlled and kinetically controlled currents from the overall current, giving valuable information about the kinetics of reaction. Sheng *et al.* [34] showed that for the HOR in acid, RDE experiments follow the diffusion current very closely (meaning essentially infinitely fast kinetics) even with high rotation rates (giving high-diffusion limiting currents), meaning that the HOR in acid is too fast to study properly with RDE and can lead to underestimation of the exchange current densities in literature [3]. On the other hand, the HOR in alkaline deviated significantly from the diffusion-only behavior, meaning that the kinetic currents can be elucidated properly in RDE experiments. These slower kinetics in alkaline were predicted to contribute significant anode overpotentials of ~130 mV if the ultralow loading of Pt used on PEM anodes [42] is employed in AFCs, underlining the need

for anode catalyst development in order to take advantage of potentially cheaper cathode catalysts in AFCs.

The other studies of nonbulk metal HOR in alkaline come from Cabot *et al.* [25,44] who used a Pt-containing gas diffusion electrode (GDE) to closely represent the electrodes of a fuel cell in their RDE experiments. They concluded that at low overpotentials (near the OCV), the Tafel reaction is the rate-determining step in a Tafel–Volmer mechanism, with the diffusion of H_2 becoming rate determining at higher overpotentials. These studies also showed that the exchange current density for HOR is lower in alkaline media for GDE.

In conclusion, the kinetics of the ORR in alkaline give the advantage of cheaper cathode catalysts, but the significant overpotential for HOR requires anode catalyst development in order to fully utilize the potential of the alkaline fuel cell.

2.3.3 The Aqueous Electrolyte AFC

The superior ORR kinetics of the AFC meant that in the early days of fuel cell development, it was the dominant technology, with the pioneering work of Bacon [48] and the use of AFCs in the Apollo space missions. The AFC employs an aqueous KOH electrolyte, usually around a 30 wt% solution, often contained in a matrix (Figure 2.6). As with other H_2/O_2 fuel cells, the HOR occurs at the

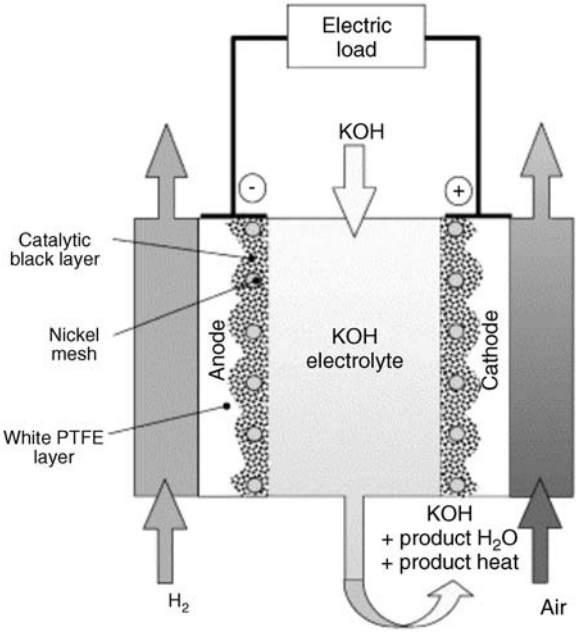

Figure 2.6 Schematic of an aqueous electrolyte AFC. Reproduced from Ref. [10].

anode and the ORR at the cathode, although the half reactions are slightly different in alkaline media as they are mediated by the OH^- anion and not protons:

$$H_2 + 2OH^- \rightleftharpoons 2H_2O + 2e^- \text{ (HOR)} \tag{2.28}$$

$$\frac{1}{2}O_2 + H_2O + 2e^- \rightleftharpoons 2OH^- \text{ (ORR)} \tag{2.29}$$

Giving the same overall redox reaction,

$$H_2 + \frac{1}{2}O_2 \rightleftharpoons H_2O \tag{2.30}$$

Note that 2 mol of water are generated at the anode and one consumed at the cathode, as opposed to 1 mol of water being produced at the cathode in acid systems. This can cause potential flooding and water management issues at the anode. The aqueous, highly caustic, electrolyte presents obvious hazards and is also susceptible to the following carbonation reaction in the presence of CO_2:

$$CO_2 + 2OH^- \rightarrow (CO_3)^{2-} + H_2O \tag{2.31}$$

The carbonate anion can precipitate out of solution in combination with a metal cation and cause blockages in the electrodes and reduction in conductivity of the electrolyte, severely hampering performance, and so only pure, CO_2-free oxygen and hydrogen could be used in these systems. Due to these disadvantages and the improvements in proton-conducting membrane technology, the AFC was overtaken by the PEM fuel cell as the main focus of research. Though there have been recent improvements in AFC technology [49], this chapter concerns the recent developments in solid polymer electrolyte alkaline technology, and so further details on AFC progress can be found in Refs [10,23].

2.3.4 The AAEM Fuel Cell

Recent developments in AAEMs have opened up the possibility of an alkaline analog of the acidic solid polymer electrolyte fuel cell. This could utilize the benefits of the alkaline cathode kinetics and at the same time eradicate the disadvantages of using an aqueous electrolyte. As the AAEM is also a polymer electrolyte membrane (sometimes abbreviated as PEM), some clarity in abbreviations is required. In this chapter, PEM refers only to the proton exchange membrane fuel cells (acidic), AAEM refers to the anion exchange membrane H_2/O_2 fuel cells, and AFC exclusively refers to the aqueous electrolyte alkaline H_2/O_2 fuel cells. Anion exchange membranes are also employed in alkaline direct alcohol fuel cells, discussion of which will refer to them as ADMFC/ADEFC (methanol/ethanol).

2.3.4.1 AAEM Principles

The AAEM fuel cell is based on the same fundamental principles of the PEM fuel cell: direct electrochemical conversion of H_2 to electricity using a solid

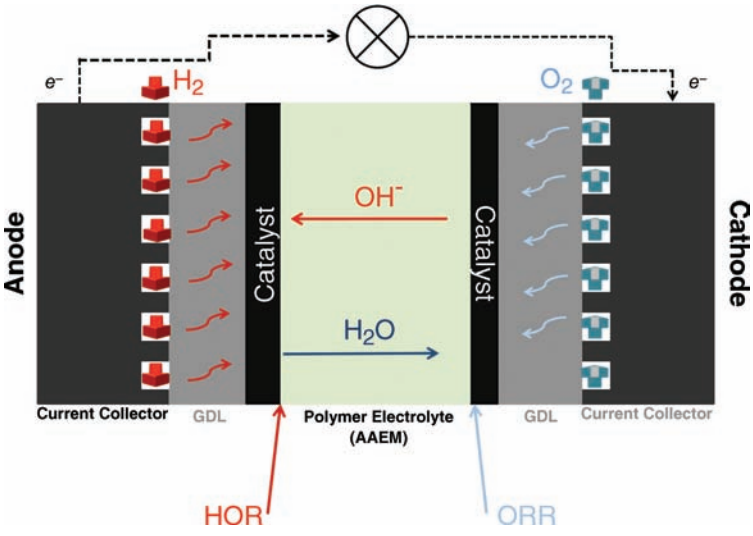

Figure 2.7 The outline of the AAEM alkaline fuel cell (cf. Figure 2.1).

electrolyte, with the key differences being the fundamental half equations (Equations 2.28 and 2.29) and the hydroxide ion-conducting membrane. The schematic of an AAEM fuel cell is shown in Figure 2.7.

The peripheral components of the AAEM fuel cell can be assumed to be the same as in PEM fuel cells, performing the same functions. Water management may be treated differently in AAEM as water is produced on the anode and consumed at the cathode, meaning there is the potential for flooding at the anode and insufficient humidification of the cathode. This is thought to offer the potential for more simple humidification, with the anode "self-humidifying," it might be the case that only the cathode requires humidification (although an interesting recent study showed retained performance when using a dry cathode stream and humidifying the anode stream only, allowing diffusion of water through the membrane to be the sole source of cathode humidification [50]).

The other major difference from the PEM system is that the membrane conducts hydroxide ions. As diffusion coefficients are roughly four times larger for H^+ than OH^-, the ionic resistivity of AAEMs is often significantly higher than that of Nafion and may require doping of the membrane with KOH solution to increase conductivity [7].

2.3.4.2 Alkaline Membranes

The use of anion exchange membrane in fuel cells is a relatively nascent technology and as such has no Nafion-like industry leader that is ubiquitous in the field [51]. A recent review of alkaline membranes by Merle [52] highlights the vast number and variety of alkaline membranes in the literature, and the comparatively few commercially available membranes. As AAEMs are solid, they contain

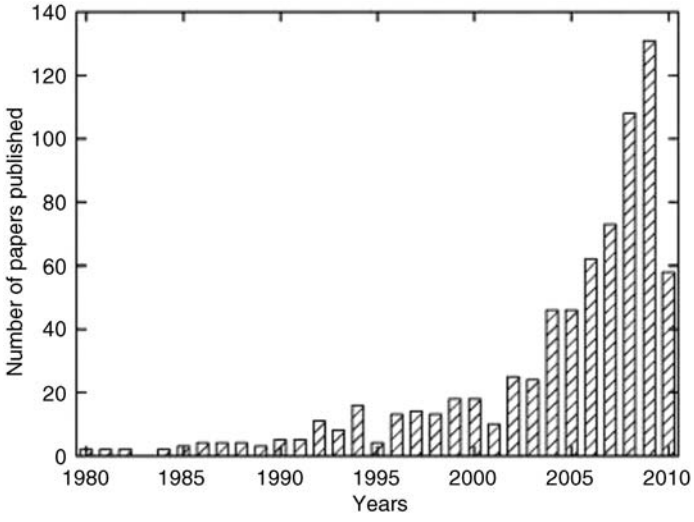

Figure 2.8 The recent increase in alkaline fuel cell publications. Reproduced from Ref. [52].

no mobile cations and so even though carbonates are still formed from the reaction of CO_2 with OH^-, there should be little precipitation of solid carbonates in the membrane. The prospect of reduced carbonate issues and lack of concentrated aqueous electrolyte in AAEMs has driven research into membrane development and solid alkaline fuel cell technology in recent years (Figure 2.8).

Just as Nafion contains negatively charged sulfonic acid groups to conduct positively charged protons, AAEMs must contain positively charged groups to conduct the negative hydroxide ion. As already mentioned, the conductivity of AAEMs is lower than that of PEMs [53]. One way of increasing the conductivity is to include more cationic groups in the polymer, but this often has the effect of reducing the mechanical strength and chemical stability of the membrane. The most common functional group in AAEMs is the quaternary ammonium group, R_4N^+ [54], which can undergo the following E2 elimination reaction (Hofmann elimination) in the presence of hydroxide (Figure 2.9).

Most work at this point has suggested that this Hofmann elimination is slow below 60 °C, but much faster at higher temperatures, resulting in significant degradation to most AAEMs above 60 °C [55]. This is an obvious limitation for

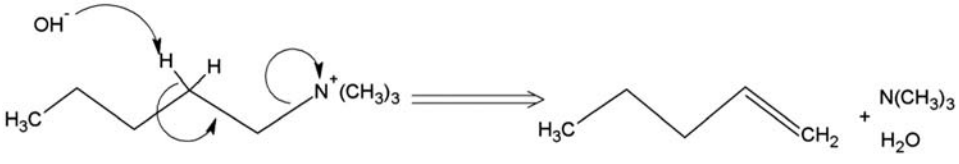

Figure 2.9 The Hofmann elimination of quaternary ammonium groups.

current alkaline membranes as the kinetic benefit of operating at higher temperatures (PEM fuel cells are mostly operated at 80 °C) is not obtainable. The weak basicity of R_4N^+ groups is also thought to contribute to the lower mobility of hydroxide in AAEMs compared with protons in PEMs. Also, although no solid carbonate precipitates, the carbonate anion is still formed, which serves to reduce the concentration of hydroxide in the membrane and may be a contributory factor to the reduced conductivity [52,56].

There are many examples of anion exchange membranes in the literature, and of many different types, as summarized in Refs [52,57], but the most promising membranes for fuel cell applications are formed by radiation grafting of R_4N^+ groups onto polymer backbones [58–66] or chemical modification of existing polymers [51,67–70]. A study by Varcoe in 2007 represented the first AAEM with conductivity over the desired mark of 10 mS cm^{-1} required for viable solid alkaline fuel cells, although the membrane required high levels of humidification to maintain good conductivity [71]. Studies previous to this often had to submerge membranes in KOH solution in order to attain sufficient conductivity [7,72]. The highest conductivity membrane was reported in 2011 by Tanaka *et al.* for use in hydrazine fuel cells, with a maximum conductivity of 114 mS cm^{-1} at 80 °C [73]. A good AAEM should have the following desirable properties:

- High chemical, mechanical, and thermal stability under operating conditions
- High conductivity of OH^- ions, >10 mS cm^{-1}
- Low electrical conductivity
- Low gas permeability
- Low thickness
- Good performance under various humidification levels

The electrodes in PEM fuel cells contain a certain amount of Nafion polymer solution to act as a binder in the ink and also to introduce some H^+ conductive substance to the triple-phase boundary [74]. For AAEM fuel cells, there is a need for an analogous ionomer solution for use in the catalyst layer [54] and so it is an important consideration for development of good electrodes for the alkaline fuel cell [64].

In summary, the improvement of AAEMs is an ongoing area of research and development. There is no one membrane of choice currently and the conductivity and stability of some membranes are still an issue. However, there are signs that good AAEM performance is close and so catalyst development for the AAEM fuel cell is required to match performance and cost of the current PEM fuel cell technology.

2.3.4.3 AAEM Fuel Cell Examples

As a new and underdeveloped technology, there is a shortage of examples of AAEM fuel cells in the literature. Some of the pioneering work in alkaline membranes and AAEM fuel cells come from the University of Surrey and the work of Varcoe and Slade [8,13,51,58,59,61,62,64–66,71,75–78]. They mainly use

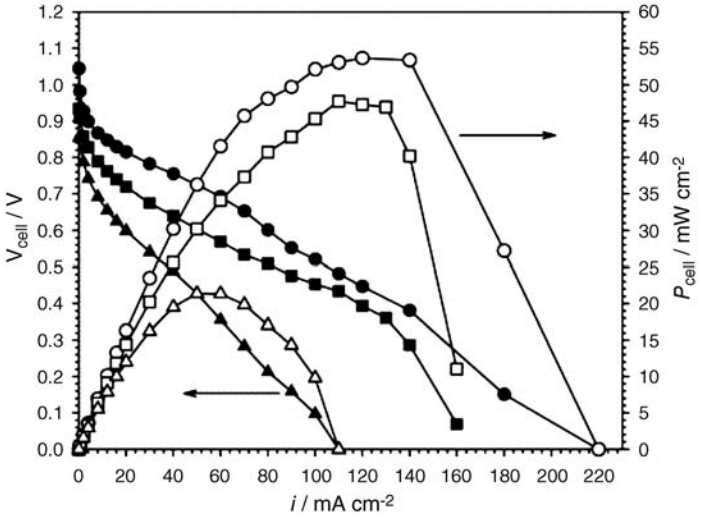

Figure 2.10 Fuel cell polarization curves (filled symbols) and power densities (empty symbols) of Pt (circles), Ag (squares), and Au (triangles) cathodes using pure oxygen. Reproduced from Ref. [8].

radiation-grafted quaternary ammonium membranes. Peak power densities of around 55 mW cm^{-2} were obtained using platinum cathodes and anodes and pure O_2 as an oxidant (corresponding to roughly 90 mA cm^{-2} at 0.6 V) [66], with worse performance when employing Au or Ag cathode catalysts (Figure 2.10) [8]. Operating a H_2/Air fuel cell with a carbonate-tolerant membrane yielded lower power densities of ~38 mW cm^{-2}, but showed better performance when the membrane was in carbonate form than when it was in hydroxide form, perhaps due to fact that the ORR proceeds more quickly in alkaline carbonate than in aqueous KOH solution [75]. A similar trend was observed for Zhou *et al.* in 2009, although with very low power densities of only 4 mW cm^{-2} [79].

Recent improvement in their membrane technology produced peak power densities of 230 mW cm^{-2} (Figure 2.11) with Pt cathodes and pure O_2 for the thinnest of the membranes (17 μm fully hydrated) [13]. It is thought that the improved performance on decreasing membrane thickness is due to the increased water crossover from the anode to the cathode, where it is consumed (Equation 2.29). Au and Ag cathodes were again tested in this study, giving reduced performance compared with Pt.

They also developed a novel reference electrode for use in an AAEM fuel cell that allowed decoupling of the cathode and anode polarizations from the overall cell polarization. It was shown that the anode polarization was significantly higher than the cathode polarization, contrary to the situation in PEM fuel cells (Figure 2.12). In addition to the already discussed slower HOR kinetics in alkaline, it is thought that flooding in the anode of AAEM fuel cells can cause high mass transport polarization, even at low current densities (note that the thicker

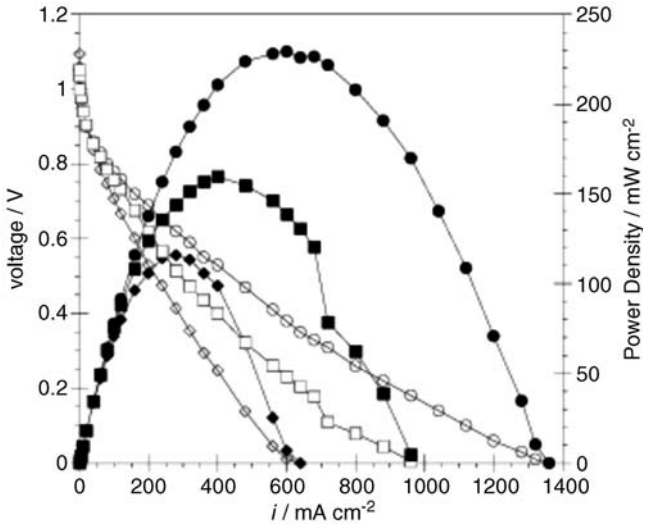

Figure 2.11 Fuel cell polarization curves (empty symbols) and power densities (filled symbols) of Pt cathodes in pure oxygen showing the effect of membrane thickness on performance. The performance improves in the order 85 μm (diamonds), 46 μm (squares), and 17 μm (circles). Reproduced from Ref. [13].

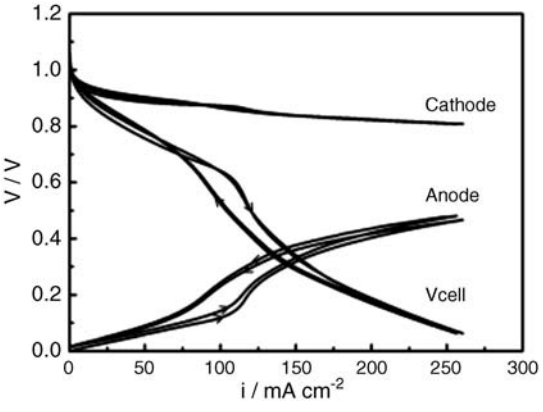

Figure 2.12 The overall polarization curve (Vcell) and its cathode and anode constituents, obtained using a novel Pd-coated Pt wire as a reference electrode. The anode polarization is significantly greater than that of the cathode. Reproduced from Ref. [76].

80 μm membrane was used in this study). They also demonstrated that as water is a reactant in the ORR (unlike in PEM), the cathode electrode design is important for good performance. Using PTFE-free cathodes, they achieved a power density of 125 mW cm^{-2} and showed a small catalytic effect from carbon only in the alkaline cell [78]. This highlights the need for greater attention to water management and catalyst layers in AAEM FCs [76–78].

Some of the earliest work on AAEM fuel cells was conducted by Agel *et al.* in 2001 [7]. They used a KOH-doped membrane, carbon-supported Pt on nickel foam electrodes, and H_2/O_2 at atmospheric pressure and ambient temperature to obtain a current density of ~25 mA cm^{-2} at 0.6 V. This study demonstrated the need for good ionic contact between the electrodes and the membrane, as the performance increased to just under 60 mA cm^{-2} at 0.6 V when an interfacial KOH gel was applied between them.

Lu *et al.* demonstrated the first fully nonplatinum AAEM cell in 2008 by using a chromium-decorated nickel cathode and a sliver anode [80]. Their quaternary ammonium polysulfone membrane was dissolved in solvent allowing control of the thickness of the cast film and impregnation into the electrode layers. The peak performance of 50 mW cm^{-2} was achieved using humidified H_2/O_2 at 60 °C with a backpressure of 1 atm.

Park *et al.* showed that a high loading of sliver (2.0 mg cm^{-2}) could produce a similar peak power density of 30 mW cm^{-2} as a Pt cathode in their aminated polysulfone membrane fuel cells, using humidified H_2/air at 60 °C (Figure 2.13) [22]. They also observed a high OCV of ~1.05 V, which, given the discussion in section, might indicate higher exchange current densities or lower fuel crossover reducing the voltage loss from OCV (Varcoe also observed a similar effect [8]).

In 2009 Gu *et al.* used a quaternary phosphonium-containing ionomer solution in conjunction with a commercially available AAEM to again demonstrate the importance of good ionic conductivity between the electrode and membrane layers [54]. A marked difference in performance was seen between MEAs with

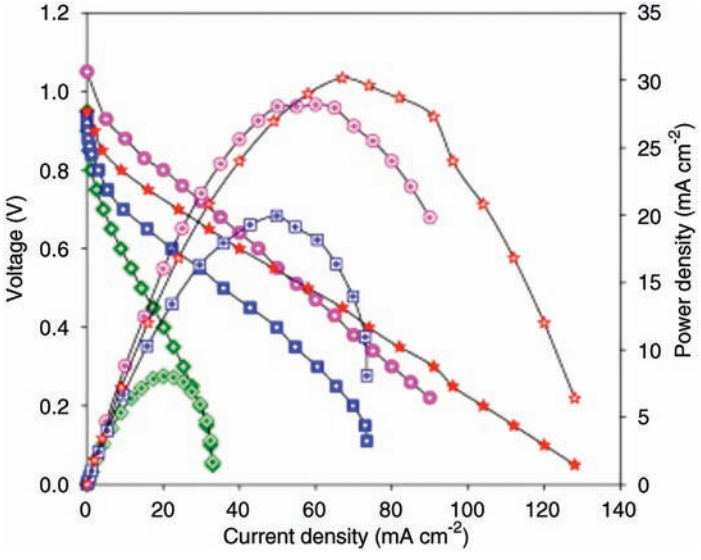

Figure 2.13 Polar curves and power densities of AAEM fuel cells with Pt anodes (0.5 mg cm^{-2}) and silver cathodes at 0.5 mg cm^{-2} (green), 1 mg cm^{-2} (blue), and 2 mg cm^{-2} (red) and with a Pt cathode (0.5 mg cm^{-2}) (pink). Reproduced from Ref. [22].

and without the ionomer solution, with a peak power density of nearly 200 mA cm^{-2} obtained at 80 °C with backpressurized H_2/O_2 gases. Mamlouk *et al.* showed a similar effect on their in-house membrane and concluded that the optimal ionomer content in the catalyst layer depended on several factors such as thickness of electrode and O_2 partial pressure. They also suggested that due to flooding problems, the anode layer should be thicker than the cathode layer [81].

A year later in 2010, the best performance from an AAEM fuel cell was demonstrated by Piana *et al.* [82]. They used a commercially available membrane in conjunction with a novel in-house ionomer solution as a catalyst binder and H_2/air (CO_2-free) at 50 °C. A peak power density of 400 mW cm^{-2} was obtained when using Pt on the anode and cathode, and 200 mW cm^{-2} when using a non-disclosed transition metal on carbon catalyst as the cathode. They also demonstrated the very interesting effect of CO_2 on the system; at low current densities, CO_2 causes the expected drastic reduction in performance due to reaction with OH^- and subsequent reduction in conductivity. However, at higher current densities, more OH^- ions are produced by the electrochemical half reactions that help to overcome this issue by a so called self-purging mechanism (Figure 2.14). There is a clear change in the polar curve representing an increase in membrane conductivity at higher current densities (although by this point a large amount of operating voltage has been lost). This has implications for the conditioning of AAEM fuel cells, with Varcoe suggesting that the cells should be quickly brought to high current densities and then polar curves taken by reducing the load back to OCV (this method produced better performance than increasing the current load from OCV) [78].

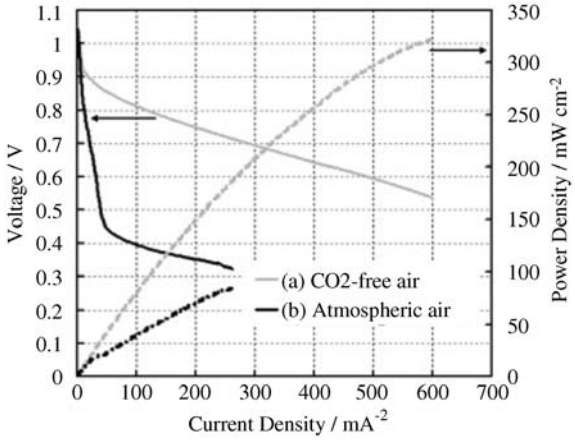

Figure 2.14 Polar and power density curves showing the effect of CO_2 on the performance of the membranes. The performance in CO_2-free air (gray) is good, but the carbonate effect has a drastic effect on performance in atmospheric air (black). On reaching higher current densities, this effect is reduced, as shown by the change in gradient of the black polar curve to match that of the CO_2-free air polar curve. Reproduced from Ref. [82].

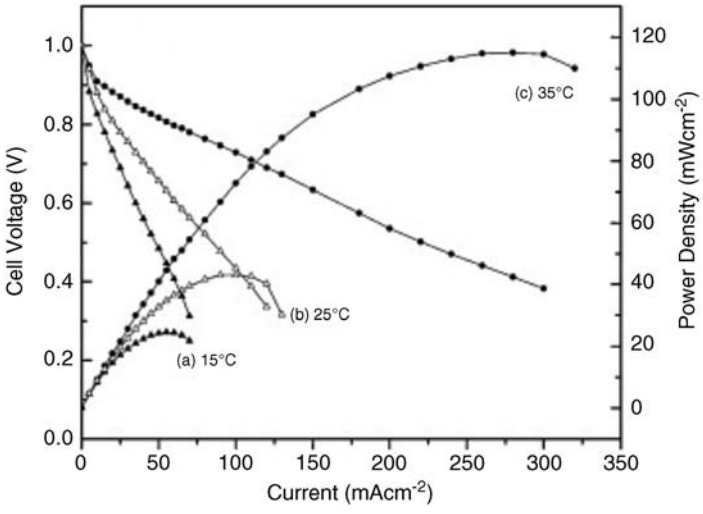

Figure 2.15 The effect of temperature on AAEM resistance and polarization performance. Reproduced from Ref. [51].

The most recent work comes from Cao *et al.* in 2012 [51]. They developed a poly(methyl vinyl ether-*alt*-malic anhydride) (PMVMA) membrane by chemical grafting of ammonium groups to the polymer. The membrane was stable up to 150° and showed increasing ion conductivity from room temperature to 60 °C. Their peak power density of 155 mW cm^{-2} was obtained at 35 °C and on H_2/O_2 and demonstrated a vast improvement over lower temperatures (and hence higher ohmic resistances) (Figure 2.15).

Some of the most promising work on AAEM fuel cells come from the Tokuyama Corporation, who are one of the commercial suppliers of alkaline membranes. Unfortunately, they publish only short conference proceedings with little details, but the work shows encouraging signs for solid alkaline fuel cells [9,50,56,63,83–85]. They have produced quaternary ammonium-containing membranes with good conductivity of ~40 mS cm^{-1} and can control the thickness between 10 and 40 μm [63]. They have achieved a peak power density of 325 mW cm^{-2} using Pt/C anodes and cathodes and CO_2-free air as the oxidant and have also confirmed a similar self-purging effect, as discussed by Piana *et al.*, at higher current densities [9,83,86]. Tokuyama were also the first to show elevated operating temperatures in AAEMs, getting improved performance, and 200 h stability from their membranes at 80 °C [84]. In 2011 they demonstrated a very interesting, and ostensibly counterintuitive, comparative performance when there was no humidification of the cathode gas stream. As the OOR in alkaline consumes water as a reactant, it is assumed to need good humidification of the cathode, but this study showed that water flux from the anode to the cathode increases when the cathode is dry, compensating for the lack of water. They also showed the catastrophic effect of not humidifying either gas stream, proving that the 2 mol of water produced by the anode HOR is not enough in itself to provide

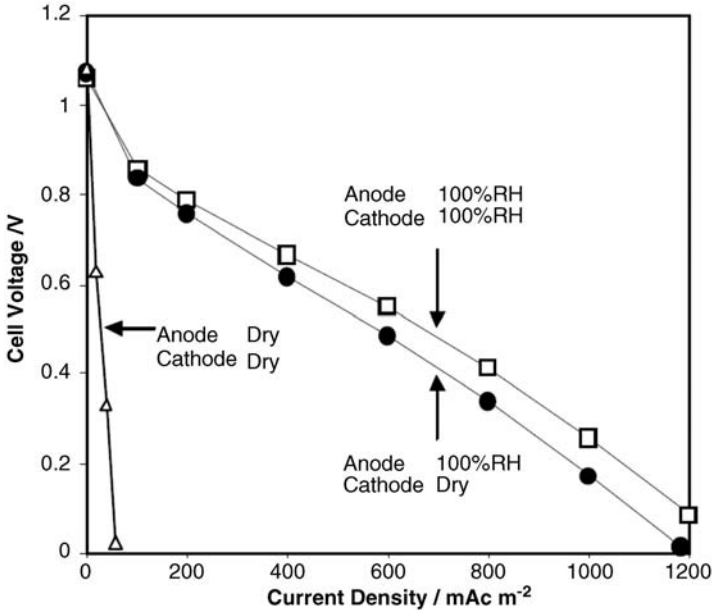

Figure 2.16 The effect of humidification on the Tokuyama AAEM. Humidification of the anode stream only (circles) shows comparable performance with humidification of both streams (squares). When there is no humidification of either gas stream (triangles), the performance is drastically reduced. Reproduced from Ref. [50].

sufficient humidification for the membrane (Figure 2.16) [50]. The potential for partially nonhumidified operation is important if AAEMs are to be used in portable devices such as automobiles.

2.4 Summary

In summary, solid alkaline fuel cells using hydrogen as a fuel represent a potential improvement in performance and reduction of cost over acidic PEM fuel cells. The technology is in the early stages of development, shown by the lack of studies to date and the variation in techniques and results in these studies, and requires further research with bespoke methods applied to the alkaline case (as opposed to trying to apply acid PEM principles to what might be a very different technology) to attain the performance levels achieved from state-of-the-art PEM fuel cells.

- Activation losses in a fuel cell are dictated by the exchange current density of a half reaction, which is a function of the activation energy of the reaction.

- The ORR is faster in the alkaline medium and the HOR is slower, meaning that the potential for alkaline fuel cells to utilize cheaper cathode catalysts must be balanced with anode catalyst considerations.
- The electrochemical half reactions are different in acid and alkaline media:

$H_2 \rightleftharpoons 2H^+ + 2e^-$	Anode, acid
$H_2 + 2OH^- \rightleftharpoons 2H_2O + 2e^-$	Anode, alkaline
$\frac{1}{2}O_2 + 2H^+ + 2e^- \rightleftharpoons H_2O$	Cathode, acid
$\frac{1}{2}O_2 + H_2O + 2e^- \rightleftharpoons 2OH^-$	Cathode, alkaline
$H_2 + \frac{1}{2}O_2 \rightleftharpoons H_2O$	Overall

- The different half reactions lead to different water management considerations in alkaline fuel cells than in PEM fuel cells.
- The use of a solid alkaline membrane negates the dangers of using aqueous alkaline electrolytes and reduces the impact of the carbonation effect.
- Alkaline membranes are not as fully developed as their acid equivalents and more research is required in order to achieve the same performance as that of PEMs. However, they represent a potential route to lower cost fuel cells via deployment of cheaper catalysts.

References

1 Nørskov, J.K., Rossmeisl, J., Logadottir, A., Lindqvist, L., Kitchin, J.R., Bligaard, T., and Jónsson, H. (2004) Origin of the overpotential for oxygen reduction at a fuel-cell cathode. *The Journal of Physical Chemistry B*, **108**, 17886–17892.

2 Wang, B. (2005) Recent development of non-platinum catalysts for oxygen reduction reaction. *Journal of Power Sources*, **152**, 1–15.

3 Chen, S. and Kucernak, A. (2004) Electrocatalysis under conditions of high mass transport: investigation of hydrogen oxidation on single submicron Pt particles supported on carbon. *The Journal of Physical Chemistry B*, **108**, 13984–13994.

4 Li, X. (2006) Principles of fuel cells. *Platinum Metals Review*, **50**, 200.

5 Srinivasan, S., Enayetullah, M.A., Somasundaram, S., Swan, D.H., Manko, D., Koch, H., and Appleby, A.J. (1989) Recent advances in solid polymer electrolyte fuel cell technology with low platinum loading electrodes. *Journal of Power Sources*, **29**, 367–387.

6 Appleby, A.J. (1993) Electrocatalysis of aqueous dioxygen reduction. *Journal of Electroanalytical Chemistry and Interfacial Electrochemistry*, **357**, 117–179.

7 Agel, E., Bouet, J., and Fauvarque, J.F. (2001) Characterization and use of anionic membranes for alkaline fuel cells. *Journal of Power Sources*, **101**, 267–274.

8 Varcoe, J.R., Slade, R.C.T., Wright, G.L., and Chen, Y. (2006) Steady-state DC and impedance investigations of H_2/O_2 alkaline membrane fuel cells with commercial Pt/C, Ag/C, and Au/C cathodes. *The Journal of Physical Chemistry B*, **110**, 21041–21049.

9 Yanagi, H., Watanabe, S., Sadasue, K., Isomura, T., Inoue, H., and Fukuta, K. (2009) Improved performance of alkaline membrane fuel cells based on newly developed electrolyte materials. *ECS Meeting Abstracts*, **902**, 341–341.

10 McLean, G.F., Niet, T., Prince-Richard, S., and Djilali, N. (2002) An assessment of alkaline fuel cell technology. *International Journal of Hydrogen Energy*, **27**, 507–526.

11 Blizanac, B.B., Ross, P.N., and Markovic, N.M. (2007) Oxygen electroreduction on Ag(111): the pH effect. *Electrochimica Acta*, **52**, 2264–2271.

12 Blizanac, B.B., Ross, P.N., and Marković, N.M. (2006) Oxygen reduction on silver low-index single-crystal surfaces in alkaline solution: rotating ring disk(Ag (hkl)) studies. *The Journal of Physical Chemistry B*, **110**, 4735–4741.

13 Poynton, S.D., Kizewski, J.P., Slade, R.C.T., and Varcoe, J.R. (2010) Novel electrolyte membranes and non-Pt catalysts for low temperature fuel cells. *Solid State Ionics*, **181**, 219–222.

14 Bidault, F., Brett, D.J.L., Middleton, P.H., Abson, N., and Brandon, N.P. (2009) A new application for nickel foam in alkaline fuel cells. *International Journal of Hydrogen Energy*, **34**, 6799–6808.

15 Bidault, F., Brett, D.J.L., Middleton, P.H., Abson, N., and Brandon, N.P. (2010) An improved cathode for alkaline fuel cells. *International Journal of Hydrogen Energy*, **35**, 1783–1788.

16 Yeager, E. (1984) Electrocatalysts for O_2 reduction. *Electrochimica Acta*, **29**, 1527–1537.

17 Wroblowa, H.S. (1976) Electroreduction of oxygen: a new mechanistic criterion. *Journal of Electroanalytical Chemistry and Interfacial Electrochemistry*, **69**, 195.

18 Marković, N.M. and Ross, P.N., Jr. (2002) Surface science studies of model fuel cell electrocatalysts. *Surface Science Reports*, **45**, 117–229.

19 Grgur, B.N., Marković, N.M., and Ross, P. N. (1997) Temperature-dependent oxygen electrochemistry on platinum low-index single crystal surfaces in acid solutions. *Canadian Journal of Chemistry*, **75**, 1465–1471.

20 Marković, N.M., Gasteiger, H.A., Grgur, B.N., and Ross, P.N. (1999) Oxygen reduction reaction on Pt(111): effects of bromide. *Journal of Electroanalytical Chemistry*, **467**, 157–163.

21 Stamenkovic, V., Markovic, N.M., and Ross, P.N., Jr. (2001) Structure-relationships in electrocatalysis: oxygen reduction and hydrogen oxidation reactions on Pt(111) and Pt(100) in solutions containing chloride ions. *Journal of Electroanalytical Chemistry*, **500**, 44–51.

22 Park, J.-S., Park, S.-H., Yim, S.-D., Yoon, Y.-G., Lee, W.-Y., and Kim, C.-S. (2008) Performance of solid alkaline fuel cells employing anion-exchange membranes. *Journal of Power Sources*, **178**, 620–626.

23 Bidault, F., Brett, D.J.L., Middleton, P.H., and Brandon, N.P. (2009) Review of gas diffusion cathodes for alkaline fuel cells. *Journal of Power Sources*, **187**, 39–48.

24 Ernest, Y. (1986) Dioxygen electrocatalysis: mechanisms in relation to catalyst structure. *Journal of Molecular Catalysis*, **38**, 5–25.

25 Alcaide, F., Brillas, E., and Cabot, P.L. (2005) Hydrogen oxidation reaction in a Pt-catalyzed gas diffusion electrode in alkaline medium. *Journal of the Electrochemical Society*, **152**, E319–E327.

26 Markovic, N., Gasteiger, H., and Ross, P.N. (1997) Kinetics of oxygen reduction on Pt (hkl) electrodes: implications for the crystallite size effect with supported Pt electrocatalysts. *Journal of the Electrochemical Society*, **144**, 1591–1597.

27 Parthasarathy, A., Srinivasan, S., Appleby, A.J., and Martin, C.R. (1992) Electrode kinetics of oxygen reduction at carbon-supported and unsupported platinum microcrystallite/Nafion® interfaces. *Journal of Electroanalytical Chemistry*, **339**, 101–121.

28 Srinivasan, S., Manko, D.J., Koch, H., Enayetullah, M.A., and Appleby, A.J. (1990) Recent advances in solid polymer electrolyte fuel cell technology with low platinum loading electrodes. *Journal of Power Sources*, **29**, 367–387.

29 Song, C., Tang, Y., Zhang, J.L., Zhang, J., Wang, H., Shen, J., McDermid, S., Li, J., and Kozak, P. (2007) PEM fuel cell

reaction kinetics in the temperature range of 23–120°C. *Electrochimica Acta*, **52**, 2552–2561.
30 Hayden, B.E., Pletcher, D., Suchsland, J.-P., and Williams, L.J. (2009) The influence of support and particle size on the platinum catalysed oxygen reduction reaction. *Physical Chemistry Chemical Physics*, **11**, 9141–9148.
31 Gasteiger, H.A. and Ross, P.N. (1996) Oxygen reduction on platinum low-index single-crystal surfaces in alkaline solution: rotating ring diskPt(hkl) studies. *The Journal of Physical Chemistry*, **100**, 6715–6721.
32 Kinoshita, K. (1990) Particle size effects for oxygen reduction on highly dispersed platinum in acid electrolytes. *Journal of the Electrochemical Society*, **137**, 845–848.
33 Gasteiger, H.A., Kocha, S.S., Sompalli, B., and Wagner, F.T. (2005) Activity benchmarks and requirements for Pt, Pt-alloy, and non-Pt oxygen reduction catalysts for PEMFCs. *Applied Catalysis B: Environmental*, **56**, 9–35.
34 Sheng, W., Gasteiger, H.A., and Shao-Horn, Y. (2010) Hydrogen oxidation and evolution reaction kinetics on platinum: acid vs alkaline electrolytes. *Journal of the Electrochemical Society*, **157**, B1529–B1536.
35 Lima, F.H.B., Zhang, J., Shao, M.H., Sasaki, K., Vukmirovic, M.B., Ticianelli, E.A., and Adzic, R.R. (2006) Catalytic activity–d-band center correlation for the O_2 reduction reaction on platinum in alkaline solutions. *The Journal of Physical Chemistry C*, **111**, 404–410.
36 Adzic, R. (1998) Recent advances in the kinetics of oxygen reduction.
37 Yang, Y.-F., Zhou, Y.-H., and Cha, C.-S. (1995) Electrochemical reduction of oxygen on small palladium particles supported on carbon in alkaline solution. *Electrochimica Acta*, **40**, 2579–2586.
38 Taylor, R.J. and Humffray, A.A. (1975) Electrochemical studies on glassy carbon electrodes: II. Oxygen reduction in solutions of high pH (pH>10). *Journal of Electroanalytical Chemistry and Interfacial Electrochemistry*, **64**, 63–84.
39 Appel, M. and Appleby, A.J. (1978) A ring-disk electrode study of the reduction of oxygen on active carbon in alkaline solution. *Electrochimica Acta*, **23**, 1243–1246.
40 Jürmann, G. and Tammeveski, K. (2006) Electroreduction of oxygen on multi-walled carbon nanotubes modified highly oriented pyrolytic graphite electrodes in alkaline solution. *Journal of Electroanalytical Chemistry*, **597**, 119–126.
41 Neyerlin, K.C., Gu, W., Jorne, J., and Gasteiger, H.A. (2007) Study of the exchange current density for the hydrogen oxidation and evolution reactions. *Journal of the Electrochemical Society*, **154**, B631–B635.
42 Gasteiger, H.A., Panels, J.E., and Yan, S.G. (2004) Dependence of PEM fuel cell performance on catalyst loading. *Journal of Power Sources*, **127**, 162–171.
43 Bagotzky, V.S. and Osetrova, N.V. (1973) Investigation of hydrogen ionization on platinum with the help of micro-electrodes. *Journal of Electroanalytical Chemistry*, **43**, 233–249.
44 Cabot, P.-L., Alcaide, F., and Brillas, E. (2009) Hydrogen reaction at open circuit in alkaline media on Pt in a gas-diffusion electrode. *Journal of Electroanalytical Chemistry*, **626**, 183–191.
45 Markovica, N.M., Sarraf, S.T., Gasteiger, H.A., and Ross, P.N. (1996) Hydrogen electrochemistry on platinum low-index single-crystal surfaces in alkaline solution. *Journal of the Chemical Society, Faraday Transactions*, **92**, 3719–3725.
46 Schmidt, T.J., Ross, P.N., Jr., and Markovic, N.M. (2002) Temperature dependent surface electrochemistry on Pt single crystals in alkaline electrolytes: Part 2. The hydrogen evolution/oxidation reaction. *Journal of Electroanalytical Chemistry*, **524–525**, 252–260.
47 Marković, N.M., Grgur, B.N., and Ross, P.N. (1997) Temperature-dependent hydrogen electrochemistry on platinum low-index single-crystal surfaces in acid solutions. *The Journal of Physical Chemistry B*, **101**, 5405–5413.

48 Bacon, F.T. (1960) The high pressure hydrogen–oxygen fuel cell. *Industrial & Engineering Chemistry*, **52**, 301–303.

49 Brushett, F.R., Naughton, M.S., Ng, J.W.D., Yin, L., and Kenis, P.J.A. (2012) Analysis of Pt/C electrode performance in a flowing-electrolyte alkaline fuel cell. *International Journal of Hydrogen Energy*, **37**, 2559–2570.

50 Isomura, T., Fukuta, K., Yanagi, H., Ge, S., and Wang, C.-Y. (2011) Impact of low cathode humidification on alkaline membrane fuel cell performance. *ECS Meeting Abstracts*, **1101**, 221.

51 Cao, Y.C., Wang, X., and Scott, K. (2012) The synthesis and characteristic of an anion conductive polymer membrane for alkaline anion exchange fuel cells. *Journal of Power Sources*, **201**, 226–230.

52 Merle, G., Wessling, M., and Nijmeijer, K. (2011) Anion exchange membranes for alkaline fuel cells: a review. *Journal of Membrane Science*, **377**, 1–35.

53 Grew, K.N. and Chiu, W.K.S. (2010) A dusty fluid model for predicting hydroxyl anion conductivity in alkaline anion exchange membranes. *Journal of the Electrochemical Society*, **157**, B327–B337.

54 Gu, S., Cai, R., Luo, T., Chen, Z., Sun, M., Liu, Y., He, G., and Yan, Y. (2009) A soluble and highly conductive ionomer for high-performance hydroxide exchange membrane fuel cells. *Angewandte Chemie: International Edition*, **48**, 6499–6502.

55 Chempath, S., Boncella, J.M., Pratt, L.R., Henson, N., and Pivovar, B.S. (2010) Density functional theory study of degradation of tetraalkylammonium hydroxides. *The Journal of Physical Chemistry C*, **114**, 11977–11983.

56 Watanabe, S., Fukuta, K., and Yanagi, H. (2010) Determination of carbonate ion in MEA during the alkaline membrane fuel cell (AMFC) operation. *ECS Transactions*, **33**, 1837–1845.

57 Couture, G., Alaaeddine, A., Boschet, F., and Ameduri, B. (2011) Polymeric materials as anion-exchange membranes for alkaline fuel cells. *Progress in Polymer Science*, **36**, 1521–1557.

58 Varcoe, J.R. and Slade, R.C.T. (2006) An electron-beam-grafted ETFE alkaline anion-exchange membrane in metal-cation-free solid-state alkaline fuel cells. *Electrochemistry Communications*, **8**, 839–843.

59 Beillard, M., Varcoe, J.R., Halepoto, D.M., Kizewski, J.P., Poynton, S.D., and Slade, R. C.T. (2008) Membrane and electrode materials for alkaline membrane fuel cells. University of Surrey, Guilford.

60 Varcoe, J.R., Slade, R.C.T., Yee, E.L.H., Poynton, S.D., and Driscoll, D.J. (2007) Investigations into the *ex situ* methanol, ethanol and ethylene glycol permeabilities of alkaline polymer electrolyte membranes. *Journal of Power Sources*, **173**, 194–199.

61 Slade, R.C.T. and Varcoe, J.R. (2005) Investigations of conductivity in FEP-based radiation-grafted alkaline anion-exchange membranes. *Solid State Ionics*, **176**, 585–597.

62 Herman, H., Slade, R.C.T., and Varcoe, J.R. (2003) The radiation-grafting of vinylbenzyl chloride onto poly (hexafluoropropylene-*co*-tetrafluoroethylene) films with subsequent conversion to alkaline anion-exchange membranes: optimisation of the experimental conditions and characterisation. *Journal of Membrane Science*, **218**, 147–163.

63 Yanagi, H. and Fukuta, K. (2008) Anion exchange membrane and ionomer for alkaline membrane fuel cells (AMFCs). *ECS Meeting Abstracts*, **802**, 783–783.

64 Varcoe, J.R. and Slade, R.C.T. (2005) Prospects for alkaline anion-exchange membranes in low temperature fuel cells. *Fuel Cells*, **5**, 187–200.

65 Danks, T.N., Slade, R.C.T., and Varcoe, J.R. (2003) Alkaline anion-exchange radiation-grafted membranes for possible electrochemical application in fuel cells. *Journal of Materials Chemistry*, **13**, 712–721.

66 Varcoe, J.R., Slade, R.C.T., and Lam How Yee, E. (2006) An alkaline polymer electrochemical interface: a breakthrough in application of alkaline anion-exchange membranes in fuel cells. *Chemical Communications*, 1428–1429.

67 Hong, J.-H., Li, D., and Wang, H. (2008) Weak-base anion exchange membranes by amination of chlorinated polypropylene

with polyethyleneimine at low temperatures. *Journal of Membrane Science*, **318**, 441–444.

68 Kostalik, H.A., Clark, T.J., Robertson, N.J., Mutolo, P.F., Longo, J.M., Abruña, H.C.D., and Coates, G.W. (2010) Solvent processable tetraalkylammonium-functionalized polyethylene for use as an alkaline anion exchange membrane. *Macromolecules*, **43**, 7147–7150.

69 Clark, T.J., Robertson, N.J., Kostalik, IV, H. A., Lobkovsky, E.B., Mutolo, P.F., Abruña, H.C.D., and Coates, G.W. (2009) A ring-opening metathesis polymerization route to alkaline anion exchange membranes: development of hydroxide-conducting thin films from an ammonium-functionalized monomer. *Journal of the American Chemical Society*, **131**, 12888–12889.

70 Wan, Y., Peppley, B., Creber, K.A.M., and Bui, V.T. (2010) Anion-exchange membranes composed of quaternized-chitosan derivatives for alkaline fuel cells. *Journal of Power Sources*, **195**, 3785–3793.

71 Varcoe, J.R. (2007) Investigations of the *ex situ* ionic conductivities at 30 degrees C of metal-cation-free quaternary ammonium alkaline anion-exchange membranes in static atmospheres of different relative humidities. *Physical Chemistry Chemical Physics*, **9**, 1479–1486.

72 Ogumi, Z. (2002) Preliminary study on direct alcohol fuel cells employing anion exchange membrane. *Electrochemistry*, **70**, 980–983.

73 Tanaka, M., Fukasawa, K., Nishino, E., Yamaguchi, S., Yamada, K., Tanaka, H., Bae, B., Miyatake, K., and Watanabe, M. (2011) Anion conductive block poly (arylene ether)s: synthesis, properties, and application in alkaline fuel cells. *Journal of the American Chemical Society*, **133**, 10646–10654.

74 Passalacqua, E., Lufrano, F., Squadrito, G., Patti, A., and Giorgi, L. (2001) Nafion content in the catalyst layer of polymer electrolyte fuel cells: effects on structure and performance. *Electrochimica Acta*, **46**, 799–805.

75 Adams, L.A., Poynton, S.D., Tamain, C., Slade, R.C., and Varcoe, J.R. (2008) A carbon dioxide tolerant aqueous-electrolyte-free anion-exchange membrane alkaline fuel cell. *ChemSusChem*, **1**, 79–81.

76 Zeng, R., Poynton, S.D., Kizewski, J.P., Slade, R.C.T., and Varcoe, J.R. (2010) A novel reference electrode for application in alkaline polymer electrolyte membrane fuel cells. *Electrochemistry Communications*, **12**, 823–825.

77 Zeng, R., Slade, R.C.T., and Varcoe, J.R. (2010) An experimental study on the placement of reference electrodes in alkaline polymer electrolyte membrane fuel cells. *Electrochimica Acta*, **56**, 607–619.

78 Tamain, C., Poynton, S.D., Slade, R.C.T., Carroll, B., and Varcoe, J.R. (2007) Development of cathode architectures customized for H_2/O_2 metal-cation-free alkaline membrane fuel cells. *The Journal of Physical Chemistry C*, **111**, 18423–18430.

79 Zhou, J., Unlu, M., Vega, J.A., and Kohl, P.A. (2009) Anionic polysulfone ionomers and membranes containing fluorenyl groups for anionic fuel cells. *Journal of Power Sources*, **190**, 285–292.

80 Lu, S., Pan, J., Huang, A., Zhuang, L., and Lu, J. (2008) Alkaline polymer electrolyte fuel cells completely free from noble metal catalysts. *Proceedings of the National Academy of Sciences of the United States of America*, **105**, 20611–20614.

81 Mamlouk, M., Scott, K., Horsfall, J.A., and Williams, C. (2011) The effect of electrode parameters on the performance of anion exchange polymer membrane fuel cells. *International Journal of Hydrogen Energy*, **36**, 7191–7198.

82 Piana, M., Boccia, M., Filpi, A., Flammia, E., Miller, H.A., Orsini, M., Salusti, F., Santiccioli, S., Ciardelli, F., and Pucci, A. (2010) H_2/air alkaline membrane fuel cell performance and durability, using novel ionomer and non-platinum group metal cathode catalyst. *Journal of Power Sources*, **195**, 5875–5881.

83 Fukuta, K., Inoue, H., Chikashige, Y., and Yanagi, H. (2010) Improved maximum power density of alkaline membrane fuel cells by the optimization of catalyst layer construction. *ECS Meeting Abstracts*, **1001**, 275–275.

84 Isomura, T., Fukuta, K., Yanagi, H., Ge, S., and Wang, C.-Y. (2010) alkaline membrane fuel cell operated at elevated temperatures. *ECS Meeting Abstracts*, **1002**, 751–751.

85 Oda, K., Kato, H., Fukuta, K., and Yanagi, H. (2010) Optimization of RRDE method for the evaluation of catalyst activity in alkaline solution. *ECS Meeting Abstracts*, **1001**, 192.

86 Inoue, H., Fukuta, K., Watanabe, S., Yanagi, H. (2009) *In-situ* observation of CO_2 through the self-purging in alkaline membrane fuel cell (AMFC). *ECS Transactions*, **19**, 23–27.

3
Catalyst Support Materials for Proton Exchange Membrane Fuel Cells

Xin Wang and Shuangyin Wang

3.1
Introduction

Proton exchange membrane fuel cell (PEMFC), as an environment-friendly technology, has been attracting extensive attention as power source for stationary, transportational, and portable applications [1–3]. In a PEMFC, hydrogen and various small organic molecules (SOMs) could be used as fuel at the anode side, whereas oxygen as oxidant is used at the cathode side. The direct electrochemical conversion of hydrogen/SOMs and oxygen into water and carbon dioxide (CO_2) produces electricity. The electrocatalytic reactions in both anode and cathode sides occur on the active surface of electrocatalysts. Conventionally, nanostructured platinum and platinum-based alloy are used as electrocatalysts in PEMFCs. In fuel cell, only electrochemical reactions that occur within the three-phase boundary (electrode–electrolyte–fuel/air) contribute to the overall performance of a PEMFC.

The key factor determining the commercialization of the fuel cell technology is its cost. The cost is predominantly related to the amount of precious metal used. Researchers are striving to reduce the precious metal content by designing better electrocatalyst and improving the overall efficiency. The move from platinum black to carbon-supported platinum catalysts has significantly cut platinum requirements. Typical loading in the electrode today is ~0.4–0.8 mg platinum cm^{-2}, which is significantly lower than 25 mg cm^{-2} with early platinum black catalysts. The US Department of Energy (DOE) has set targets of 0.3 mg cm^{-2} for 2010 and 0.2 mg cm^{-2} for 2015.

It is well known that the activity of a catalyst depends significantly on the size of the Pt particles and their dispersion pattern over the support structures. It has been found that the optimal dispersion pattern and Pt particle size can be obtained by using an appropriate preparation procedure on an ideal supporting material.

The ideal catalysts support should have the following structure and properties:

1) High surface area and good electrical properties
2) Reactant gas access to the electrocatalysts

Materials for Low-Temperature Fuel Cells, First Edition. Edited by Bradley Ladewig, San P. Jiang, and Yushan Yan.

3) Good corrosion resistance
4) High chemical and electrochemical stability under fuel cell operating conditions

In a carbon-supported metal electrocatalyst, the electronic interaction between metal and carbon support has a significant effect on its electrochemical performance [4]. For carbon-supported Pt electrocatalyst, carbon could accelerate the electron transfer at the electrode–electrolyte interface, leading to an accelerated electrode process. Typically, the electrons are transferred from platinum clusters to the oxygen species on the surface of a carbon support material and the chemical bond formation or the charge transfer process occurs at the contacting phase, which is considered to be beneficial to the enhancement of the catalytic properties in terms of activity and stability of the electrocatalysts. Experimentally, the investigation into the electron interaction between metal catalyst and support materials could be realized by various physical, spectroscopic, and electrochemical approaches. The electron donation behavior of Pt to carbon support materials has been demonstrated by the electron spin resonance (ESR) X-ray photoelectron spectroscopy (XPS) studies, with the conclusion that the electron interaction between Pt and carbon support depends on their Fermi level of electrons. It is considered that the electronic structure change of Pt on carbon support induced by the electron interaction has positive effect toward the enhancement of the catalytic properties and the improvement of the stability of the electrocatalyst system. However, the exact quantitative relationship between electronic interaction of carbon-supported catalyst and its electrocatalytic performance is still not yet fully established [4].

3.2
Current Status of Support Materials and Role of Carbon as Support in Fuel Cells

Carbon materials are promising catalyst supports in fuel cells, due to their chemical inertness, wide electrochemical windows, and excellent charge mobilities. The most popular and widely used carbon material for fuel cell electrocatalysts is carbon black, because of its large specific surface area and low price. There are various types of carbon blacks, such as Acetylene Black, Vulcan XC-72, and Ketjen Black, and these are usually manufactured by pyrolyzing hydrocarbons such as natural gas or oil fractions derived from petroleum processing. Generally, highly dispersed, supported catalysts cannot be prepared from low-surface-area carbon blacks (e.g., Acetylene Black). It has been concluded by Antolini [5] that the carbon black characteristics have a significant effect on the dispersion of the supported electrocatalyst metal nanoparticles and on their subsequent electrocatalytic activity for reactions in fuel cells. It was found that the Pt particle size decreases with the increase of the specific surface area of carbon black. High-surface-area carbon blacks (e.g., Ketjen Black) could support highly dispersed catalyst nanoparticles. However, Ketjen Black-supported catalysts showed high ohmic resistance and mass

transport limitation during fuel cell operation. Vulcan XC-72 with a surface area of $\sim 250\,m^2\,g^{-1}$ has been widely used as a catalyst support in fuel cells.

Despite the high surface area of the carbon black particles, the carbon black-based electrocatalyst support has two main problems: (i) due to its dense structure, the carbon black-based support has significant mass transfer limitations, leading to a very low Pt utilization; (ii) carbon black is known to undergo electrochemical oxidation into surface oxides as well as CO_2 at the cathode in the fuel cell. As carbon black corrodes, noble metal nanoparticles (e.g., Pt) on carbon black will detach from the electrode and possibly aggregate to larger particles, resulting in Pt surface area loss, which subsequently lowers the performance of PEM fuel cells [6].

A great deal of effort has also been devoted to seeking new carbon materials, including ordered mesoporous carbon (OMC), carbon nanofibers (CNFs), carbon nanotubes (CNTs), carbon nanohorns (CNHs), carbon nanocoils (CNCs), carbon aerogels (CAGs), and graphene. This chapter begins by briefly describing the various possible promising alternative catalyst supports employed in PEMFCs.

3.3
Novel Carbon Materials as Electrocatalyst Support for Fuel Cells

3.3.1
Mesoporous Carbon as Support Materials for Fuel Cells

On carbon black, there exist lots of micropores (<2 nm), which makes the supply of fuel unsmooth and results in limited catalytic activity for fuel cells. Meanwhile, the micropores on carbon black are poorly connected with relatively low conductivity. Alternatively, mesoporous carbon (MPC) (2–50 nm) has been developed to support nanoelectrocatalysts in fuel cells. Two categories could be classified based on their structure and morphology. One is the ordered mesoporous carbon, which is usually prepared via the template strategy. The other one is disordered mesoporous carbon (DOMC), in which the pore structure is irregularly interconnected with low conductivity and wide pore size distribution. Comparing these two kinds of mesoporous carbons, it could be found that OMC is preferred as electrocatalyst support in fuel cell due to its high surface area, high conductivity, and facilitated mass transport within the pore channels. The electrocatalysts supported on OMC have shown excellent performance in PEMFC electrode reactions. The as-observed improved performance of fuel cell on OMC-supported electrocatalysts is well understandable, as the OMC as support materials would lead to the high and uniform dispersion of metal nanoparticles (electrocatalysts) to enhanced mass transport due to the ordered pore structures of OMC. In a typical electrocatalytic reactions, such as electrode reactions in fuel cells, reactions occur only at a specific nanoscale zone, named as triple-phase boundary (TPB), which is accessible to reactants and products, electrolytes, and electrons. It is difficult for the conventional carbon black as

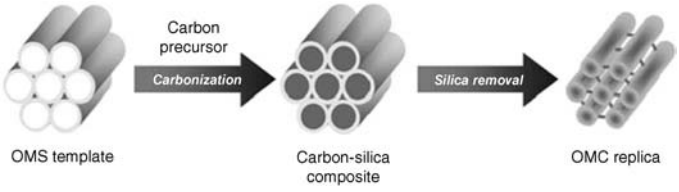

Figure 3.1 Schematic representation of the synthesis procedures of OMC from an OMS template [7].

support material to form TPB as it contains many microspores, which the reactants/products and electrolytes are difficult to access. On the other hand, the macroporous carbon with larger pore size (>50 nm) has relatively low surface area and low conductivity, making it unsuitable as catalyst support material. Considering its high surface area, large pore volumes, and highly regular interconnected pore structure, OMC could allow a good dispersion of catalyst nanoparticles and an efficient mass transport (reactants/products and electrolytes) [5,7].

The synthesis of OMC involves the use of ordered mesoporous silica (OMS) template with a specific pore topology [7]. As illustrated in Figure 3.1, the appropriate carbon precursor (carbon sources such as sucrose, furfuryl alcohol, acetylene gas, pyrrole, and acrylonitrile) is fed into the pores of the template via the infiltration approach, followed by its carbonization to achieve the silica–carbon composite and template removal in ethanol–water solution of HF or NaOH to obtain the mesoporous carbon replica. The structure of the as-obtained OMC strongly depends on the structure of the used template. Chang *et al.* [7] have reviewed the synthesis of OMC as support materials for fuel cell applications. The rod- and tube-type mesoporous carbon structures can be realized by filling carbon precursors in the template pores and coating carbon precursors as a thin film on the pore walls of the template, respectively. In order to get the well-defined structure of OMC, the template should have three-dimensional interconnected pore structure. On the other hand, the carbonization of the carbon precursors should be confined exclusively within the mesopores of the ordered mesoporous silica templates with sufficient carbon precursor filling; therefore, before the pyrolysis process, the carbon source should be converted to a cross-linked polymer induced by the use of the acid polymerization catalysts [5,7].

Various synthesis methods of mesoporous carbon based on different mesoporous silicate or aluminosilicate templates have been developed [5,7]. The first report on the synthesis of OMC used mesoporous silica MCM-48 with the bicontinuous cubic Ia3d symmetry as the template; the as-prepared OMC was denoted as CMK-1. Thereafter, various OMCs with different pore topologies have been actively investigated. For these OMCs, the uniform mesopores are interconnected, resulting in the appearance of distinct X-ray diffraction lines below 2 theta of 5. Meanwhile, they have a large surface area and high pore volume. The other structural parameters such as pore diameters, particle morphologies and sizes, and microstructures of carbon frameworks could be tuned by

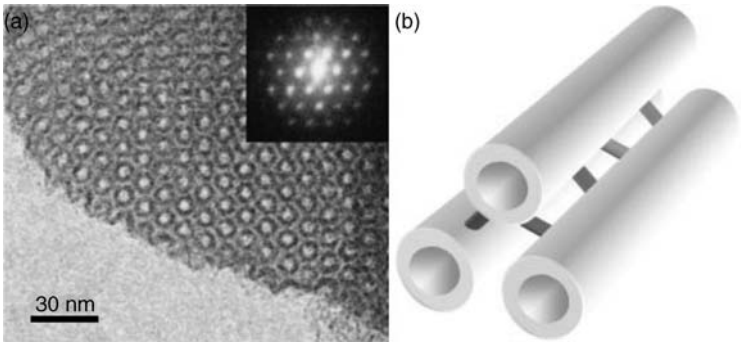

Figure 3.2 Ordered nanoporous carbon obtained by template synthesis using ordered mesoporous silica SBA-15 [8].

rational experimental design of the synthesis process. Joo *et al.* [8] successfully synthesized highly ordered, rigid arrays of nanoporous carbon with uniform and tunable diameters by using ordered mesoporous silicas as templates, the removal of which leaves a partially ordered graphitic framework. The as-synthesized OMC materials were demonstrated to support a high dispersion of platinum nanoparticles, exceeding that of other common microporous carbon materials, including carbon black, charcoal, and activated carbon fibers. On this material, the particle size of Pt electrocatalysts could be controlled to 3 nm with high dispersion, resulting in significantly enhanced electrocatalytic activity for oxygen reduction reaction (ORR) in fuel cell [7].

Ding *et al.* [9] successfully prepared CMK-3 ordered carbon by use of SBA-15 as silica template (Figure 3.2). Pt nanoparticles were supported on the as-obtained CMK-3 for fuel cell reaction: oxygen reduction. The electrocatalytic activity toward ORR of Pt/CMK-3 is much higher than that of the commercial catalyst. By the replication of mesoporous silica SBA-15(⊥) template, Mou and coworkers [10] prepared ordered mesoporous thin-film carbon materials of short channels vertical to the film followed by the deposition of Pt–Ru nanoparticles. The advantage of the as-designed structure is demonstrated with the enhanced electrocatalytic activity for methanol oxidation, resulting from the increased nanocatalysts' utilization efficiency with the short nanochannels of the thin-film carbon structure. The well-dispersed, highly stable Pt–Ru nanoparticles of ~2–3 nm on carbon mesoporous materials (Pt–Ru–CMMs) were synthesized by Liu *et al.* [11] directly using SBA-15 mesoporous silica as the template, furfuryl alcohol and trimethylbenzene as the primary carbon source, and platinum and ruthenium acetylacetonates as the cofeeding metal and carbon precursors. All the TEM images (Figure 3.3) for various Pt–Ru–CMMs exhibit a uniform array of mesopores with a long-range order. It can be seen that for all the supported Pt–CMM, Pt–Ru–CMMs, and Ru–CMM catalysts, monometal (Pt and Ru) and Pt–Ru alloy are uniformly dispersed and studded on the surface of the carbon rods. Further studies by X-ray absorption spectroscopy confirmed that a highly alloyed state of the Pt–Ru nanoparticles is responsible for the superior

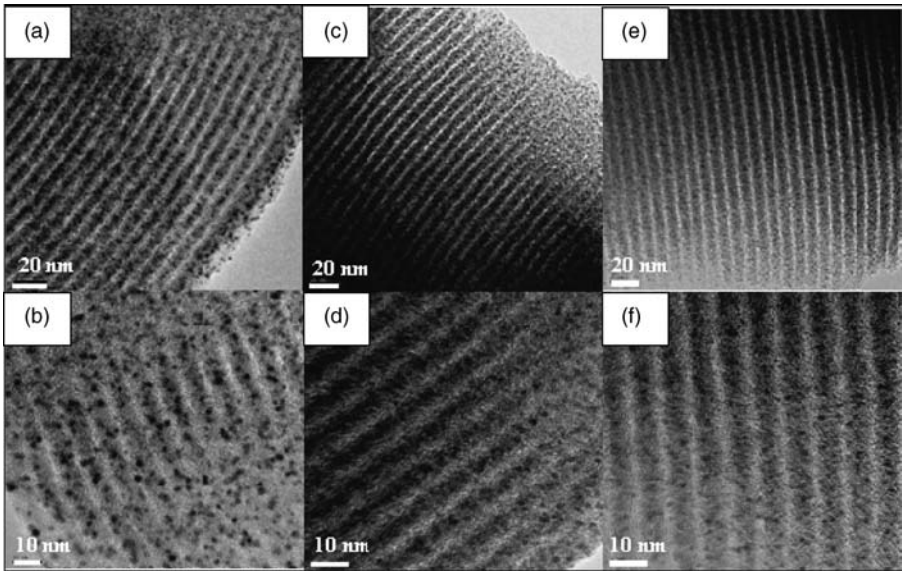

Figure 3.3 TEM images of (a and b) Pt_{100}–CMM, (c and d) $Pt_{50}Ru_{50}$–CMM, and (e and f) Ru_{100}–CMM [11].

electrocatalytic performance observed for the Pt–Ru–CMMs, compared with typical commercial electrocatalysts. The $Pt_{50}Ru_{50}$–CMM sample was found to possess the best electrocatalytic performance and long-term durability and should appeal to direct methanol fuel cell (DMFC) applications as anodic electrocatalyst.

Yu *et al.* [12] reported the synthesis of uniform porous carbon replicas with interesting morphological variation against a colloidal crystal template by inducing different polymerization processes of phenol and formaldehyde as a carbon precursor. The processes of controlling the morphology in this work were simple and were well performed just by altering the acid catalyst sites, which control the initiation sites of the acid-catalyzed condensation reaction from the same precursor. In particular, these highly ordered uniform porous carbons resulted in much improved catalytic activity for methanol oxidation as a catalyst support in a fuel cell. Zhao *et al.* [13] synthesized ordered graphitic mesoporous carbon (GMPC) by chemical vapor deposition (CVD) of benzene in the pores of mesoporous SBA-15 pure silica template without loading any catalytic species. It was observed that the CVD method affords highly ordered mesoporous carbon with graphitic pore walls and low carbon shrinkage because of the high degree of infiltration of pyrolytic carbon. The catalytic performance of the mesoporous carbon as a support for Pt catalyst in room-temperature methanol oxidation was examined, showing that the specific activity of Pt nanoparticles on mesoporous carbon is higher than that of a commercial Pt/C (E-TEK) catalyst. Joo *et al.* [14] reported the effect of graphitic character of OMCs on the performance of OMC-supported catalysts for direct methanol fuel cells. Two OMC samples with hexagonal mesostructure were prepared from phenanthrene and sucrose by

nanoreplication method using mesoporous silica as a template. Structural characterizations revealed that both OMCs exhibited large surface area and uniform mesopores, while the OMC synthesized from phenanthrene exhibited lower sheet resistance than the OMC derived from sucrose. The Pt nanoparticles were supported on both OMCs with very high dispersion. In DMFC single-cell test, the OMC-supported Pt catalysts exhibited much higher performance than the commercial catalyst, which may be attributed to the high surface area and uniform mesopore networks of OMC. In particular, it was found that the performance of OMC-supported catalysts can be significantly enhanced by lowering the resistance of OMC [14]. On the other hand, Yan and coworkers [15] investigated the durability of graphitic mesoporous carbons, which were synthesized by heat-treating polymer-templated mesoporous carbon at 2600 °C. The electrochemical durability of GMPC as Pt catalyst support (Pt/GMPC) is compared with that of carbon black (Pt/XC-72). Comparisons indicate that the Pt/GMPC is much more stable than Pt/XC-72.

Carbon aerogels with high pore volumes and high surface areas have been developed as Pt supports in the MEA cathode of a H_2/air PEM fuel cell. It is shown that carbon aerogels with different initial pore sizes have similar kinetic activity, but very different diffusion polarization losses: the larger the pore size of the initial carbon aerogel, the higher the mass transport polarization [16,17]. However, the chemical stability of the catalyst is limited due to the amorphous property of carbon aerogel.

Nitrogen-doped carbon materials shows good catalysts support in terms of catalytic activity and stability [18,19]. A graphitic carbon nitride with three-dimensionally extended highly ordered pore arrays has been reported as a support for a Pt–Ru alloy catalyst of a DMFC anode. The nanostructured C_3N_4 has 73–83% higher power density than Vulcan XC-72, a commercial carbon black. In comparison with OMC, this ordered macroporous C_3N_4 possesses a lower surface area, but higher conductivity and better electrocatalytic activity owing to its improved graphiticity and framework N atom-enhanced electron transfer rate [20].

The very high stability of conductive boron-doped diamond makes it attractive as a durable catalyst support for PEM fuel cells. The boron-doped diamond-supported catalysts have shown excellent stability toward ORR [21] and the electrochemical oxidation of methanol [22]. However, there are still some problems with doped diamonds as electrocatalyst supports: the low conductivity, the low surface area, and the poor dispersion of the metal particles. In addition, it is still difficult to realize a homogeneous and controllable boron doping level in diamond powders [23].

3.3.2
Graphite Nanofibers as Support Materials for Fuel Cells

Graphite nanofibers (GNFs) have generated great interest as support materials due to their good graphitic structures and high electrical conductivity [6,24].

Various graphitic nanofibers such as platelet, ribbon, and herringbone have been used as support materials for fuel cell electrocatalysts. GNFs are usually synthesized by decomposing carbon-containing gases over certain metal surfaces. In the structure of GNFs, the basal plane is exposed only at the edge regions. On the other hand, different from the structure of CNTs, there is no hollow cavity in GNFs. Due to its unique structure, GNF could be directly used to support metal nanoparticles without any pretreatment, which would normally have detrimental effect on the perfect structure of graphite fiber, as it is believed that platelets and herringbone structures of GNFs can present potentially reactive groups for metal deposition. Various synthesis methods have been developed to support metal nanoelectrocatalyst on graphite nanofibers for the potential applications in fuel cells. Gangeri *et al.* [24] deposited Pt by incipient wetness impregnation on GNFs. The performances of platinum supported on carbon nanofibers (Pt/GNFs) as alternative electrodes for PEM fuel cells are compared with those of a commercial Pt–carbon black. Carbon nanofibers were grown by chemical vapor deposition on two different types of microshaped carbon supports (felt and cloth) and then Pt was deposited on these nano/microcomposite carbon supports. The analysis of the results and in particular of the polarization curves indicate that (i) Pt/GNF materials are better electrocatalyst than the commercial one and (ii) Pt/GNF materials give the lowest mass transfer losses. The electrochemical analysis pointed out that new electrode material based on both Pt nanoclusters and carbon nanostructures could be very interesting for fuel cells applications. The studies on the effect of the microscopic structure of graphitic nanofiber on the electrocatalytic performance of the supported catalysts must be interesting. The potential of graphite nanofiber-supported platinum catalysts as an electrode for fuel cell applications was investigated by Bessel *et al.* [25] using the electrochemical oxidation of methanol as a probe reaction. Various types of graphite nanofibers were used and the behavior of supported platinum particles on these materials was compared with that when the metal was dispersed on Vulcan carbon (XC-72). Catalysts consisting of 5 wt% platinum supported on "platelet-" and "ribbon-"type graphite nanofibers, which expose mainly edge sites to the reactants, were found to exhibit activities comparable with that displayed by ~25 wt% platinum on Vulcan carbon. Furthermore, the graphite nanofiber-supported metal particles were observed to be significantly less susceptible to CO poisoning than the traditional catalyst systems. This improvement in performance is believed to be linked to the fact that the metal particles adopt specific crystallographic orientations when dispersed on the highly tailored graphite nanofiber structures.

Lukehart and coworkers [26] successfully prepared a Pt–Ru/graphitic carbon nanofiber nanocomposite exhibiting high relative performance as a direct methanol fuel cell anode catalyst. Multistep deposition and reactive decomposition of a single-source molecular precursor of Pt and Ru metal on herringbone graphitic carbon nanofibers affords a Pt–Ru/GNF nanocomposite containing Pt–Ru alloy nanoclusters widely dispersed on the GNF support. The nanocomposite has a total metal content of 42 wt% with a bulk Pt/Ru atomic ratio of about 1:1 and

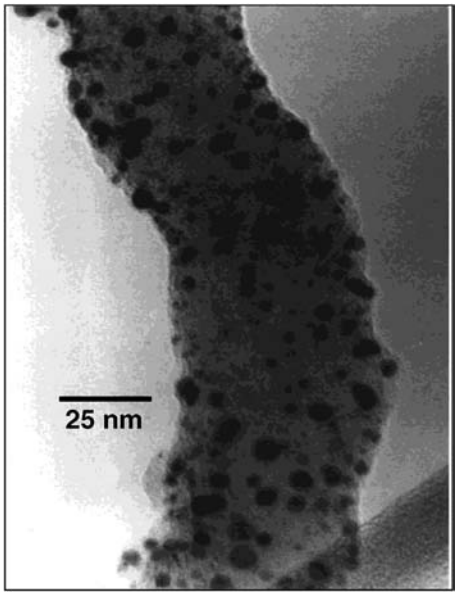

Figure 3.4 Bright-field TEM micrograph of the Pt–Ru/GNF nanocomposite [26].

metal alloy nanoclusters having average particle sizes 7 nm as measured directly from TEM images, as shown in Figure 3.4. XRD and electrochemical analysis of the nanocomposite as-prepared and stored under ambient conditions reveals the presence of small amounts of Ru metal and oxidized metal species. Comparative testing of this nanocomposite and an unsupported Pt–Ru colloid of similar surface area and catalyst particle size as anode catalysts in a working direct methanol fuel cell reveals a 50% increase in the performance for the Pt–Ru/GNF nanocomposite.

More recently, Kang and coworkers [27] successfully prepared surface-reconstructed graphite nanofibers as the support for the cathode catalyst of fuel cells. The GNFs were synthesized by high-temperature graphitization of catalytically grown carbon nanofibers. In contrast to CNTs, the GNFs show exposed graphitic edges on the surface. Upon graphitization, adjacent graphite edges on the GNFs would be largely coalesced, which causes the surface reconstruction on the GNFs. The as-prepared GNFs exhibit both a high degree of graphitization and a strong interaction with Pt nanoparticles and they produce an improved cathode performance in DMFCs. As shown by the TEM images in Figure 3.5, the pristine GNFs exhibit a typical herringbone structure, in which the graphite layers decline toward the axis of the nanofibers. After graphitization, the graphite layers became well aligned in the GNFs (Figure 3.5c and d), suggesting a higher extent of graphitization, Furthermore, from Figure 3.5d, we can see that the graphite edges exposed on the surface of the pristine GNFs were largely changed into a number of loops, showing a surface reconstruction during the graphitization. These nanoloops were formed by the zipping of adjacent graphite edges to

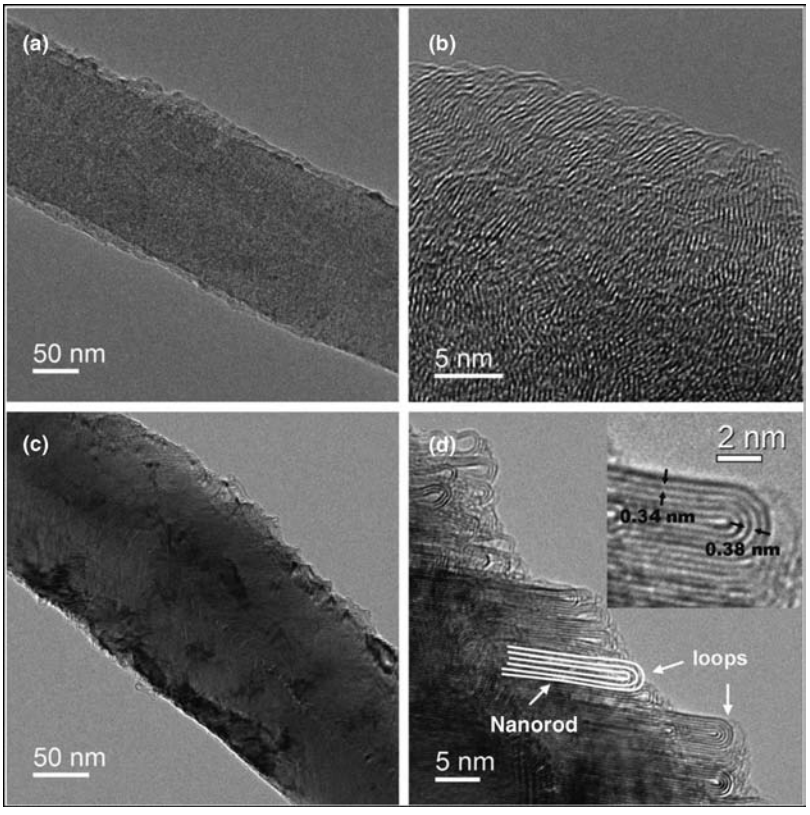

Figure 3.5 TEM and HRTEM images of GNFs (a–b) and surface-reconstructed GNFs (c and d); the inset in part (d) shows a magnified image of the formed loops [27].

minimize the surface energy, since graphite edges possess carbon dangling bonds with a higher surface energy. Due to the surface reconstruction on the GNFs, Pt nanoparticles with a size of ~3 nm could still be uniformly dispersed on the highly graphitized GNF support without any further pretreatment. The Pt/GNF catalyst shows an improved performance in the single DMFC test compared with the Pt/CNF and Pt/Vulcan catalysts, which could be ascribed to the high graphitization degree of GNFs that might result in higher electron conduction and a more hydrophobic surface for water removal of Pt/GNF. The high degree of graphitization of GNFs also improves the durability of Pt/GNF for long-term application [27].

3.3.3
Carbon Nanotubes as Support Materials for Fuel Cells

CNTs with unique electrical and structural properties have attracted great interest in applications such as superconductivity, hydrogen storage, field emission,

and heterogeneous catalysis. CNTs are widely studied as support material for Pt and Pt alloy catalysts in fuel cells due to their high surface area, excellent electronic conductivity, and high chemical stability. Since pristine CNTs are chemically inert, it is necessary to activate the graphitic surface of the nanotubes in order to anchor and deposit catalytic nanoparticles [28–33]. The deposition, distribution, and size of metal nanoparticles supported on CNTs depend strongly on the surface treatment and surface properties of CNTs. The activity of Pt nanoparticles is also significantly affected by the nature of their interaction with CNTs and the intrinsic properties of CNTs. Many reviews are available dealing with the synthesis of CNTs and their characteristics as a novel catalyst support.

The synthesis of CNTs involves the catalytic decomposition of carbon source materials either in gas or solid phase [5,33]. The typical techniques for the synthesis of CNTs include CVD, arc discharge, and laser vaporization synthesis. The as-produced CNTs usually have high molecular weight and strong hydrophobic surface forming bundles, which usually results in the poor dispersion of metal particles on CNTs and limits the overall electrocatalytic activity of the CNT-supported electrocatalysts [5,6,33]. The electrocatalytic activity of metal nanoelectrocatalysts strongly depends on the dispersion and particle size of the electrocatalyst on carbon support materials. On the other hand, the dispersion, distribution, and particle size of metal nanoelectrocatalyst supported on CNTs are significantly affected by the surface properties of CNTs, which could be modified by various functionalization strategies. Extensive research activities have been conducted on the surface functionalization of CNTs. Basically, the surface functionalization could be classified into two categories: covalent and noncovalent modification. Covalent surface modification of the CNTs involves a permanent change to the materials surface, such that it is functionalized with reactive groups that can later form a covalent bond with another molecule. On the other hand, noncovalent surface modification does not involve the formal chemical bond formation between a molecule and the surface of CNT. Examples of this type of interaction include van der Waals forces, electrostatic forces, hydrogen bonding, and other attractive forces [30–33].

As the most commonly used functionalization method, CNTs are usually functionalized by the harsh oxidative processes, such as refluxing in the concentrated mixture of HNO_3 and H_2SO_4 to generate functional groups on the sidewalls and tube tips. As a result of this kind of acid treatment, the perfect aromatic conjugate ring structure of CNT surface can be destroyed. Correspondingly, the CNTs can be functionalized with functional groups such as hydroxyl, carboxyl, and carbonyl, which have strong interaction and anchoring ability toward metal ions and metal nanoparticles. Yu *et al.* [34] treated CNTs using mixed acids (HNO_3–H_2SO_4). They proposed a mechanism of Pt deposition on the CNTs, as shown in Figure 3.6. When CNTs are refluxed with a mixture of HNO_3–H_2SO_4, the surface graphitic layers would react with the oxidants and produce a high density of various surface functional groups. When the Pt ions were introduced into the system, they would interact with and attach to these

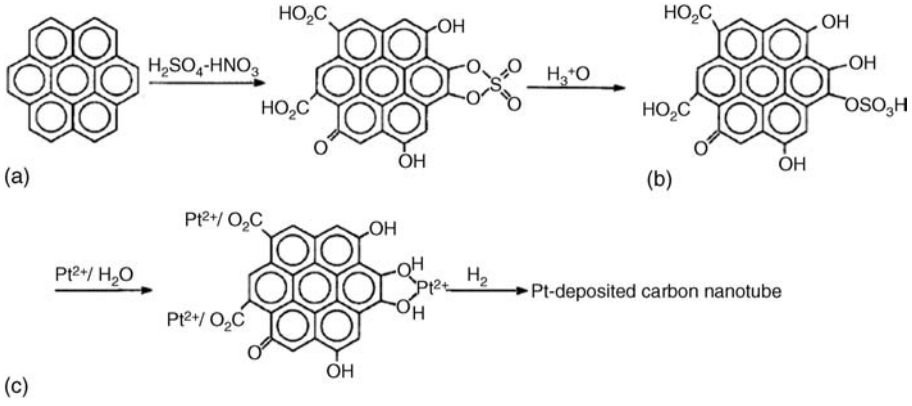

Figure 3.6 Functionalization of carbon nanotube and the deposition of Pt nanoparticles [34].

surface functional groups through an ion exchange or coordination reaction and serve as nucleation precursors. A well-dispersed deposition of the Pt metal nanoparticles on the surface of CNTs was obtained after the reduction of the surface Pt^{2+} ions by hydrogen [33,34]. Xu *et al.* [35] reported the influence of the treatment method on the deposition of Pt nanoparticles. They reported that the reflux with the mixture of H_2SO_4 and HNO_3 solutions followed by the immersion in the H_2O_2 solution are effective pretreatment methods for depositing the Pt nanoparticles on the CNT surface (denoted as hybrid process). Pt nanoparticles with a size of 3 nm can be obtained on the CNT surface using this process. The nanoparticles produced by this hybrid process exhibit the best catalytic properties compared with other pure acid treatment, which indicates that they are relatively small and distributed homogeneously on CNT [33,35].

With the similar acid treatment (surface oxidation) process, the sonochemically assisted treatment was also developed as an effective method of functionalizing the CNT surface [33,36]. For example, Xing [36] has shown that Pt nanoparticles could be uniformly deposited on sonochemically treated CNTs, as confirmed by the transmission electron microscopy (TEM) images in Figure 3.7. The as-prepared Pt/CNTs electrocatalyst has a much higher catalytic activity than those supported on carbon black when used in PEMFCs.

Although covalent fictionalization strategies have been extensively developed, such chemical oxidation method reduces the electrical conductivity and corrosion resistance of CNTs, due to the introduction of a large number of defects onto the surface of CNTs. Corrosion of carbon or CNT supports has been identified as one of the main reasons for the loss of the electrochemical active surface area of Pt electrocatalysts and the reduced durability during fuel cell operation [30–33]. Therefore, there is a need to develop a better and more effective functionalization method that can not only introduce high density and homogeneous surface functional groups but also has little or no structural damage to CNTs. Hsin *et al.* [37] reported a functionalization method of MWCNTs by an *in situ*

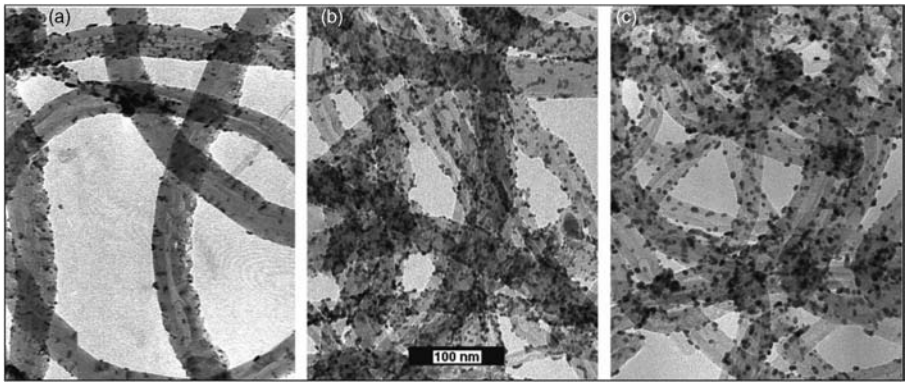

Figure 3.7 TEM images of Pt nanoparticles deposited on the sonochemically treated carbon nanotubes with Pt loading of 10, 20, and 30 wt% shown in parts (a–c), respectively [36].

polymerization of PVP as supports to deposit Pt and Pt–Ru nanoparticles. Others coated CNTs with poly(sodium 4-styrenesulfonate) (PSS) and poly (diallyldimethylammonium chloride) (PDDA) prior to the attachment of charged Au colloidal nanoparticles, but in order to achieve a better adsorption of polyelectrolytes, CNTs are generally treated by acid oxidation prior to the coating of polyelectrolyte, which inevitably introduces surface defects and causes some structural damage to CNTs.

Recently, the noncovalent functionalization of CNTs has attracted particular attention because it enables the properties of the hybrids of nanoparticles and CNTs to be tailored while still preserving nearly all the intrinsic properties of CNTs. Wang and coworkers [38] assembled semiconductor and metal nanoparticles on multiwalled carbon nanotubes by use of pyrene-containing molecules as interlinkers, but in this case, the dispersion of nanoparticles on carbon nanotubes is not satisfactory, as indicated by the formation of nanoparticle aggregates. Correa-Duarte *et al.* [39] used multilayer assembled CNTs of PSS and PDDA as templates to support silica-coated Au nanoparticles. Sacher and coworkers [40] have successfully functionalized MWCNTs with thiol groups via a π–π interaction with benzyl mercaptan. As demonstrated in Figure 3.8, the functionalized CNT surface interacts strongly with Pt nanoparticles through the formation of Pt−S bonds and results in a very high Pt nanoparticle loading (both high dispersion and narrow size distribution). The prepared Pt/MWCNT composite showed higher electrocatalytic activity and enhanced CO tolerance in comparison with other catalysts. Such a promising synthesis procedure can be extended to the fabrication of other precious metal catalysts supported on CNT for fuel cells [32].

Wang *et al.* [30] used the polyelectrolyte functionalization techniques to functionalize CNTs. PDDA, a water-soluble quaternary ammonium with positive charge, was used to wrap CNTs in aqueous solution. This noncovalent functionalization not only leads to a high density and homogeneous dispersion

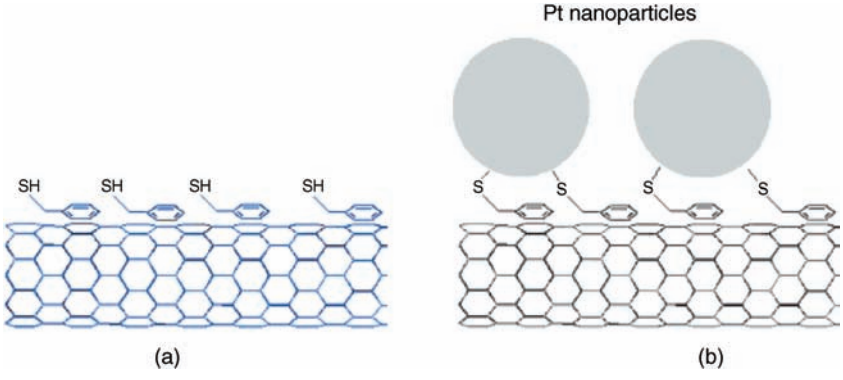

Figure 3.8 Functionalization of CNTs with benzyl mercaptan and subsequent Pt deposition [41].

of surface functional groups on MWCNTs but also preserves the intrinsic properties of MWCNTs without damaging their perfect surface structure. Because of the positive surface charge on MWCNTs, a large amount of negatively charged Pt precursor can be anchored onto MWCNT surface via electrostatic interaction. The subsequent reduction by EG with the presence of these highly functionalized CNTs yields Pt nanoparticles with uniform distribution and high density.

The further work by Wang *et al.* [31] demonstrated that this functionalization strategy could achieve high density of functional groups uniformly introduced onto the CNT surface, which would allow a high loading of metal nanoparticles on CNTs. The relationship between the electrocatalytic activity and interconnectivity of Pt nanoparticles on CNT was investigated. It is found that the electrocatalytic activities of Pt/CNT catalysts are fundamentally correlated with the interconnectivity of Pt nanoparticles on CNTs. The magnitude of the interconnectivity of Pt nanoparticles is a critical factor influencing their electrocatalytic activity, and the interconnected Pt nanoparticles are more active than the isolated Pt nanoparticles. The high electrocatalytic activity of highly interconnected Pt nanoparticles is considered to be related to the increased active intergrain boundaries, which promote significantly the electrocatalytic activity of Pt nanoparticles. On the other hand, the interconnected Pt nanoparticles would significantly weaken their chemical adsorption with oxygen-containing species (i.e., CO_{ad} and OH_{ad}), resulting in the promoted electrocatalytic activity for CO and methanol oxidation and oxygen reduction. The increase of interconnectivity of Pt nanoparticles also reduces the interface resistance among particles for electron transfer [31,41].

Similarly, polyelectrolytes with various characteristic functional groups as interlinkers to anchor Pt nanoparticles were used to functionalize CNTs as Pt electrocatalyst support. The effect of interlinkers between Pt nanoparticles and carbon nanotubes on the electrocatalytic activity for methanol oxidation was investigated, as demonstrated in Figure 3.9 [42]. It was found that polyanions

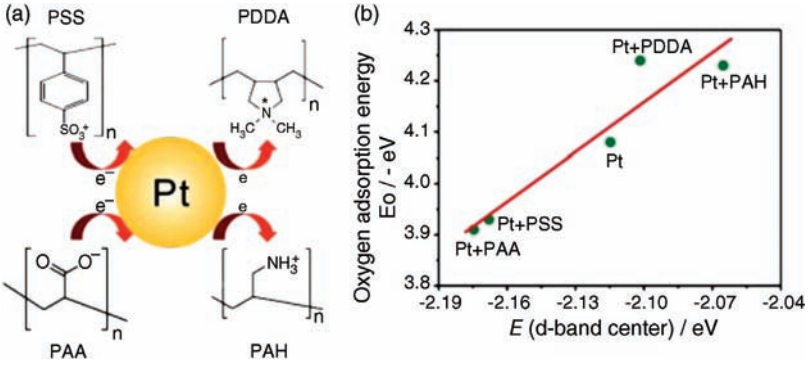

Figure 3.9 (a) The possible effect of the charged functional groups of polyanions (PSS and PAA) and polycations (PDDA and PAH) on the electron donor–acceptor behavior of Pt NP. (b) Correlation between the adsorption energy of O and the d-band center of Pt slabs [42].

(poly(styrenesulfonic acid) (PSS), poly(acrylic acid sodium) (PAA)) have a beneficial effect on methanol electrooxidation on Pt nanoparticles supported on CNTs via modifying their electronic structure through charge transfer from polyanions to Pt sites and supply of oxygen-containing species, as evidenced by X-ray photoelectron spectroscopy (XPS) results. The increased electron density around Pt sites by the charge transfer from polyanions would cause partial filling of Pt 5d-bands, resulting in the downshift of d-band center and weaker chemisorption with oxygen-containing species (e.g., COad). The weakened chemisorption of CO on Pt nanoparticles would promote the methanol electrooxidation. However, polycations would have an adverse effect on the electronic structure and chemisorption properties of Pt nanoparticles. On the other hand, the long-term stability testing shows that polycations functionalized CNTs as Pt support would enhance its stability by the stronger interaction between Pt nanoparticles and CNTs contributed by the electrostatic attraction forces [42].

Recently, bifunctional molecules have also been used to modify the surface of CNTs as electrocatalyst support [32]. It involves the adsorption of 1-aminopyrene (1-AP) molecules onto the surface of MWCNTs. 1-AP contains a pyrenyl group and an amino functional group. The pyrenyl group, being highly aromatic in nature, is known to interact strongly with the basal plane of graphite via π-stacking. In a similar manner, the pyrenyl group of 1-AP could also strongly interact with the sidewalls of MWCNTs, immobilizing 1-AP on the MWCNTs. When the pH of the solution is controlled at slight acidic, the amino groups of 1-AP immobilized on the MWCNT surface are protonated and become weakly positively charged. This leads to the electrostatic attraction of the negatively charged $PtCl_6^{2-}$, followed by the subsequent self-assembly of positively charged Ru^{3+}, on the 1-AP-MWCNTs. The microwave-assisted polyol treatment in the presence of ethylene glycol as reducing agent reduces the Pt–Ru precursors, forming Pt–Ru nanoparticles on MWCNTs. These surface groups may also serve as anchoring

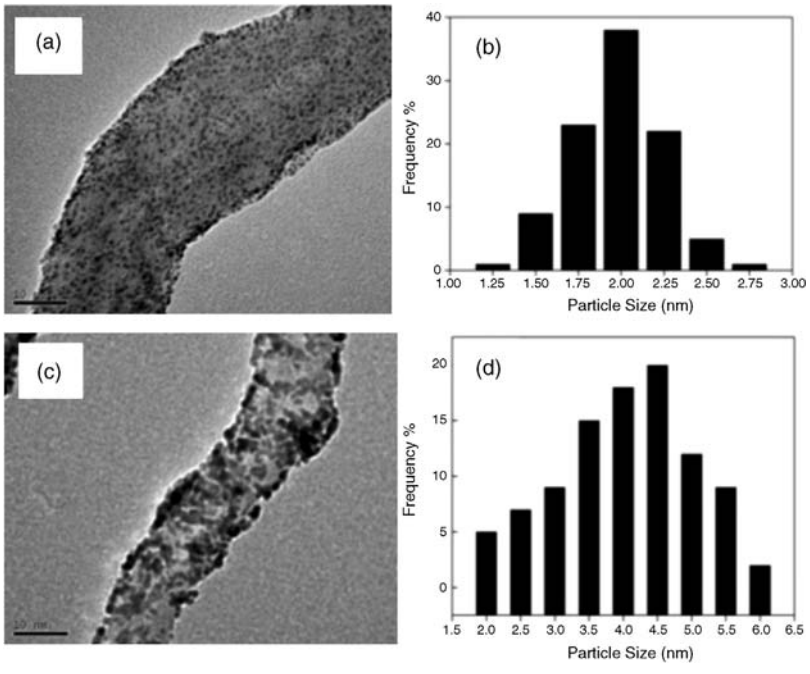

Figure 3.10 TEM images and distribution histograms of Pt–Ru nanoparticles on 1-AP-MWCNTs (a and b) and AO-MWCNTs (c and d). The Pt–Ru loading was 40 wt% [32].

sites for the direct deposition of reduced metal nanoparticles, which are normally negatively charged. Different from the acid-oxidized MWCNTs, where the harsh chemical acids are used to produce carboxylic acid sites on the surface, the 1-AP-functionalization treatment preserves the integrity and the electronic structure of MWCNTs. As proven in Figure 3.10, fine metal nanoparticles with narrow size distribution were deposited on 1-AP-CNTs with a uniform distribution, as a result of the generation of evenly distributed functional groups on the surface of CNTs. The average particle size is 2 nm, and no aggregation occurs, even at high Pt–Ru loading. However, on the acid-oxidized CNTs, Pt–Ru nanoparticles tend to form aggregates of large particle size due to the poor distribution of functional groups introduced by the harsh acid oxidation. The density of Pt–Ru electrocatalysts could be effectively controlled by adjusting the feeding concentration of the metal precursors. As a result, Pt–Ru nanoparticles on 1-AP-MWCNTs have higher electrochemical surface area, much better activity, and enhanced stability for methanol electrochemical oxidation in acid solution than those on AO-MWCNTs [32].

On the basis of the above examples, we may conclude that the noncovalent functionalization of CNTs could facilely and effectively equip CNTs with specified functional groups with high density. These surface groups function as active sites to anchor metal precursors or metal nanoparticles, resulting in well-

dispersed, narrow-distributed, loading-controlled metal nanoparticles/CNT electrocatalysts. In addition to the physical role, that is, affecting the dispersion, size, and loading of catalyst nanoparticles, the specified functional groups may also interact with catalyst nanoparticles and affect their intrinsic electrochemical activities. To date, most strategies to tune the activity have been limited to the modification of Pt with other metals, while no specific attention has been paid to the anchoring groups connecting the metal nanoparticles and the support material, which may be equally important. This direction is certainly worth further studying. Thus, the noncovalent functionalization strategy is an attractive method for the decoration of CNTs with size- and shape-controlled Pt-based nanoparticles and other nanocatalysts.

Carbon nanocoils, as well as carbon nanotubes, constitute a new class of carbon nanomaterials with properties that differ significantly from other forms of carbon. The structure of a nanocoil is similar to that of MWCNTs, except helical shape. The catalysts supported on carbon nanocoils exhibited better electrocatalytic performance compared with the catalyst supported on Vulcan XC-72 carbon. In particular, the Pt–Ru alloy catalyst supported on the CNC, which has both good crystallinity and a large surface area, showed a superior electrocatalytic performance, compared with other CNC catalysts [43]. A fullerene (C_{60}) film electrode was also suggested as a catalyst support for methanol oxidation after electrodeposition of Pt on these fullerene nanoclusters [44].

3.3.4
Graphene as Support Materials for Fuel Cells

Graphene is an ideal catalyst support, mainly due to its high electrical conductivity, excellent mechanical properties, high specific surface area, unique graphitic basal plane structure, and potential low manufacturing cost [45,46]. Yoo *et al.* [47] deposited Pt subnanoclusters on graphene nanosheets (GNS), giving rise to significant modification to the properties of Pt nanocluster electrocatalysts, and very high activities for methanol oxidation reaction were observed. The Pt/GNS electrocatalyst also revealed quite a different characteristic for CO oxidation among the measured catalyst samples. It is found that Pt particles below 0.5 nm in size are formed on GNS, which would acquire specific electronic structures of Pt, modifying its catalytic activities. Sharma *et al.* [48] reported the synthesis of Pt electrocatalysts supported on reduced graphene oxide by a microwave-assisted polyol reduction method. Because a variety of oxygen functional groups (O-moieties) are attached on the edge planes as well as on either side of the basal planes, well-dispersed nanoclusters on the surface of the reduced graphene sheets are envisaged. Such anticipation was confirmed by high-resolution TEM observations (Figure 3.11b). It is worth mentioning that these Pt NPs anchored onto the RGO surface can also prevent π–π stacking between the layers and create functional separation between individual sheets. This system was tested for potential use as an anode material through the electrooxidation of methanol. Compared with the commercial carbon-supported Pt electrocatalysts, the Pt/

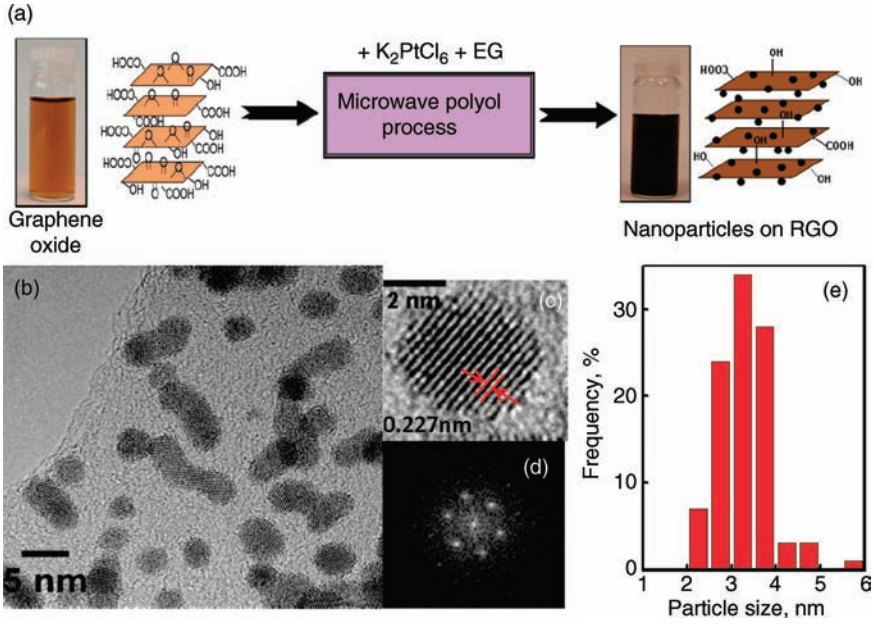

Figure 3.11 (a) Scheme of synthesis of Pt/RGO hybrids. (b) TEM image of Pt/RGO. (c) HRTEM image. (d) FFTs of a single Pt NP. (e) Pt NPs size distribution on Pt/RGO [48].

RGO showed an unprecedented CO poisoning tolerance, high electrochemical active surface area, and high catalytic mass activity for methanol oxidation reaction, demonstrated by increases of 110, 134, and 60%, respectively. It was found that the high concentration of oxygen functional groups on reduced graphene oxide plays a major role in the removal of carbonaceous species on the adjacent Pt sites, underlining a synergetic effect between the oxygen moieties on graphene support and Pt nanoparticles. The present microwave-assisted synthesis of Pt/RGO provides a new path to prepare electrocatalysts with excellent electrocatalytic activity and CO tolerance, which is of great significance in energy-related applications [45].

More recently, Lin and coworkers [49] reported a new method to deposit metal oxides and metal nanoparticles on graphene and form stable metal–metal oxide–graphene triple junctions for electrocatalysis applications in fuel cells (Figure 3.12). They first synthesized indium tin oxide (ITO) nanocrystals directly on functionalized graphene sheets, forming an ITO–graphene hybrid. Platinum nanoparticles are then deposited, forming a unique triple junction structure (Pt–ITO–graphene). Their DFT calculations indicate that the deposition of Pt nanoparticles is thermodynamically favored and stabilized at the metal oxide–graphene junctions. The defects and functional groups on graphene also help improve the stability of the catalysts. Pt–ITO–graphene nanocomposites were investigated as electrocatalysts for oxygen reduction for potential application in

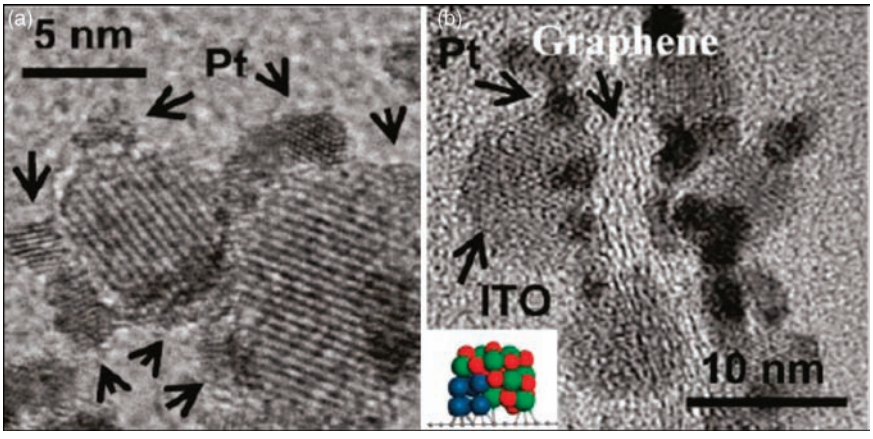

Figure 3.12 TEM images of Pt–ITO–graphene (a) and the cross section TEM images of Pt–ITO–graphene (b) [49].

PEM fuel cells. The ITO–graphene hybrid substrates possess the desired properties of the metal oxide and graphene sheets. The graphene sheets function as a scaffold that provides the high surface area and greatly increases the electrical conductivity. The ITO nanoparticles are evenly dispersed and protect graphene from corrosion, improving the durability of the substrate. The unique triple junction structure in the nanocomposite with a high surface area, good metal dispersion, and good electrical conductivity makes such materials suitable for PEM fuel cell applications. The electrochemical tests show that the performance of Pt supported on ITO–graphene hybrid substrates, especially the durability, is not only better than that of Pt supported on graphene sheets but also better than the widely used Pt electrocatalysts supported with other carbon materials (e.g., Vulcan carbon XC72 and carbon nanotubes) [49].

Wang *et al.* [45] developed highly effective electrocatalysts for HCOOH oxidation through DFAFCs using simultaneously assembled Pt and Au nanoparticles on noncovalently functionalized graphene supports. The noncovalent functionalization method for carbon nanotubes based on positively charged PDDA is also very effective for functionalization of graphene without detrimental effects on its electronic properties. Pt and Au nanoparticles with various ratios are simultaneously self-assembled onto PDDA-functionalized graphene with high uniformity and controlled densities and compositions, forming Pt and Au nanoparticle electrocatalysts on PDDA-functionalized graphene (or Pt–Au/PDDA–G) for HCOOH oxidation. The principle of the self-assembly of mixed Pt and Au nanoparticles on PDDA-functionalized graphene is shown in Figure 3.13. The results indicate that the Pt–Au/PDDA–G electrocatalysts show superb electrochemical activity toward HCOOH oxidation, and the mass-specific current density for HCOOH oxidation on a Pt1Au8/PDDA–G catalyst (Pt:Au ratio of 1 : 8) is 32 times higher than that on Pt/PDDA–G catalysts [45].

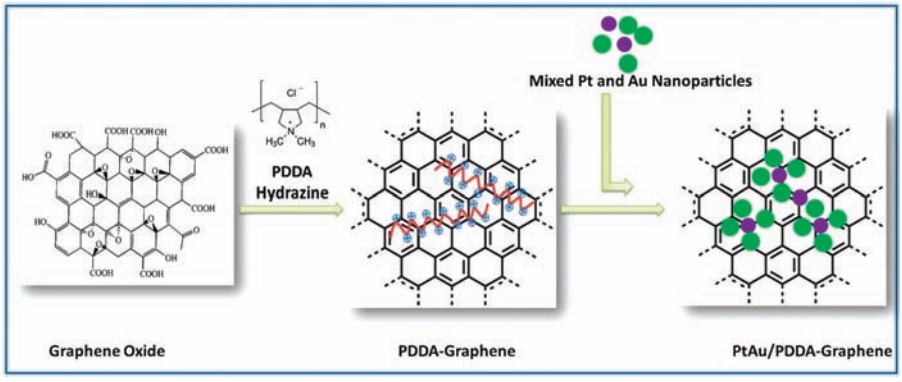

Figure 3.13 Self-assembly of mixed Pt and Au nanoparticles onto PDDA-functionalized graphene [45].

3.3.5
Nitrogen-Doped Carbon Materials

Nitrogen-doped carbon material (e.g., CNTs and graphene) is recognized as a good support for Pt catalyst. The doping of CNTs with other elements (e.g., nitrogen) could be a particularly interesting way to modify their electrical and mechanical properties. The introduction of N modifies the structure of the CNT, leading to (i) high surface areas, (ii) a high density of defects, (iii) chemically active impurity sites, and (iv) narrow tubes (the numbers of walls decrease with N inclusion) [33].

The doped nitrogen atoms not only provide the anchoring sites for the metal particles but also act as chemically active sites for fuel cell reactions. The N sites in N–CNTs are reported to bind strongly to metals, leading to excellent metal dispersion in metal/N–CNT materials. The surface modifications induced in CNTs by N doping can thus enhance the reactivity and selectivity of carbon-supported catalysts in many catalytic applications [33]. Therefore, it should be possible to avoid functionalization processes that use strong acid treatments, as it is relatively easy to deposit metal catalysts onto N–CNTs [33].

The nitrogen functionality in the carbon nanotube support determines the size of Pt by bonding with lone pairs of electrons at the nitrogen site in a sp^2 hybridized orbital in the plane of the ring. These N-sites, which predominate in untreated carbon black, were less negative than oxygen sites. The assumption was that during catalysis, Pt might bind more strongly to pyridinic sites, thereby preventing Pt particles from sintering to the extent observed on untreated carbons. The increased electron donation from pyridinic N-functionality to Pt might be responsible for the enhancement in kinetics of methanol oxidation [18,19].

Nitrogen-doped carbon nanotubes (N–CNTs) have recently been reported to have significant catalytic activity toward ORR in alkaline conditions (Figure 3.14) [51]. This ORR activity along with the morphology and properties of the

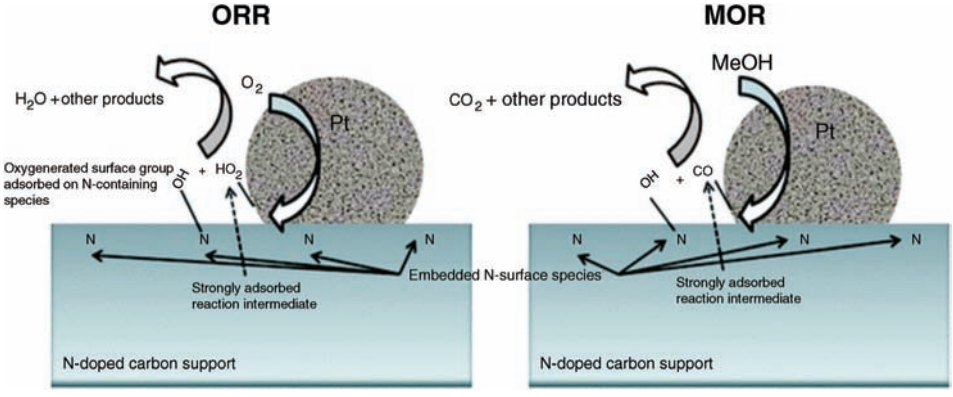

Figure 3.14 Schematic of possible bifunctional ORR and MOR mechanisms involving oxophilic C–N defects near C/Pt catalyst particle interface in the case of low-density Pt catalyst (not to scale). The adsorbed oxygen-containing surface species facilitate reaction of strongly absorbed intermediate reaction species that would otherwise block catalyst active sites, thereby increasing the net turnover frequency of the electrochemical reaction [50].

N–CNT materials is directly related to the type of nitrogen–carbon precursor and growth catalyst utilized. This electrocatalytic activity was attributed directly to the incorporation of nitrogen into the graphitic structure of CNTs, resulting in enhanced structural and electronic properties. Recently, Chen and coworkers [52] utilized nitrogen-doped carbon nanotubes as platinum nanoparticle support materials and elucidated the significant effect of the nitrogen precursor solution on N–CNT growth. N–CNTs synthesized from a nitrogen-rich ethylenediamine (ED) precursor solution (ED–CNT) were found to have superior catalytic activity toward the ORR compared with undoped CNTs. When utilized as platinum nanoparticle supports, Pt/N–CNTs displayed significantly enhanced electrocatalytic activity toward the ORR compared with nitrogen-free Pt/CNTs, with the increase in performance being attributed to the distinct structural and electronic enhancements resulting from heterogeneous nitrogen doping. The performance of Pt/N–CNTs as a cathodic catalyst for proton exchange membrane fuel cell operation was found to be significantly higher than that of Pt/CNT. Polarization and power density curves for Pt/N–CNTs and Pt/CNTs in a single-cell H_2/O_2 MEA system fabricated by a decal method are displayed in Figure 3.15. The peak power density for Pt/ED–CNTs was 1.04 W cm^{-2}, an increase of ~16.9% over that of Pt/CNTs (0.89 W cm^{-2}). At a cell voltage of 0.6 V, Pt/ED–CNTs displayed a current density of 1.55 A cm^{-2}, ~24% higher than Pt/CNTs (1.25 A cm^{-2}). Pt/ED–CNTs display improved ORR catalytic activity compared with Pt/CNTs under fuel cell conditions.

Ramaprabhu and coworkers investigated the nitrogen-doped graphene nanoplatelets as the catalyst support of Pt for ORR [53]. In this case, the nitrogen-doped graphene was made by nitrogen plasma treatment of graphene. The MEA constructed with Pt/N–graphene as the ORR catalyst showed a maximum power

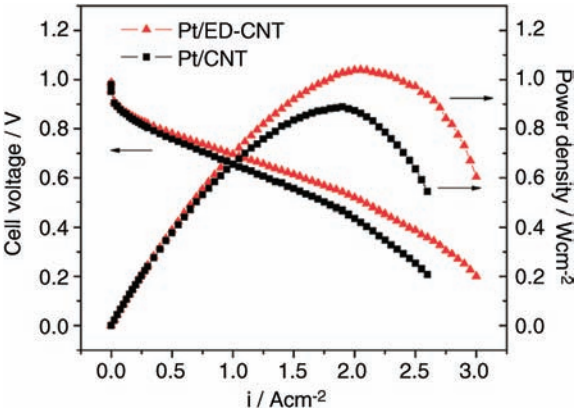

Figure 3.15 MEA polarization and power curves for 0.2 $mg_{Pt}\,cm^{-2}$ Pt/ED-CNT and Pt/CNT cathodic catalyst loading, with 0.2 $mg_{Pt}\,cm^{-2}$ commercial Pt/C as anodic catalyst in a single-cell H_2/O_2 system with a Nafion 112 PEM [52].

density of 440 $mW\,cm^{-2}$, whereas the MEA with Pt/graphene showed a maximum power density of 390 $mW\,cm^{-2}$. The improved performance with Pt/N–graphene as an ORR catalyst can be attributed to the formation of pentagons and heptagons and increase in the reactivity of neighboring carbon atoms because of nitrogen doping. It has been reported that nitrogen doping introduces disorder in the graphene stacking and these disorder structures and the defects can act as good anchoring sites for the deposition of Pt particles [53].

3.4
Conductive Metal Oxide as Support Materials

In addition to conventional carbon materials, various conductive metal oxides, including TiO_x, WO_x, SnO_2, IrO_2, ITO, and so on, were also used as support or cosupport of electrocatalysts. Conducting oxides are corrosion resistant with good thermal and electrochemical stability in fuel cell environment. The use of metal oxide as support material has potentially strong metal–support interaction (SMSI) that allows the tuning of activity in addition to stability. Metal–metal oxide catalysts are believed to operate via the bifunctional mechanism [54].

The promotion effect of TiO_2 nanotubes in the methanol oxidation can be rationalized on the basis of SMSI as well as OH adsorption on Ti ion site facilitating the oxidation of CO on Pt sites, which are otherwise poisons to the metallic sites and thus render these metallic sites unsuitable for methanol oxidation. A pictorial model of these postulates is given in Figure 3.16 [55].

To improve the electron conductivity, substoichiometric titania (Ti_4O_7) and Nb-doped TiO_2 were attempted as support and their activities for both the hydrogen oxidation reaction and the oxygen reduction reaction were compared with that of Vulcan XC-72-supported Pt catalyst under PEMFC operation [56–60].

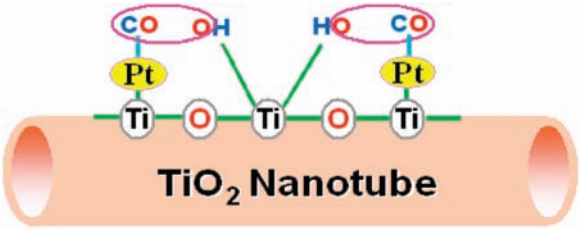

Figure 3.16 A possible mechanism for the removal of CO poisoning intermediates during methanol oxidation over TiO_2 nanotube-supported Pt catalysts [55].

It has been reported that a Pt/TiO_2 catalyst exhibits a higher active surface area than Pt supported on carbon, and thus improves the activity for oxygen reduction. Drew *et al.* [61] showed a boosting of methanol oxidation by Pt–Ru supported on TiO_2 and carbon fiber. Titanium oxide with designed nanostructures was used to support electrocatalysts for fuel cells. Shanmugam and Gedanken [62] utilized the carbon-coated anatase titania (CCT) TiO_2@C core–shell structure to support Pt nanoparticles for ORR and MOR. The particles have a dark TiO_2 core surrounded by a faint carbon shell; the size of the composite nanoparticles is around 20–40 nm. The average size of Pt on CCT is 5–8 nm. It is clear from the HRTEM studies that a few carbon layers surround the anatase TiO_2 core. However, the thickness of the shell varies from 2 to 4 nm on the CCT. It is also observed that as the temperature increases, the carbon content and the thickness of the carbon layers change. The as-prepared electrocatalysts showed a higher catalytic activity and improved durability toward both ORR and MOR compared with the commercial Pt/C electrocatalysts [63].

For example, Kowal *et al.* [63] successfully synthesized the ternary $PtRhSnO_2/C$ electrocatalyst, effective in splitting the C−C bond of ethanol at room temperature and causing its predominant oxidation to CO_2. The analyses reveal that its catalytic activity rests on the synergy between the three constituents of the electrocatalyst. SnO_2 by strongly adsorbing water [64,65] and interacting with the Pt and Rh deposited on its surface apparently precludes the Rh and Pt sites from reacting with H_2O to form metal–OH, making them available for ethanol oxidation. SnO_2 with H_2O provides OH species to oxidize the dissociated CO at Rh sites, and Pt facilitates ethanol dehydrogenation. It also modifies the electronic structure of Rh to afford moderate bonding to ethanol, intermediates, and products, which facilitates C−C bond breaking and, therefore, ethanol oxidation. The DFT calculations demonstrated that the oxidation of ethanol on $PtRh/SnO_2$ proceeds through oxametallacyclic conformation that facilitates the direct cleavage of the C−C bond at a reasonable rate. The high activity of Pt–Ru for methanol oxidation and the lack of it for ethanol oxidation seem to be due to a high propensity of Ru to form RuOH in interaction with H_2O at potentials $E > 0{:}0\,V$. This reaction cannot be suppressed in the OH−OH repulsion with SnOH, as it happens with weakly bonded RhOH. RuOH does not adsorb ethanol and cannot split the C−C bond. This work demonstrated the significant role of tin oxide for alcohol oxidation [63].

Tungsten oxides (WO_{3-x}) have been the subject of interest and have been used as a support material for fuel cell catalysts [66–69]. It has been reported that catalysts made of Pt nanoparticles supported on WO_3 exhibit excellent CO tolerance and higher catalytic activity. For example, the electrocatalytic activity of a Pt/WO_3-based electrode toward the oxygen reduction reaction in phosphoric acid was reported to be twice as high as that of Pt on carbon [69]. Sun and coworkers [69] successfully grew tungsten oxide nanowires ($W_{18}O_{49}$ NWs) on carbon paper by chemical vapor deposition. The well-dispersed Pt nanoparticles, with a size distribution from 2 to 4 nm, were deposited on the surface of $W_{18}O_{49}$ NWs through a simple reductive process. The resulting $Pt/W_{18}O_{49}$ NWs/carbon paper composites formed a three-dimensional electrode structure. In comparison with conventional Pt/C electrocatalyst, the $Pt/W_{18}O_{49}$ NWs/carbon paper composite exhibited higher electrocatalytic activity toward the oxygen reduction reaction and better CO tolerance in a single-cell polymer electrolyte membrane fuel cell. $Pt/Ti_{0.7}W_{0.3}O_2$ has been proposed as another promising highly stable and CO-tolerant electrocatalyst for PEM fuel cells. Initial tests indicated that $Pt/Ti_{0.7}W_{0.3}O_2$ is more stable than Pt/C and PtRu/C catalysts. After 500 cycles, the loss in the integrated coulombic charge of the CV for the new catalyst was only 5%, while it was more than 30% in the case of a commercial E-TEK PtRu/C catalyst [70]. Suzuki *et al.* [71] reported sulfate zirconia as Pt support for use in PEMFC. The electrocatalytic activity of $Pt/S–ZrO_2$ was lower than that of the Pt/C.

3.5
Metal Carbides and Metal Nitrides as Catalyst Supports

Tungsten carbides (WCs), exhibited Pt-like catalytic properties because near the Fermi level, the electronic density of states of tungsten carbides resembles that of noble metal platinum [72]. Its low price and good CO tolerance make it an interesting alternative to the noble metal catalyst. Thus, in the last decades, tungsten carbides have been tested as alternative Pt electrocatalysts for PEMFCs.

Tungsten carbide was found to be more thermally and electrochemically stable than carbon supports. However, its stability in acid electrolyte is not satisfactory because WC can be corroded in sulfuric acid [73–75]. Tungsten carbide is not suitable as cathode catalyst or support for acidic fuel cells, owing to its low corrosion resistance under acidic and oxidative conditions. Titanium diboride (TiB_2) exhibits many superior properties, including high melting point, great hardness, good electrical and high thermal conductivity, and excellent thermal stability and corrosion resistance in acidic medium. The stability of Pt/TiB_2 is approximately four times better than that of the commercial Pt/C [76]. Recently, it was also reported that titanium nitride-supported Pt for PEM fuel cells showed higher catalytic performance than conventional Pt/C catalysts, but the durability of TiN as the support material is not clear as yet [77,78]. Further studies are necessary to understand TiN as a catalyst support and especially evaluate its durability properties [79].

3.6
Conducting Polymer as Support Materials for Fuel Cells

Recently, attention has also been given to the use of conductive polymers (CPs) as electrocatalyst supports and promising results have been obtained [80–82]. By suitably combining conductive polymer and metal nanoparticles, new electrocatalysts with higher surface areas and enhanced methanol oxidation activity can be generated. Conducting polymers have received much attention because of their high accessible surface area, low resistance, and high stability. Given their conductive and stable three-dimensional structure, CPs can act as suitable supports for low-temperature fuel cell catalysts. Conducting polymer/metal–nanoparticle composites allow a facile flow of electronic charges through the polymer matrix during the electrochemical process. CPs with porous structures and high surface areas are employed as a matrix to incorporate noble metal catalysts for some electrochemical reactions of importance for application in fuel cells such as hydrogen and methanol oxidation and oxygen reduction [81]. The main reason for incorporating metallic particles into porous polymeric matrices is to increase the specific area of the active surface and thereby improve catalytic efficiency. Another reason is the higher tolerance of polymer-supported platinum particles to poisoning due to the adsorption of CO species, in comparison with the serious problem of poisoning of bulk and carbon-supported platinum electrodes. Indeed, the catalyst is poisoned by the strong adsorption of CO present in H_2 or of CO-like intermediate species formed during alcohol oxidation, which block the active Pt sites, lowering its electrocatalytic activity [81,82]. Moreover, CPs are not only electron-conducting but also proton-conducting materials, so they can replace Nafion in the catalyst layer of fuel cell electrode and provide enhanced performance. In this case, theoretically only a two-phase boundary is necessary for electron and ion transfer during reactions in fuel cells compared with the three-phase boundary required when carbon is used as support, the overall catalyst utilization should be significantly increased (Figure 3.17) [82].

Among conducting polymers, conductive polyaniline (PANI) can be considered as a promising catalyst support material owing to its good electrical conductivity, high environmental stability, and the merit of simple preparation by both chemical and electrochemical processes. There are different methods reported in the literature for the synthesis of conducting PANI, and these can be classified into two methodologies: template-assisted and template-free syntheses. Extensive work has been carried out on the fabrication and characterization of PANI. Chen *et al.* [83] prepared a novel polyaniline nanofiber-supported Pt nanoelectrocatalyst for DMFCs. Polyaniline nanofibers (PaniNFs) with a 60 nm diameter are synthesized by a scalable interfacial polymerization without the use of a template or functional dopant. PaniNF-supported Pt electrocatalyst (Pt/PaniNFs) and carbon black-supported Pt electrocatalyst (Pt/C) are prepared by an ethylene glycol reduction method. The Pt nanoparticles deposited onto PaniNFs have a smaller diameter and narrower particle size distribution than the Pt nanoparticles deposited onto carbon black. The Pt/PaniNFs catalyst shows a higher

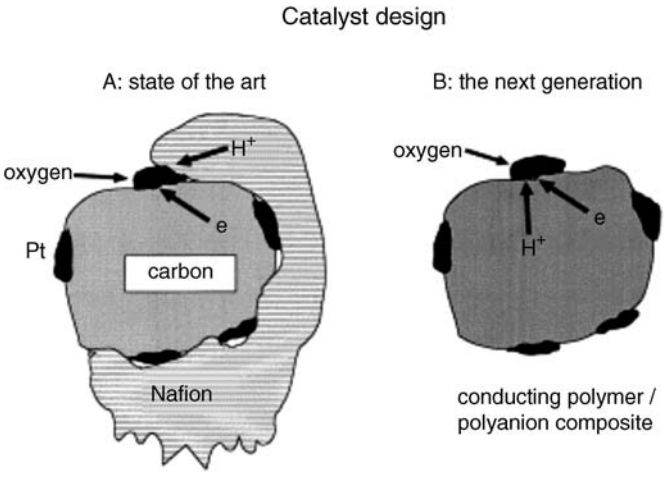

Figure 3.17 PEM fuel cell catalyst layer illustration of three-phase boundary versus two-phase boundary [82].

electrochemical active surface area (ECSA) and higher methanol oxidation reaction catalytic activity than the Pt/C [83].

Poly(*N*-acetylaniline) (PAANI), one of the substituted polyaniline conducting polymers, was successfully used as a support for fuel cell catalysts [84]. PEDOT/PSS has also been reported as support material, with activities for oxygen reduction of Pt/PEDOT/PSS comparable with that obtained with commercial carbon-supported catalysts. However, long-term stability of PEDOT/PSS has to be improved and conductivity is still lower compared with carbon materials [85]. Choi *et al.* electrodeposited Pt–Ru catalysts on poly(*N*-vinyl carbazole) (PVK) and poly(9-(4-vinyl-phenyl)carbazole) (P4VPCz). The performance of DMFCs with carbon-supported Pt–Ru showed better performance than that of the Pt–Ru/PVK composite due to its low electronic conductivity [86].

3.7
Conducting Polymer-Grafted Carbon Materials

The Pt catalyst is dispersed on a high-surface-area electronically conductive support, which facilitates the passage of electrons from the catalyst to the external circuit, but cannot conduct protons. Proton-conducting materials such as Nafion® are often added to facilitate transfer of the protons from the catalyst layer to the membrane interface. Therefore, proton conduction may depend dramatically on the formulation of the thickness of the catalyst layer. Recent advances in catalyst design have begun to address this limitation. As with electron conduction, thinner catalyst layers help reduce resistive losses due to proton conduction. Also, carbon is relatively hydrophobic, and as such the boundary

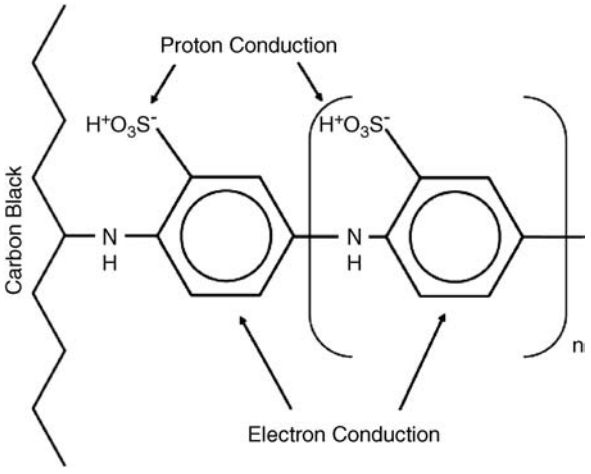

Figure 3.18 Catalysts with surface-modified carbon blacks show enhanced proton and electron conduction [89].

contact between the reactive gases, water, and the surface of the solid electrodes made of carbon contributes to high electrical contact resistance and ohmic power loss in the fuel cell, resulting in lower efficiency of the fuel cell. Furthermore, conducting polymer grafted on the carbon surface to impart protonic conductivity and the surface chemistry of the catalyst support can be tailored appropriately, as illustrated in Figure 3.18. However, such changes must be carefully performed to minimize any adverse impact on other important features of the catalyst. Also, the catalyst may lose stability due to sintering of platinum particles, dissolution of platinum, and corrosion of the carbon support.

Sintering of platinum particles on the carbon support decreases catalytically active surface areas. The sintering of the catalyst can be reduced by strengthening the strong metal–support interaction. Grafting of polymer on the carbon support decreases the sintering of the metal particles. The conducting polymer-grafted carbon material aids the uniform dispersion and stabilization of metal particles by anchoring to heteroatoms, namely, N, O, S, and so on, present in the conducting polymer. The heteroatom (nitrogen or sulfur) in the polymer backbone acts as a Lewis base that can anchor the platinum particles effectively and resist the agglomeration and sintering of metal (e.g., platinum (Pt)) crystallite particles [87,88].

3.8
3M Nanostructured Thin Film as Support Materials for Fuel Cells

The 3M nanostructured thin film (NSTF) catalyst support has also been well developed, which consists of oriented, nanometer-sized crystalline organic whiskers, synthesized by sublimation and subsequent annealing of an organic

pigment material based on a perylene dicarboximide compound [90,91]. This pigment material gives a monolayer of oriented crystalline whiskers with number densities. The whiskers have a rectangular cross section of around 30–50 nm and an average length of 0.5–1 μm. Earlier work by Debe *et al.* [90,91] demonstrated the higher stability and durability of NSTF catalysts in comparison with conventional carbon-supported dispersed Pt catalysts. Furthermore, the organic crystalline whisker support also epitaxially affects the subsequent nucleation and growth of Pt whiskerettes on whisker sides, maximizing the amount of Pt(111) surface facets [92]. In addition to being an excellent catalyst support, the NSTF support is a good substrate for the rapid screening of a wide range of potential underlayer materials for fuel cell applications. Underlayer materials that show promise could feasibly be used on NSTF to modify the dimensions and morphology of the catalyst support whisker or on their own as particulate catalysts supports to replace conventional high-surface-area carbon supports. The NSTF technology is useful for studying underlayer materials because a wide range of elements and compounds can be prepared through sputter depositions and because their high aspect ratio and surface area allow subsequent preparation of high-surface-area platinum-based catalysts for realistic fuel cell testing under realistic conditions [90,91].

3.9 Summary and Outlook

Various types of support materials, including carbon materials (i.e., carbon black, ordered mesoporous carbon, graphitic nanofiber, CNT, and graphene), conductive metal oxide, and conducting polymers, have been extensively investigated for fuel cell applications. The catalyst support materials are used to increase the metal nanoparticle loading and dispersion, which would thus improve the utilization efficiency and durability of the precious metal catalysts. The properties of support materials exhibit great influence on the catalytic activity, durability, and even cost of fuel cells. The requirements of suitable support materials for fuel cell electrocatalysts are high electrochemically accessible surface area, good electron conductivity, appropriate porosity for mass transport, and good electrochemical and thermal stability under fuel cell operation conditions. The most commonly used catalyst support is carbon black. However, there are several disadvantages of carbon black as discussed in this chapter; therefore, the development of alternative support materials for fuel cell applications has attracted a lot of attention in the past decade.

OMC is a promising candidate due to its high surface area, high conductivity, and facilitated mass transport within the pore channels. The electrocatalysts supported on OMC have shown excellent performance in PEMFC electrode reactions. The as-observed improved performance of fuel cell on OMC-supported electrocatalysts is well understandable, as OMC would lead to uniform dispersion of metal nanoparticles and enhanced mass transport due to its high surface area

and interconnected pore structures. Graphite nanofibers have generated great interest as support materials because of their good graphitic structures, low resistance, and high electrical conductivity. Different from the structure of CNTs, there is no hollow cavity in GNFs and the basal plane is exposed only at the edge regions. Due to its unique structure, GNF could be directly used to support metal nanoparticles without any pretreatment, which would usually destroy the perfect structure of graphite fiber, as it is believed that platelets and herringbone structures of GNFs usually present potentially reactive groups for metal deposition. CNTs are widely studied as support material for Pt and Pt alloy catalysts in fuel cells due to their high surface area, excellent electronic conductivity, and high chemical stability. However, the deposition, distribution and size of Pt or Pt alloy nanoparticles supported on CNTs depend strongly on the surface treatment and surface properties of CNTs. The activity of Pt nanoparticles is also significantly affected by the nature of their interaction with CNTs and the intrinsic properties of CNTs. Since pristine CNTs are chemically inert, it is necessary to activate the graphitic surface of the nanotubes in order to anchor and deposit catalytic nanoparticles. Various functionalization methods have been developed, including covalent and noncovalent functionalization. The noncovalent functionalization strategy could introduce amounts of functional groups onto the surface of CNT uniformly without any damage to the perfect structure of CNTs. Due to its unique electronic and mechanical properties, graphene has been attracting more and more attention. Graphene and chemically modified graphene sheets have higher conductivity and surface area compared with carbon nanotubes and have found lots of potential applications. Meanwhile, other different types of support materials such as metal oxide, conducting polymer, and so on were also discussed.

Although various support materials have been developed to support nanostructured electrocatalysts for fuel cells, the performance of the as-obtained catalysts is still far from the research target for large-scale fuel cell commercialization in terms of activity, durability, and cost. More extensive research work needs to be done, taking into consideration these three objectives: activity, durability, and cost.

References

1 Borup, R., Meyers, J., Pivovar, B., Kim, Y.S., Mukundan, R., Garland, N., Myers, D., Wilson, M., Garzon, F., Wood, D., Zelenay, P., More, K., Stroh, K., Zawodzinski, T., Boncella, J., Mcgrath, J.E., Inaba, M., Miyatake, K., Hori, M., Ota, K., Ogumi, Z., Miyata, S., Nishikata, A., Zyun, S., Uchimoto, Y., Yasuda, K., Kimijima, K.-I., and Iwashita, N. (2007) Scientific aspects of polymer electrolyte fuel cell durability and degradation. *Chemical Reviews*, 3904–3951.

2 Markovic, N.M. and Ross, P.N. (2002) Surface science studies of model fuel cell electrocatalysts. *Surface Science Reports*, **45** (4–6), 121–229.

3 Rajalakshmi, N., Pandiyan, S., and Dhathathreyan, K.S. (2008) Design and development of modular fuel cell stacks for various applications. *International Journal of Hydrogen Energy*, **33**, 449–454.

4 Yu, X. and Ye, S. (2007) Recent advances in activity and durability enhancement of Pt/C catalytic cathode in PEMFC: Part I. Physico-chemical and electronic

interaction between Pt and carbon support, and activity enhancement of Pt/C catalyst. *Journal of Power Sources*, **172** (1), 133–144.

5 Antolini, E. (2009) Carbon supports for low-temperature fuel cell catalysts. *Applied Catalysis B: Environmental*, **88** (1–2), 1–24.

6 Shao, Y.Y., Liu, J., Wang, Y., and Lin, Y.H. (2009) Novel catalyst support materials for PEM fuel cells: current status and future prospects. *Journal of Materials Chemistry*, **19** (1), 46–59.

7 Chang, H., Joo, S.H., and Pak, C. (2007) Synthesis and characterization of mesoporous carbon for fuel cell applications. *Journal of Materials Chemistry*, **17** (30), 3078–3088.

8 Joo, S.H., Choi, S.J., Oh, I., Kwak, J., Liu, Z., Terasaki, O., and Ryoo, R. (2001) Ordered nanoporous arrays of carbon supporting high dispersions of platinum nanoparticles. *Nature*, **412** (6843), 169–172.

9 Ding, J., Chan, K.-Y., Ren, J., and Xiao, F.-S. (2005) Platinum and platinum–ruthenium nanoparticles supported on ordered mesoporous carbon and their electrocatalytic performance for fuel cell reactions. *Electrochimica Acta*, **50** (15), 3131–3141.

10 Lin, M.-L., Huang, C.-C., Lo, M.-Y., and Mou, C.-Y. (2008) Well-ordered mesoporous carbon thin film with perpendicular channels: application to direct methanol fuel cell. *Journal of Physical Chemistry C*, **112** (3), 867–873.

11 Liu, S.-H., Yu, W.-Y., Chen, C.-H., Lo, A.-Y., Hwang, B.-J., Chien, S.-H., and Liu, S.-B. (2008) Fabrication and characterization of well-dispersed and highly stable PtRu nanoparticles on carbon mesoporous material for applications in direct methanol fuel cell. *Chemistry of Materials*, **20** (4), 1622–1628.

12 Yu, J.-S., Kang, S., Yoon, S.B., and Chai, G. (2002) Fabrication of ordered uniform porous carbon networks and their application to a catalyst supporter. *Journal of the American Chemical Society*, **124** (32), 9382–9383.

13 Su, F., Zeng, J., Bao, X., Yu, Y., Lee, J.Y., and Zhao, X.S. (2005) Preparation and characterization of highly ordered graphitic mesoporous carbon as a Pt catalyst support for direct methanol fuel cells. *Chemistry of Materials*, **17** (15), 3960–3967.

14 Joo, S.H., Pak, C., You, D.J., Lee, S.-A., Lee, H.I., Kim, J.M., Chang, H., and Seung, D. (2006) Ordered mesoporous carbons (OMC) as supports of electrocatalysts for direct methanol fuel cells (DMFC): effect of carbon precursors of OMC on DMFC performances. *Electrochimica Acta*, **52** (4), 1618–1626.

15 Shanahan, P.V., Xu, L., Liang, C., Waje, M., Dai, S., and Yan, Y.S (2008) Graphitic mesoporous carbon as a durable fuel cell catalyst support. *Journal of Power Sources*, **185** (1), 423–427.

16 Du, H., Li, B., Kang, F., Fu, R., and Zeng, Y. (2007) Carbon aerogel supported Pt-Ru catalysts for using as the anode of direct methanol fuel cells. *Carbon*, **45** (2), 429–435.

17 Marie, J., Chenitz, R., Chatenet, M., Berthon-Fabry, S., Cornet, N., and Achard, P. (2009) Platinum supported on resorcinol-formaldehyde based carbon aerogels for PEMFC electrodes: influence of the carbon support on electrocatalytic properties. *Journal of Power Sources*, **190**, 423–434.

18 Maiyalagan, T., Viswanathan, B., and Varadaraju, U.V. (2005) Nitrogen containing carbon nanotubes as supports for Pt: alternate anodes for fuel cell applications. *Electrochemistry Communications*, **7**, 905–912.

19 Maiyalagan, T. (2008) Synthesis and electro-catalytic activity of methanol oxidation on nitrogen containing carbon nanotubes supported Pt electrodes. *Applied Catalysis B: Environmental*, **80** (3–4), 286–295.

20 Kim, M., Hwang, S., and Yu, J.S. (2007) Novel ordered nanoporous graphitic C_3N_4 as a support for Pt–Ru anode catalyst in direct methanol fuel cell. *Journal of Material Chemistry*, **17**, 1656–1659.

21 Roustom, B.El., Sine, G., Foti, G., and Comninellis, C. (2007) A novel method for the preparation of bi-metallic (Pt-Au) nanoparticles on boron doped diamond (BDD) substrate: application to the oxygen

reduction reaction. *Journal of Applied Electrochemistry*, **37**, 1227–1236.
22 Fischer, A.E. and Swain, G.M. (2005) Preparation and characterization of boron-doped diamond powder: a possible dimensionally stable electrocatalyst support material. *Journal of the Electrochemical Society*, **152** (9), B369–B375.
23 Salazar-Banda, G.R., Eguiluz, K.I.B., and Avaca, L.A. (2007) Boron-doped diamond powder as catalyst support for fuel cell applications. *Electrochemistry Communications*, **9** (1), 59–64.
24 Gangeri, M., Centi, G., Malfa, A.L., Perathoner, S., Vieira, R., Pham-Huu, C., and Ledoux, M.J. (2005) Electrocatalytic performances of nanostructured platinum-carbon materials. *Catalysis Today*, **102–103**, 50–57.
25 Bessel, C.A., Laubernds, K., Rodriguez, N.M., and Baker, R.T.K. (2001) Graphite nanofibers as an electrode for fuel cell applications. *The Journal of Physical Chemistry B*, **105** (6), 1115–1118.
26 Steigerwalt, E.S., Deluga, G.A., Cliffel, D.E., and Lukehart, C.M. (2001) A PtRu/graphitic carbon nanofiber nanocomposite exhibiting high relative performance as a direct-methanol fuel cell anode catalyst. *The Journal of Physical Chemistry B*, **105** (34), 8097–8101.
27 Gan, L., Du, H., Li, B., and Kang, F. (2011) Surface-reconstructed graphite nanofibers as a support for cathode catalysts of fuel cells. *Chemical Communications*, **47** (13), 3900–3902.
28 Girishkumar, G., Hall, T.D., Vinodgopal, K., and Kamat, P.V. (2006) Single wall carbon nanotube supports for portable direct methanol fuel cells. *Journal of Physical Chemistry B*, **110** (1), 107–114.
29 Li, W., Liang, C., Zhou, W., Qiu, J., Zhou, Z., Sun, G., and Xin, Q. (2003) Preparation and characterization of multiwalled carbon nanotube-supported platinum for cathode catalysts of direct methanol fuel cells. *Journal of Physical Chemistry B*, **107** (26), 6292–6299.
30 Wang, S., Jiang, S.P., and Wang, X. (2008) Polyelectrolyte functionalized carbon nanotubes as a support for noble metal electrocatalysts and their activity for methanol oxidation. *Nanotechnology*, **19** (26), 265601.
31 Wang, S.Y., Jiang, S.P., White, T.J., Guo, J., and Wang, X. (2009) Electrocatalytic activity and interconnectivity of Pt nanoparticles on multiwalled carbon nanotubes for fuel cells. *Journal of Physical Chemistry C*, **113** (43), 18935–18945.
32 Wang, S.Y., Wang, X., and Jiang, S.P. (2008) PtRu nanoparticles supported on 1-aminopyrene-functionalized multiwalled carbon nanotubes and their electrocatalytic activity for methanol oxidation. *Langmuir*, **24** (18), 10505–10512.
33 Saha, M.S. and Kundu, A. (2010) Functionalizing carbon nanotubes for proton exchange membrane fuel cells electrode. *Journal of Power Sources*, **195** (19), 6255–6261.
34 Yu, R., Chen, L., Liu, Q., Lin, J., Tan, K.-L., Ng, S.C., Chan, H.S.O., Xu, G.-Q., and Hor, T.S.A. (1998) Platinum deposition on carbon nanotubes via chemical modification. *Chemistry of Materials*, **10** (3), 718–722.
35 Xu, C., Chen, J., Cui, Y., Han, Q., Choo, H., Liaw, P.K., and Wu, D. (2006) Influence of the surface treatment on the deposition of platinum nanoparticles on the carbon nanotubes. *Advanced Engineering Materials*, **8** (1–2), 73–77.
36 Xing, Y. (2004) Synthesis and electrochemical characterization of uniformly-dispersed high loading Pt nanoparticles on sonochemically-treated carbon nanotubes. *The Journal of Physical Chemistry B*, **108** (50), 19255–19259.
37 Hsin, Y.L., Hwang, K.C., and Yeh, C.-T. (2007) Poly(vinylpyrrolidone)-modified graphite carbon nanofibers as promising supports for PtRu catalysts in direct methanol fuel cells. *Journal of the American Chemical Society*, **129** (32), 9999–10010.
38 Li, X.L., Liu, Y.Q., Fu, L., Cao, L.C., Wei, D.C., and Wang, Y. (2006) Efficient synthesis of carbon nanotube–nanoparticle hybrids. *Advanced Functional Materials*, **16** (18), 2431–2437.

39 Correa-Duarte, M.A., Sobal, N., Liz-Marzán, L.M., and Giersig, M. (2004) Linear assemblies of silica-coated gold nanoparticles using carbon nanotubes as templates. *Advanced Materials*, **16** (23–24), 2179–2184.

40 Yang, D.Q., Hennequin, B., and Sacher, E. (2006) XPS demonstration of interaction between benzyl mercaptan and multiwalled carbon nanotubes and their use in the adhesion of Pt nanoparticles. *Chemistry of Materials*, **18** (21), 5033–5038.

41 Wang, S. (2010) Nanostructured electrocatalysts for proton exchange membrane fuel cells (PEMFCs). Ph.D. thesis, Nanyang Technological University, Singapore.

42 Wang, S., Yang, F., Jiang, S.P., Chen, S., and Wang, X. (2010) Tuning the electrocatalytic activity of Pt nanoparticles on carbon nanotubes via surface functionalization. *Electrochemistry Communications*, **12** (11), 1646–1649.

43 Park, K.-W., Sung, Y.-E., Han, S., Yun, Y., and Hyeon, T. (2004) Origin of the enhanced catalytic activity of carbon nanocoil-supported PtRu alloy electrocatalysts. *Journal of Physical Chemistry B*, **108** (3), 939–944.

44 Lee, G., Shim, J.H., Kang, H., Nam, K.M., Song, H., and Park, J.T. (2009) Monodisperse Pt and PtRu/C60 hybrid nanoparticles for fuel cell anode catalysts. *Chemical Communications*, (33), 5036–5038.

45 Wang, S., Wang, X., and Jiang, S.P. (2011) Self-assembly of mixed Pt and Au nanoparticles on PDDA-functionalized graphene as effective electrocatalysts for formic acid oxidation of fuel cells. *Physical Chemistry Chemical Physics*, **13** (15), 6883–6891.

46 Ha, H.W., Kim, I.Y., Hwang, S.J., and Ruoff, R.S. (2011) One-pot synthesis of platinum nanoparticles embedded on reduced graphene oxide for oxygen reduction in methanol fuel cells. *Electrochemical and Solid-State Letters*, **14** (7), B70–B73.

47 Yoo, E., Okata, T., Akita, T., Kohyama, M., Nakamura, J., and Honma, I. (2009) Enhanced electrocatalytic activity of Pt subnanoclusters on graphene nanosheet surface. *Nano Letters*, **9** (6), 2255–2259.

48 Sharma, S., Ganguly, A., Papakonstantinou, P., Miao, X., Li, M., Hutchison, J.L., Delichatsios, M., and Ukleja, S. (2010) Rapid microwave synthesis of CO tolerant reduced graphene oxide-supported platinum electrocatalysts for oxidation of methanol. *The Journal of Physical Chemistry C*, **114** (45), 19459–19466.

49 Kou, R., Shao, Y., Mei, D., Nie, Z., Wang, D., Wang, C., Viswanathan, V.V., Park, S., Aksay, I.A., Lin, Y., Wang, Y., and Liu, J. (2011) Stabilization of electrocatalytic metal nanoparticles at metal–metal oxide–graphene triple junction points. *Journal of the American Chemical Society*, **133** (8), 2541–2547.

50 Zhou, Y., Neyerlin, K., Olson, T.S., Pylypenko, S., Bult, J., Dinh, H.N., Gennett, T., Shao, Z., and O'Hayre, R. (2010) Enhancement of Pt and Pt-alloy fuel cell catalyst activity and durability via nitrogen-modified carbon supports. *Energy and Environmental Science*, **3** (10), 1437–1446.

51 Gong, K.P., Du, F., Xia, Z.H., Durstock, M., and Dai, L.M. (2009) Nitrogen-doped carbon nanotube arrays with high electrocatalytic activity for oxygen reduction. *Science*, **323** (5915), 760–764.

52 Higgins, D.C., Meza, D., and Chen, Z. (2010) Nitrogen-doped carbon nanotubes as platinum catalyst supports for oxygen reduction reaction in proton exchange membrane fuel cells. *The Journal of Physical Chemistry C*, **114** (50), 21982–21988.

53 Imran Jafri, R., Rajalakshmi, N., and Ramaprabhu, S. (2010) Nitrogen doped graphene nanoplatelets as catalyst support for oxygen reduction reaction in proton exchange membrane fuel cell. *Journal of Materials Chemistry*, **20**, 7114–7711.

54 Lv, R., Cui, T., Jun, M.-S., Zhang, Q., Cao, A., Su, D.S., Zhang, Z., Yoon, S.-H., Miyawaki, J., Mochida, I., and Kang, F. (2011) Open-ended, N-doped carbon nanotube–graphene hybrid nanostructures as high-performance catalyst support. *Advanced Functional Materials*, **21**, 999–1006.

55 Maiyalagan, T., Viswnathan, B., and Varadaraju, U.V. (2006) Electro-oxidation of methanol on TiO_2 nanotube supported platinum electrodes. *Journal of Nanoscience and Nanotechnology*, **6** (7), 2067–2071.

56 Ioroi, T., Siroma, Z., Fujiwara, N., Yamazaki, S.-I., and Yasuda, K. (2005) Sub-stoichiometric titanium oxide-supported platinum electrocatalyst for polymer electrolyte fuel cells. *Electrochemistry Communications*, **7** (2), 183–188.

57 Huang, S.-Y., Ganesan, P., and Popov, B.N. (2010) Electrocatalytic activity and stability of niobium-doped titanium oxide supported platinum catalyst for polymer electrolyte membrane fuel cells. *Applied Catalysis B: Environmental*, **96** (1–2), 224–231.

58 Beak, S., Jung, D., Nahm, K.S., and Kim, P. (2010) Preparation of highly dispersed Pt on TiO_2-modified carbon for the application to oxygen reduction reaction. *Catalysis Letters*, **134** (3–4), 288–294.

59 Lee, J.-M., Han, S.-B., Kim, J.-Y., Lee, Y.-W., Ko, A.-R., Roh, B., Hwang, I., and Park, K.-W. (2010) TiO_2@carbon core–shell nanostructure supports for platinum and their use for methanol electrooxidation. *Carbon*, **48**, 2290–2296.

60 He, D., Yang, L., Kuang, S., and Cai, Q. (2007) Fabrication and catalytic properties of Pt and Ru decorated TiO_2*n*CNTs catalyst for methanol electrooxidation. *Electrochemistry Communications*, **9**, 2467–2472.

61 Drew, K., Girishkumar, G., Vinodgopal, K., and Kamat, P.V. (2005) Boosting fuel cell performance with a semiconductor photocatalyst: TiO_2/Pt–Ru hybrid catalyst for methanol oxidation. *The Journal of Physical Chemistry B*, **109** (24), 11851–11857.

62 Shanmugam, S. and Gedanken, A. (2007) Carbon-coated anatase TiO_2 nanocomposite as a high-performance electrocatalyst support. *Small*, **3** (7), 1189–1193.

63 Kowal, A., Li, M., Shao, M., Sasaki, K., Vukmirovic, M.B., Zhang, J., Marinkovic, N.S., Liu, P., Frenkel, A.I., and Adzic, R.R. (2009) Ternary Pt/Rh/SnO_2 electrocatalysts for oxidizing ethanol to CO_2. *Nature Materials*, **8** (4), 325–330.

64 Pang, H.L., Lu, J.P., Chen, J.H., Huang, C.T., Liu, B., and Zhang, X.H. (2009) Preparation of SnO_2-CNTs supported Pt catalysts and their electrocatalytic properties for ethanol oxidation. *Electrochimica Acta*, **54**, 2610–2615.

65 Du, C., Chen, M., Cao, X., Yin, G., and Shi, P. (2009) A novel CNT@SnO_2 core–sheath nanocomposite as a stabilizing support for catalysts of proton exchange membrane fuel cells. *Electrochemistry Communications*, **11** (2), 496–498.

66 Hobbs, B.S. and Tseung, A.C.C. (1969) High performance, platinum activated tungsten oxide fuel cell electrodes. *Nature*, **222** (5193), 556–558.

67 Maiyalagan, T. and Viswanathan, B. (2008) Catalytic activity of platinum/tungsten oxide nanorod electrodes towards electro-oxidation of methanol. *Journal of Power Sources*, **175** (2), 789–793.

68 Saha, M.S., Banis, M.N., Zhang, Y., Li, R., Sun, X., Cai, M., and Wagner, F.T. (2009) Tungsten oxide nanowires grown on carbon paper as Pt electrocatalyst support for high performance proton exchange membrane fuel cells. *Journal of Power Sources*, **192** (2), 330–335.

69 Raghuveer, V. and Viswanathan, B. (2005) Synthesis, characterization and electrochemical studies of Ti-incorporated tungsten trioxides as platinum support for methanol oxidation. *Journal of Power Sources*, **144**, 1–10.

70 Subban, C.V., Zhou, Q., Hu, A., Moylan, T.E., Wagner, F.T., and Disalvo, F.J. (2010) Sol–gel synthesis, electrochemical characterization, and stability testing of $Ti_{0.7}W_{0.3}O_2$ nanoparticles for catalyst support applications in proton-exchange membrane fuel cells. *Journal of the American Chemical Society*, **132** (49), 17531–17536.

71 Suzuki, Y., Ishihara, A., Mitsushima, S., Kamiya, N., and Ota, K.-I. (2007) Sulfated-zirconia as a support of Pt catalyst for

polymer electrolyte fuel cells. *Electrochemical and Solid-State Letters*, **10** (7), B105–B107.

72 Chhina, H., Campbell, S., and Kesler, O. (2007) Thermal and electrochemical stability of tungsten carbide catalyst supports. *Journal of Power Sources*, **164** (2), 431–440.

73 Wang, Y., Song, S., Maragou, V., Shen, P.K., and Tsiakaras, P. (2009) High surface area tungsten carbide microspheres as effective Pt catalyst support for oxygen reduction reaction. *Applied Catalysis B: Environmental*, **89** (1–2), 223–228.

74 Ganesan, R., Ham, D.J., and Lee, J.S. (2007) Platinized mesoporous tungsten carbide for electrochemical methanol oxidation. *Electrochemistry Communications*, **9** (10), 2576–2579.

75 Nie, M., Shen, P.K., Wu, M., Wei, Z., and Meng, H. (2006) A study of oxygen reduction on improved Pt-WC/C electrocatalysts. *Journal of Power Sources*, **162** (1), 173–176.

76 Yin, S., Mu, S., Lv, H., Cheng, N., Pan, M., and Fu, Z. (2010) A highly stable catalyst for PEM fuel cell based on durable titanium diboride support and polymer stabilization. *Applied Catalysis B: Environmental*, **93** (3–4), 233–240.

77 Ottakam Thotiyl, M.M., Ravikumar, T., and Sampath, S. (2010) Platinum particles supported on titanium nitride: an efficient electrode material for the oxidation of methanol in alkaline media. *Journal of Materials Chemistry*, **20** (47), 10643–10651.

78 Musthafa, O.T.M. and Sampath, S. (2008) High performance platinized titanium nitride catalyst for methanol oxidation. *Chemical Communications*, (1), 67–69.

79 Avasarala, B. and Haldar, P. (2011) On the stability of TiN-based electrocatalysts for fuel cell applications. *International Journal of Hydrogen Energy*, **36** (6), 3965–3974.

80 Huang, S.-Y., Ganesan, P., and Popov, B.N. (2009) Development of conducting polypyrrole as corrosion-resistant catalyst support for polymer electrolyte membrane fuel cell (PEMFC) application. *Applied Catalysis B: Environmental*, **93** (1–2), 75–81.

81 Antolini, E. and Gonzalez, E.R. (2009) Polymer supports for low-temperature fuel cell catalysts. *Applied Catalysis A: General*, **365** (1), 1–19.

82 Qi, Z., Lefebvre, M.C., and Pickup, P.G. (1998) Electron and proton transport in gas diffusion electrodes containing electronically conductive proton-exchange polymers. *Journal of Electroanalytical Chemistry*, **459** (1), 9–14.

83 Chen, Z., Xu, L., Li, W., Waje, M., and Yan, Y. (2006) Polyaniline nanofibre supported platinum nanoelectrocatalysts for direct methanol fuel cells. *Nanotechnology*, **17** (20), 5254.

84 Jiang, C. and Lin, X. (2007) Preparation of three-dimensional composite of poly(*N*-acetylaniline) nanorods/platinum nanoclusters and electrocatalytic oxidation of methanol. *Journal of Power Sources*, **164** (1), 49–55.

85 Tintula, K.K., Pitchumani, S., Sridhar, P., and Shukla, A.K. (2010) PEDOT-PSSA as an alternative support for Pt electrodes in PEFCs. *Bulletin of Materials Science*, **33** (2), 157–163.

86 Choi, J.-H., Park, K.-W., Lee, H.-K., Kim, Y.-M., Lee, J.-S., and Sung, Y.-E. (2003) Nano-composite of PtRu alloy electrocatalyst and electronically conducting polymer for use as the anode in a direct methanol fuel cell. *Electrochimica Acta*, **48** (19), 2781–2789.

87 Zhu, Z.-Z., Wang, Z., and Li, H.-L. (2008) Functional multi-walled carbon nanotube/polyaniline composite films as supports of platinum for formic acid electrooxidation. *Applied Surface Science*, **254** (10), 2934–2940.

88 Selvaraj, V. and Alagar, M. (2007) Pt and Pt-Ru nanoparticles decorated polypyrrole/multiwalled carbon nanotubes and their catalytic activity towards methanol oxidation. *Electrochemistry Communications*, **9** (5), 1145–1153.

89 He, C., Desai, S., Brown, G., and Bollepalli, S. (2005) PEM fuel cell catalysts: cost, performance, and durability. *Electrochemical Society Interface*, **14** (3), 41–44.

90 Debe, M.K., Schmoeckel, A.K., Vernstrom, G.D., and Atanasoski, R. (2006) High voltage stability of nanostructured thin film catalysts for PEM fuel cells. *Journal of Power Sources*, **161** (2), 1002–1011.

91 Garsuch, A., Stevens, D.A., Sanderson, R.J., Wang, S., Atanasoski, R.T., Hendricks, S., Debe, M.K., and Dahn, J.R. (2010) Alternative catalyst supports deposited on nanostructured thin films for proton exchange membrane fuel cells. *Journal of the Electrochemical Society*, **157** (2), B187–B194.

4
Anode Catalysts for Low-Temperature Direct Alcohol Fuel Cells

Wenzhen Li

4.1
Introduction

Low-temperature polymer electrolyte fuel cells are promising electrochemical energy devices that can directly transform the chemical energy stored in a fuel (e.g., H_2 and alcohols) into electrical energy with low emission and high efficiency [1–8]. This electrochemical process does not obey Carnot cycle limitation, so higher energy efficiencies can be achieved through fuel cells: 40–50% in electrical energy and 80–85% in total energy (electricity + heat production) [6]. Hydrogen is considered the most convenient fuel for vehicle applications, because the kinetics of hydrogen oxidation is very fast and the product is only water. However, hydrogen itself is merely an energy carrier, not a natural resource. The production, transportation, and storage of hydrogen have encountered huge technical challenges [9]. Compared with hydrogen, small liquid alcohol fuels have obvious advantages, including high energy density and thermodynamic energy conversion efficiency, comparable electromotive force (thermodynamic potential), and complete elimination of hydrogen production and storage accessories [1,6,7]. In addition, many alcohols can be massively obtained from renewable biomass feedstocks [10–12]. For example, methanol can be produced from fermentation of agricultural products from biomass; ethanol is one of the major fuels obtained from agriculture fermentation (first-generation bioethanol); ethylene glycol (EG) can be obtained in large quantity by heterogeneous hydrogenation of cellulose; and glycerol is a main by-product of biodiesel production. They are potentially cheap and abundant, and can be widely distributed by using the present infrastructures for liquid fuels. Therefore, low-temperature direct alcohol fuel cells (DAFCs) have emerged as clean and sustainable mobile power sources for portable electronics, and potentially for transportation systems.

Table 4.1 shows the thermodynamic properties of selected alcohol fuels at standard conditions. Although their electromotive forces are slightly lower than

Materials for Low-Temperature Fuel Cells, First Edition. Edited by Bradley Ladewig, San P. Jiang, and Yushan Yan.

Table 4.1 The transferred electrons (N_e), electromotive force (E°), volume energy density (W_e), and thermodynamic energy conversion efficiency (ε_{rev}) of electrooxidation of selected alcohols at standard conditions.

Fuel	N_e	E° (V)	W_e (kW h l^{-1})	ε_{rev} (%)
Hydrogen	2	1.23	2.6 (liquid H_2)	83
Methanol	6	1.18	4.8	97
Ethanol	12	1.15	6.3	97
Ethylene glycol	10	1.22	5.9	99
Glycerol	14	1.22	6.3	99

hydrogen, the thermodynamic energy conversion efficiencies of methanol, ethanol, ethylene glycol, and glycerol are in the range of 97–99%, which is higher than that of hydrogen (83%). The mass and volume energy densities of the alcohols are also higher than that of hydrogen.

Despite their attractive thermodynamic advantages and practical system benefits, current direct alcohol fuel cells have the significant disadvantage of having lower output power density and efficiency than hydrogen–proton exchange membrane fuel cells (PEMFCs). Besides the urgent need for the development of advanced polymer membranes that can reduce both enhanced ion conductivity and alcohol crossover, the sluggish alcohol reaction kinetics must be significantly improved for widespread applications of DAFCs. For instance, the overpotential of methanol oxidation is >0.3 V at 0.5 A cm^{-2} on the state-of-the-art PtRu/C catalyst, which is much higher than hydrogen oxidation reaction (only 0.02 V) [4]. The ethanol oxidation has a similar slow kinetics. More serious, since the C−C bond of ethanol is difficult to break at low temperatures (e.g., <90 °C), the major electrooxidation products are acetaldehyde and acetic acid, and CO_2 is only <10% on the current PtSn catalysts [6,13]. The incomplete ethanol oxidation leads to low ethanol utilization and energy conversion efficiency.

Efficient direct transformation of chemical energy stored in small organic molecules into electricity has been a long-term goal for scientists. Significant research efforts have been made in recent decades to acquire a deep understanding of the mechanisms of electrocatalytic oxidation of alcohols, and to further develop more efficient anode catalysts for DAFCs. This chapter focuses on anode catalytic materials for low-temperature DAFCs. First, the acquired knowledge of electrooxidation of alcohols (methanol, ethanol, ethylene glycol, and glycerol) in both acid and alkaline media, and state-of-the-art anode catalysts are presented. Second, the recently developed catalyst preparation methods and novel carbon support materials are reviewed. Finally, the future research challenges and opportunities in this field are discussed.

4.2
Anode Catalysts for Direct Methanol Fuel Cells: Improved Performance of Binary and Ternary Catalysts

4.2.1
Principles of Direct Methanol Fuel Cells

A typical proton exchange membrane (PEM)-based direct methanol fuel cell comprises anode, PEM, and cathode. At the anode, methanol is oxidized to produce CO_2; at the cathode, oxygen reacts with protons and electrons to produce water:

$$CH_3OH + H_2O \rightarrow CO_2 + 6H^+ + 6e^- \quad +0.05\,\text{V versus SHE} \quad \text{(anode)} \qquad (4.1)$$

$$3/2O_2 + 6H^+ + 6e^- \rightarrow 3H_2O \quad +1.23\,\text{V versus SHE} \quad \text{(cathode)} \qquad (4.2)$$

The total reaction is

$$CH_3OH + 3/2O_2 \rightarrow CO_2 + 2H_2O \quad +1.18\,\text{V} \qquad (4.3)$$

4.2.2
Reaction Mechanisms and Catalysts for Methanol Electrooxidation

In the past decades, a significant number of fundamental investigations have been carried out in the field of low-temperature electrooxidation of small organic molecules [14–38]. Electrochemical studies have been carried out in combination with spectroscopy [21,27,28], mass spectroscopy [25,31], physiochemical tools [20,30], as well as theoretical calculations (e.g., DFT) [38] in order to examine the adsorbed species and reactive intermediates on the electrode surface during the alcohol oxidation, and thus to elucidate the alcohol reaction pathways.

From a general point of view, at ambient pressure and temperature, all electrooxidations of short-chain aliphatic alcohols (in acid) require the presence of the expensive precious metal Pt. However, as is well known, Pt is readily poisoned by CO-like intermediate species formed during methanol oxidation at low temperatures. It has been found that Pt-based binary or ternary catalysts, Pt-M_1, Pt-M_1-M_2 (M = Ru, Sn, etc.) can improve the reaction kinetics of methanol electrooxidation based on the bifunctional effect (promoted mechanism by the second metal) [17,19,22,24,26] and/or on the tuned electronic properties of Pt (the intrinsic mechanism) [28,29,36]. The bifunctional effect is illustrated in the following equations:

$$Pt + CH_3OH \rightarrow Pt - (CH_3OH)_{ads} \qquad (4.4)$$

$$Pt - (CH_3OH)_{ads} \rightarrow Pt - (CO)_{ads} + 4H^+ + 4e^- \qquad (4.5)$$

$$M + H_2O \rightarrow M - (H_2O)_{ads} \qquad (4.6)$$

$$M-(H_2O)_{ads} \rightarrow M-(OH)_{ads} + H^+ + e^- \tag{4.7}$$

$$Pt-(CO)_{ads} + M-(OH)_{ads} \rightarrow Pt + M + CO_2 + H^+ + e^- \tag{4.8}$$

After methanol adsorption on Pt catalysts, dehydrogenation (C—H bond cleavage or C—H activation) of methanol proceeds to produce $CO_{(ads)}$. Equations 4.6 and 4.7 relate to water activation on M. Pt and M cooperate to oxidize $CO_{(ads)}$ to yield CO_2 (Equation 4.8). The rate-determining step has long been thought to be within these steps (4.6)–(4.8). It is worth mentioning that using DFT and single-crystal model catalyst, Wieckowski and coworkers have calculated the energetic for CH_3OH dehydrogenation steps and elucidated that methanol dehydrogenation (Equation 4.5) proceeds via the following reaction path [38]:

$$\begin{aligned} CH_3OH_{ads} &\rightarrow CH_2OH_{ads} + H_{ads} \rightarrow CHOH_{ads} + 2H_{ads} \\ &\rightarrow COH_{ads} + 3H_{ads} \rightarrow CO_{ads} + 4H_{ads} \end{aligned} \tag{4.9}$$

The intrinsic mechanism states that M could modify the electronic properties of Pt, and as a consequence, change the adsorption of oxygen-containing species and even the dissociative adsorption of methanol. The CO adsorption on Pt is stabilized by two simultaneous effects: electron transfer (donation) from the CO-filled 5σ molecular orbital to the empty dσ band of Pt, and back-donation of electrons from metal dπ orbital to empty $2\pi^*$ antibonding orbital of CO. The generation of an σ-type bond strengthens the p-type bond and vice versa. In the Pt–M alloys, a modification of the empty electron state density of Pt occurs, with a shift of the Fermi energy level with respect to the energy of CO molecular orbital. This generates the synergistic effect to weaken the Pt—CO bond, and thus facilitates the methanol oxidation kinetics.

Among all the Pt-based alloys, PtRu was found to be the best candidate catalysts for methanol eletrooxidation [17,18,39–41]. The composition and structure of PtRu strongly affect the catalytic activity. It has been reported that 40–60 at.% Ru gives the optimum catalytic activity to methanol oxidation. In the early study, synthesis of PtRu alloy was emphasized, because Ru sites are required to locate close to Pt sites to promote oxidation of CO (Equation 4.10), according to the bifunctional mechanism. In addition, a closer Pt–Ru interaction will promote electronic effects of Pt, which could lead to facile removal of CO_{ads}. With the advancement of research, it was found that the formation of a PtRu alloy was not an essential requirement for a high methanol oxidation activity. Rolison *et al.* found that if Ru existed as hydrous oxide, the methanol oxidation activity would be greatly improved [42–44]. Ren *et al.* also showed that the more RuO_xH_y content, the better the DMFC performance [45]. The benefits of RuO_xH_y were attributed to the conductivity of its electrons and protons and the innate possession of surface OH groups. Although the preferable Ru form is still under debate, it is encouraging to find that PtRu-based ternary and quarterly catalysts can further improve methanol oxidation activity. Experimental and combinational high-throughput methods

have been employed and it has been found that the "promotional" elements include W, Mo, Ir, Os, Ni, Co, V, Rh, and so on. Reddington *et al.* demonstrated that $Pt_{44}Ru_{41}Os_{10}Ir_5$ is the best composition in both half-cell and single DMFC tests among more than 600 Pt–Ru–Os–Ir quaternary catalysts [33]. Kim *et al.* found that PtRuSn is a better catalyst than PtRu, and ascribed the enhancement of MOR activity to the synergistic effects of Ru as a water activator and Sn as an electronic modifier of Pt [46]. It was noted that the third and fourth element amount should be kept lower than a certain amount, otherwise its presence will have a negative effect on the catalyst performance. In general, Pt–Sn catalysts present a higher CO oxidation activity, but lower methanol oxidation activity, probably due to a decreased methanol adsorption and dehydrogenation on Pt–Sn. Binary Pt–W, Pt–Ni, and Pt–Co catalysts have also demonstrated a certain degree of MOR improvement than pure Pt, but the activity improvement is less than PtRu [47–49].

The development of direct methanol fuel cell technology in the last decades has achieved very interesting results. The peak power density of a PEM-based DMFC can reach 500 mW cm^{-2} and 300 mW cm^{-2} under oxygen and air feed operation, respectively. At a fuel cell voltage of 0.5 V, 200 mW cm^{-2} has been reported at a temperature close to or above 100 °C under pressured conditions, with a Pt loading of 1–2 mg cm^{-2}. However, at ambient temperature and passive air-breathing mode operation, the power density range remains between 10 and 40 mW cm^{-2} [4]. The high energy density of DMFCs makes them a competitive replacement of current Li ion batteries for a global portable electronics market of 6 billion dollars. As a comparison, the alkaline membrane-based DMFC has a much lower performance than peak power density, that is, ~80 mW cm^{-2} for Pd/multiwalled nanotubes (MWNTs) anode DMFC [50]. Therefore, the alkaline membranes have more advantages for direct C_{2+} alcohol fuel cells, as discussed in the following sections.

4.3 Anode Catalysts for Direct Ethanol Fuel Cells: Break C—C Bond to Achieve Complete 12-Electron-Transfer Oxidation

Ethanol is a biorenewable molecule. It is manufactured through photosynthesis causing an agricultural feedstock, such as sugarcane, corn, grain, wheat, cotton, and many types of cellulose wastes and harvests. Using ethanol as fuel has a big advantage of reducing CO_2 footprints in the atmosphere, because the absorption of CO_2 by living plant matter will be used as the feedstock to produce it [51]. The current utilization of ethanol fuel is as blends of gasoline with denatured ethanol, that is, E85 is 85% ethanol-mixed gasoline, which has recently appeared at fueling stations in the United States, mainly in the Midwest. However, all internal combustion engines are limited by the Carnot cycle. In principle, generation of electricity through direct ethanol fuel cells is a more efficient way to utilizing ethanol [6].

4.3.1 Principles of PEM-Direct Ethanol Fuel Cells

In an acid electrolyte, the anode, cathode, and overall reactions are as follows:

$$C_2H_5OH + 3H_2O \rightarrow 2CO_2 + 12H^+ + 12e^- \quad +0.085\,\text{V versus SHE} \quad \text{(anode)} \tag{4.10}$$

$$3O_2 + 12H^+ + 12e^- \rightarrow 6H_2O \quad +1.23\,\text{V versus SHE} \quad \text{(cathode)} \tag{4.11}$$

$$C_2H_5OH + 3O_2 \rightarrow 2CO_2 + 3H_2O \quad +1.15\,\text{V} \quad \text{(overall)} \tag{4.12}$$

The thermodynamic reversible energy efficiency at standard conditions is 97%, which is defined as the ratio of the electrical energy produced, and the heat of the combustion at constant pressure. However, under the working conditions, with a current j, the cell voltage is lower than the equilibrium potential; therefore, the practical energy efficiency is lower. For example, for a direct ethanol fuel cell working at 0.55 V and 100 mA cm^{-2} with 80% selectivity to CO_2 and 20% selectivity to acetic acid, the efficiency is

$$\varepsilon_{\text{cell}} = \varepsilon_F \times \varepsilon_E \times \varepsilon_{\text{rev}} = (0.2 \times 4/12 + 0.8 \times 1) \times (0.55/1.15) \times 0.97 = 40\%$$

The potential efficiency $\varepsilon_E = 48\%$ (0.55/1.15). The Faradic efficiency ε_F is associated with the product distribution (catalyst selectivity). For CO_2 product, the Faradic efficiency is 100% (12/12), while for acetic acid product, only four electrons are transferred, and the Faradic efficiency is 33% (4/12). Although higher current densities are not necessarily associated with complete oxidation of ethanol, improving the anode catalyst selectivity to CO_2 will increase the overall DEFC efficiency and fuel utilization.

4.3.2 Reaction Mechanisms and Catalysts for Ethanol Electrooxidation

The complete electrooxidation of ethanol is a complex 12-electron-transfer reaction and various reaction intermediates can be formed during the ethanol oxidation process. The electrochemical oxidation of ethanol in acid electrolyte requires Pt, which is primarily involved in two key steps – cleavage of C−H and C−C bonds – occurring during the oxidation process.

Based on half-cell and single fuel cell tests, *in situ* FTIR spectroscopy, and chromatograph studies, a proposed overall scheme for ethanol oxidation on Pt-based catalysts is summarized in Figure 4.1 [52]. The first step is the dissociative adsorption of ethanol through either O-adsorption or C-adsorption (step 1) [53,54], leading to the formation of adsorbed acetaldehyde (step 2). Acetaldehyde has been examined at potential <0.6 V versus RHE. It could be readsorbed according to step 3 and react with adsorbed OH to generate acetic acid through a bifunctional mechanism as shown in step 4. This step does not break the C−C bond and often occurs at >0.6 V RHE. The adsorbed CH_3CHOH could also undergo further dehydrogenation (step 5) and react with adsorbed OH to

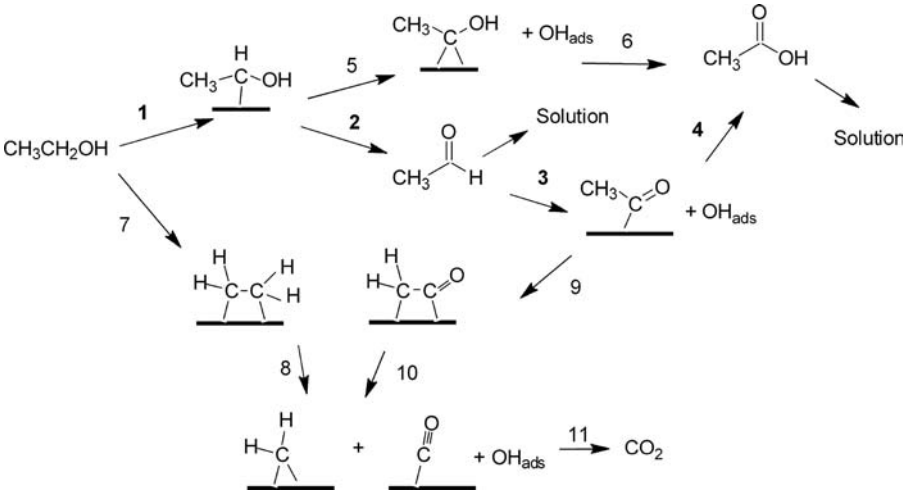

Figure 4.1 Proposed mechanisms for ethanol oxidation reaction [52].

produce acetic acid directly (step 6) [6]. There is still some controversy on whether acetic acid is formed through acetaldehyde or through CH_3COH (steps 5 and 6).

Pt is able to break the C−C bond, leading to adsorbed CO species at relatively low anode potentials: from 0.3 V RHE, the adsorbed peak has clearly been shown in SNIFTIRS spectrum [55]. One can consider two distinct sequences: steps 7 and 8 or steps 9 and 10. The first sequence assumes that ethanol must be adsorbed by the C−H bond cleavage in both carbon atoms and the second sequence assumes that the rupture of the C−H bond of the intermediate formed after the acetaldehyde adsorption. The CO_{ads} species thus react with adsorbed OH to produce CO_2 through step 11. Trace amount of CH_4 at the potential of <0.4 V has been detected, thus the following reaction may occur [53,54]:

$$\mathrm{Pt-(COCH_3)_{ads} + Pt \rightarrow Pt-(CO)_{ads} + Pt-(CH_3)_{ads}}, \quad \text{at } E > 0.3\,\mathrm{V\ SHE} \tag{4.13}$$

$$\mathrm{Pt-(CH_3)_{ads} + Pt-(H)_{ads} \rightarrow 2Pt + CH_4}, \quad \text{at } E < 0.4\,\mathrm{V\ SHE} \tag{4.14}$$

It is interesting to note that only acetic acid, acetaldehyde, and CO_2 have been detected by HPLC from the outlet of the anode compartment of a DEFC with Pt/C catalyst [56], while depending on electrode potentials, acetaldehyde, acetic acid, CO_2, and trace amounts of CH_4 can be found in electrolysis half-cell. It is also found that acetaldehyde can be exclusively produced at a potential <0.35 V versus RHE on a Pt catalyst in a long-time electrolysis experiment; no acetic acid was detected in the potential range [6]. This implies that the alcohol product distribution depends on electric energy input.

In an acid electrolyte, Pt-based catalysts have shown better EOR activity than other platinum group metal (PGM)-based ones. However, Pt itself is readily poisoned by various C_1, C_2 intermediate species. Binary and ternary Pt-based

catalysts, including Ru, Sn, Pb, Pd, and so on, have been thoroughly investigated to improve the kinetics of ethanol oxidation. Sn appeared to be the most promising one [2,7,57–59]. Xin Lab has examined Pt–M (M = Ru, Sn, Pd, and W) catalysts in single PEM-DEFC and found the activity order to be PtSn > PtRu > PtPd > Pt. W and Mo were also alloyed with Pt_1Ru_1 catalysts and still show inferior EOR activity compared with PtSn [60–65]. Lamy and coworkers studied PtSn/C(90 : 10, 50 : 50), PtRu/C(90 : 10, 80 : 10), and $Pt_{86}Sn_{10}Ru_4$/C and demonstrated that PtSn has a much higher EOR activity than Pt [52,56,66,67]. The product distributions of EOR on PtSn catalysts, however, have been changed compared with Pt:An increase in the acetic acid yield and a decrease in acetaldehyde and CO_2 yield. The presence of Sn seems to allow the activation of water molecules and the oxidation of acetaldehyde species into acetic acid at low potentials through bifunctional mechanism. At the same time, Sn dilutes the adjacent Pt atom concentration, thus decreasing the possibility of dissociative adsorption of ethanol with two carbons, which can directly lead to CO_2 production. The function of Sn may also include some electronic effects (ligand effect) on the CO oxidation reaction [68]. Wang *et al.* studied Pt/C, PtRu/C, and Pt_3Sn/C using *in situ* FTIR spectroscopy and online DEMS studies, and also found that the additions of Ru and Sn do not promote C−C bond cleavage, and that the total CO_2 production was <2% contributed to current [13]. Therefore, the previous work shows that the higher ethanol oxidation current density on the PtSn/C catalysts results from higher yields of C_2 products, not from improved complete ethanol oxidation to CO_2.

The recent research efforts are toward discovering new catalyst compositions and structures that can simultaneously break C−C bond to achieve complete EOR and to increase (or at least maintain) the EOR activity. The addition of Rh to Pt seems to promote the C−C bond breakage, however, the overall EOR activity is lower than PtSn [69,70]. Adzic and coworkers group recently demonstrated that a ternary Pt/Rh/SnO_2 nanostructured catalyst can better break C−C bond and promote EOR kinetics [71]. The EOR specific activity on $PtRhSnO_2$/C was much higher than $PtSnO_2$/C and PtRu/C catalysts. The onset potential of EOR on $PtRhSnO_2$/C negatively shifted 180 mV (0.330–0.150 V versus SHE) compared with PtRu/C, as shown in Figure 4.2b. The potential-dependent peak near 2342 cm^{-1} for the signature peak asymmetric stretch vibration of CO_2 appears at 0.78 V on Pt(111) electrode, but shifts to above 0.30 V on $RhSnO_2$/Pt(111) electrode, indicating cleavage of the C−C bond in ethanol, as shown in Figure 4.2c and d. Based on DFT calculations, the dehydrogenation (of β-H) and C−C breakage steps (16 and 17) are of critical importance for achieving complete decomposition and oxidation of ethanol.

$$^*CH_3CH_2OH \rightarrow ^*CH_3CH_2O + H^* \tag{4.15}$$

$$\rightarrow ^*CH_2CH_2O + 2H^* \tag{4.16}$$

$$\rightarrow ^*CH_2 + ^*CH_2O + 2H^* \tag{4.17}$$

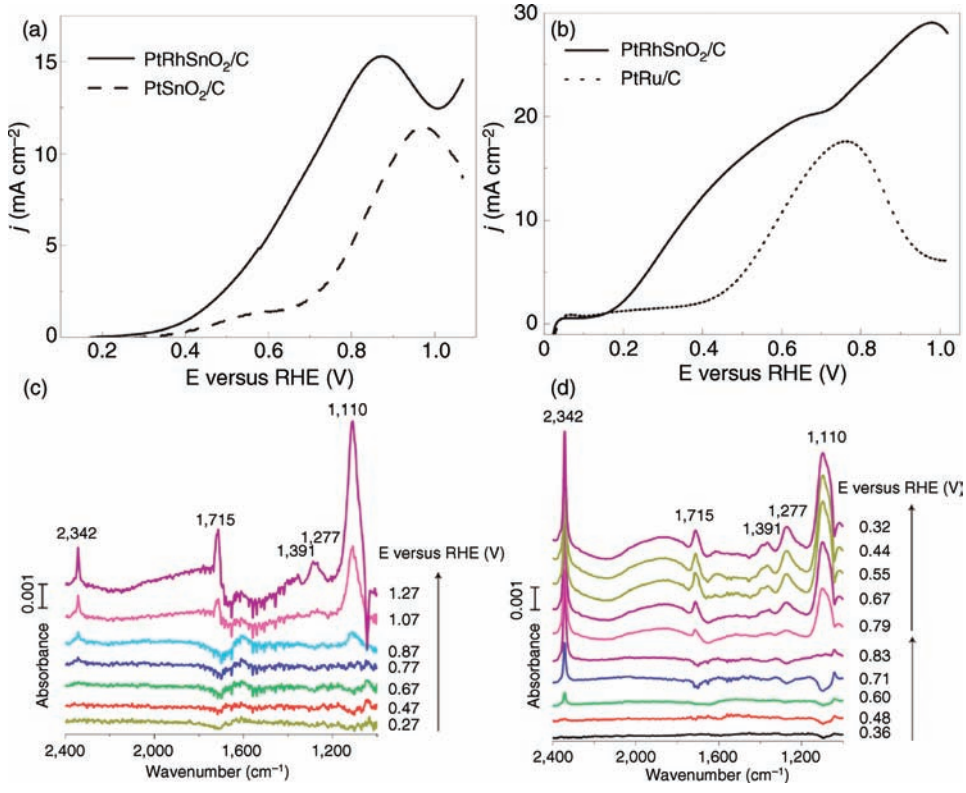

Figure 4.2 Current–potential curves comparing the activity of $PtRhSnO_2/C$ with that of several other catalysts for ethanol oxidation. Electrocatalyst compositions – $PtRhSnO_2/C$: 30 nmol Pt, 8 nmol Rh, and 60 nmol SnO_2; $PtSnO_2/C$: 30 nmol Pt and 60 nmol SnO_2 (a); $PtRhSnO_2/C$: 25 nmol Pt, 5 nmol Rh, and 20 nmol SnO_2; PtRu/C: 25 nmol Pt and 25 nmol Ru. (b) 0.1 M $HClO_4$+ 0.2 M ethanol, 50 mVs. *In situ* IRRAS spectra recorded during ethanol electrooxidation on the Pt(111) electrode (c), and $PtRhSnO_2/C$ in 0.1 M $HClO_4$ + 0.2 M ethanol solution (d) [71].

Ethanol decomposition on $RhPt/SnO_2$ occurs through an oxametallacyclic conformation ($-CH_2CHO$). The two steps, Equations 4.16 and 4.17, can be achieved by incorporating the element Rh with more lying-d band, especially when it is alloyed with Pt.

4.3.3
Anion Exchange Membrane-Based Direct Ethanol Fuel Cells (AEM-DEFCs)

The kinetics of both oxygen reduction and alcohol oxidation can be more significantly improved in a high-pH electrolyte than in a low-pH one, due to enhanced ion transport and facile charge transfer in alkali [72]. The anion exchange membrane direct ethanol fuel cells build upon AEM electrolyte and are directly fed with ethanol fuel. At the anode, the ethanol reacts with OH^- to produce CO_2 (complete oxidation), while at the cathode, oxygen reacts with H_2O and

electrons to yield OH^-. The anode, cathode, and overall reactions and their theoretical potentials are shown in Equations 4.18–4.20.

$$C_2H_5OH + 12OH^- \rightarrow 2CO_2 + 9H_2O + 12e^- \quad -0.75\,\text{V versus SHE} \quad \text{(anode)} \tag{4.18}$$

$$3O_2 + 6H_2O + 12e^- \rightarrow 12\,OH^- \quad +0.40\,\text{V versus SHE} \quad \text{(cathode)} \tag{4.19}$$

$$C_2H_5OH + 3O_2 \rightarrow 2CO_2 + 3H_2O \quad +1.15\,\text{V} \quad \text{(overall)} \tag{4.20}$$

The current AEMs are mainly based on quaternary ammonium hydroxide (QAOH) polymers [73]. They have demonstrated good thermal and chemical stability. The OH^- conductivity of a commercial AEM, such as Tokuyama A201, is as high as $38\,\text{mS}\,\text{cm}^{-1}$ [74]. These AEMs can be operated at 80 °C without structural changes. Under such low-temperature operations, undesirable decomposition of alcohol does not occur. Serious problems traditionally associated with electrolyte carbonation for liquid alkaline fuel cells can be overcome using a solid AEM electrolyte. There are no mobile cations, that is, K^+, in AEMs, so it is not easy to form precipitations (i.e., K_2CO_3) that block or destroy an electrolyte and alleviate all cation-related issues. The anions cross from cathode to anode, thus minimizing alcohol crossover problem. The AEMFCs also have price advantages over PEMFCs due to low-cost AEM membrane (hydrocarbon polymer versus poly(perfluorosulfonic acid) PEM, that is, Nafion). Owing to a less corrosive basic working environment, inexpensive non-PGMs, such as Ag and Fe/Co–N have demonstrated very competitive oxygen reduction reaction (ORR) activity and durability and can be used as AEMFC cathode catalysts [72,75,76]. All the merits have gained anion exchange membrane a lot of research attention in recent years.

4.3.4
Anode Catalysts for AEM-DEFCs

Pd has demonstrated the highest EOR activity in high-pH media among all known single-metal catalysts [5,7]. Pd is more abundant on the Earth's crust: 200 times higher than Pt (0.6 versus 0.003 ppb). Pd has a lower price than Pt. The EOR activity on Pd highly depends on pH [77,78]. Liang *et al.* suggested an EOR mechanism in high-pH media by using CV study [79]. They showed that the α-C is first activated on a Pd surface to dehydrate 2 H atoms, and to break O−H, "ethoxi" ($-CH_3CO$) forms. Ethoxi reacts with adsorbed −OH to produce acetate, this is the rate-determining step. A subtle balance between the ethanol and OH^- concentrations is required for high oxidation activity because the prevalence of either species in solution may hinder the necessary adsorption of both species, thus resulting in a lower EOR activity.

$$Pd + OH^- \rightarrow Pd - (OH)_{ads} + e^- \tag{4.21}$$

$$Pd - (CH_3CH_2OH)_{ads} + 3OH^- \rightarrow Pd - (CH_3CO)_{ads} + 3H_2O + 3e^- \tag{4.22}$$

$$Pd - (CH_3CO)_{ads} + Pd - (OH)_{ads} \rightarrow Pd - (CH_3COOH)_{ads} + Pd \tag{4.23}$$

DFT calculations on model Pd clusters have shown that dehydrogenation hardly occurs without the assistance of OH^-. Both α-C and H from the hydroxyl taking part in the ethanol oxidation are facile in the presence of OH^-, leading to the formation of acetaldehyde [78]. However, its oxidation peak has not been observed in the CV scan.

Binary Pd-M (M = Ru, Au, Sn, Cu, etc.) catalysts have been investigated and they demonstrated improved EOR activity. Chen *et al.* found that Pd–Ru shows higher activity toward methanol, ethanol, and ethylene glycol than Pd, the optimum composition being 1 : 1 [80]. PdAu and PdSn catalysts show better tolerance to poisoning species than Pt catalyst [81]. The effects of addition of various oxides (NiO, CeO_2, etc.) to carbon-supported Pd have been studied. Among them, NiO showed the highest peak current density. The possible function of oxide is because OH_{ads} species could be easily formed on the surface of oxide, the formation of OH_{ads} can assist transformation of CO-like poisoning intermediates on the Pd surface to CO_2 or other products [82]. It is interesting to note that ternary metal Pd–Ni–Zn catalysts demonstrated the highest EOR activity (its specific activity in half-cell test is $>3600\,A\,g_{Pd}^{-1}$) and excellent reaction stability [5,83,84]. The Pd-based catalysts can accelerate the EOR kinetics, but it is difficult to break the C−C bond in high-pH media. The products are exclusively carboxylates, especially for primary alcohols, that is, ethanol and isopropanol [85]. Although polyols (i.e., glycerol) may undergo C−C bond scission to form carbonate, it is still a minor reaction path, the major products being various carbohydrates [86,87].

To date, AEM-DEFCs have exhibited higher performance than PEM-DEFCs [5]. For example, an active AEM-DEFC with the Pd–Ni–Zn/C anode catalyst and Fe–Co–N/C cathode catalyst (from Acta) shows a peak power density of 200 mW cm^{-2} at 80 °C and 2 atm O_2 back pressure [83]. For PEM-DAFC, the higher alcohols, such as ethanol, ethylene glycol, and glycerol, are difficult to be oxidized even on Pt and Pt-based catalysts, unless the temperature is increased to >130 °C. The state-of-the-art PEM-DEFC with a PtSn anode catalyst has a peak power density of 50–70 mW cm^{-2} [60,64]. However, current AEM-DEFCs need liquid base mixed with alcohol fuel to provide sufficient OH^- for improving its reaction kinetics. The development of more effective anion exchange ionomer, construction of ordered electrode architectures, and examination of long-term reaction stability are the necessary research tasks for developing efficient and durable AEM-DEFCs.

4.4
Anode Catalysts for Direct Polyol Fuel Cells (Ethylene Glycol, Glycerol): Cogenerate Electricity and Valuable Chemicals Based on Anion Exchange Membrane Platform

4.4.1
Overview of Electrooxidation of Polyols

It has been known that the catalyst activity toward alcohol oxidation reaction can be significantly enhanced in alkaline electrolyte [2,88]. A recent study by Koper

and coworkers shows that the first deprotonation step in alcohol oxidation is a base-catalyzed step, and the second deprotonation depends on the ability of the electrode materials (i.e., Au or Pt) to abstract the H_β [87]. Theoretical DFT calculations further show that the adsorbed OH species are essential to accelerate many steps in alcohol oxidation, that is, the activation energy of the first deprotonation step in the absence of OH^- is as high as 204, 116 kJ mol^{-1} on Au and Pt catalysts, respectively, while it drops one order of magnitude (22 and 18 kJ mol^{-1} on Au and Pt) with assistance of adsorbed OH^- [89]. These works indicate that the base catalysis is the main driver behind the high oxidation activity of alcohols in alkaline electrolyte, but not the catalyst interaction with hydroxide.

Due to the enhanced oxidation kinetics in high-pH media, anion exchange membrane fuel cells using biomass-derived alcohol fuels (e.g., ethanol and glycerol) have recently attracted increasing attention. Accumulated evidences have shown that breaking C−C bond of C_{2+} alcohol on metal catalysts at low temperatures is very difficult, especially in high-pH media [5]. For example, the main products of ethanol oxidation are acetaldehyde and acetic acid (or acetate). This lowers the Faradic efficiency to 17–33% for direct ethanol fuel cells [6]. The use of polyol fuels can be an interesting alternative, because in the polyols, each carbon has a hydroxyl (−OH) group that can be fully oxidized to carbonyl (−CO) or carboxyl (−COOH) group; therefore, more electrons are generated even without breaking C−C bonds, and the fuel cell's Faradic efficiency improves. In addition, ethylene glycol and glycerol have competitive energy densities (5.2 and 5.0 kWh kg^{-1} for ethylene glycol and glycerol, respectively, versus 6.1 and 8.0 kWh kg^{-1} for methanol and ethanol, respectively), and they are nonflammable and nontoxic fuels.

The complete oxidation of two hydroxyl groups of ethylene glycol to oxalate without breaking C−C bond is as follows, and the Faradic efficiency is 80%.

$$CH_2OH - CH_2OH + 14OH^- \rightarrow 2{CO_3}^{2-} + 10H_2O + 10e^- \tag{4.24}$$

$$CH_2OH - CH_2OH + 10\,OH^- \rightarrow (COO - COO)^{2-} + 8H_2O + 8e^- \tag{4.25}$$

The complete oxidation of three hydroxyl groups of glycerol to mesoxalate without breaking two C−C bonds is as follows, and the Faradic efficiency is 71.5%.

$$CH_2OH - CHOH - CH_2OH + 20\,OH^- \rightarrow 3{CO_3}^{2-} + 14H_2O + 14e^- \tag{4.26}$$

$$CH_2OH - CHOH - CH_2OH + 12\,OH^- \rightarrow (COO - CO - COO)^{2-} + 10H_2O + 10e^- \tag{4.27}$$

In addition, incomplete oxidation of polyols leads to production of higher valued chemicals, such as dihydroacetone, which is a valuable tanning agent, hydroxypyruvic acid, which is a flavor component and a possible starting material for DL-serine synthesis, and tartronic and mesoxalic acids, which are important intermediates for novel polymer and pharmaceutical synthesis. Therefore, research on cogeneration of electricity and higher valued chemicals from polyols

based on anion exchange membrane fuel cell platform will not only be attractive for developing electrochemical power sources but will also help to open new routes for conversion and utilization of biomass resources.

4.4.2
Reaction Mechanisms and Catalysts for Ethylene Glycol Electrooxidation

The oxidation of EG is more complex than that of ethanol due to its two adjacent hydroxyl groups. The investigation into EG electrooxidation in alkaline media started from the mid-1970s. Since the complete oxidation of EG needs up to 10 electrons, various reactive species and reaction intermediates could be produced through several consecutive and parallel steps. Figure 4.3 illustrates the general reaction scheme for electrooxidation of EG [5]. Compounds in boxes have been detected in anode compartment of DEFCs using HPLC, among them glyoxylic acid was in trace amount over $Pt_{0.45}Pd_{0.45}Bi_{0.1}/C$ catalyst at 0.58 V for 360 min [90]. The compounds in circles have been exclusively detected in half cells using IR spectroscopy, and they are the reaction intermediates including glycolaldehyde and glyoxal. There are two paths for EG oxidation: poisoning and nonpoisoning paths. The nonpoisoning path stops at oxalate, because oxalate is very slowly oxidized on electrocatalysts, especially Pd surface. Oxalate is not a main product and it comes from further oxidation of glycolate (glycolic acid) or glycoxalate (glyoxalic acid) depending on pH. The poisoning path leads to the production of C_1 products, that is, carbonate, due to C–C bond scission in the process of further oxidation of glycolate. The applied potential plays a key role in

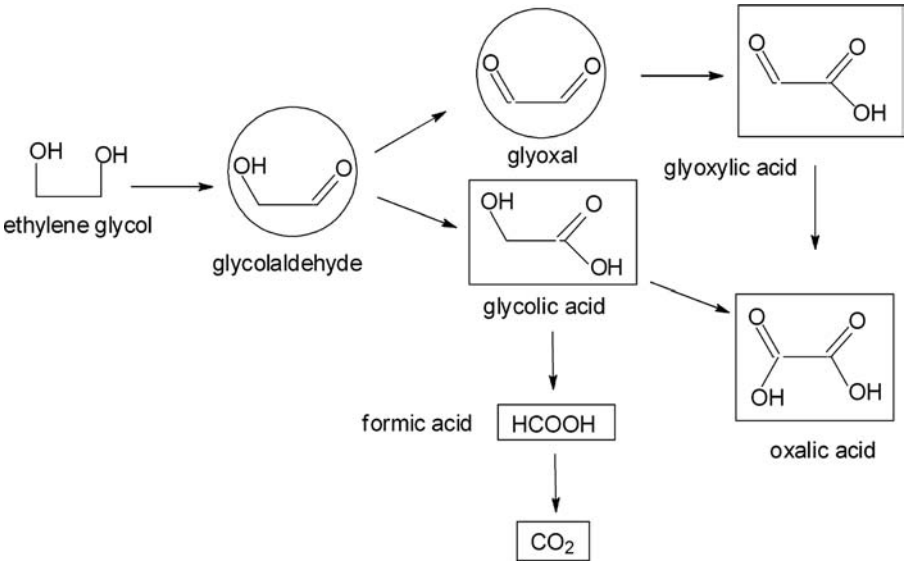

Figure 4.3 Proposed mechanism for ethylene glycol oxidation [5].

C−C bond cleavage: no C−C bond cleavage occurs at <400 mV over Pt catalyst, while the C−C bond of EG was cleaved in EG oxidation at 500 mV, which led to CO poisoning [91].

The EG electrooxidation kinetics and product distribution are quite different over Pt and Au. Cyclic voltammetry shows that the onset potential is more positive, but the peak current is larger on Au than on Pt, which indicates quite different reaction pathways. Weaver group studied the EG electrooxidation pathways in alkaline electrolytes on Pt and Au. They found that the Au featured the successive formation of partially oxidized C_2 solution-phase species *en route* to oxalate and carbonate production, while Pt was able to oxidize EG to carbonate through a sequence of chemisorbed (rather than solution-phase) intermediates [92]. Au is a very good catalyst for electrooxidation of aldehydes and alcohols in high-pH media. The electrooxidation of EG on Pd in alkaline media does not diverge that much compared with that on Pt: glycolate, oxylate, and carbonate seem to form at the same potential with an increase of oxalate and carbonate formation at the consumption of glycolate. Low pH favoring C−C bond scission is because a high OH coverage of the Pd/Pt surface is required for yielding only carboxylate products.

The activity of EG electrooxidation can be improved using binary or ternary catalysts either by alloying PGM (i.e., Pt or Pd) with different metals or by modifying the PGM surface by foreign metal ad-atoms [90,93–95]. Pt-M ad-atom (M = Bi, Cd, Cu, Pb, Re, Ru, Ti) catalysts have been studied and Pb and Bi were found to be able to improve the EG oxidation current density close to diffusion-limited value, attributed to bifunctional theory of electrocatalysts. Coutanceau and coworkers studied Pt, Pt–Pd, and Pt–Pd–Bi alloy catalysts for EG oxidation in both liquid alkaline electrolytes and AEM-based direct EG fuel cells. They found that the addition of Bi could decrease the onset potential by 70 mV, while Pt–Pd–Bi does not change the onset potential but leads to enhanced current density. EG is converted to glycolic acid, oxalic acid, and formic acid on Pt/C, while no formic acid but trace amounts of glyoxalic acid were observed on PtPdBi/C. They proposed that Bi favors the adsorption of OH species and depresses the C−C bond cleavage, which is likely due to dilution of surface Pt atoms [90]. The function of Pd is to only limit the poisoning of Pt sites by changing the composition of chemisorbed species. Nanostructured Pd–(Ni–Zn)/C and Pt–(Ni–Zn–P)/C have demonstrated to be much more active than smooth Pd electrodes up to 3300 A g_{Pd}^{-1}, and have also changed the oxidation product distributions: mixture of glycolate, oxalate, and carbonate were obtained, while most glycolate yielded on Pd/C catalyst. This indicates that Pd–(Ni–Zn)/C could promote C−C bond cleavage for a more complete oxidation [5].

4.4.3 Reaction Mechanisms and Catalysts for Glycerol Electrooxidation

Glycerol can be by-produced in large amounts in the biodiesel production [10,11]. Glycerol electrooxidation has been studied for its possible use in fuel

cells. In alkaline media, Pt, Pd, and Au have demonstrated distinct behaviors to glycerol electrooxidation. Pt/C shows a 150 mV lower onset potential and higher peak current than Pd and Au, while Au has a higher onset potential but broader GOR active potential region, which is due to its high redox potential. The Pd–Au alloy (atomic ratio of Pd–Au: 0.3 : 0.7, 0.5 : 0.5) catalysts presented comparatively lower onset potential than monometal Au/C and Pd/C ones, but still higher than Pt/C [96].

The oxidation products include glyceric acid, tartronic acid, glycolic acid, formic acid, oxalic acid, CO_2, and so on, and their distributions depend on the catalyst composition and structure and operation potential (anode overpotential) [5,50,86–88,96]. For example, an AEM-DGFC with a Pd/carbon nanotube (CNT) anode catalyst provided stable current for 8.4 h, producing 3070 C and achieving 28.6% conversion. About 4 mmol of glycerol was consumed to produce 27% glycerate, 23% tartronate, 4% glycolate, 15% oxalate, 9% formate, and 22% carbonate [50]. An electrolysis cell operated at 0.1 A and 0.6–0.7 V for 15 h in 2 M KOH + 2 M glycerol produced 35% glycerate, 36% tartronate, 3% glycolate, 14% oxalate, 2.5% formate, and 12.5% carbonate [97]. Based on these results, a reaction mechanism for glycerol oxidation is proposed, as shown in Figure 4.4. The primary OH is first oxidized to produce glyceric acid, and then the other end OH is oxidized to yield tartronic acid, glycolic acid is subsequently produced due to C−C bond scission. Glycolic and formic acids are further oxidized to produce oxalic acid, and CO_2, respectively.

Recently, Kwon and Koper used a self-designed onsite sample collection and off-line HPLC analysis system to study the mechanism of glycerol electrooxidation on Pt and Au electrodes [86]. They found a strong correlation between applied potential, catalyst (Pt and Au), and oxidation product distribution. On the Pt electrode, only glyceric acid was examined at relatively low potential, that is, <0.4 V (versus RHE), in 0.1 M NaOH + 0.1 M glycerol at 25 °C. Beyond this potential, glycolic acid and formic acid are produced due to C−C bond breaking. As the potential increases to ~0.5 V, tartronic acid and oxalic acid were examined. On the Au electrode, the onset potential of glycerol oxidation (at 0.65 V) is much higher than that of Pt. The glyceric acid is the only product under potential of ~ <0.8 V, while glycolic acid and formic acid were detected at a scan

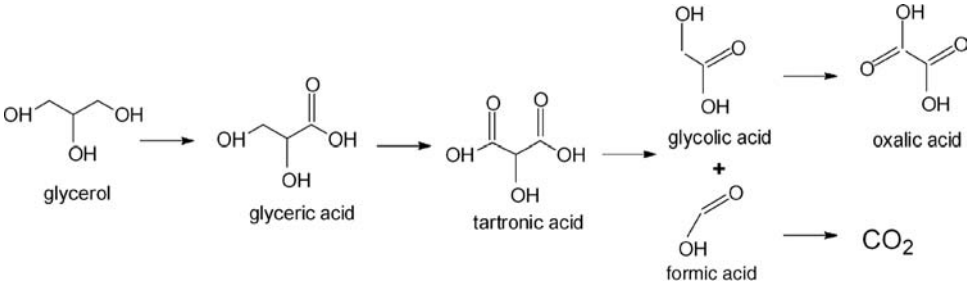

Figure 4.4 Proposed mechanism of glycerol oxidation on Pd catalysts. Adapted from Ref. [50].

potential of >0.8 V. No tartronic acid and oxalic acid were observed throughout the potential range of 1–1.8 V. This approach enables the monitoring of soluble reaction products during voltammetry with HPLC and allows new insights into mechanisms of complex multistep electrode reactions.

Controlled partial (selective) oxidation of glycerol using molecular oxygen in an aqueous-phase heterogeneous catalytic system under moderate conditions (i.e., 30–80 °C, 3–10 bar) represents a very attractive process for its low environmental impact, especially when compared with current stoichiometric oxidations; therefore, they have been extensively studied in recent years [89,98–105]. It was found that precious metals, such as Pt, Pd, Rh, and Au, are active, selective, and stable catalysts. The partial oxidation of glycerol can selectively produce value-added products. It has been found that in low-pH media, DHA can be produced with a selectivity of 35% on PtBi catalysts, while in high-pH media, the primary OH will be preferentially oxidized, and diverse products, such as C_3 acid (glyceric acid, tartronic acid), C_2 acids (glycolic acid, oxalic acid), and C_1 acid (formic acid) are produced. In heterogeneous catalysis, catalyst size and structure, the support (C or oxides), reaction conditions (i.e., temperature, O_2 pressure, ratio of catalyst to glycerol), and oxidant (O_2 or H_2O_2) are found to be able to influence the catalyst selectivity. Au is unique in heterogeneous catalytic oxidation of glycerol: The TOF is close to zero (no reaction) in the absence of a base, but a 100% selectivity to glyceric acid can be obtained at a glycerol conversion of 56% in an optimized high-pH environment [106,107]. High selectivity of glycolic acid can be achieved using H_2O_2 as oxidant. The identified electrocatalytic oxidation pathways are compared with reported heterogeneous catalytic oxidation pathways, as shown in Figure 4.5. More experimental and theoretical research efforts are needed to compare the heterogeneous catalytic oxidation and electrocatalytic oxidation of polyols, and may lead to the development of novel electrocatalysts that can efficiently cogenerate higher valued chemicals and electricity.

The AEM-DGFCs have demonstrated encouraging performance. For example, an AEM-DGFC with Pd–Ni–Zn/C anode and Fe–Co–N/C cathode catalysts have shown a maximum power density of 120 mW cm^{-2}, which is competitive to PEM-based DMFCs and two to three orders of magnitude higher than current biofuel cell with glycerol fuel (normally <1 mW cm^{-2}) [5]. Higher polyols than EG and glycerol, such as erythritol and xylitol, have been used as fuels in AEM-DAFCs with PtRu/C anode catalyst [108]. They showed lower performances than the AEM-DAFCs with EG and glycerol fuels. The reaction products have not been carefully examined and detailed mechanisms are required to be understood.

4.5 Synthetic Methods of Metal Electrocatalysts

High-performance practical electrocatalysts are essential to enhancing electrooxidation of alcohols for direct alcohol fuel cells. The overall electrocatalytic

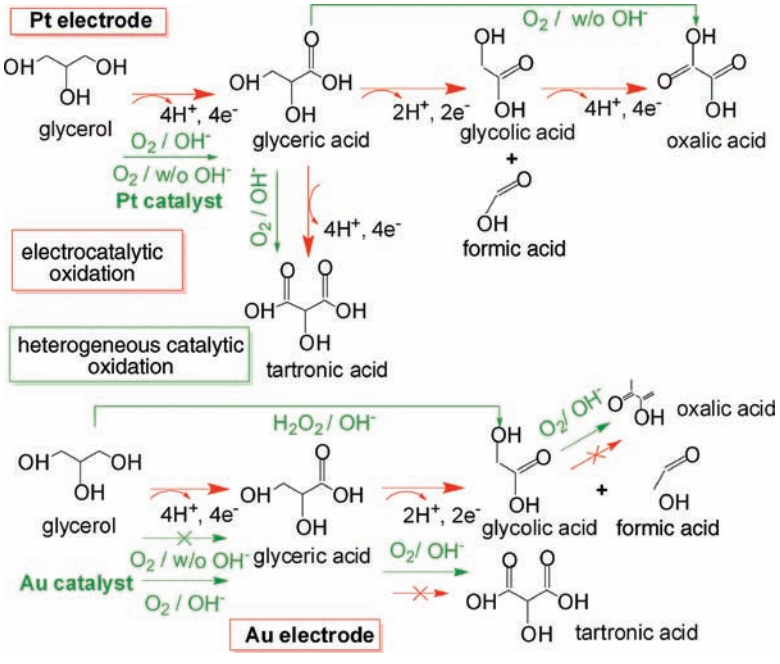

Figure 4.5 The proposed glycerol electrooxidation pathways using online collection and off-line HPLC analysis (marked in red arrows) (adapted from Ref. [87]), and reported heterogeneous catalytic oxidation of glycerol pathways (marked in green arrows) (adapted from Ref. [89]).

functions were found to be determined by local electronic property of the surface metal (d-band shift, electronic effects) [109], availability of presenting special geographic plane/facet (geometric effects) [110,111], and surface arrangements of different metals (ensemble effects) [112]. Research on single-crystal catalysts combined with theoretical calculations (e.g., DFT) have been extensively conducted in the past decades, and have provided valuable insights into the relationships of structure–catalytic functions [110,113]. For example, it was found that the overpotential for CO oxidation is lowered in the sequence of Pt (111) < Pt (554) < Pt (553), and the peak potential difference between Pt(553) and Pt(111) was as high as 0.17 V [114]. A Pt(111)skin-Ni(111) catalyst can exhibit over 90 times higher oxygen reduction reaction activity due to loose OH^- coverage on Pt skin with the modified electronic structure (optimized d-band center shift) [109,115]. However, it is still a big challenge to accurately synthesize real-world catalysts mimicking the single-crystal structures. The crucial considerations for synthesizing practical catalysts include control of the particle size, size distribution, shape (crystallographic facet), electronic structure (i.e., core–shell), nominal composition, surface composition, ensemble arrangements, alloying degree, oxide content of catalytic materials, and so on [116–118]. The long-term stability of metal catalyst and support in hostile electrochemical

environments is another practical concern [119]. The preparation method thus becomes a key factor determining the activity, selectivity, and stability of electrocatalysts.

The synthesis of real-world metal catalysts can be generally classified into "top-down" physical (from macroscale to nano dimensions) routes and "bottom-up" chemical (from molecular/atomic scale to nanoscale) routes [120]. The physical routes proceed with atomization of metals in a vacuum by thermal evaporation or sputtering, and so on [121–123]. The metal catalysts prepared by physical methods have low contaminations, and can be applied to fundamental studies. However, physical methods lacks of control over the size, size distribution, and shape of metallic particles. In contrast to physical methods, chemical methods are more flexible to precisely control the particle size, shape, and structure [124]. Recently, wet chemical synthesis approaches have emerged as one of the most promising methods to accurately control size, shape, structure, and surface facets of metallic nanostructures [118,124–140]; thus, they hold great potential for serving as high-performance catalysts. A typical wet chemical synthesis involves chemical reduction of dissoluble metal precursors in aqueous or organic phase to nucleus, controlled growth to the finally desired metal nanoparticles in the presence/absence of stabilizing agents and deposition on appropriate carbon supports. Despite the great progress in electrochemical approaches (i.e., underpotential deposition) to accurate synthesis of core–shell (skin layer) metal nanoparticles, the following section focuses only on recent advances in chemical reduction synthesis of carbon-supported electrocatalysts [141,142].

4.5.1 Impregnation Method

Impregnation method involves soaking up of a dissolved metal precursor into the pores of carbon support, and subsequently reducing the precursor into metal nanoparticles using reducing agent such as HCHO, HCOONa, $NaBH_4$, NH_2NH_2, H_2, and so on at optimized conditions [143–158]. Since the nucleation formation and particle growth are mainly confined within the carbon-support pores, the morphology of the porous substrate and the pore size distribution play a key role in terms of penetration and wetting of the precursor and also providing confinement for nanoparticle growth. In addition, the reduction kinetics and mass transfer of reducing agent also affect the number of nucleus and nucleation rate, thus controlling the particle size and particle size distribution. In order to achieve uniform dispersion of metal particles on carbon support, ethanol or isopropanol can be employed as solvent, and surface oxidation treatment of carbon support could also improve hosting metal nanoparticles. Under optimized synthesis conditions, the particle size prepared by the impregnation method can be controlled within 10 nm. The impregnation method is simple and easy to scale-up; therefore, it has been the most common method used for electrocatalyst preparation over the years. The major drawback is the lack of precise control of particle size, except when the porous substrate has a narrow

pore size distribution, that is, in highly ordered mesoporous carbon (OMC) [147]. In addition, it is hard to regulate the shape and structure of catalysts using the impregnation method. Employing an organic molecule containing two metals, such as Pt and Ru as precursor, represents a significant progress in the impregnation technique. Lukehart and coworkers synthesized (η-C_2H_4) (Cl) Pt(μ-Cl) (2)Ru(Cl) (η(3): η(3)-2,7-dimethyloctadienediyl) molecule and impregnated it onto XC-72R carbon black, and after a heat treatment under appropriate gas atmosphere, PtRu/C 16 wt% and PtRu/C 50 wt% catalysts were obtained with small particle size (3.4 and 5.0 nm, respectively) and good Pt–Ru alloy structures [146]. Although the PtRu/C catalysts demonstrated higher methanol oxidation activity than commercial PtRu/C competitors, the extra complex synthesis steps may not be suitable for a large-scale synthesis.

4.5.2 Colloidal Method

The colloid method is a widely adopted method for preparing metallic nanoparticles with precisely controlled size, shapes, and structures [125–135,137–141]. This method includes preparation of metallic colloids first and subsequent deposition on carbon support. One crucial approach is to prevent colloid aggregations using stabilizing agents, which include polymer, copolymer, surfactants, ligands, solvents, long-chain alcohols, organometallics, and so on. Effectively separating and controlling the nucleation and particle growth steps is essential for regulating the colloid size. Narrow size distributions are usually achieved either by steric hindrance of organic molecules on the metal surface or by electrostatic stabilization between nanoparticles. Watanabe *et al.* invented an elegant oxide colloid route to prepare PtRu/C. They first prepared colloidal PtRu oxides in aqueous phase with strict control of pH during adding reaction agents, and then reduced the oxide colloids by bubbling H_2 to obtain high-dispersion PtRu/C with a small particle size (2–3 nm) [159]. Bönnemann and Richards developed a delicate organic-phase reduction route to accurately control metal catalyst particle size and size distribution. NR_4BR_3H was used to reduce organic metal precursors in THF [130]. Binary and ternary catalysts such as PtRu/C, PtRuSn/C, PtRuW/C, and PtRuMo/C have been prepared through the "Bönnemann" method and showed higher performance than commercial PtRu/C catalyst [48,160].

4.5.2.1 Polyol Method

Polyol synthesis has been extensively studied for preparation of monometallic and multimetallic colloids in a polyol or diol (generally ethylene glycol), which serves as both solvent and temperature-dependent reducing agent (Figure 4.6) [126,133,139,161–164]. The presence of polyvinylpyrrolidone (PVP) can help control the particle size, shape, and structures. The key process of this method involves the reduction of inorganic precursors at an elevated temperature, sometimes close to the boiling point of polyol. It is found that at higher reduction

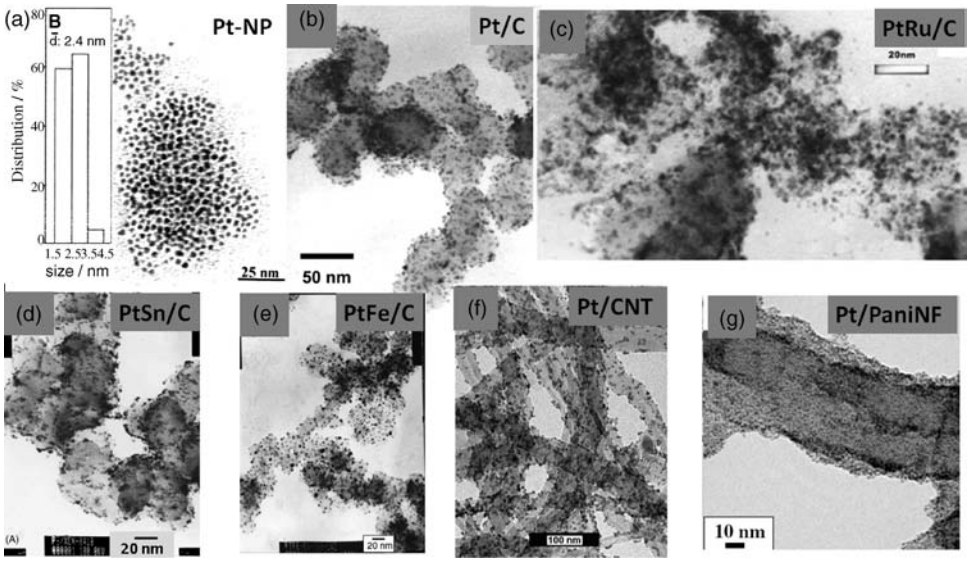

Figure 4.6 Pt and Pt-based electrocatalysts synthesized using polyol method (in the absence of PVP). (a) Pt nanoparticle ($D = 2.4$ nm [165]. (b) Pt/C (40 wt%, $D = 2.9$ nm [168]. (c) PtRu/C (20 Pt wt %, $D = 1.9$ nm [60]. (d) PtSn/C (20 Pt wt %, $D = 1.9$ nm [62]. (e) PtFe/C (20 Pt wt %, $D = 3.4$ nm [173]. (f) Pt/CNTs (30 wt%, $D = 4.46$ nm [174]. (g) Pt/polyaniline nanofibers (PaniNF, 30 wt%, $D = 2.1$ nm [176].

rates, the growth process leads to the production of thermodynamic-favored shape, while at low reduction rates, the nucleation and growth will be kinetically controlled and the shape of final products deviate from thermodynamic-favored shapes. Therefore, precise size and shape control can be achieved through rationally tuning the reaction kinetics, particularly at the seeding stage. Pt nanostructures, such as nanodendrites [139], nanorods, nanobars [152], and so on, can be accurately prepared through this method. However, the presence of stabilizers may cause intrinsic catalytic activity loss, and the postprocess for removal of stabilizers may lead to catalyst particle aggregation or shape/structure changes.

Polyol synthesis method in the absence of PVP was reported by Wang group to prepare homogeneous Pt, Rh, and Ru colloids with an average particle size of 2–4 nm [165]. Later, supported noble metal or noble metal/transition metal nanoparticles were prepared [60–65,166–179]. Xin and coworkers synthesized carbon-supported Pt, PtRu, PtPd, PtIr, PtSn, PtW, and PtFe catalysts with a sharp particle size distribution of 2–5 nm [60–65,166,168,170–173,175,177]. This method is simple and very easy to scale up. The inorganic compounds such as H_2PtCl_6, $RuCl_3$, $PdCl_2$, $SnCl_2$, $FeCl_2$, and so on served as metal precursors. The water content in the synthesis system was found to be able to control the particle size and size distribution. The reduction was conducted in an alkaline environment at 135–150 °C for 3–4 h, and the pH had to be adjusted back to 2–3 to separate the metal colloids from solvent and deposit them onto carbon support. Good alloy structures could be obtained through this method. It is very

attractive for large-scale synthesis because of the simple procedures and low material cost. However, it has to some extent failed for the synthesis of noble metal/transition metal alloy catalysts. Because EG is a weak reducing agent, transitional metal could not be fully reduced; therefore, its content is low in the final bimetallic catalysts. That is, the Fe content in the resulted PtFe/C catalyst was detected only 1/3–1/4 of its setting value [173].

4.5.2.2 Organic-Phase Method

In 2000, Sun et al researchers at IBM reported an elegant organic-phase method to prepare Fe–Pt magnetic nanoparticles with a diameter of 4–5 nm [129,180]. This approach was quickly adopted by catalysis researchers to prepare metal catalysts [134,135,137,181–188]. In nonpolar organic solvents, precious metal and transitional metal precursors have more intimate contacts and closer redox potentials; this can facilitate formation of a homogeneous bimetal nucleus, leading to the growth of controlled bimetallic nanoparticles. In the synthesis, the transitional metal precursor can be fully reduced by injecting a strong organic reducing agent, for example, $LiBetH_3$. Different C_{18}, C_{16} surfactants (e.g., oleylamine, oleic acid, octadecene, etc.) served as stabilizers that can selectively bond on specific metal facets, thus not only protecting particles from aggregations but also guiding the metal nucleus to grow into desired shapes (i.e., nanowires, nanorods, and nanoleaves) [134,184,186,188] and structures (e.g., core–shell) [135].

Figure 4.7a briefly illustrates the overall synthesis scheme. Sun *et al.* first developed this elegant synthesis route to prepare Fe–Pt magnetic materials with very narrow size distribution (4–5 nm), as shown in Figure 4.7b. Because metal precursors in the organic solvent have intimate contacts and closer redox potentials, better multimetallic catalysts can be obtained. PtCr/C, PtCo/CNT, and PdNi/C catalysts prepared through this method have very narrow size distributions of 2–5 nm and good alloy structures (Figure 4.7c–e). PdFe nanowires with

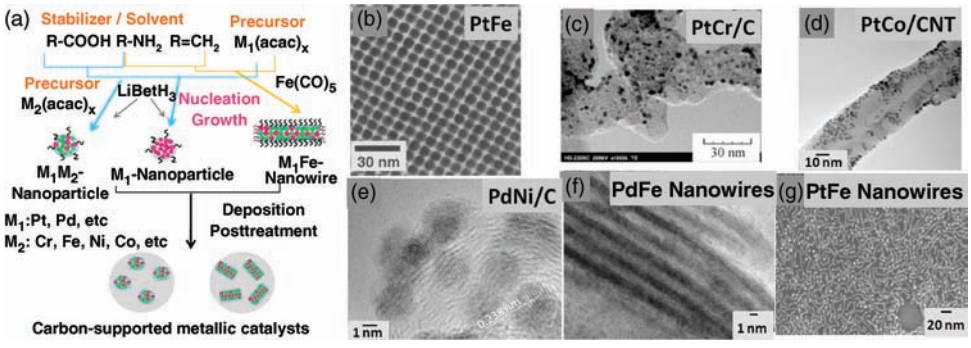

Figure 4.7 (a) Schematic illustration of the organic-phase method. Examples of catalysts prepared through this method. (b) PtFe nanoparticles [129]. (c) PtCr/C (28 wt%, $D = 2.3$ nm [187]. (d) PtCo/CNT (20 Pt wt %, $D = 2.0$ nm [180]. (e) PdNi/C (20 Pt wt %, $D = 2.4$ nm [187]. (f) PdFe nanoleaves ($D = 1.8$ nm, $L = 100$ nm [190]. (g) PtFe nanowires ($D = 2.7$ nm) [188].

a diameter of 2–3 nm and tunable length of 10–100 nm and Pd (111)-rich surface have been synthesized by changing the ratio of oleylamine and octadecene (Figure 4.7f). The PdNi/C prepared through this method has demonstrated very high reactivity to ethanol oxidation reaction in liquid alkaline electrolyte; this may be due to special interaction between surface Pd and Ni.

However, the surfactants need to be removed for electrocatalytic applications. It has been reported that surfactants could be removed under thermal treatment at a moderate temperature of 250 °C for a longer time, for example, 4 h [185]. It was also found that organic acid treatment and electrochemical tests may facilitate surfactant removal and achieve a higher reactivity [187].

4.5.3
Microemulsion Method

The microemulsion method consists of dispersion of two immiscible liquids containing reducing agent and metal precursors. It offers a unique flexibility in the simultaneous control of size and composition of mixed metal nanoparticles [189–196]. The chemical reduction of metal precursors is confined within a microemulsion, which is a tiny drop of precursor containing liquid engulfed by surfactant molecules. The microemulsion is uniformly dispersed in a continuous liquid phase, which is immiscible to the precursor-containing liquid phase. The size of the microemulsion is on the order of a few to hundreds of nanometers and is determined by the balance of surface free energy mediated by the surfactant molecules and the free energy difference arising from the immiscibility of the two liquid phases. The dispersed liquid phase is an oil, and water forms the continuous medium. The reverse microemulsion is the water-in-oil microemulsion. Since chemical steps are conducted within the microemulsion, which serves as a nanoscale reactor, a narrow particle size distribution (i.e., 2–5 nm) can thus be obtained. The introduction of a reducing agent, for example, hydrazine, $NaBH_4$, into the microemulsion is achieved by stirring. The reaction time is on the order of minutes. The size and distribution of the metal nanoparticle can be further controlled by a two-microemulsion method with the reducing agent also confined in a separate emulsion. It is possible to control the particle size by varying the water-to-surfactant molar ratio. The additional advantage is the possible synthesis of bimetal electrocatalysts on carbon support. Normally, a better alloy structure can be achieved. However, the microemulsion method cannot be used to control shape. It uses expensive surfactant molecules with extra cleaning steps and may not be suitable for large-scale synthesis.

4.5.4
Other Methods

Some unconventional synthesis techniques have been adopted in industrial catalyst manufactures. For example, 3 M researchers have developed an elegant PVD method to prepare nanostructured thin-film catalysts (NTFC) with extraordinary

activity and durability [123]. Spray conversion reaction process was successfully developed by Cabot company [197]. Droplets containing metal precursors and carbon support were first generated and thermal decomposed under controlled temperature and pressure to form uniform disperse catalyst nanoparticles on carbon. The PtRu/C catalyst has a uniform crystalline size of 2–4 nm and shows high catalytic activity, excellent durability, and reduced cost.

4.6
Carbon Nanomaterials as Anode Catalyst Support

Catalyst support is an integrated part of an electrocatalyst. Its main functions are hosting high-dispersion Pt nanoparticles from aggregation and providing continuous electric conduction paths within the three-phase boundary of the electrode. It was a milestone in the fuel cell catalyst R&D history that one order of magnitude of Pt loading in electrode could be reduced by replacing Pt black with highly disperse Pt nanoparticles supported on carbon black. Appropriate carbon support should possess excellent electric conductivity, large surface area, reasonable pore structure, and good electrochemical durability [116]. Carbon black is a widely used support for low-temperature fuel cell catalysts, and it can be produced by the oil furnace and acetylene processes. Carbon black has a good compromise between the surface area and electric conductivity. Due to its low cost and abundant availability, oil furnace carbon black, for example, Vulcan XC-72, has been broadly used for supporting electrocatalysts. It has a surface area of 200–300 $m^2 g^{-1}$, but composed of a large portion of micropores of <2 nm. Supply of reactant gas may not occur smoothly within a micropore of <2 nm. In addition, the electrochemical stability of carbon black has been reported to be a potential problem for real fuel cell operations, the loss of carbon support under high operation potential could lead to Pt agglomeration and leaching [119,198]. There is a clear need to seek more suitable catalyst support for low-temperature fuel cells. In recent decades, various carbon nanomaterials such as fullerene (C_{60}), carbon nanotubes, graphene, and mesoporous carbons have been discovered and synthesized, and further greatly promoted new research areas in nanotechnology and nanomaterials. These nanocarbons have been extensively studied as next generation of electrocatalyst support materials and many exciting progress have been made.

4.6.1
Carbon Nanotubes

Since its discovery [199], CNTs have attracted enormous attention as a novel catalyst material due to their high aspect ratio and unique electronic properties [166,167,172,174,175,177,178,199–206]. CNT is an allotrope of carbon with a cylindrical nanostructure made from curved graphite sheets. CNTs can be classified as single–walled nanotubes (SWNTs), double-walled nanotubes (DWNTs),

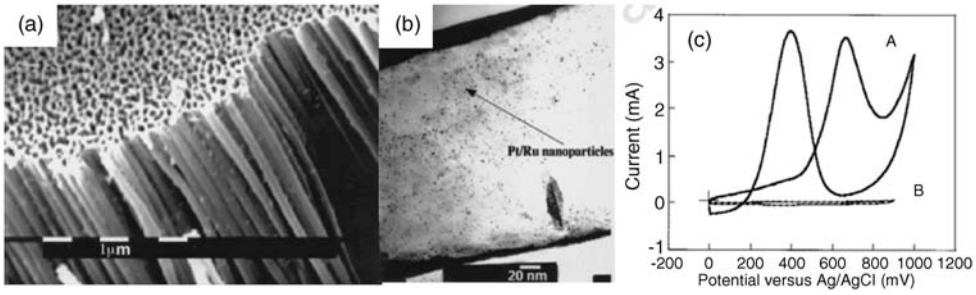

Figure 4.8 TEM images of carbon nanotubule (a) and PtRu/CNT (b), and cyclic voltammograms of methanol oxidation on A: after deposition of Pt/Ru nanoparticle, and B: before deposition of Pt/Ru nanoparticles, 2 M methanol + 1 M H_2SO_4 (c) [200].

and MWNTs. They can be prepared through arc discharge, chemical vapor deposition, laser radiation, and so on. The tube diameter ranges from 0.7to 100 nm, and tube length varies from submicrometer to centimeter. CNT is a unique 1D carbon material and possesses an excellent electric conductivity. The electric conductivity of MWNTs is 1000–2000 S cm^{-1}, which is much greater than 4–10 S cm^{-1} for carbon black XC-72. In addition, there is no micropores in CNTs compared with about 50% micropores for XC-72.

Che *et al.* first explored porous alumina template to prepare carbon nanotubule with a diameter of 200 nm and wall thickness of 20 nm (Figure 4.8). After impregnating PtRu precursors into the CNT, HF was employed to remove Al_2O_3 frames. Small and uniform PtRu nanoparticles (1.59 ± 0.3 nm) were obtained after 3 h H_2 reduction at 580 °C. The carbon nanotubule-supported PtRu nanoparticles have demonstrated very large and characteristic methanol oxidation waves in acid electrolyte [200]. Using a similar method, Rajesh *et al.* studied the methanol oxidation activity on a series of MWNTs (200 nm in diameter) and found their activity sequence is PtRu/MWNTs > Pt-WO_3/MWNTs > PtRu/XC-72 [203].

Before the synthesis of CNT-supported catalysts, it is necessary to functionalize the CNT outer wall surface with oxygenate groups in order to anchor the metal nanoparticles. Li *et al.* used a H_2SO_4–HNO_3 mixture to surface-treat MWNTs and various functional groups, such as hydroxyl (−OH), cabonyl (−CO), and carboxyl (−COOH), could be grafted on the CNT surface. They used polyol method to prepare 10 wt% Pt/MWNTs cathode catalyst for DMFC and demonstrated a 43% peak power density enhancement [186,202]. Liu *et al.* prepared PtRu/CNTs with a diameter of 2–6 nm using a microwave-promoted polyol synthesis approach and showed a competitive MOR activity compared with commercial PtRu/C (E-TEK) in single DMFC test [167]. Single-walled carbon nanohorn (SWNHs) is a special type of CNT prepared by Iijima. Pt and PtRu nanoparticles were deposited on the outer wall of SWNH and showed a significant enhancement in DMFC performance. The catalytic activity improvements were attributed to high electric conductivity (low internal resistance), high

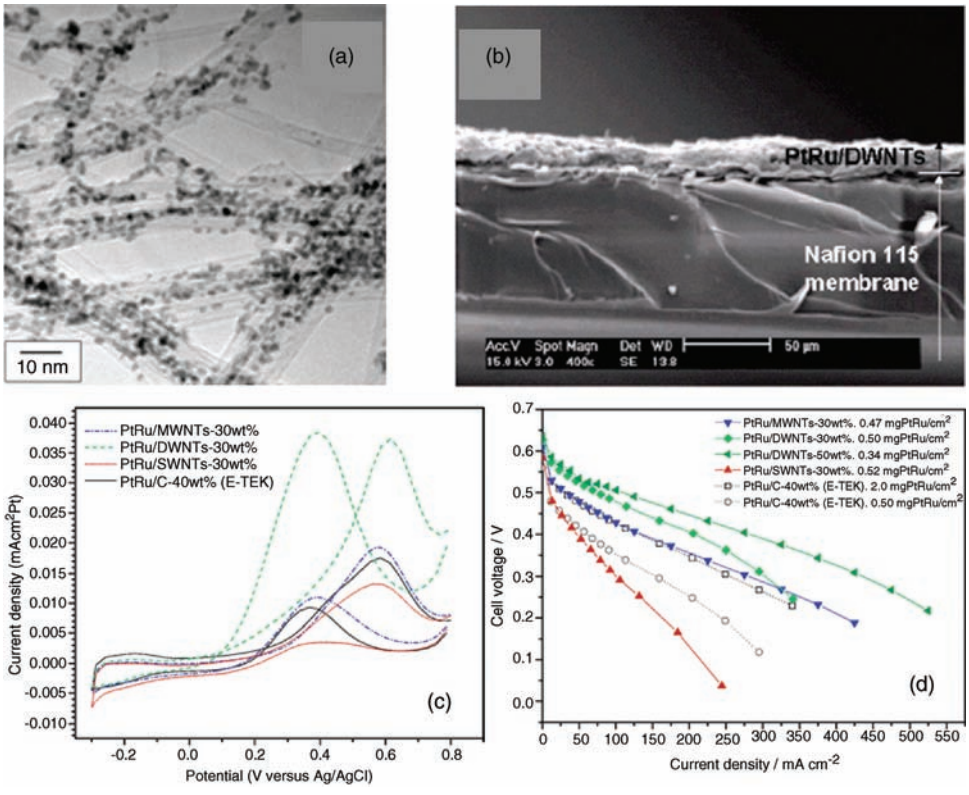

Figure 4.9 (a) TEM image of PtRu/DWNTs (50 wt%). (b) SEM image of PtRu/DWNTs thin film. (c) Polarization curve of methanol oxidation in 0.5 M H_2SO_4 + 0.5 M methanol on PtRu/CNT catalysts. (d) Single DMFC with PtRu/CNTs anode catalysts [177].

purity (i.e., low sulfur content in CNTs), and a thinner catalyst layer thickness. Recently, Li *et al.* compared three types of CNT (MWNT, DWNT, and SWNT)-supported PtRu catalysts with similar PtRu particle size (2–5 nm), and achieved very different MOR activities (Figure 4.9). PtRu/DWNTs show the best MOR activity. It can reduce precious metal loading by 75%, while still obtain a 68% power density enhancement, which was attributed to its "pure" metallic property (unlike SWNTs: a mixture of semiconductor and conductor) and a special metal support interaction [177]. Detailed investigations are needed to explain this extraordinary benefit acquired from small-diameter carbon nanotubes.

In order to improve the catalyst utilization and reactant mass transport, some research efforts have been made to develop techniques that enable to directly grow CNTs onto gas diffusion layer to obtain ordered electrode structures. Sun *et al.* directly grew CNTs on Co-Ni catalysts previously deposited on a carbon paper, and then supported small Pt nanoparticles (1.2 nm) through ion exchange method [204]. Yan and coworkers used underpotential deposition method to deposit Pt nanoparticles on CNTs, which were directly grew on carbon paper

substrate using a catalytic chemical deposition approach [205]. Both the CNT-based electrodes showed improved performance compared with Pt/C catalyst-based electrodes. Yan and coworkers further developed a filtration method to make ordered CNT-based electrode. In detail, they employed hydrophilic Nylon filter to facilitate formation of a hydrophobic CNT catalyst thin film. Pt/MWNTs thin-film electrode-based MEA demonstrated excellent single fuel cell performance in mass transport-controlled region, which indicated a better gas diffusion was achieved inside the ordered electrode [175].

Due to their high graphite structure, the CNTs have shown greater electrochemical durability than carbon black. The measured corrosion current for carbon black was 0.5 mA mg^{-1}, which is higher than that for MWNTs (0.2 mA mg^{-1}). The electrochemical surface area of Pt/MWNTs dropped 25% after a durability test under a constant potential of 0.9 V in 0.5 M H_2SO_4 at 60 °C for 170 h, while that of Pt/CB had dropped 80%. The average particle size of Pt/MWNTs grew from 2.8 nm to 3.0 nm, while that for Pt/CB grew from 2.5 to 5.0 nm [207]. Higher electrochemical stability makes CNTs very attractive for fuel cell catalyst supports.

4.6.2
Carbon Nanofibers

Carbon nanofiber (CNF) is an important 1D nanocarbon, which has also been extensively studied as electrocatalyst support [146,151,203,208–212]. Compared with expensive CNT, CNFs are cheap, attributed to their large-scale chemical vapor deposition manufacture route. CNFs can be made in different forms, such as platelet, ribbon, and herringbone. Bessel *et al.* employed impregnation method to prepare Pt/CNFs with small particle size. It was interesting to find Pt nanoparticles look like plates, which suggested a strong metal–support interaction. Five wt% Pt/CNFs showed a similar activity of methanol oxidation as 30 wt% Pt/CB [208]. Lukehart and coworkers prepared 40 wt% PtRu/CNFs with a particle size of 5–9 nm, and demonstrated a 50% MOR activity enhancement compared with unsupported PtRu catalysts [146,151]. Recently, Li *et al.* showed that CNF-based catalysts can effectively increase the Nafion content in the electrode (from 30 to 50%); this was because 1D CNFs provide continuous electric conduction paths, which could not be easily cut off by ionic conductor. This work may open up a new strategy to fabrication of high-performance fuel cell electrodes by using 1D carbon materials.

4.6.3
Ordered Mesoporous Carbons

OMCs have highly ordered mesoporous structures with very narrow pore size distributions. Uniform and small metal catalysts can be easily prepared even using impregnation method. Ordered mesoporous carbons are one type of

carbon support that have been extensively studied for direct alcohol fuel cell catalysts [147,213]. The OMC can be synthesized via nanocasting technique using ordered mesoporous silica materials as the hard template [147,213–216]. Insertion of carbon precursors within the ordered mesopores of the OMS templates, their carbonization by thermal treatment at high temperatures under inert conditions, and subsequent removal of the silica templates result in the synthesis of OMC materials. The physical and chemical properties of OMC, such as pore size, connectivity, morphology, surface functionality, electric conductivity, and thermal stability, can be well controlled by adjusting OMS template, carbon precursor, carbonation temperature, heating environment, posttreatment, and so on. Soft-templating methods (self-assembly) can also be employed to directly synthesize OMC via an organic–organic self-assembly between carbon precursors and organic templates [217–219]. The resulting OMC have a confined mesopore size, high surface area (700–2000 $m^2 g^{-1}$), and high pore volume (1–2 $cm^3 g^{-1}$). Very small Pt or PtRu nanoparticles of <3 nm can be easily controlled, simply through impregnation method, due to the OMC's large surface area and unique pore structure. The Pt/OMC cathode catalyst-based DMFC shows a 104 mW cm^{-2} at 0.45 V at 50 °C, which can reduce Pt loading by three times (from 6 to 2 mg cm^{-2}) [220]. Samsung has demonstrated a small DMFC system with 20 MEAs (25 cm^2) could deliver a power density of 80 mW cm^{-2} at 8 V using a 0.75 M methanol solution under ambient operation condition, and it can operate a Notebook for 10 h using pure 100 ml methanol.

4.6.4
Graphene Sheets

Graphene, a two-dimensional carbon material with single (or a few) atomic layer, has attracted great attention from both fundamental science and applied research [221,222]. The combination of the high surface area (theoretical value of 2630 $m^2 g^{-1}$), high conductivity, unique graphitized basal plane structure, and potential low manufacturing cost makes graphene sheets a very promising candidate for fuel cell catalyst support [223–227]. In addition, graphene nanosheets (GNS) have been found to be able to modify the properties of Pt clusters supported on them. The Pt/GNS showed four times higher current density (0.12 mA cm^{-2}) than that of Pt/CB (0.03 mA cm^{-2}). CO oxidation study indicated that Pt/GNS has a much smaller CO adsorption rate by about 40 times than that of Pt/carbon black. The Pt particles supported on GNS was smaller than 0.5 nm, which would acquire the specific electronic properties of Pt, thus modifying its catalytic activities [224]. The Pt-functionalized graphene sheets (FGS) retained 49.8% of the original electrochemical surface area, while the commercial catalyst kept only 33.6% after an electrochemical durability test. Therefore, Pt on FGSs is much more stable than commercial catalyst under electrochemical durability tests, due to its more graphite structure [223].

4.7 Future Challenges and Opportunities

Low-temperature direct alcohol fuel cells have received enormous attention for future electrochemical power sources. Anode catalyst is one of the most critical components to determine the overall DAFC performance and lifetime. Extensive research efforts have been made on understanding the relationships of structure–catalyst functions, *in situ* characterizing reaction intermediates, elucidating electrocatalytic reaction mechanisms, and thus developing novel catalytic materials. Although great progress has been made in the preparation of highly efficient fuel cell catalysts, a large-scale, accurate synthesis of fuel cell catalysts at the nano or atomic scale with high activity, durability/reliability, and stability is yet to be achieved. The synthesis methods should be cost-effective, simple, and easy to scale up. These catalysts could be heterogeneous nanoarchitectures with multiple functions supported on durable supports, or directly deposited on electrodes. Restructuring of the nanostructured catalysts (change in surface composition, facets, ensemble configuration, and electronic structures) under real electrochemical reactions often occurs and significantly influences the activity and durability; understanding the catalyst restructuring to gain deep insights into structure change–catalyst function under real electrocatalytic processes is essential before their real applications. The fast developed nanotechnology, *in situ* characterization techniques, and advanced computation capabilities have great potential to assist developing advanced catalytic materials.

In order to improve the Faradic efficiency and fuel utilization, the desired final product of alcohol oxidation is CO_2. However, breaking the C−C bonds of alcohols for direct C_{2+} alcohol fuel cells remains a great challenge, especially at low temperatures (e.g., <90 °C) and low anode overpotentials. For primary alcohol oxidation, such as ethanol oxidation, nanostructured PtRhSn/C has demonstrated a strong ability to both improve reaction kinetics and break C−C bond. Future research efforts using both combinational chemistry methods and theoretical calculations may lead to the development of efficient ternary or even quarterly PtSn-based catalysts for complete alcohol oxidation.

In another aspect, high reaction kinetics is sometimes associated with partial oxidation of alcohols. Cogeneration of electricity and higher valued chemicals from biorenewable polyols will make biofuel production more profitable and attractive. Efficient cogeneration depends on the development of highly selective electrocatalysts. The catalyst selectivity towards polyols electrooxidation is related to catalyst kind and structure, operation potential, and reaction condition [96,228–233]. Their relations should be thoroughly understood by combining experimental, analysis (e.g., spectroscopy, chromatography), and theoretical research tools. Heterogeneous catalytic processing of biorenewable compounds has made significant progress in recent years. Learning the knowledge developed from selective heterogeneous catalytic oxidation may guide the development of highly selective electrocatalytic oxidation catalysts for low-temperature alcohol fuel cells.

The oxygen reduction reaction at the cathode of a DAFC is a long-term scientific challenge. Its overpotential is over 200 mV even at the open-circuit voltage on the most active Pt catalysts. The alcohol crossover results in a short-circuit potential (extra 150–200 mV loss) at the cathode, thus seriously deteriorating the fuel cell efficiency and fuel utilization. Developing highly active low loading noble metal anode catalysts and alcohol-tolerant non-PGM cathode catalysts is in great demand for high-performance DAFCs. Since the anions cross from cathode to anode, the alcohol crossover issue can be significantly minimized through using AEMFCs. However, big disadvantages of current anion exchange membranes are their low anion conductivity and unsatisfied chemical stability (short lifetime). Liquid base, such as NaOH or KOH, has to mix with alcohol fuels to improve the local pH-surrounded catalyst sites in order to improve the DAFC performance. The penetration of carbonate salts into electrode pores will reduce reactant gas mass transfer and lead to low fuel cell performance. Development of novel polymers for high-performance anion exchange membranes should be regarded as of same important research priority as the electrocatalysts for next-generation low-temperature low/zero liquid base alcohol fuel cells.

Acknowledgments

The author would like to acknowledge the contributions of Li group members at Michigan Technological University and the support of US National Science Foundation (CBET-1032547 and CBET-1159448). The donors of the American Chemical Society Petroleum Research Fund are also acknowledged. Li thanks Dr. Zhou, Weijiang, for his fruitful discussion.

References

1 Wasmus, S. and Küver, A. (1999) Methanol oxidation and direct methanol fuel cells: a selective review. *Journal of Electroanalytical Chemistry*, **461** (1–2), 14–31.

2 Lamy, C., Belgsir, E.M., and Léger, J.M. (2001) Electrocatalytic oxidation of aliphatic alcohols: application to the direct alcohol fuel cell (DAFC). *Journal of Applied Electrochemistry*, **31** (7), 799–809.

3 Gasteiger, H.A., Kocha, S.S., Sompalli, B., and Wagner, F.T. (2005) Activity benchmarks and requirements for Pt, Pt-alloy, and non-Pt oxygen reduction catalysts for PEMFCs. *Applied Catalysis B: Environmental*, **56** (1–2), 9–35.

4 Aricò, A.S., Baglio, V., and Antonucci, V. (2009) Direct methanol fuel cells: history, status and perspectives, in *Electrocatalysis of Direct Methanol Fuel Cells: From Fundamentals to Applications* (eds. H. Liu and J. Zhang), Wiley-VCH Verlag GmbH, Weinheim, pp. 1–78.

5 Bianchini, C. and Shen, P.K. (2009) Palladium-based electrocatalysts for alcohol oxidation in half cells and in direct alcohol fuel cells. *Chemical Reviews*, **109** (9), 4183–4206.

6 Lamy, C., Coutanceau, C., and Leger, J.-M. (2009) The direct ethanol fuel cell: a challenge to convert bioethanol cleanly into electric energy, in *Catalysis for*

Sustainable Energy Production (eds P. Barbaro and C. Bianchini), Wiley-VCH Verlag GmbH, Weinheim, pp. 1–46.

7 Antolini, E. and Gonzalez, E.R. (2010) Alkaline direct alcohol fuel cells. *Journal of Power Sources*, **195** (11), 3431–3450.

8 Yu, E.H., Krewer, U., and Scott, K. (2010) Principles and materials aspects of direct alkaline alcohol fuel cells. *Energies*, **3** (8), 1499–1528.

9 U.S. DOE (2011) 2010 Annual Progress Report: DOE Hydrogen Program, in Related Information, U.S. Department of Energy.

10 Huber, G.W., Iborra, S., and Corma, A. (2006) Synthesis of transportation fuels from biomass: chemistry, catalysts, and engineering. *Chem Rev.*, **3**7 (52), 4044–4098.

11 van Santen, R.A. (2007) Renewable catalytic technologies: a perspective, in *Catalysis for Renewables: From Feedstock to Energy Production* (eds G. Centi and R. A.van Santen), Wiley-VCH Verlag GmbH, Weinheim, pp. 1–19.

12 Huber, G.W. (2008) *Breaking the Chemical and Engineering Barriers to Lignocellulosic Biofuels: Next Generation Hydrocarbon Biorefineries*, National Science Foundation, Chemical, Bioengineering, Environmental and Transport Systems Division, Washington, DC.

13 Wang, Q., Sun, G.Q., Jiang, L.H., Xin, Q., Sun, S.G., Jiang, Y.X., Chen, S.P., Jusys, Z., and Behm, R.J. (2007) Adsorption and oxidation of ethanol on colloid-based Pt/C, PtRu/C and Pt3Sn/C catalysts: *in situ* FTIR spectroscopy and on-line DEMS studies. *Physical Chemistry Chemical Physics*, **9** (21), 2686–2696.

14 Justi, E.W. and Winsel, A.W. (1955) 821 688.

15 Bagotzky, V.S. and Vassilyev, Y.B. (1967) Mechanism of electro-oxidation of methanol on the platinum electrode. *Electrochimica Acta*, **12** (9), 1323–1343.

16 Cathro, K. (1969) The oxidation of water-soluble organic fuels using platinum-tin catalysts. *Journal of Electroanalytical Chemistry and Interfacial Electrochemistry*, **16**, 1608–1611.

17 Watanabe, M. and Motoo, S. (1975) Electrocatalysis by ad-atoms: Part II. Enhancement of the oxidation of methanol on platinum by ruthenium ad-atoms. *Journal of Electroanalytical Chemistry and Interfacial Electrochemistry*, **60** (3), 267–273.

18 Janssen, M.M.P. and Moolhuysen, J. (1976) Binary systems of platinum and a second metal as oxidation catalysts for methanol fuel cells. *Electrochimica Acta*, **21** (11), 869–878.

19 Andrew, M.R., McNicol, B.D., Short, R.T., and Drury, J.S. (1977) Electrolytes for methanol-air fuel cells. I. The performance of methanol electro-oxidation catalysts in sulphuric acid and phosphoric acid electrolytes. *Journal of Applied Electrochemistry*, **7** (2), 153–160.

20 Markovic, N.M., Widelov, A., Ross, P.N., Monterio, O.R., and Brown, I.G. (1977) Electrooxidation of CO and CO/H_2 mixtures on a Pt-Sn catalyst prepared by an implantation method. *Catalysis Letters*, **43**, 161–166.

21 Beden, B., Kadirgan, F., Lamy, C., and Leger, J.M. (1981) Electrocatalytic oxidation of methanol on platinum-based binary electrodes. *Journal of Electroanalytical Chemistry and Interfacial Electrochemistry*, **127** (1–3), 75–85.

22 Shibata, M. and Motoo, S. (1985) Electrocatalysis by ad-atoms: Part XI. Enhancement of acetaldehyde oxidation by Shole control and oxygen adsorbing ad-atoms. *Journal of Electroanalytical Chemistry and Interfacial Electrochemistry*, **187** (1), 151–159.

23 Cameron, D.S., Hards, G.A., Harrison, B., and Potter, R.J. (1987) Direct methanol fuel cells. *Platinum Metals Reviews*, **31**, 173–181.

24 Aramata, A., Kodera, T., and Masuda, M. (1988) Electrooxidation of methanol on platinum bonded to the solid polymer electrolyte, Nafion. *Journal of Applied Electrochemistry*, **18** (4), 577–582.

25 Goodenough, J.B., Hamnett, A., Kennedy, B.J., Manoharan, R., and Weeks, S.A. (1988) Methanol oxidation on unsupported and carbon supported Pt + Ru anodes. *Journal of Electroanalytical*

Chemistry and Interfacial Electrochemistry, **240** (1–2), 133–145.

26 Parsons, R. and VanderNoot, T. (1988) The oxidation of small organic molecules: a survey of recent fuel cell related research. *Journal of Electroanalytical Chemistry and Interfacial Electrochemistry*, **257** (1–2), 9–45.

27 Ticanelli, E., Beery, J.G., Paffett, M.T., and Gottesfeld, S. (1989) An electrochemical, ellipsometric, and surface science investigation of the PtRu bulk alloy surface. *Journal of Electroanalytical Chemistry and Interfacial Electrochemistry*, **258** (1), 61–77.

28 Christensen, P.A., Hamnett, A., and Troughton, G.L. (1993) The role of morphology in the methanol electro-oxidation reaction. *Journal of Electroanalytical Chemistry*, **362** (1–2), 207–218.

29 Marković, N.M., Gasteiger, H.A., Ross, P.N., Jr., Jiang, X., Villegas, I., and Weaver, M.J. (1995) Electro-oxidation mechanisms of methanol and formic acid on Pt-Ru alloy surfaces. *Electrochimica Acta*, **40** (1), 91–98.

30 McBreen, J. and Mukerjee, S. (1995) *In situ* X-ray absorption studies of a Pt-Ru electrocatalyst. *Journal of the Electrochemical Society*, **142** (10), 3399–3404.

31 Ravikumar, M.K. and Shukla, A.K. (1996) Effect of methanol crossover in a liquid-feed polymer-electrolyte direct methanol fuel cell. *Journal of the Electrochemical Society*, **143** (8), 2601–2606.

32 Gurau, B., Viswanathan, R., Liu, R., Lafrenz, T.J., Ley, K.L., Smotkin, E.S., Reddington, E., Sapienza, A., Chan, B.C., Mallouk, T.E., and Sarangapani, S. (1998) Structural and electrochemical characterization of binary, ternary, and quaternary platinum alloy catalysts for methanol electro-oxidation1. *The Journal of Physical Chemistry B*, **102** (49), 9997–10003.

33 Reddington, E., Sapienza, A., Gurau, B., Viswanathan, R., Sarangapani, S., Smotkin, E.S., and Mallouk, T.E. (1998) Combinatorial electrochemistry: a highly parallel, optical screening method for discovery of better electrocatalysts. *Science*, **280** (5370), 1735–1737.

34 Sun, S.G. (1998) Studying electrocatalytic oxidation of small organic molecules with in-situ infra spectroscopy, in *Electrocatalysis (Frontiers in Electrochemistry)* (eds J. Lipkowski and P.N. Ross), Wiley-VCH Verlag GmbH, Weinheim, pp. 243–290.

35 Liu, R., Iddir, H., Fan, Q., Hou, G., Bo, A., Ley, K.L., Smotkin, E.S., Sung, Y.E., Kim, H., Thomas, S., and Wieckowski, A. (2000) Potential-dependent infrared absorption spectroscopy of adsorbed CO and X-ray photoelectron spectroscopy of arc-melted single-phase Pt, PtRu, PtOs, PtRuOs, and Ru electrodes. *The Journal of Physical Chemistry B*, **104** (15), 3518–3531.

36 Iwasita, T. (2002) Electrocatalysis of methanol oxidation. *Electrochimica Acta*, **47** (22–23), 3663–3674.

37 Piela, P., Eickes, C., Brosha, E., Garzon, F., and Zelenay, P. (2004) Ruthenium crossover in direct methanol fuel cell with Pt-Ru black anode. *Journal of the Electrochemical Society*, **151** (12), A2053–A2059.

38 Cao, D., Lu, G.Q., Wieckowski, A., Wasileski, S.A., and Neurock, M. (2005) Mechanisms of methanol decomposition on platinum: a combined experimental and *ab initio* approach. *The Journal of Physical Chemistry B*, **109** (23), 11622–11633.

39 Brockris, J.O.M. and Wroblowa, H. (1964) Activity of electrolytically deposited platinum and ruthenium by the electrooxidation of methanol. *Journal of Electroanalytical Chemistry and Interfacial Electrochemistry*, **7**, 428.

40 Petry, G.A., Podlovchenko, B.I., Frukmin, A.N., and Lal, H. (1965) The behavior of platinized-platinum and platinum-ruthenium electrodes in methanol solutions. *Journal of Electroanalytical Chemistry and Interfacial Electrochemistry*, **10**, 253.

41 Méli, G., Léger, J.M., Lamy, C., and Durand, R. (1993) Direct electrooxidation of methanol on highly dispersed platinum-based catalyst electrodes:

temperature effect. *Journal of Applied Electrochemistry*, **23** (3), 197–202.
42 Rolison, D.R., Hagans, P.L., Swider, K.E., and Long, J.W. (1999) Role of hydrous ruthenium oxide in Pt–Ru direct methanol fuel cell anode electrocatalysts: the importance of mixed electron/proton conductivity. *Langmuir*, **15** (3), 774–779.
43 Long, J.W., Stroud, R.M., Swider-Lyons, K.E., and Rolison, D.R. (2000) How to make electrocatalysts more active for direct methanol oxidation avoid PtRu bimetallic alloys!. *The Journal of Physical Chemistry B*, **104** (42), 9772–9776.
44 Rolison, D.R. (2003) Catalytic nanoarchitectures: the importance of nothing and the unimportance of periodicity. *Science*, **299** (5613), 1698–1701.
45 Ren, X., Wilson, M.S., and Gottesfeld, S. (1996) High performance direct methanol polymer electrolyte fuel cells. *Journal of the Electrochemical Society*, **143** (1), L12–L15.
46 Kim, T., Kobayashi, K., Takahashi, M., and Nagai, M. (2005) Effect of Sn in Pt-Ru-Sn ternary catalysts for CO/H_2 and methanol electrooxidation. *Chemistry Letters*, **34** (6), 798–799.
47 Page, T., Johnson, R., Hormes, J., Noding, S., and Rambabu, B. (2000) A study of methanol electro-oxidation reactions in carbon membrane electrodes and structural properties of Pt alloy electro-catalysts by EXAFS. *Journal of Electroanalytical Chemistry*, **485** (1), 34–41.
48 Park, K.-W., Choi, J.-H., Kwon, B.-K., Lee, S.-A., Sung, Y.-E., Ha, H.-Y., Hong, S.-A., Kim, H., and Wieckowski, A. (2002) Chemical and electronic effects of Ni in Pt/Ni and Pt/Ru/Ni alloy nanoparticles in methanol electrooxidation. *The Journal of Physical Chemistry B*, **106** (8), 1869–1877.
49 Antolini, E., Salgado, J.R.C., and Gonzalez, E.R. (2006) The methanol oxidation reaction on platinum alloys with the first row transition metals: the case of Pt–Co and –Ni alloy electrocatalysts for DMFCs: a short review. *Applied Catalysis B: Environmental*, **63** (1–2), 137–149.
50 Bambagioni, V., Bianchini, C., Marchionni, A., Filippi, J., Vizza, F., Teddy, J., Serp, P., and Zhiani, M. (2009) Pd and Pt–Ru anode electrocatalysts supported on multi-walled carbon nanotubes and their use in passive and active direct alcohol fuel cells with an anion-exchange membrane (alcohol=methanol, ethanol, glycerol). *Journal of Power Sources*, **190** (2), 241–251.
51 Farrell, A.E., Plevin, R.J., Turner, B.T., Jones, A.D., O'Hare, M., and Kammen, D.M. (2006) Ethanol can contribute to energy and environmental goals. *Science*, **311** (5760), 506–508.
52 Simões, F.C., dos Anjos, D.M., Vigier, F., Léger, J.M., Hahn, F., Coutanceau, C., Gonzalez, E.R., Tremiliosi-Filho, G., de Andrade, A.R., Olivi, P., and Kokoh, K.B. (2007) Electroactivity of tin modified platinum electrodes for ethanol electrooxidation. *Journal of Power Sources*, **167** (1), 1–10.
53 Iwasita, T. and Pastor, E. (1994) A DEMS and FTIR spectroscopic investigation of adsorbed ethanol on polycrystalline platinum. *Electrochimica Acta*, **39** (4), 531–537.
54 Pastor, E. and Iwasita, T. (1994) D/H exchange of ethanol at platinum electrodes. *Electrochimica Acta*, **39** (4), 547–551.
55 Perez, J.M., Beden, B., Hahn, F., Aldaz, A., and Lamy, C. (1989) "*In situ*" infrared reflectance spectroscopic study of the early stages of ethanol adsorption at a platinum electrode in acid medium. *Journal of Electroanalytical Chemistry and Interfacial Electrochemistry*, **262** (1–2), 251–261.
56 Rousseau, S., Coutanceau, C., Lamy, C., and Léger, J.M. (2006) Direct ethanol fuel cell (DEFC): electrical performances and reaction products distribution under operating conditions with different platinum-based anodes. *Journal of Power Sources*, **158** (1), 18–24.
57 Lamy, C., Lima, A., LeRhun, V., Delime, F., Coutanceau, C., and Léger, J.-M. (2002) Recent advances in the development of direct alcohol fuel cells

(DAFC). *Journal of Power Sources*, **105** (2), 283–296.

58 Lamy, C., Rousseau, S., Belgsir, E.M., Coutanceau, C., and Léger, J.M. (2004) Recent progress in the direct ethanol fuel cell: development of new platinum–tin electrocatalysts. *Electrochimica Acta*, **49** (22–23), 3901–3908.

59 Ermete, A. (2007) Catalysts for direct ethanol fuel cells. *Journal of Power Sources*, **170** (1), 1–12.

60 Zhou, W.J., Zhou, Z.H., Song, S.Q., Li, W.Z., Sun, G.Q., Tsiakaras, P., and Xin, Q. (2003) Pt based anode catalysts for direct ethanol fuel cells. *Applied Catalysis B: Environmental*, **46** (2), 273–285.

61 Zhao, X., Li, W., Jiang, L., Zhou, W., Xin, Q., Yi, B., and Sun, G. (2004) Multi-wall carbon nanotube supported Pt-Sn nanoparticles as an anode catalyst for the direct ethanol fuel cell. *Carbon*, **42** (15), 3263–3265.

62 Zhou, W.J., Li, W.Z., Song, S.Q., Zhou, Z.H., Jiang, L.H., Sun, G.Q., Xin, Q., Poulianitis, K., Kontou, S., and Tsiakaras, P. (2004) Bi- and tri-metallic Pt-based anode catalysts for direct ethanol fuel cells. *Journal of Power Sources*, **131** (1–2), 217–223.

63 Zhou, W.J., Song, S.Q., Li, W.Z., Sun, G. Q., Xin, Q., Kontou, S., Poulianitis, K., and Tsiakaras, P. (2004) Pt-based anode catalysts for direct ethanol fuel cells. *Solid State Ionics*, **175** (1–4), 797–803.

64 Zhou, W.J., Zhou, B., Li, W.Z., Zhou, Z.H., Song, S.Q., Sun, G.Q., Xin, Q., Douvartzides, S., Goula, M., and Tsiakaras, P. (2004) Performance comparison of low-temperature direct alcohol fuel cells with different anode catalysts. *Journal of Power Sources*, **126** (1–2), 16–22.

65 Zhou, W.J., Song, S.Q., Li, W.Z., Zhou, Z.H., Sun, G.Q., Xin, Q., Douvartzides, S., and Tsiakaras, P. (2005) Direct ethanol fuel cells based on PtSn anodes: the effect of Sn content on the fuel cell performance. *Journal of Power Sources*, **140** (1), 50–58.

66 Vigier, F., Coutanceau, C., Hahn, F., Belgsir, E.M., and Lamy, C. (2004) On the mechanism of ethanol electro-oxidation on Pt and PtSn catalysts: electrochemical and *in situ* IR reflectance spectroscopy studies. *Journal of Electroanalytical Chemistry*, **563** (1), 81–89.

67 Vigier, F., Rousseau, S., Coutanceau, C., Leger, J.-M., and Lamy, C. (2006) Electrocatalysis for the direct alcohol fuel cell. *Topics in Catalysis*, **40** (1), 111–121.

68 Liu, P., Logadottir, A., and Nørskov, J.K. (2003) Modeling the electro-oxidation of CO and H_2/CO on Pt, Ru, PtRu and Pt_3Sn. *Electrochimica Acta*, **48** (25–26), 3731–3742.

69 de Souza, J.P.I., Queiroz, S.L., Bergamaski, K., Gonzalez, E.R., and Nart, F.C. (2002) Electro-oxidation of ethanol on Pt, Rh, and PtRh electrodes: a study using DEMS and *in-situ* FTIR techniques. *The Journal of Physical Chemistry B*, **106** (38), 9825–9830.

70 Colmati, F., Antolini, E., and Gonzalez, E.R. (2008) Preparation, structural characterization and activity for ethanol oxidation of carbon supported ternary Pt–Sn–Rh catalysts. *Journal of Alloys and Compounds*, **456** (1–2), 264–270.

71 Kowal, A., Li, M., Shao, M., Sasaki, K., Vukmirovic, M.B., Zhang, J., Marinkovic, N.S., Liu, P., Frenkel, A.I., and Adzic, R.R. (2009) Ternary Pt/Rh/SnO_2 electrocatalysts for oxidizing ethanol to CO_2. *Nature Materials*, **8** (4), 325–330.

72 Spendelow, J.S. and Wieckowski, A. (2007) Electrocatalysis of oxygen reduction and small alcohol oxidation in alkaline media. *Physical Chemistry Chemical Physics*, **9** (21), 2654–2675.

73 Varcoe, J.R. and Slade, R.C.T. (2005) Prospects for alkaline anion-exchange membranes in low temperature fuel cells. *Fuel Cells*, **5** (2), 187–200.

74 Yanagi, H. and Fukuta, K. (2008) Anion exchange membrane and ionomer for alkaline membrane fuel cells (AMFCs). *ECS Transactions*, **16** (2), 257–262.

75 Blizanac, B.B., Ross, P.N., and Markovic, N.M. (2007) Oxygen electroreduction on Ag(1 1 1): the pH effect. *Electrochimica Acta*, **52** (6), 2264–2271.

76 Li, X., Popov, B.N., Kawahara, T., and Yanagi, H. (2011) Non-precious metal catalysts synthesized from precursors of carbon, nitrogen, and transition metal for

oxygen reduction in alkaline fuel cells. *Journal of Power Sources*, **196** (4), 1717–1722.

77 Xu, H. and Hou, X. (2007) Synergistic effect of modified Pt/C electrocatalysts on the performance of PEM fuel cells. *International Journal of Hydrogen Energy*, **32** (17), 4397–4401.

78 Cui, G., Song, S., Shen, P.K., Kowal, A., and Bianchini, C. (2009) First-principles considerations on catalytic activity of Pd toward ethanol oxidation. *The Journal of Physical Chemistry C*, **113** (35), 15639–15642.

79 Liang, Z.X., Zhao, T.S., Xu, J.B., and Zhu, L.D. (2009) Mechanism study of the ethanol oxidation reaction on palladium in alkaline media. *Electrochimica Acta*, **54** (8), 2203–2208.

80 Chen, Y., Zhuang, L., and Lu, J. (2007) Non-Pt anode catalysts for alkaline direct alcohol fuel cells. *Chinese Journal of Catalysis*, **28** (10), 870–874.

81 He, Q., Chen, W., Mukerjee, S., Chen, S., and Laufek, F. (2009) Carbon-supported PdM (M=Au and Sn) nanocatalysts for the electrooxidation of ethanol in high pH media. *Journal of Power Sources*, **187** (2), 298–304.

82 Shen, P.K. and Xu, C. (2006) Alcohol oxidation on nanocrystalline oxide Pd/C promoted electrocatalysts. *Electrochemistry Communications*, **8** (1), 184–188.

83 Bianchini, C., Bambagioni, V., Filippi, J., Marchionni, A., Vizza, F., Bert, P., and Tampucci, A. (2009) Selective oxidation of ethanol to acetic acid in highly efficient polymer electrolyte membrane-direct ethanol fuel cells. *Electrochemistry Communications*, **11** (5), 1077–1080.

84 Bambagioni, V., Bevilacqua, M., Filippi, J., Marchionni, A., Moneti, S., Vizza, F., and Bianchini, C. (2010) Direct alcohol fuel cells as chemical reactors for the sustainable production of energy and chemicals: energy and chemicals from renewables by electrocatalysis. *Chemistry Today*, **28** (3), 518–528.

85 Santasalo-Aarnio, A., Kwon, Y., Ahlberg, E., Kontturi, K., Kallio, T., and Koper, M.T.M. (2011) Comparison of methanol, ethanol and iso-propanol oxidation on Pt and Pd electrodes in alkaline media studied by HPLC. *Electrochemistry Communications*, **13** (5), 466–469.

86 Kwon, Y. and Koper, M.T.M. (2010) Combining voltammetry with HPLC: application to electro-oxidation of glycerol. *Analytical Chemistry*, **82** (13), 5420–5424.

87 Kwon, Y., Lai, S.C.S., Rodriguez, P., and Koper, M.T.M. (2011) Electrocatalytic oxidation of alcohols on gold in alkaline media: base or gold catalysis? *Journal of the American Chemical Society*, **133** (18), 6914–6917.

88 Roquet, L., Belgsir, E.M., Léger, J.M., and Lamy, C. (1994) Kinetics and mechanisms of the electrocatalytic oxidation of glycerol as investigated by chromatographic analysis of the reaction products: potential and pH effects. *Electrochimica Acta*, **39** (16), 2387–2394.

89 Zope, B.N., Hibbitts, D.D., Neurock, M., and Davis, R.J. (2010) Reactivity of the gold/water interface during selective oxidation catalysis. *Science*, **330** (6000), 74–78.

90 Demarconnay, L., Brimaud, S., Coutanceau, C., and Léger, J.M. (2007) Ethylene glycol electrooxidation in alkaline medium at multi-metallic Pt based catalysts. *Journal of Electroanalytical Chemistry*, **601** (1–2), 169–180.

91 Matsuoka, K., Iriyama, Y., Abe, T., Matsuoka, M., and Ogumi, Z. (2005) Electro-oxidation of methanol and ethylene glycol on platinum in alkaline solution: poisoning effects and product analysis. *Electrochimica Acta*, **51** (6), 1085–1090.

92 Chang, S.C., Ho, Y., and Weaver, M.J. (1991) Applications of real-time FTIR spectroscopy to the elucidation of complex electroorganic pathways: electrooxidation of ethylene glycol on gold, platinum, and nickel in alkaline solution. *Journal of the American Chemical Society*, **113** (25), 9506–9513.

93 Kohlmüller, H. (1976) Anodic oxidation of ethylene glycol with noble metal alloy catalysts. *Journal of Power Sources*, **1** (3), 249–256.

94 Kadirgan, F., Beden, B., and Lamy, C. (1983) Electrocatalytic oxidation of ethylene-glycol: Part II. Behaviour of platinum-ad-atom electrodes in alkaline medium. *Journal of Electroanalytical Chemistry and Interfacial Electrochemistry*, **143** (1–2), 135–152.

95 Dalbay, N. and Kadirgan, F. (1991) Electrolytically co-deposited platinum: palladium electrodes and their electrocatalytic activity for ethylene glycol oxidation – a synergistic effect. *Electrochimica Acta*, **36** (2), 353–356.

96 Simões, M., Baranton, S., and Coutanceau, C. (2010) Electro-oxidation of glycerol at Pd based nano-catalysts for an application in alkaline fuel cells for chemicals and energy cogeneration. *Applied Catalysis B: Environmental*, **93** (3–4), 354–362.

97 Bambagioni, V., Bevilacqua, M., Bianchini, C., Filippi, J., Lavacchi, A., Marchionni, A., Vizza, F., and Shen, P.K. (2010) Self-sustainable production of hydrogen, chemicals, and energy from renewable alcohols by electrocatalysis. *ChemSusChem*, **3** (7), 851–855.

98 Besson, M. and Gallezot, P. (2000) Selective oxidation of alcohols and aldehydes on metal catalysts. *Catalysis Today*, **57** (1–2), 127–141.

99 Mallat, T. and Baiker, A. (2004) Oxidation of alcohols with molecular oxygen on solid catalysts. *Chemical Reviews*, **104** (6), 3037–3058.

100 Ketchie, W.C., Fang, Y.-L., Wong, M.S., Murayama, M., and Davis, R.J. (2007) Influence of gold particle size on the aqueous-phase oxidation of carbon monoxide and glycerol. *Journal of Catalysis*, **250** (1), 94–101.

101 Corma, A. and Garcia, H. (2008) Supported gold nanoparticles as catalysts for organic reactions. *Chemical Society Reviews*, **37** (9), 2096–2126.

102 Della Pina, C., Falletta, E., Prati, L., and Rossi, M. (2008) Selective oxidation using gold. *Chemical Society Reviews*, **37** (9), 2077–2095.

103 Hutchings, G.J. (2008) Nanocrystalline gold and gold palladium alloy catalysts for chemical synthesis. *Chemical Communications*, (10), 1148–1164.

104 Zhou, C.-H., Beltramini, J.N., Fan, Y.-X., and Lu, G.Q. (2008) Chemoselective catalytic conversion of glycerol as a biorenewable source to valuable commodity chemicals. *Chemical Society Reviews*, **37** (3), 527–549.

105 Dimitratos, N., Lopez-Sanchez, J., and Hutchings, G. (2009) Green catalysis with alternative feedstocks. *Topics in Catalysis*, **52** (3), 258–268.

106 Carrettin, S., McMorn, P., Johnston, P., Griffin, K., and Hutchings, G.J. (2002) Selective oxidation of glycerol to glyceric acid using a gold catalyst in aqueous sodium hydroxide. *Chemical Communications*, (7), 696–697.

107 Carrettin, S., McMorn, P., Johnston, P., Griffin, K., Kiely, C.J., and Hutchings, G.J. (2003) Oxidation of glycerol using supported Pt, Pd and Au catalysts. *Physical Chemistry Chemical Physics*, **5** (6), 1329–1336.

108 Matsuoka, K., Iriyama, Y., Abe, T., Matsuoka, M., and Ogumi, Z. (2005) Alkaline direct alcohol fuel cells using an anion exchange membrane. *Journal of Power Sources*, **150** (0), 27–31.

109 Stamenkovic, V.R., Fowler, B., Mun, B.S., Wang, G., Ross, P.N., Lucas, C.A., and Marković, N.M. (2007) Improved oxygen reduction activity on $Pt_3Ni(111)$ via increased surface site availability. *Science*, **315** (5811), 493–497.

110 Marković, N.M. and Ross, P.N., Jr. (2002) Surface science studies of model fuel cell electrocatalysts. *Surface Science Reports*, **45** (4–6), 117–229.

111 Tian, N., Zhou, Z.-Y., and Sun, S.-G. (2008) Platinum metal catalysts of high-index surfaces: from single-crystal planes to electrochemically shape-controlled nanoparticles. *The Journal of Physical Chemistry C*, **112** (50), 19801–19817.

112 Arenz, M., Stamenkovic, V., Schmidt, T.J., Wandelt, K., Ross, P.N., and Markovic, N.M. (2003) The electro-oxidation of formic acid on Pt-Pd single crystal bimetallic surfaces. *Physical Chemistry Chemical Physics*, **5** (19), 4242–4251.

113 Somorjai, G.A. (1994) *Introduction to Surface Chemistry and Catalysis*, John Wiley & Sons, Inc., New York.

114 Lebedeva, N.P., Koper, M.T.M., Herrero, E., Feliu, J.M., and van Santen, R.A. (2000) Cooxidation on stepped Pt[*n*(111) × (111)] electrodes. *Journal of Electroanalytical Chemistry*, **487** (1), 37–44.

115 Stamenkovic, V.R., Mun, B.S., Arenz, M., Mayrhofer, K.J.J., Lucas, C.A., Wang, G., Ross, P.N., and Markovic, N.M. (2007) Trends in electrocatalysis on extended and nanoscale Pt-bimetallic alloy surfaces. *Nature Materials*, **6** (3), 241–247.

116 Ralph, T.R. and Hogarth, M.P. (2002) Catalysis for low temperature fuel cells Part 1: the cathode challenges. *Platinum Metals Review*, **46** (1), 3–14.

117 Ermete, A. (2003) Formation of carbon-supported PtM alloys for low temperature fuel cells: a review. *Materials Chemistry and Physics*, **78** (3), 563–573.

118 Somorjai, G., Tao, F., and Park, J. (2008) The nanoscience revolution: merging of colloid science, catalysis and nanoelectronics. *Topics in Catalysis*, **47** (1), 1–14.

119 Borup, R., Meyers, J., Pivovar, B., Kim, Y.S., Mukundan, R., Garland, N., Myers, D., Wilson, M., Garzon, F., Wood, D., Zelenay, P., More, K., Stroh, K., Zawodzinski, T., Boncella, J., McGrath, J.E., Inaba, M., Miyatake, K., Hori, M., Ota, K., Ogumi, Z., Miyata, S., Nishikata, A., Siroma, Z., Uchimoto, Y., Yasuda, K., Kimijima, K.-I., and Iwashita, N. (2007) Scientific aspects of polymer electrolyte fuel cell durability and degradation. *Chemical Reviews*, **107** (10), 3904–3951.

120 Chan, K.-Y., Ding, J., Ren, J., Cheng, S., and Tsang, K.Y. (2004) Supported mixed metal nanoparticles as electrocatalysts in low temperature fuel cells. *Journal of Materials Chemistry*, **14** (4), 505–516.

121 Sasaki, T., Koshizaki, N., Terauchi, S., Umehara, H., Matsumoto, Y., and Koinuma, M. (1997) Preparation of Pt/TiO_2 nanocomposite films using co-sputtering method. *Nanostructured Materials*, **8** (8), 1077–1083.

122 Yan, X.M., Ni, J., Robbins, M., Park, H.J., Zhao, W., and White, J.M. (2002) Silver nanoparticles synthesized by vapor deposition onto an ice matrix. *Journal of Nanoparticle Research*, **4** (6), 525–533.

123 Debe, M.K., Schmoeckel, A.K., Vernstrom, G.D., and Atanasoski, R. (2006) High voltage stability of nanostructured thin film catalysts for PEM fuel cells. *Journal of Power Sources*, **161** (2), 1002–1011.

124 Astruc, D. (2008) *Nanoparticles and Catalysis*, Wiley-VCH Verlag GmbH, Weinheim.

125 Ahmadi, T.S., Wang, Z.L., Green, T.C., Henglein, A., and El-Sayed, M.A. (1996) Shape-controlled synthesis of colloidal platinum nanoparticles. *Science*, **272** (5270), 1924–1925.

126 Toshima, N. and Yonezawa, T. (1998) Bimetallic nanoparticles-novel materials for chemical and physical applications. *New Journal of Chemistry*, **22** (11), 1179–1201.

127 Crooks, R.M., Zhao, M., Sun, L., Chechik, V., and Yeung, L.K. (2000) Dendrimer-encapsulated metal nanoparticles: synthesis, characterization, and applications to catalysis. *Accounts of Chemical Research*, **34** (3), 181–190.

128 Murray, C.B., Kagan, C.R., and Bawendi, M.G. (2000) Synthesis and characterization of monodisperse nanocrystals and close-packed nanocrystal assemblies. *Annual Review of Materials Science*, **30**, 545–610.

129 Sun, S., Murray, C.B., Weller, D., Folks, L., and Moser, A. (2000) Monodisperse FePt nanoparticles and ferromagnetic FePt nanocrystal superlattices. *Science*, **287** (5460), 1989–1992.

130 Bönnemann, H. and Richards, R.M. (2001) Nanoscopic metal particles: synthetic methods and potential applications. *European Journal of Inorganic Chemistry*, **2001** (10), 2455–2480.

131 Jana, N.R., Gearheart, L., and Murphy, C.J. (2001) Seed-mediated growth approach for shape-controlled synthesis of spheroidal and rod-like gold nanoparticles using a surfactant template. *Advanced Materials*, **13** (18), 1389–1393.

132 Roucoux, A., Schulz, J., and Patin, H. (2002) Reduced transition metal colloids:

a novel family of reusable catalysts? *Chemical Reviews*, **102** (10), 3757–3778.

133 Sun, Y. and Xia, Y. (2002) Shape-controlled synthesis of gold and silver nanoparticles. *Science*, **298** (5601), 2176–2179.

134 Wang, C., Hou, Y., Kim, J., and Sun, S. (2007) A general strategy for synthesizing FePt nanowires and nanorods. *Angewandte Chemie: International Edition*, **46** (33), 6333–6335.

135 Alayoglu, S., Nilekar, A.U., Mavrikakis, M., and Eichhorn, B. (2008) Ru-Pt core–shell nanoparticles for preferential oxidation of carbon monoxide in hydrogen. *Nature Materials*, **7** (4), 333–338.

136 Somorjai, G. and Park, J. (2008) Colloid science of metal nanoparticle catalysts in 2D and 3D structures: challenges of nucleation, growth, composition, particle shape, size control and their influence on activity and selectivity. *Topics in Catalysis*, **49** (3), 126–135.

137 Wang, C., Daimon, H., Onodera, T., Koda, T., and Sun, S. (2008) A general approach to the size- and shape-controlled synthesis of platinum nanoparticles and their catalytic reduction of oxygen. *Angewandte Chemie*, **120** (19), 3644–3647.

138 Chen, J., Lim, B., Lee, E.P., and Xia, Y. (2009) Shape-controlled synthesis of platinum nanocrystals for catalytic and electrocatalytic applications. *Nano Today*, **4** (1), 81–95.

139 Lim, B., Jiang, M., Camargo, P.H.C., Cho, E.C., Tao, J., Lu, X., Zhu, Y., and Xia, Y. (2009) Pd-Pt bimetallic nanodendrites with high activity for oxygen reduction. *Science*, **324** (5932), 1302–1305.

140 Xie, X., Li, Y., Liu, Z.-Q., Haruta, M., and Shen, W. (2009) Low-temperature oxidation of CO catalysed by Co_3O_4 nanorods. *Nature*, **458** (7239), 746–749.

141 Zhang, J., Vukmirovic, M.B., Xu, Y., Mavrikakis, M., and Adzic, R.R. (2005) Controlling the catalytic activity of platinum-monolayer electrocatalysts for oxygen reduction with different substrates. *Angewandte Chemie: International Edition*, **44** (14), 2132–2135.

142 Zhang, J., Sasaki, K., Sutter, E., and Adzic, R.R. (2007) Stabilization of platinum oxygen-reduction electrocatalysts using gold clusters. *Science*, **315** (5809), 220–222.

143 Goodenough, J.B., Hamnett, A., Kennedy, B.J., Manoharan, R., and Weeks, S.A. (1990) Porous carbon anodes for the direct methanol fuel cell: I. The role of the reduction method for carbon supported platinum electrodes. *Electrochimica Acta*, **35** (1), 199–207.

144 Román-Martínez, M.C., Cazorla-Amorós, D., Yamashita, H., and de Miguel, S., and Scelza, O.A. (1999) XAFS study of dried and reduced PtSn/C catalysts: nature and structure of the catalytically active phase. *Langmuir*, **16** (3), 1123–1131.

145 Takasu, Y., Fujiwara, T., Murakami, Y., Sasaki, K., Oguri, M., Asaki, T., and Sugimoto, W. (2000) Effect of structure of carbon-supported PtRu electrocatalysts on the electrochemical oxidation of methanol. *Journal of the Electrochemical Society*, **147** (12), 4421–4427.

146 Boxall, D.L., Deluga, G.A., Kenik, E.A., King, W.D., and Lukehart, C.M. (2001) Rapid synthesis of a Pt_1Ru_1/carbon nanocomposite using microwave irradiation: a DMFC anode catalyst of high relative performance. *Chemistry of Materials*, **13** (3), 891–900.

147 Joo, S.H., Choi, S.J., Oh, I., Kwak, J., Liu, Z., Terasaki, O., and Ryoo, R. (2001) Ordered nanoporous arrays of carbon supporting high dispersions of platinum nanoparticles. *Nature*, **412** (6843), 169–172.

148 Dickinson, A.J., Carrette, L.P.L., Collins, J.A., Friedrich, K.A., and Stimming, U. (2002) Preparation of a Pt-Ru/C catalyst from carbonyl complexes for fuel cell applications. *Electrochimica Acta*, **47** (22–23), 3733–3739.

149 Fujiwara, N., Yasuda, K., Ioroi, T., Siroma, Z., and Miyazaki, Y. (2002) Preparation of platinum–ruthenium onto solid polymer electrolyte membrane and the application to a DMFC anode. *Electrochimica Acta*, **47** (25), 4079–4084.

150 Pozio, A., Silva, R.F., De Francesco, M., Cardellini, F., and Giorgi, L. (2002) A

novel route to prepare stable Pt-Ru/C electrocatalysts for polymer electrolyte fuel cell. *Electrochimica Acta*, **48** (3), 255–262.

151 Steigerwalt, E.S., Deluga, G.A., and Lukehart, C.M. (2002) Pt-Ru/carbon fiber nanocomposites: synthesis, characterization, and performance as anode catalysts of direct methanol fuel cells. A search for exceptional performance. *The Journal of Physical Chemistry B*, **106** (4), 760–766.

152 Xiong, L., Kannan, A.M., and Manthiram, A. (2002) Pt–M (M=Fe, Co, Ni and Cu) electrocatalysts synthesized by an aqueous route for proton exchange membrane fuel cells. *Electrochemistry Communications*, **4** (11), 898–903.

153 Venkataraman, R., Kunz, H.R., and Fenton, J.M. (2003) Development of new CO tolerant ternary anode catalysts for proton exchange membrane fuel cells. *Journal of the Electrochemical Society*, **150** (3), A278–A284.

154 Kawaguchi, T., Sugimoto, W., Murakami, Y., and Takasu, Y. (2004) Temperature dependence of the oxidation of carbon monoxide on carbon supported Pt, Ru, and PtRu. *Electrochemistry Communications*, **6** (5), 480–483.

155 Lizcano-Valbuena, W.H., de Azevedo, D.C., and Gonzalez, E.R. (2004) Supported metal nanoparticles as electrocatalysts for low-temperature fuel cells. *Electrochimica Acta*, **49** (8), 1289–1295.

156 Vigier, F., Coutanceau, C., Perrard, A., Belgsir, E.M., and Lamy, C. (2004) Development of anode catalysts for a direct ethanol fuel cell. *Journal of Applied Electrochemistry*, **34** (4), 439–446.

157 Li, W., Sun, G., Yan, Y., and Xin, Q. (2005) Supported noble metal electrocatalysts in low temperature fuel cells. *Progress in Chemistry*, **17** (5), 761–772.

158 Cui, Z., Liu, C., Liao, J., and Xing, W. (2008) Highly active PtRu catalysts supported on carbon nanotubes prepared by modified impregnation method for methanol electro-oxidation. *Electrochimica Acta*, **53** (27), 7807–7811.

159 Watanabe, M., Uchida, M., and Motoo, S. (1987) Preparation of highly dispersed Pt + Ru alloy clusters and the activity for the electrooxidation of methanol. *Journal of Electroanalytical Chemistry and Interfacial Electrochemistry*, **229** (1–2), 395–406.

160 Götz, M. and Wendt, H. (1998) Binary and ternary anode catalyst formulations including the elements W, Sn and Mo for PEMFCs operated on methanol or reformate gas. *Electrochimica Acta*, **43** (24), 3637–3644.

161 Hirai, H., Nakao, Y., and Toshima, N. (1979) Preparation of colloidal transition metals in polymers by reduction with alcohols or ethers. *Journal of Macromolecular Science: Part A – Chemistry*, **13** (6), 727–750.

162 Toshima, N., Yonezawa, T., and Kushihashi, K. (1993) Polymer-protected palladium–platinum bimetallic clusters: preparation, catalytic properties and structural considerations. *Journal of the Chemical Society, Faraday Transactions*, **89** (14), 2537–2543.

163 Camargo, P.H.C., Xiong, Y., Ji, L., Zuo, J.M., and Xia, Y. (2007) Facile synthesis of tadpole-like nanostructures consisting of Au heads and Pd tails. *Journal of the American Chemical Society*, **129** (50), 15452–15453.

164 Xiong, Y., Cai, H., Wiley, B.J., Wang, J., Kim, M.J., and Xia, Y. (2007) Synthesis and mechanistic study of palladium nanobars and nanorods. *Journal of the American Chemical Society*, **129** (12), 3665–3675.

165 Wang, Y., Ren, J., Deng, K., Gui, L., and Tang, Y. (2000) Preparation of tractable platinum, rhodium, and ruthenium nanoclusters with small particle size in organic media. *Chemistry of Materials*, **12** (6), 1622–1627.

166 Li, W., Liang, C., Qiu, J., Zhou, W., Han, H., Wei, Z., Sun, G., and Xin, Q. (2002) Carbon nanotubes as support for cathode catalyst of a direct methanol fuel cell. *Carbon*, **40** (5), 791–794.

167 Liu, Z., Lee, J.Y., Chen, W., Han, M., and Gan, L.M. (2003) Physical and electrochemical characterizations of microwave-assisted polyol preparation of

carbon-supported PtRu nanoparticles. *Langmuir*, **20** (1), 181–187.

168 Zhou, Z., Wang, S., Zhou, W., Wang, G., Jiang, L., Li, W., Song, S., Liu, J., Sun, G., and Xin, Q. (2003) Novel synthesis of highly active Pt/C cathode electrocatalyst for direct methanol fuel cell. *Chemical Communications*, (3), 394–395.

169 Bock, C., Paquet, C., Couillard, M., Botton, G.A., and MacDougall, B.R. (2004) Size-selected synthesis of PtRu nano-catalysts: reaction and size control mechanism. *Journal of the American Chemical Society*, **126** (25), 8028–8037.

170 Jiang, L., Zhou, Z., Li, W., Zhou, W., Song, S., Li, H., Sun, G., and Xin, Q. (2004) Effects of treatment in different atmosphere on Pt_3Sn/C electrocatalysts for ethanol electro-oxidation. *Energy & Fuels*, **18** (3), 866–871.

171 Li, H., Xin, Q., Li, W., Zhou, Z., Jiang, L., Yang, S., and Sun, G. (2004) An improved palladium-based DMFCs cathode catalyst. *Chemical Communications*, (23), 2776–2777.

172 Li, W., Liang, C., Qiu, J., Li, H., Zhou, W., Sun, G., and Xin, Q. (2004) Multi-walled carbon nanotubes supported Pt-Fe cathodic catalyst for direct methanol fuel cell. *Reaction Kinetics and Catalysis Letters*, **82** (2), 235–240.

173 Li, W., Zhou, W., Li, H., Zhou, Z., Zhou, B., Sun, G., and Xin, Q. (2004) Nano-structured Pt–Fe/C as cathode catalyst in direct methanol fuel cell. *Electrochimica Acta*, **49** (7), 1045–1055.

174 Xing, Y. (2004) Synthesis and electrochemical characterization of uniformly-dispersed high loading Pt nanoparticles on sonochemically-treated carbon nanotubes. *The Journal of Physical Chemistry B*, **108** (50), 19255–19259.

175 Li, W., Wang, X., Chen, Z., Waje, M., and Yan, Y. (2005) Carbon nanotube film by filtration as cathode catalyst support for proton-exchange membrane fuel cell. *Langmuir*, **21** (21), 9386–9389.

176 Chen, Z., Xu, L., Li, W., Waje, M., and Yan, Y. (2006) Polyaniline nanofibre supported platinum nanoelectrocatalysts for direct methanol fuel cells. *Nanotechnology*, **17** (20), 5254.

177 Li, W., Wang, X., Chen, Z., Waje, M., and Yan, Y. (2006) Pt-Ru supported on double-walled carbon nanotubes as high-performance anode catalysts for direct methanol fuel cells. *The Journal of Physical Chemistry B*, **110** (31), 15353–15358.

178 Knupp, S.L., Li, W., Paschos, O., Murray, T.M., Snyder, J., and Haldar, P. (2008) The effect of experimental parameters on the synthesis of carbon nanotube/nanofiber supported platinum by polyol processing techniques. *Carbon*, **46** (10), 1276–1284.

179 Avasarala, B., Murray, T., Li, W., and Haldar, P. (2009) Titanium nitride nanoparticles based electrocatalysts for proton exchange membrane fuel cells. *Journal of Materials Chemistry*, **19** (13), 1803–1805.

180 Sun, S. and Zeng, H. (2002) Size-controlled synthesis of magnetite nanoparticles. *Journal of the American Chemical Society*, **124** (28), 8204–8205.

181 Liu, Z., Ada, E.T., Shamsuzzoha, M., Thompson, G.B., and Nikles, D.E. (2006) Synthesis and activation of PtRu alloyed nanoparticles with controlled size and composition. *Chemistry of Materials*, **18** (20), 4946–4951.

182 Luo, J., Njoki, P.N., Lin, Y., Mott, D., and Wang, L.Y., and Zhong, C.-J. (2006) Characterization of carbon-supported AuPt nanoparticles for electrocatalytic methanol oxidation reaction. *Langmuir*, **22** (6), 2892–2898.

183 Yano, H., Kataoka, M., Yamashita, H., Uchida, H., and Watanabe, M. (2007) Oxygen reduction activity of carbon-supported Pt-M (M=V, Ni, Cr, Co, and Fe) alloys prepared by nanocapsule method. *Langmuir*, **23** (11), 6438–6445.

184 Li, W. and Haldar, P. (2009) Supportless PdFe nanorods as highly active electrocatalyst for proton exchange membrane fuel cell. *Electrochemistry Communications*, **11** (6), 1195–1198.

185 Li, W., Chen, Z., Xu, L., and Yan, Y. (2010) A solution-phase synthesis method to highly active Pt-Co/C electrocatalysts for proton exchange membrane fuel cell. *Journal of Power Sources*, **195** (9), 2534–2540.

186 Zhang, Z., More, K.L., Sun, K., Wu, Z., and Li, W. (2011) Preparation and characterization of PdFe nanoleaves as electrocatalysts for oxygen reduction reaction. *Chemistry of Materials*, **23** (6), 1570–1577.

187 Zhang, Z., Xin, L., Sun, K., and Li, W. (2011) Pd–Ni electrocatalysts for efficient ethanol oxidation reaction in alkaline electrolyte. *International Journal of Hydrogen Energy*, **36** (20), 12686–12697.

188 Zhang, Z., Li, M., Wu, Z., and Li, W. (2011) Ultra-thin PtFe-nanowires as durable electrocatalysts for fuel cells. *Nanotechnology*, **22** (1), 015602.

189 Shinoda, K. and Friberg, S. (1975) Microemulsions: colloidal aspects. *Advances in Colloid and Interface Science*, **4** (4), 281–300.

190 Bommarius, A.S., Holzwarth, J.F., Wang, D.I.C., and Hatton, T.A. (1990) Coalescence and solubilizate exchange in a cationic four-component reversed micellar system. *The Journal of Physical Chemistry*, **94** (18), 7232–7239.

191 Wang, J., Ee, L.S., Ng, S.C., Chew, C.H., and Gan, L.M. (1997) Reduced crystallization temperature in a microemulsion-derived zirconia precursor. *Materials Letters*, **30** (1), 119–124.

192 Wu, M.-L., Chen, D.-H., and Huang, T.-C. (2001) Preparation of Au/Pt bimetallic nanoparticles in water-in-oil microemulsions. *Chemistry of Materials*, **13** (2), 599–606.

193 Liu, Z., Lee, J.Y., Han, M., Chen, W., and Gan, L.M. (2002) Synthesis and characterization of PtRu/C catalysts from microemulsions and emulsions. *Journal of Materials Chemistry*, **12** (8), 2453–2458.

194 Zhang, X. and Chan, K.-Y. (2002) Water-in-oil microemulsion synthesis of platinum–ruthenium nanoparticles, their characterization and electrocatalytic properties. *Chemistry of Materials*, **15** (2), 451–459.

195 Rojas, S., García-García, F.J., Järas, S., Martínez-Huerta, M.V., Fierro, J.L.G., and Boutonnet, M. (2005) Preparation of carbon supported Pt and PtRu nanoparticles from microemulsion: electrocatalysts for fuel cell applications. *Applied Catalysis A: General*, **285** (1–2), 24–35.

196 Xiong, L. and Manthiram, A. (2005) Catalytic activity of Pt–Ru alloys synthesized by a microemulsion method in direct methanol fuel cells. *Solid State Ionics*, **176** (3–4), 385–392.

197 Lei, H., Atanassova, P., Sun, Y., and Blizanac, B. (2009) State-of-the-art electrocatalysts for direct methanol fuel cells, in *Electrocatalysis of Direct Methanol Fuel Cells:From Fundamentals to Applications* (eds. H. Liu and J. Zhang), Wiley-VCH Verlag GmbH, Weinheim, pp. 197–226.

198 Shao-Horn, Y., Ferreira, P., and la O, G.J. (2006) Instability of Pt/C electrocatalysts in proton exchange membrane fuel cells: a mechanistic investigation. *ECS Meeting Abstracts*, **503** (2), 200.

199 Iijima, S. (1991) Helical microtubules of graphitic carbon. *Nature*, **354** (6348), 56–58.

200 Che, G., Lakshmi, B.B., Fisher, E.R., and Martin, C.R. (1998) Carbon nanotubule membranes for electrochemical energy storage and production. *Nature*, **393** (6683), 346–349.

201 Britto, P.J., Santhanam, K.S.V., Rubio, A., Alonso, J.A., and Ajayan, P.M. (1999) Improved charge transfer at carbon nanotube electrodes. *Advanced Materials*, **11** (2), 154–157.

202 Li, W., Liang, C., Zhou, W., Qiu, J., Zhenhua, Sun, G., and Xin, Q. (2003) Preparation and characterization of multiwalled carbon nanotube-supported platinum for cathode catalysts of direct methanol fuel cells. *The Journal of Physical Chemistry B*, **107** (26), 6292–6299.

203 Rajesh, B., Ravindranathan Thampi, K., Bonard, J.M., Xanthopoulos, N., Mathieu, H.J., and Viswanathan, B. (2003) Carbon nanotubes generated from template carbonization of polyphenyl acetylene as the support for electrooxidation of methanol. *The Journal of Physical Chemistry B*, **107** (12), 2701–2708.

204 Sun, X., Li, R., Villers, D., Dodelet, J.P., and Désilets, S. (2003) Composite electrodes made of Pt nanoparticles

deposited on carbon nanotubes grown on fuel cell backings. *Chemical Physics Letters*, **379** (1–2), 99–104.

205 Wang, C., Waje, M., Wang, X., Tang, J.M., Haddon, R.C., and Yushan (2003) Proton exchange membrane fuel cells with carbon nanotube based electrodes. *Nano Letters*, **4** (2), 345–348.

206 Li, L. and Xing, Y. (2007) Pt–Ru nanoparticles supported on carbon nanotubes as methanol fuel cell catalysts. *The Journal of Physical Chemistry C*, **111** (6), 2803–2808.

207 Wang, X., Li, W., Chen, Z., Waje, M., and Yan, Y. (2006) Durability investigation of carbon nanotube as catalyst support for proton exchange membrane fuel cell. *Journal of Power Sources*, **158** (1), 154–159.

208 Bessel, C.A., Laubernds, K., Rodriguez, N.M., and Baker, R.T.K. (2001) Graphite nanofibers as an electrode for fuel cell applications. *Journal of Physical Chemistry B*, **105** (6), 1115–1118.

209 Serp, P., Corrias, M., and Kalck, P. (2003) Carbon nanotubes and nanofibers in catalysis. *Applied Catalysis A: General*, **253** (2), 337–358.

210 Guo, J., Sun, G., Wang, Q., Wang, G., Zhou, Z., Tang, S., Jiang, L., Zhou, B., and Xin, Q. (2006) Carbon nanofibers supported Pt–Ru electrocatalysts for direct methanol fuel cells. *Carbon*, **44** (1), 152–157.

211 Lee, K., Zhang, J., Wang, H., and Wilkinson, D.P. (2006) Progress in the synthesis of carbon nanotube- and nanofiber-supported Pt electrocatalysts for PEM fuel cell catalysis. *Journal of Applied Electrochemistry*, **36** (5), 507–522.

212 Hsin, Y.L., Hwang, K.C., and Yeh, C.-T. (2007) Poly(vinylpyrrolidone)-modified graphite carbon nanofibers as promising supports for PtRu catalysts in direct methanol fuel cells. *Journal of the American Chemical Society*, **129** (32), 9999–10010.

213 Chai, G.S., Yoon, S.B., Yu, J.-S., Choi, J.-H., and Sung, Y.-E. (2004) Ordered porous carbons with tunable pore sizes as catalyst supports in direct methanol fuel cell. *The Journal of Physical Chemistry B*, **108** (22), 7074–7079.

214 Lee, J., Yoon, S., Hyeon, T., Oh, S.M., and Bum Kim, K. (1999) Synthesis of a new mesoporous carbon and its application to electrochemical double-layer capacitors. *Chemical Communications*, (21), 2177–2178.

215 Ryoo, R., Joo, S.H., and Jun, S. (1999) Synthesis of highly ordered carbon molecular sieves via template-mediated structural transformation. *The Journal of Physical Chemistry B*, **103** (37), 7743–7746.

216 Lu, A.H. and Schüth, F. (2006) Nanocasting: a versatile strategy for creating nanostructured porous materials. *Advanced Materials*, **18** (14), 1793–1805.

217 Liang, C., Hong, K., Guiochon, G.A., Mays, J.W., and Dai, S. (2004) Synthesis of a large-scale highly ordered porous carbon film by self-assembly of block copolymers. *Angewandte Chemie: International Edition*, **43** (43), 5785–5789.

218 Meng, Y., Gu, D., Zhang, F., Shi, Y., Yang, H., Li, Z., Yu, C., Tu, B., and Zhao, D. (2005) Ordered mesoporous polymers and homologous carbon frameworks: amphiphilic surfactant templating and direct transformation. *Angewandte Chemie*, **117** (43), 7215–7221.

219 Tanaka, S., Nishiyama, N., Egashira, Y., and Ueyama, K. (2005) Synthesis of ordered mesoporous carbons with channel structure from an organic–organic nanocomposite. *Chemical Communications*, (16), 2125–2127.

220 Kim, H.-T., You, D.J., Yoon, H.-K., Joo, S.H., Pak, C., Chang, H., and Song, I.-S. (2008) Cathode catalyst layer using supported Pt catalyst on ordered mesoporous carbon for direct methanol fuel cell. *Journal of Power Sources*, **180** (2), 724–732.

221 Novoselov, K.S., Geim, A.K., Morozov, S.V., Jiang, D., Zhang, Y., Dubonos, S.V., Grigorieva, I.V., and Firsov, A.A. (2004) Electric field effect in atomically thin carbon films. *Science*, **306** (5696), 666–669.

222 Geim, A.K. and Novoselov, K.S. (2007) The rise of graphene. *Nature Materials*, **6** (3), 183–191.

223 Guo, S., Dong, S., and Wang, E. (2009) Three-dimensional Pt-on-Pd bimetallic nanodendrites supported on graphene nanosheet: facile synthesis and used as an advanced nanoelectrocatalyst for methanol oxidation. *ACS Nano*, **4** (1), 547–555.

224 Kou, R., Shao, Y., Wang, D., Engelhard, M. H., Kwak, J.H., Wang, J., Viswanathan, V. V., Wang, C., Lin, Y., Wang, Y., Aksay, I. A., and Liu, J. (2009) Enhanced activity and stability of Pt catalysts on functionalized graphene sheets for electrocatalytic oxygen reduction. *Electrochemistry Communications*, **11** (5), 954–957.

225 Li, Y., Tang, L., and Li, J. (2009) Preparation and electrochemical performance for methanol oxidation of Pt/graphene nanocomposites. *Electrochemistry Communications*, **11** (4), 846–849.

226 Seger, B. and Kamat, P.V. (2009) Electrocatalytically active graphene–platinum nanocomposites: role of 2-D carbon support in PEM fuel cells. *The Journal of Physical Chemistry C*, **113** (19), 7990–7995.

227 Yoo, E., Okata, T., Akita, T., Kohyama, M., Nakamura, J., and Honma, I. (2009) Enhanced electrocatalytic activity of Pt subnanoclusters on graphene nanosheet surface. *Nano Letters*, **9** (6), 2255–2259.

228 Zhang, Z.Y., Xin, L., and Li, W. (2012) Electrocatalytic oxidation of glycerol on Pt/C in anion-exchange membrane fuel cell: cogeneration of electricity and valuable chemicals. *Applied Catalysis B: Environmental*, **119**, 40–48.

229 Xin, L., Zhang, Z.Y., Qi, J., Chadderdon, D., and Li, W.Z. (2012) Electrocatalytic oxidation of ethylene glycol (EG) on supported Pt and Au catalysts in alkaline media: reaction pathway investigation in three-electrode cell and fuel cell reactors. *Applied Catalysis B: Environmental*, **125**, 85–94.

230 Zhang, Z.Y., Xin, L., and Li, W. (2012) Supported gold nanoparticles as anode catalyst for anion-exchange membrane-direct glycerol fuel cell (AEM-DGFC). *International Journal of Hydrogen Energy*, **37** (11), 9393–9401.

231 Xin, L., Zhang, Z.Y., Wang, Z.C., and Li, W.Z. (2012) Simultaneous generation of mesoxalic acid and electricity from glycerol on a gold anode catalyst in anion-exchange membrane fuel cells. *ChemCatChem*, **4** (8), 1105–1114.

232 Zhang, Z.Y., Xin, L., Qi, J., Chadderdon, D.J., Sun, K., Warsko, K.M., and Li, W.Z. (2014) Selective electro-oxidation of glycerol to tartronate or mesoxalate on Au nanoparticle catalyst via electrode potential tuning in anion-exchange membrane electro-catalytic flow reactor. *Applied Catalysis B: Environmental*, **147**, 871–878.

233 Qi, J., Xin, L., Chadderdon, D.J., Qiu, Y., Jiang, Y., Benipal, N., Liang, C.H., and Li, W.Z. (2014) Electrocatalytic selective oxidation of glycerol to tartronate on Au/C anode catalysts in anion exchange membrane fuel cells with electricity cogeneration. *Applied Catalysis B: Environmental*, **154**, 360–368.

5
Membranes for Direct Methanol Fuel Cells

Bradley P. Ladewig, Benjamin M. Asquith, and Jochen Meier-Haack

5.1
Introduction

This chapter reviews the current state of the art in membranes for direct methanol fuel cells (DMFCs), with a particular focus on research developments (as opposed to commercial products, of which there are few). The focus is exclusively on membranes; however, given the tight integration that is necessary between membranes and the adjacent fuel/oxidant distribution layers, catalysts, and support materials, there is some mention of these materials as they must necessarily be compatible with the selected membrane. Given the difficulty in finding reliable cost data for most of the membrane materials, a review of the cost-effectiveness of the membranes is not attempted, although for similar cation exchange membranes at least a cursory attempt at cost-effectiveness can be derived from the cost of the membrane precursors and solvents used in the synthesis [1].

5.2
Basic Principles of Direct Methanol Fuel Cell Operation

Direct methanol fuel cells are a class of polymer electrolyte membrane (PEM) fuel cells that typically employ a cation exchange membrane to separate the anode and cathode compartments. To illustrate the basic principles of DMFC operations, we shall take a typical, liquid-feed cell with a cation exchange membrane (alkaline exchange membranes are an alternative, and these are discussed later in this chapter). This is depicted in Figure 5.1.

The feed to the cell is methanol in water. The concentration of this solution may vary over quite a significant range. Highly concentrated feeds are preferred to minimize the amount of water that must be carried with the system (most proposed DMFC applications are mobile systems and hence smaller, lightweight overall systems are preferred), and provide a higher concentration of the reactant at the anode electrocatalyst. However, there are significant drawbacks of using

Materials for Low-Temperature Fuel Cells, First Edition. Edited by Bradley Ladewig, San P. Jiang, and Yushan Yan.

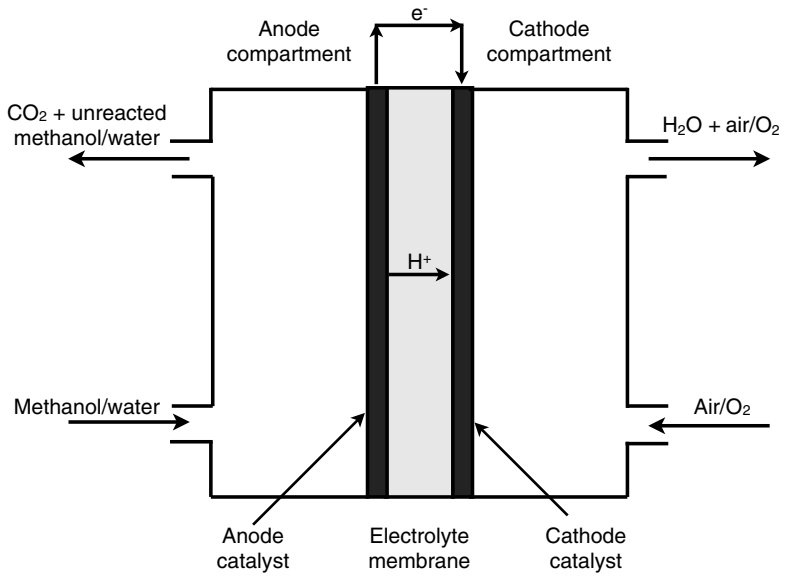

Figure 5.1 Schematic of a single cell DMFC.

concentrated anode feed solutions, most notably the increased methanol transport through the membrane, which results from the higher concentration gradient driving force. This is called "methanol crossover" and is one of the top challenges to be addressed in DMFC research.

The methanol reacts at the anode to form carbon dioxide, protons, and electrons. The protons are transported through the membrane to the cathode, while the electrons are collected by the current collector and pass through an external circuit, where they do useful work. At the cathode, the electrons recombine with the protons and oxygen to produce water, which must be removed from the cathode.

5.3 Membranes for Direct Methanol Fuel Cells

As outlined in the previous section, the performance requirements for DMFC membranes are superficially quite straightforward. The membrane should possess high proton conductivity, while being essentially completely resistant to electron conduction. At the same time, it should have minimal methanol permeability, which owing to the similarity between methanol and water molecules, often implies that the membrane also has low water permeability. Both of these should apply at the desired operational temperature of the fuel cell, and given the poor electrode kinetics at lower temperatures, it is often desirable to operate DMFCs at higher temperatures around 100 °C.

These two characteristics alone are sufficient to identify promising candidate materials for DMFC operation; however, as has been highlighted by numerous authors [2–4], there are many more characteristics such as chemical and thermal stability, processability, cost, environmental impact, ability to be formed into MEAs, and so on that impact on the selection of a suitable membrane material.

5.3.1 Perfluorosulfonic Acid Membranes

The most well-known and well-studied membrane materials for DMFCs are perfluorosulfonic acid membranes, such as Nafion (shown in Figure 5.2). These macromolecules combine two different functionalities in a single macromolecule: first, the hydrophobic nature, which impacts the high chemical and thermal stability, and second, the hydrophilic sulfonic acid regions, which are responsible for the water update and ion exchange capability. In the presence of water, these membranes phase separate into hydrophobic and hydrophilic domains [5], and a significant body of work has been conducted into characterizing the phase-separated microstructure of perfluorosulfonic acid membranes. A detailed discussion is beyond the scope of this chapter, but the interested reader should consult the excellent review by Mauritz and Moore [6].

Perfluorosulfonic acid membranes have several key characteristics that make them very suitable for DMFCs, including (i) their excellent chemical stability (owing to the perfluorinated backbone of the molecule), which makes them resistant to degradation in both oxidative and reductive environments, and (ii) their high proton conductivity, which may be as high as $0.2\,S\,cm^{-1}$ [7]. However, at elevated temperatures, especially beyond around 90 °C, the performance of perfluorosulfonic acid membranes falls away due to (i) dehydration of the membrane, which reduces the available charge carriers and hence the proton conductivity, (ii) loss of mechanical strength as the polymer softens, and (iii) crossover of gaseous species, which is primarily a problem in hydrogen PEM fuel cells but is also undesirable in DMFCs where oxygen and nitrogen at the cathode may permeate through to the anode.

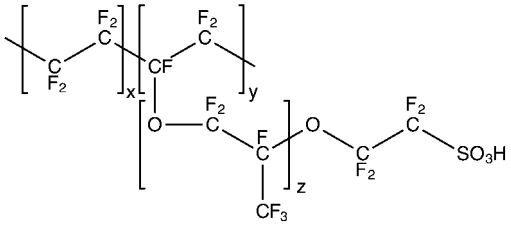

Figure 5.2 Chemical structure of Nafion.

A number of companies have produced commercial perfluorosulfonic acid membranes, with trade names including Nafion, Flemion, Aciplex, Aquivion, and Fumion [8]. However, since methanol readily transports across these membranes, the efficiency of DMFCs operating with these membranes is rather low, as the methanol reacts at the cathode to produce carbon dioxide and water (reducing the coulombic efficiency of the cell). It is, therefore, important to modify the properties of these membranes to suppress as much as possible the methanol crossover.

An enormous range of modifications have been explored, and a full review of these is beyond the scope of this chapter. Some of the more successful ones have included the incorporation of functionalized inorganic nanoparticles [2,3].

5.3.2
Poly(styrene)-Based Electrolytes

Among the styrene-based electrolytes, there are various different classes that have been considered as potential DMFC membranes. In all cases, the membranes contain sulfonic acid moieties (as shown in Figure 5.3), as in pefluorsulfonic acid membranes, although the pK_a of the sulfonic acid groups are not as highly acidic as in perfluorosulfonic acid membranes, where the highly electronegative fluorine molecules lead to a highly charged SO_3^- group. In any case, random copolymers (where the distribution of sulfonic acid groups throughout the polymer chain is randomly distributed depending on the proportions of the reactants) have been investigated, including sulfonated poly(styrene) [9–12], and random copolymers of poly(styrene) and poly(styrene sulfonic acid) [13,14]. Sulfonated poly(styrene) can be easily synthesized by copolymerizing styrene-based monomers with sulfonated styrene-based monomers or by postsulfonation of poly(styrenes) by straightforward sulfonation reactions. The postsulfonation route is most common, and in this approach, the ion exchange capacity and hence conductivity of the membrane can be tailored by controlling the reaction conditions (typically concentration of the sulfonating agent, reaction time, and temperature).

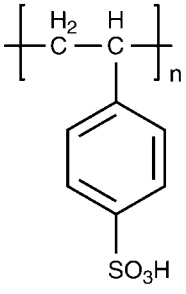

Figure 5.3 Repeat unit of sulfonated poly(styrene).

5.3.3
Poly(arylene ether)-Type Polymers

This group of DMFC membrane materials includes poly(arylene ether ether ketones) and poly(arylene ether sulfones). They are good candidates for DMFC membranes because of their excellent chemical stability in oxidizing and reducing environments and the ability to tailor the ionic conductivity by controlling the proportion of sulfonated units in the polymer. Just as with poly(styrene)-based membranes, the sulfonation may be achieved by direct copolymerization of sulfonated (or a mixture of sulfonated and nonsulfonated) monomers or by postpolymerization modification through an electrophilic aromatic sulfonation. This postpolymerization approach, while straightforward, leads to materials with varying properties since it is impossible to achieve tight control of the degree of sulfonation and the precise location of the sulfonated sites [15]. Indeed, at high degrees of sulfonation, the polymer will usually degrade or become highly susceptible to swelling/dissolution in water (Figure 5.4).

5.3.4
Poly(ether ether) Ketone-Type Polymers

Poly(ether ether) ketone (PEEK) and poly(ether ether ketone ketone) (PEEKK) are highly stable polymers with good potential for application in DMFCs [10,17,18]. They are semicrystalline and display excellent chemical and thermal stability. They may be sulfonated through direct polymerization of sulfonated monomers or by postsulfonation, the latter again leading to materials with less tightly controlled degree and location of sulfonation, but with the attraction that it is a simple and low-cost approach [19].

Sulfonated PEEK (referred to as SPEEK and depicted in Figure 5.5) has been investigated extensively for its potential application in DMFCs, in particular when made into composite membranes containing other components such as functionalized nanoparticles. Several excellent reviews have covered this topic [20].

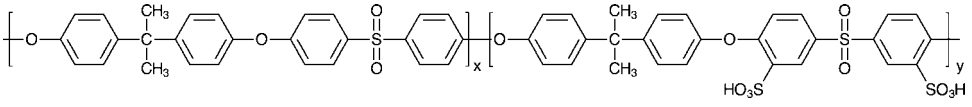

Figure 5.4 Disulfonated poly(arylene ether sulfone) copolymer synthesized using a direct copolymerization technique [16].

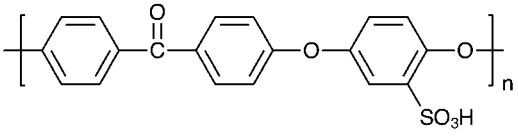

Figure 5.5 Repeat unit of SPEEK.

5.3.5
Polybenzimidazoles

Polybenzimidazoles (PBIs, with a typical structure shown in Figure 5.6) have received considerable interest in the DMFC membrane community because of their stability and proton conductivity at temperatures higher than most other polymer systems can tolerate. This is partly due to the fact that PBI-based membranes are themselves basic ($pK_a \sim 5.5$), and are rendered proton conductive by soaking them in an acid such as phosphoric acid, whereby they form a single-phase polymer with good chemical stability and proton conductivity. The fact that they do not require hydration to become conductive, as, for example, perfluorosulfonic acid-type membranes do, means they can be deployed at temperatures of 100–200 °C. This is particularly attractive from a chemical kinetic perspective, since the anode and cathode kinetics are greatly enhanced at these elevated temperatures. The drawback however is that such elevated temperatures are not appropriate for many of the portable applications toward which DMFCs are targeted (e.g., replacement of lithium batteries in electronic devices). Various PBI and PBI composite membranes have been proposed or tested in high-temperature PEM and DMFC systems [21–31].

5.3.6
Polysulfones and Polyethersulfones

Polysulfone (PSU) (typical structure shown in Figure 5.7) and polyethersulfone (PES) (typical structure shown in Figure 5.8) are highly versatile engineering polymers that have been applied in a variety of applications, including gas separation, membrane filtration, pervaporation, and electrodialysis. They have excellent chemical and mechanical stability, a relatively high glass transition temperature, and are easily cast as films from common aprotic solvents such as 1-methyl-2-pyrrolidone (NMP) [32] and *N,N*-dimethylacetamide (DMAc) [33]. PSU has most commonly been evaluated for DMFCs as a blend with other

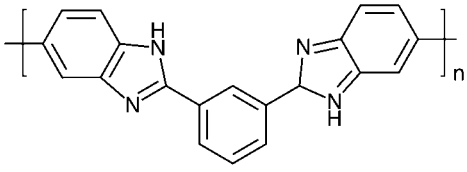

Figure 5.6 Polybenzimidazole.

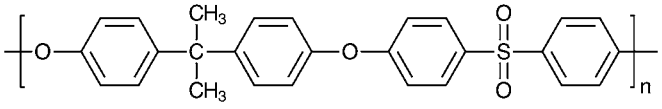

Figure 5.7 Repeat unit of poly(sulfone).

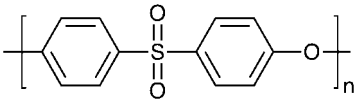

Figure 5.8 Repeat unit of poly(ether sulfone).

polymers or inorganic components [34–41], and despite most PSU composite membranes displaying lower proton conductivity than Nafion, the DMFC performance, at least with low feed concentrations, is often superior to that of Nafion-based DMFCs due to the reduced methanol crossover [42].

5.3.7
Polyimides

Polyimides are another class of polymer that have been extensively researched for DMFC applications due to their high chemical and thermal stability [43–50]. Specifically, the six-membered rings are more stable than five-membered rings due to decreased ring strain.

5.3.8
Grafted Polymer Electrolyte Membranes

Grafting is an interesting approach to preparing conductive membranes for DMFCs, because instead of using chemical functionalization approaches as described in the previous section, a hydrophobic nonconductive polymer is exposed to a radiation source, which causes the formation of radicals and functional groups, to which other functional groups can be grafted and polymerized, such as styrene or styrene sulfonic acid monomers.

Utilizing this approach, Pall company has produced commercial membranes called IonClad®, which are composed of poly(styrene sulfonic acid) grafted onto a perfluorinated polymer backbone. Tricoli *et al.* evaluated two of these membranes (IonClad R-1010 and R-4010) for their potential in DMFCs, and found that although their conductivity was approximately the same as Nafion 117 over the range of 20–60 °C, they had only a quarter of the methanol permeability of Nafion, making them good candidates for application in DMFCs [51].

5.3.9
Block Copolymers

Block copolymers are an attractive approach to the preparation of DMFC membranes, because their highly controlled polymer architecture means that the ionic and nonionic domains can be on the same polymer backbone in a defined sequence. Furthermore, through careful control of the block lengths, the microphase separation can also be controlled to a certain extent. Kim *et al.* prepared partially sulfonated polystyrene-block-poly(ethylene-ran-

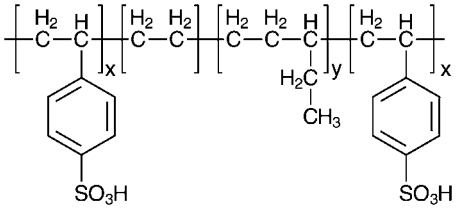

Figure 5.9 SSEBS repeat unit [53].

butylene)-block-polystyrene (SSEBS) copolymers and evaluated their proton conductivity and methanol permeability (Figure 5.9). They were able to achieve proton conductivities similar to Nafion 117 at 34 mol% sulfonation, where the methanol uptake of the block copolymer was approximately half that of Nafion 117. The lower methanol uptake was attributed to a more well-defined microstructure (which is characteristic of block copolymers) compared with Nafion, as determined by small-angle X-ray scattering [52].

5.3.10
Composite Polymer Membranes

As already pointed out in Section 5.3.1, it is often difficult to achieve the required membrane properties using a polymer material alone, and so an enormous amount of effort has been devoted in recent years to enhancing or changing the properties of polymer membranes by making them into composite materials.

Specifically, in DMFC-focused research, this has often focused on the premise that incorporating filler materials, such as inorganic nanoparticles, will hinder the passage of methanol through the membrane, reducing the methanol crossover. Obviously, such an approach also relies on the proton conductivity not being concurrently hindered, or at least not to the same extent; however, this is not always the case. Many membrane materials have been reported that show a significant reduction in methanol permeability, and yet also display at least some reduction in proton conductivity. Some notable exceptions are those materials in which the inorganic filler material is itself proton conductive or has surface acid groups, and hence play the dual role of hindering bulk molecular transport (i.e., water and methanol diffusion) while contributing additional proton transport sites [2].

A full review of the entire suite of composite membranes is well beyond the scope of this chapter; however, interested readers may consult the review of Neburchilov *et al.* [8].

5.4
Membrane Properties Summary

Table 5.1 summarizes a *selection* of DMFC membranes from the literature, classified by general membrane type. The first entries relate to Nafion 115 and 117

Table 5.1 Summary of membrane proton conductivity and methanol permeability performance data.

Membrane material	Proton conductivity (mS cm^{-1})	Methanol permeability ($cm^2 s^{-1}$) $\times 10^6$	Reference
Nafion			
Nafion 117	100	1.76	[51]
Nafion 117	75	0.9	[54]
Nafion 117	67	1.98	[55]
Nafion 115	90	1.04	[56]
Nafion composites			
Nafion/functionalized silica nanocomposite	6.9	0.358	[2]
Nafion/montmorillonite nanocomposite	78	0.1	[57]
Nano-silica-layered Nafion composite	77	0.92	[58]
Nafion/poly(vinyl alcohol) blend	20	0.65	[59]
Nafion/ORMOSILS composite	19	1.75	[60]
Other polymer systems			
Sulfonated poly(styrene)	50	0.52	[12]
Sulfonated poly(ether ether ketone)	70	0.3	[10]
Sulfonated poly(arylene ether) copolymer	100	0.81	[61]
Copolyimide membranes BAPS-50	40	0.33	[62]
Copolyimide membranes BAPS-60	50	0.45	[62]
Sulfonated polyphosphazene	35	0.13	[54]
Phosphonated polyphosphazene	55	0.14	[54]
Sulfonated poly(styrene-*b*-ethylene-*r*-butadiene-*b*-styrene) block copolymer	45	2.6	[52]
Sulfonated polysulfone	5	0.06	[56]
Sulfonated polybenzimidazole doped	0.001	2.5	[63]
Sulfonated polyimide	120	0.57	[11]
Sulfonated polystyrene and sulfonated poly(2,6-dimethyl-1,4-phenylene oxide) blend	34	2.35	[9]
Sulfonated poly(ether ether ketone ketone)	40	0.575	[64]
Sulfonated poly(ethersulfone)-Cardo	4	0.210	[65]
Poly(vinylidene fluoride-hexafluoropropylene) copolymer/Nafion blend	2	0.2	[66]
Cross-linked poly(vinyl alcohol)/poly (2-acrylamido-2-methyl-1-propanesulfonic	90	0.6	[67]
Sulfonated poly(styrene)/poly (tetrafluoroethylene) composite	110	0.67	[68]

Adapted from Ref. [4].

and serve as baseline results with which many of the others may be compared. It must be noted that the apparatus and method used to determine proton conductivity and methanol permeability vary somewhat between different groups, and so absolute comparisons are difficult to make with any validity based on this

tabulated data alone. The purpose of this table is simply to summarize, in a concise manner, a snapshot of the current state of the art in DMFC membrane properties.

5.5 Conclusions

In conclusion, a broad range of membranes for direct methanol fuel cells have been summarized from the perspective of the chemical structure of the polymer material. While a significant number of materials have been shown in some respects to surpass the performance of Nafion, there still remain the need for critical materials research in the area of DMFC membranes. Specifically, membrane materials that do not rely on hydration to be highly proton conductive need to be developed – this is considered to be the only truly viable means by which to achieve membranes that do not suffer from unacceptable levels of methanol crossover. These materials need to be stable and nonswelling in water/methanol solutions, and electrochemically stable under the operating conditions of a working DMFC.

References

1 Yee, R.S.L., Rozendal, R.A., Zhang, K., and Ladewig, B.P. (2012) Cost effective cation exchange membranes: a review. *Chemical Engineering Research and Design*, **90** (7), 950–959.

2 Ladewig, B.P., Knott, R.B., Hill, A.J., Riches, J.D., White, J.W., Martin, D.J., Da Costa, J.C.D., and Lu, G.Q. (2007) Physical and electrochemical characterization of nanocomposite membranes of nafion and functionalized silicon oxide. *Chemistry of Materials*, **19** (9), 2372–2381.

3 Ladewig, B.P., Knott, R.B., Martin, D.J., Diniz da Costa, J.C., and Lu, G.Q. (2007) Nafion-MPMDMS nanocomposite membranes with low methanol permeability. *Electrochemistry Communications*, **9** (4), 781–786.

4 Lufrano, F., Baglio, V., Staiti, P., Antonucci, V., and Arico, A.S. (2013) Performance analysis of polymer electrolyte membranes for direct methanol fuel cells. *Journal of Power Sources*, **243**, 519–534.

5 Kreuer, K.D. (2001) On the development of proton conducting polymer membranes for hydrogen and methanol fuel cells. *Journal of Membrane Science*, **185** (1), 29–39.

6 Mauritz, K.A. and Moore, R.B. (2004) State of understanding of Nafion. *Chemical Reviews*, **104** (10), 4535–4585.

7 Savadogo, O. (1998) Emerging membranes for electrochemical systems: (I) solid polymer electrolyte membranes for fuel cell systems. *Journal of New Materials for Electrochemical Systems*, **1** (1), 47–66.

8 Neburchilov, V., Martin, J., Wang, H., and Zhang, J. (2007) A review of polymer electrolyte membranes for direct methanol fuel cells. *Journal of Power Sources*, **169** (2), 221–238.

9 Jung, B., Kim, B., and Yang, J.M. (2004) Transport of methanol and protons through partially sulfonated polymer blend membranes for direct methanol fuel cell. *Journal of Membrane Science*, **245** (1–2), 61–69.

10 Gil, M., Ji, X., Li, X., Na, H., Hampsey, J. E., and Lu, Y. (2004) Direct synthesis of sulfonated aromatic poly(ether ether ketone) proton exchange membranes for fuel cell applications. *Journal of Membrane Science*, **234** (1–2), 75–81.

11 Yin, Y., Fanga, J., Cui, Y., Tanaka, K., Kita, H., and Okamoto, K.I. (2003) Synthesis, proton conductivity and methanol permeability of a novel sulfonated polyimide from 3-(2′,4′-diaminophenoxy) propane sulfonic acid. *Polymer*, **44** (16), 4509–4518.

12 Carretta, N., Tricoli, V., and Picchioni, F. (2000) Ionomeric membranes based on partially sulfonated poly(styrene): synthesis, proton conduction and methanol permeation. *Journal of Membrane Science*, **166** (2), 189–197.

13 Bae, B. and Kim, D. (2003) Sulfonated polystyrene grafted polypropylene composite electrolyte membranes for direct methanol fuel cells. *Journal of Membrane Science*, **220** (1–2), 75–87.

14 Jung, D.H., Myoung, Y.B., Cho, S.Y., Shin, D.R., and Peck, D.H. (2001) A performance evaluation of direct methanol fuel cell using impregnated tetraethyl-orthosilicate in cross-linked polymer membrane. *International Journal of Hydrogen Energy*, **26** (12), 1263–1269.

15 Miyatake, K. and Hay, A.S. (2001) Synthesis and properties of poly(arylene ether)s bearing sulfonic acid groups on pendant phenyl rings. *Journal of Polymer Science, Part A: Polymer Chemistry*, **39** (19), 3211–3217.

16 Harrison, W.L., Hickner, M.A., Kim, Y.S., and McGrath, J.E. (2005) Poly(arylene ether sulfone) copolymers and related systems from disulfonated monomer building blocks: synthesis, characterization, and performance – a topical review. *Fuel Cells*, **5** (2), 201–212.

17 Li, L., Zhang, J., and Wang, Y. (2003) Sulfonated poly(ether ether ketone) membranes for direct methanol fuel cell. *Journal of Membrane Science*, **226** (1–2), 159–167.

18 Kobayashi, T., Rikukawa, M., Sanui, K., and Ogata, N. (1998) Proton-conducting polymers derived from poly(ether-etherketone) and poly(4-phenoxybenzoyl-1,4-phenylene). *Solid State Ionics*, **106** (3–4), 219–225.

19 Yee, R.S.L., Zhang, K., and Ladewig, B.P. (2013) The effects of sulfonated poly (ether ether ketone) ion exchange preparation conditions on membrane properties. *Membranes*, **3** (3), 182–195.

20 Liu, B., Robertson, G.P., Guiver, M.D., Sun, Y.M., Liu, Y.L., Lai, J.Y., Mikhailenko, S., and Kaliaguine, S. (2006) Sulfonated poly(aryl ether ether ketone ketone)s containing fluorinated moieties as proton exchange membrane materials. *Journal of Polymer Science, Part B: Polymer Physics*, **44** (16), 2299–2310.

21 Diaz, L.A., Abuin, G.C., and Corti, H.R. (2012) Methanol sorption and permeability in Nafion and acid-doped PBI and ABPBI membranes. *Journal of Membrane Science*, **411–412**, 35–44.

22 Haghighi, A.H., Hasani-Sadrabadi, M.M., Dashtimoghadam, E., Bahlakeh, G., Shakeri, S.E., Majedi, F.S., Hojjati Emami, S., and Moaddel, H. (2011) Direct methanol fuel cell performance of sulfonated poly (2,6-dimethyl-1,4-phenylene oxide)-polybenzimidazole blend proton exchange membranes. *International Journal of Hydrogen Energy*, **36** (5), 3688–3696.

23 Ahmad, H., Kamarudin, S.K., Hasran, U. A., and Daud, W.R.W. (2011) A novel hybrid Nafion-PBI-ZP membrane for direct methanol fuel cells. *International Journal of Hydrogen Energy*, **36** (22), 14668–14677.

24 Yu, S. and Benicewicz, B.C. (2009) Synthesis and properties of functionalized polybenzimidazoles for high-temperature PEMFCs. *Macromolecules*, **42** (22), 8640–8648.

25 Oono, Y., Sounai, A., and Hori, M. (2009) Influence of the phosphoric acid-doping level in a polybenzimidazole membrane on the cell performance of high-temperature proton exchange membrane fuel cells. *Journal of Power Sources*, **189** (2), 943–949.

26 Pasupathi, S., Ji, S., Jan Bladergroen, B., and Linkov, V. (2008) High DMFC performance output using modified acid–base polymer blend. *International Journal of Hydrogen Energy*, **33** (12), 3132–3136.

27 Lobato, J., Cañizares, P., Rodrigo, M.A., Linares, J.J., and López-Vizcaíno, R. (2008) Performance of a vapor-fed polybenzimidazole (PBI)-based direct methanol fuel cell. *Energy and Fuels*, **22** (5), 3335–3345.

28 Wycisk, R., Chisholm, J., Lee, J., Lin, J., and Pintauro, P.N. (2006) Direct methanol fuel cell membranes from Nafion-polybenzimidazole blends. *Journal of Power Sources*, **163**, 9–17.

29 Wycisk, R., Lee, J.K., and Pintauro, P.N. (2005) Sulfonated polyphosphazene-polybenzimidazole membranes for DMFCs. *Journal of the Electrochemical Society*, **152** (5), A892–A898.

30 Silva, V.S., Ruffmann, B., Vetter, S., Mendes, A., Madeira, L.M., and Nunes, S. P. (2005) Characterization and application of composite membranes in DMFC. *Catalysis Today*, **104** (2–4), 205–212.

31 Li, Q., He, R., Jensen, J.O., and Bjerrum, N.J. (2003) Approaches and recent development of polymer electrolyte membranes for fuel cells operating above 100°C. *Chemistry of Materials*, **15** (26), 4896–4915.

32 Kim, J.H. and Lee, K.H. (1998) Effect of PEG additive on membrane formation by phase inversion. *Journal of Membrane Science*, **138** (2), 153–163.

33 Chakrabarty, B., Ghoshal, A.K., and Purkait, M.K. (2008) Preparation, characterization and performance studies of polysulfone membranes using PVP as an additive. *Journal of Membrane Science*, **315** (1–2), 36–47.

34 Lufrano, F., Baglio, V., Di Blasi, O., Staiti, P., Antonucci, V., and Aricò, A.S. (2012) Solid polymer electrolyte based on sulfonated polysulfone membranes and acidic silica for direct methanol fuel cells. *Solid State Ionics*, **216**, 90–94.

35 Zhu, Y. and Manthiram, A. (2011) Synthesis and characterization of polysulfone-containing sulfonated side chains for direct methanol fuel cells. *Journal of Power Sources*, **196** (18), 7481–7487.

36 Lufrano, F., Baglio, V., Staiti, P., Stassi, A., Aric, A.S., and Antonucci, V. (2010) Investigation of sulfonated polysulfone membranes as electrolyte in a passive-mode direct methanol fuel cell mini-stack. *Journal of Power Sources*, **195** (23), 7727–7733.

37 Abu-Thabit, N.Y., Ali, S.A., and Javaid Zaidi, S.M. (2010) New highly phosphonated polysulfone membranes for PEM fuel cells. *Journal of Membrane Science*, **360** (1–2), 26–33.

38 Lufrano, F., Baglio, V., Staiti, P., Arico, A.S., and Antonucci, V. (2008) Polymer electrolytes based on sulfonated polysulfone for direct methanol fuel cells. *Journal of Power Sources*, **179** (1), 34–41.

39 Vernersson, T., Lafitte, B., Lindbergh, G., and Jannasch, P. (2006) A sulfophenylated polysulfone as the DMFC electrolyte membrane: an evaluation of methanol permeability and cell performance. *Fuel Cells*, **6** (5), 340–346.

40 Lufrano, F., Baglio, V., Staiti, P., Arico, A.S., and Antonucci, V. (2006) Development and characterization of sulfonated polysulfone membranes for direct methanol fuel cells. *Desalination*, **199** (1–3), 283–285.

41 Manea, C. and Mulder, M. (2002) Characterization of polymer blends of polyethersulfone/sulfonated polysulfone and polyethersulfone/sulfonated polyetheretherketone for direct methanol fuel cell applications. *Journal of Membrane Science*, **206** (1–2), 443–453.

42 Fu, Y.Z. and Manthiram, A. (2006) Synthesis and characterization of sulfonated polysulfone membranes for direct methanol fuel cells. *Journal of Power Sources*, **157** (1), 222–225.

43 Li, Y., Jin, R., Cui, Z., Wang, Z., Xing, W., Qiu, X., Ji, X., and Gao, L. (2007) Synthesis and characterization of novel sulfonated polyimides from 1,4-bis(4-aminophenoxy)-naphthyl-2,7-disulfonic acid. *Polymer*, **48** (8), 2280–2287.

44 Yin, Y., Yamada, O., Tanaka, K., and Okamoto, K.I. (2006) On the development of naphthalene-based sulfonated polyimide membranes for fuel cell applications. *Polymer Journal*, **38** (3), 197–219.

45 Meyer, G., Gebel, G., Gonon, L., Capron, P., Marscaq, D., Marestin, C., and Mercier, R. (2006) Degradation of sulfonated polyimide membranes in fuel

cell conditions. *Journal of Power Sources*, **157** (1), 293–301.

46 Yamada, O., Yin, Y., Tanaka, K., Kita, H., and Okamoto, K.I. (2005) Polymer electrolyte fuel cells based on main-chain-type sulfonated polyimides. *Electrochimica Acta*, **50** (13), 2655–2659.

47 Watari, T., Fang, J., Tanaka, K., Kita, H., Okamoto, K.I., and Hirano, T. (2004) Synthesis, water stability and proton conductivity of novel sulfonated polyimides from 4,4′-bis(4-aminophenoxy)biphenyl-3,3′-disulfonic acid. *Journal of Membrane Science*, **230** (1–2), 111–120.

48 Woo, Y., Oh, S.Y., Kang, Y.S., and Jung, B. (2003) Synthesis and characterization of sulfonated polyimide membranes for direct methanol fuel cell. *Journal of Membrane Science*, **220** (1–2), 31–45.

49 Guo, X., Fang, J., Watari, T., Tanaka, K., Kita, H., and Okamoto, K.I. (2002) Novel sulfonated polyimides as polyelectrolytes for fuel cell application: 2. Synthesis and proton conductivity of polyimides from 9,9-bis(4-aminophenyl)fluorene-2,7-disulfonic acid. *Macromolecules*, **35** (17), 6707–6713.

50 Fang, J., Guo, X., Harada, S., Watari, T., Tanaka, K., Kita, H., and Okamoto, K.I. (2002) Novel sulfonated polyimides as polyelectrolytes for fuel cell application: 1. Synthesis, proton conductivity, and water stability of polyimides from 4,4′-diaminodiphenyl ether-2,2′-disulfonic acid. *Macromolecules*, **35** (24), 9022–9028.

51 Tricoli, V., Carretta, N., and Bartolozzi, M. (2000) Comparative investigation of proton and methanol transport in fluorinated ionomeric membranes. *Journal of the Electrochemical Society*, **147** (4), 1286–1290.

52 Kim, J., Kim, B., and Jung, B. (2002) Proton conductivities and methanol permeabilities of membranes made from partially sulfonated polystyrene-block-poly(ethylene-ran-butylene)-block-polystyrene copolymers. *Journal of Membrane Science*, **207** (1), 129–137.

53 Ganguly, A. and Bhowmick, A.K. (2008) Sulfonated styrene-(ethylene-*co*-butylene)-styrene/montmorillonite clay nanocomposites: synthesis, morphology, and properties. *Nanoscale Research Letters*, **3** (1), 36–44.

54 Zhou, X., Weston, J., Chalkova, E., Hofmann, M.A., Ambler, C.M., Allcock, H.R., and Lvov, S.N. (2003) High temperature transport properties of polyphosphazene membranes for direct methanol fuel cells. *Electrochimica Acta*, **48**, 2173–2180.

55 Elabd, Y.A., Napadensky, E., Sloan, J.M., Crawford, D.M., and Walker, C.W. (2003) Triblock copolymer ionomer membranes: Part I. Methanol and proton transport. *Journal of Membrane Science*, **217** (1–2), 227–242.

56 Pedicini, R., Carbone, A., Saccà, A., Gatto, I., Di Marco, G., and Passalacqua, E. (2008) Sulphonated polysulphone membranes for medium temperature in polymer electrolyte fuel cells (PEFC). *Polymer Testing*, **27** (2), 248–259.

57 Song, M.K., Park, S.B., Kim, Y.T., Rhee, H.W., and Kim, J. (2003) Nanocomposite polymer membrane based on cation exchange polymer and nano-dispersed clay sheets. *Molecular Crystals and Liquid Crystals*, **407**, 15/[411]–423/[419].

58 Kim, D., Scibioh, M.A., Kwak, S., Oh, I.H., and Ha, H.Y. (2004) Nano-silica layered composite membranes prepared by PECVD for direct methanol fuel cells. *Electrochemistry Communications*, **6** (10), 1069–1074.

59 DeLuca, N.W. and Elabd, Y.A. (2006) Nafion/poly(vinyl alcohol) blends: effect of composition and annealing temperature on transport properties. *Journal of Membrane Science*, **282** (1–2), 217–224.

60 Kim, Y.J., Choi, W.C., Woo, S.I., and Hong, W.H. (2004) Proton conductivity and methanol permeation in Nafion^{TM}/ORMOSIL prepared with various organic silanes. *Journal of Membrane Science*, **238** (1–2), 213–222.

61 Kim, S.Y., Sumner, M.J., Harrison, W.L., Riffle, J.S., McGrath, J.E., and Pivovar, B.S. (2004) Direct methanol fuel cell performance of disulfonated poly(arylene ether benzonitrile) copolymers. *Journal of*

the Electrochemical Society, **151** (12), A2150–A2156.

62 Einsla, B.R., Yu, S.K., Hickner, M.A., Hong, Y.T., Hill, M.L., Pivovar, B.S., and McGrath, J.E. (2005) Sulfonated naphthalene dianhydride based polyimide copolymers for proton-exchange-membrane fuel cells: II. Membrane properties and fuel cell performance. *Journal of Membrane Science*, **255** (1–2), 141–148.

63 Pu, H., Liu, Q., and Liu, G. (2004) Methanol permeation and proton conductivity of acid-doped poly (*N*-ethylbenzimidazole) and poly (*N*-methylbenzimidazole). *Journal of Membrane Science*, **241** (2), 169–175.

64 Li, X., Zhao, C., Lu, H., Wang, Z., and Na, H. (2005) Direct synthesis of sulfonated poly(ether ether ketone ketone)s (SPEEKKs) proton exchange membranes for fuel cell application. *Polymer*, **46** (15), 5820–5827.

65 Li, L. and Wang, Y. (2005) Sulfonated polyethersulfone Cardo membranes for direct methanol fuel cell. *Journal of Membrane Science*, **246** (2), 167–172.

66 Cho, K.-Y., Eom, J.-Y., Jung, H.-Y., Choi, N.-S., Lee, Y.M., Park, J.-K., Choi, J.-H., Park, K.-W., and Sung, Y.-E. (2004) Characteristics of PVdF copolymer/Nafion blend membrane for direct methanol fuel cell (DMFC). *Electrochimica Acta*, **50** (2–3), 583–588.

67 Qiao, J., Hamaya, T., and Okada, T. (2005) New highly proton-conducting membrane poly(vinylpyrrolidone) (PVP) modified poly(vinyl alcohol)/2-acrylamido-2-methyl-1-propanesulfonic acid (PVA-PAMPS) for low temperature direct methanol fuel cells (DMFCs). *Polymer*, **46** (24), 10809–10816.

68 Shin, J.P., Chang, B.J., Kim, J.H., Lee, S.B., and Suh, D.H. (2005) Sulfonated polystyrene/PTFE composite membranes. *Journal of Membrane Science*, **251** (1–2), 247–254.

6
Hydroxide Exchange Membranes and Ionomers

Shuang Gu, Junhua Wang, Bingzi Zhang, Robert B. Kaspar, and Yushan Yan

6.1
Introduction

This chapter focuses on an important component of fuel cells: hydroxide-conducting polymer electrolytes (i.e., hydroxide exchange membranes (HEMs) and hydroxide exchange ionomers (HEIs)). It summarizes the property requirements and fabrications of such membranes and ionomers and also discusses the general structure–property relationship emphasizing contributions from the cationic functional group, polymer main chain, and chemical cross-linking. It is hoped that the establishment of the structure–property relationship can provide guidance to the future research directions, especially in the design and development of high-performance polymer electrolytes for fuel cells. Although the discussion through most of this chapter is specifically for fuel cells, it should be generally applicable to other devices such as electrolyzers, flow batteries, and solar hydrogen generators. In formulating this chapter, the literature cited covers up to the 2011, mostly from 2001 to 2011.

6.1.1
Definition

An HEM is a membrane-form polymer electrolyte capable of conducting hydroxide anions (OH^-), and an HEI is a binder-form polymer electrolyte capable of not only conducting hydroxide anions but also creating triple-phase boundary in the electrode catalyst layer. HEMs and HEIs are already used in hydroxide exchange membrane fuel cells (HEMFCs) and can also be used in many other electrochemical energy conservation and storage devices.

6.1.2
Functions

As ionic conductors, HEMs and HEIs substantially control the performance and durability of HEMFCs through their hydroxide conductivity and chemical/

Materials for Low-Temperature Fuel Cells, First Edition. Edited by Bradley Ladewig, San P. Jiang, and Yushan Yan.

physical stability. As supporting electrolytes, they facilitate electrode kinetics and enable the use of nonprecious metal catalysts.

6.1.3 Features

As with the conventional proton exchange membranes (PEMs) whose chief application is in proton exchange membrane fuel cells (PEMFCs), HEMs are thin-membrane polymer electrolytes, and thus HEMFCs can achieve high energy density and power density. The difference is in the conducting ion: HEMs conduct hydroxides; PEMs conduct protons.

HEMs are drastically different from hydroxide-conducting liquid alkaline solutions (e.g., aqueous KOH) whose performance in alkaline fuel cells (AFCs) is fundamentally limited by carbon dioxide contamination (e.g., from air) [1]. In alkaline solutions, metal cations are freely moving, whereas in HEMs, organic cations are immobilized in a polymer matrix by covalent bonds. This immobilization prevents the formation of carbonate precipitates, which is one of the major drawbacks of liquid-solution electrolytes in AFCs. Although hydroxide in HEMs can react with carbon dioxide to form carbonate anion (CO_3^{2-}) or bicarbonate anion (HCO_3^-) that lowers ionic conductivity, these counterions completely revert to hydroxide during fuel cell operation through a self-purging process [2]. In addition, there is no electrolyte leakage in HEMs simply because the electrolyte is a solid. As with liquid alkaline solutions, HEMs are known to be compatible with nonprecious metal catalysts [3,4], indicating that HEMs are promising next-generation fuel cell electrolytes.

6.2 Requirements

For high-performance HEMFC applications, HEMs and HEIs are required to have high hydroxide conductivity, excellent chemical stability, sufficient physical stability, controlled solubility, and other important properties.

6.2.1 High Hydroxide Conductivity

High hydroxide conductivity is the most crucial requirement for high-performance HEMs, as hydroxide conductivity directly dictates the membrane resistance at a given membrane thickness (typically 50 μm). A low membrane resistance is particularly important to mitigate resistance-induced cell voltage loss, especially at large current densities. HEMs usually have lower ionic (hydroxide) conductivity than PEMs, largely because hydroxides have intrinsically lower mobility than protons (20.50 versus $36.25 \times 10^{-4}\,cm^2\,V^{-1}\,S^{-1}$ at 25 °C) [5], even though

hydroxide has the highest ionic mobility among all known anions. In comparison with ~100 mS cm^{-1} of proton conductivity of a typical commercial PEM (Nafion 212, 50 μm) at 20 °C, ~50 mS cm^{-1} hydroxide conductivity would be expected for high-performance HEMs.

Besides increasing hydroxide conductivity, another strategy to lower resistance of the membrane is to reduce its thickness. HEMFCs can operate with even thinner membranes (e.g., 10/28 μm for Tokuyama Co.'s A901/A201 products [6]), largely because HEMFCs have, in principle, lower fuel (e.g., H_2) crossover than PEMFCs. In PEMFCs, ions flow from anode to cathode, in the same direction as fuel crossover; in HEMFCs, ions flow from cathode to anode, in the opposite direction. Even if its ionic conductivity is only half as high, an HEM that is half as thick as a PEM will hold the same membrane resistance.

6.2.2 Excellent Chemical Stability

Excellent chemical stability is another important requirement for high-performance HEMs, as it determines HEMs' durability and operating conditions (e.g., cell temperature). The chemical stability required here involves alkaline, thermal, and oxidative aspects. Alkaline chemical stability is particularly important because in HEMs, the hydroxide anion itself is a strong nucleophilic attacker and has been confirmed to be responsible for membrane degradation [7]. Sufficient thermal chemical stability is also required for durable HEMs as cell temperature is preferably elevated (e.g., up to 60–80 °C) for high-performance HEMFC operation [8]. At the same time, the presence of a strong oxidant (typically oxygen) and highly active catalysts in HEMFCs also requires HEMs to have enough oxidative chemical stability. From an engineering perspective, 5000 h of durability is generally expected for HEMFC applications.

6.2.3 Sufficient Physical Stability

In parallel with chemical stability, sufficient physical stability is also required for durable high-performance HEMs. Physical stability comprises dimensional and mechanical aspects. Dimensional stability is a measure of HEMs' resistance to size changes in each dimension during dry–wet cycling. Usually, dimensional stability is represented by the swelling ratio: a low swelling ratio means high dimensional stability, and vice versa. Sometimes, water uptake can also be used to describe the dimensional stability. High dimensional stability is required for durable HEMs because, in practice, HEMFCs are subjected to frequent on-off cycling. Also, HEMs require sufficient mechanical stability (or mechanical strength), for example, to be safely incorporated into a membrane–electrode assembly (MEA) in which high pressure is applied to tighten the interface between the membrane and the electrodes.

6.2.4
Controlled Solubility

High solvent resistance is important to increase HEMs' durability and lifetime, but specific solubility in low-boiling-point water-miscible solvents (e.g., lower alcohols, tetrahydrofuran, and acetone) is critical for HEIs' application and performance [8]. The low boiling point (<100 °C) ensures that the HEI's organic solvent will evaporate faster than water, and water miscibility guarantees that water can be used as a cosolvent in the HEI solution. Both of these requirements aim to prevent the catalyst from contacting the pure organic solvent, which would lead to severe safety issues and catalyst poisoning. In addition, good solubility enables the HEIs to create efficient triple-phase boundary to support the electrochemical reactions in HEMFC electrodes.

6.2.5
Other Important Properties

Low fuel crossover and low gas permeability are also important for high-performance HEMs. In fuel cells, when the fuel crosses over through the electrolyte from anode to cathode (or the oxidant permeates from cathode to anode), the cathode (or anode) potential is contaminated by fuel oxidation (or oxidant reduction), which lowers overall cell voltage. Additionally, HEMs must show low electrical conductivity to minimize internal short-circuiting that occurs when electrons pass directly through the membrane from anode to cathode without going through the external circuit.

6.3
Fabrications and Categories

In general, HEMs can be prepared by polymer functionalization, monomer polymerization, or membrane radiation-grafting methods. Other methods including chemical cross-linking or physical cross-linking (polymer blending, pore filling, and van der Waals interaction tuning technique) can also be applied to prepare reinforced HEMs.

6.3.1
Polymer Functionalization

Currently, polymer functionalization is the most frequently used method to prepare HEMs. A commercial or laboratory-made polymer serves as the starting material. In general, a haloalkylation (typically, chloromethylation [9]) or halogenation (e.g., bromination [10]) reaction is conducted to create haloalkyl groups in the starting polymer. Next, a cationic functional group (e.g., quaternary ammonium or quaternary phosphonium) is formed through a quaternization

reaction with the corresponding precursor (e.g., tertiary amine [9] or tertiary phosphine [8]). This preparation method is simple and reliable, as well as flexible: The polymer backbone and cationic functional groups can be chosen almost entirely independently, granting access to diverse HEMs with distinctive chemical structures. However, with direct functionalization, it can be difficult to control precisely the initial degree of haloalkylation (or halogenation) and in turn the degree of functionalization in the final membrane. The other drawback is that the functional sites in the polymer matrix are usually limited to those that are most reactive for the initial haloalkylation/halogenation step.

6.3.2 Monomer Polymerization

Monomer polymerization is an equally important method to prepare HEMs. The starting material is a monomer that contains either the final cationic functional group or its precursor. An HEM polymer is then synthesized directly by polymerizing the monomer, for example, through unsaturated bonds [11] or aromatic phenol groups [12]. Usually, the polymerization is achieved by a ring opening or nucleophilic condensation reaction. The greatest advantage of this method is its flexibility in designing chemical structures. Furthermore, the degree of functionalization can be controlled precisely in the polymerization step by tuning the ratio of monomers with functional groups (or the precursor) and monomers without. The drawback of this method is the complexity of synthesizing the monomeric starting material. In addition, the choice of functional groups is limited because some are incompatible with the polymerization reaction.

6.3.3 Membrane Radiation Grafting

Membrane radiation grafting is another method to prepare HEMs, which was especially used in the early stages of HEM research. The starting material is a nonfunctionalized membrane, mostly polymerized fluoroalkylene [13–15]. The membrane is radiated with gamma rays or electron beams [15] to create polymer radicals, and then haloalkyl-containing unsaturated monomer (predominantly, vinylbenzyl chloride) is linked to the polymer matrix via reaction with the radicals. Finally, the polymer is functionalized through the haloalkyl group in the grafted monomer, as in polymer functionalization. The most noticeable feature of this method is that it does not require a membrane formation step as the membrane is already the starting material; membrane thickness can also be easily tuned in advance. The main drawback of this method is the poor material stability as the polymerized fluoroaklylene is exclusively used as the polymer – this is required by the nature of the radiation methods – and C—F bonds are known to be prone to degradation in alkaline media [16]. Additionally, it is challenging to control the degree of grafting. Another concern for this method is the expected high gas permeability caused by radiation damage to the membrane.

6.3.4 Reinforcement Methods

Chemical cross-linking has been used extensively to prepare chemically reinforced HEMs with high dimensional stability and excellent solvent resistance. The structure and properties of chemical cross-linking are discussed in Section 6.6.

Physical methods such as polymer blending [17], pore filling [18], and van der Waals interaction tuning [19] have also been used to prepare physically reinforced HEMs. In polymer blending, a reinforcing material (usually a hydrophobic and nonionic polymer, for example, polysulfone) is blended with a polymer that contains cationic functional groups. In pore filling, a reinforcing porous membrane substrate is filled with functionalized polymer. In van der Waals interaction tuning, a high-electron-density polymer matrix is paired with a high-dipole-moment functional group (e.g., quaternary phosphonium) to enhance interactions among polymer chains, increasing the HEM's dimensional stability without compromising solubility.

6.4 Structure and Properties of Cationic Functional Group

The cationic functional group has been the central focus in HEM chemical structure because it dominates hydroxide conductivity through its basicity as well as its density (i.e., ion exchange capacity, IEC). The intrinsic nature of the functional group also determines solubility and controls chemical stability. Currently, two major types of cationic functional groups are available: one type based on nitrogen atoms and the other type based on phosphorus ones.

6.4.1 Quaternary Nitrogen-Based Cationic Functional Groups

There are nonconjugated (including tetraalkyl and cycloalkyl ammonium) and conjugated (including pyridinium, guanidinium, and imidazolium) types of quaternary nitrogen-based cationic functional groups (Table 6.1).

6.4.1.1 Tetraalkyl Ammonium

Tetraalkyl ammonium is the most frequently used cationic functional group in HEMs and anion exchange membranes (AEMs) [30]. As the simplest tetraalkyl ammonium structure, trimethyl benzyl quaternary ammonium is the most typical cationic functional group in HEM polymers, where the trimethyl groups serve as side groups and the benzyl group is usually from the polymer matrix. The quaternary nitrogen atom bears one unit of positive charge, which is electro-balanced by one unit of negative charge on hydroxide.

Table 6.1 Chemical structures of HEMs' cationic functional groups.

Category	Example	
Quaternary nitrogen	Tetraalky ammonium [13]	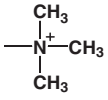
	Cycloalkyl ammonium [20–24]	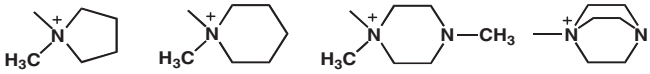
	Pyridinium [25]	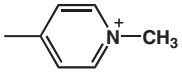
	Guanidinium [26,27]	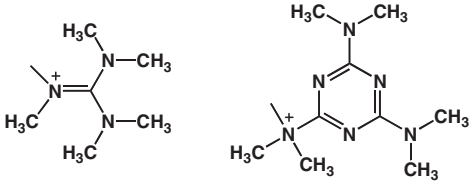
	Imidazolium [28,29]	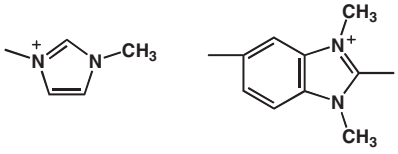
Quaternary phosphorus	Tris(2,4,6-trimethoxy phenyl) phosphonium [8]	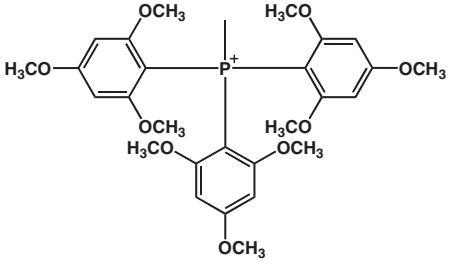

The biggest advantage of trimethyl-based cationic functional groups is that they are the most chemically stable tetraalkyl ammonium cations [7]. The introduction of even longer subgroups (e.g., ethyl or propyl) will lead to severe degradation through the well-known Hoffmann elimination mechanism where β-hydrogens are available. The basicity of trimethyl benzyl ammonium hydroxide has been found to be moderate in comparison with other cation hydroxides, leading to mild hydroxide conductivity at a given IEC. For example, the specific conductivity or the IEC-normalized hydroxide conductivity of trimethyl ammonium-functionalized polymer (19 mS g cm^{-1} mmol^{-1} [31]) is about half that of

Table 6.2 Specific solubility and specific conductivity of cationic functional group-based polymers.

Cationic functional group		Specific solubility[a)]	Specific conductivity[b)] (mS g mmol^{-1})
Quaternary nitrogen-based	Ammonium	N/A	19 [31]
	Pyridinium	N/A	0.1[c)] [33]
	Guanidinium	Lower alcohols	20[d)] [34]
	Imidazolium	Tetrahydrofuran (THF)	8.4 [32]
Quaternary phosphorus-based	Phosphonium	Lower alcohols	39 [5]

a) The solubility in low-boiling-point water-miscible organic solvents.
b) IEC-normalized hydroxide conductivity at room temperature from polysulfone backbone-based HEM without cross-linking.
c) Polystyrene as backbone.
d) Trifluoride poly(sulfone arylene ether sulfone) as backbone.

the quaternary phosphonium one (39 mS g cm^{-1} mmol^{-1} [5]) (Table 6.2), but about twice that of the imidazolium one (8.4 mS g cm^{-1} mmol^{-1} [32]) where they use the same polysulfone matrix and have the similar homogeneous membrane structure. The tetraalkyl ammonium cationic functional groups have been observed to have very limited specific solubility in low-boiling-point water-miscible solvents, preventing them from being used as a high-performance solubilized ionomer for electrode applications.

6.4.1.2 Cycloalkyl Ammonium

The cycloalkyl ammonium cationic group is another type of ammonium where one or more cycloalkyl (instead of linear alkyl) subgroups are linked to the nitrogen atom. Existing cycloalkyl ammonium cationic groups include bicyclo six-membered ring systems (diazabicyclo-based ammonium [20] and azabicyclo-based ammonium [21]), monocyclo six-membered ring systems (piperazine-based ammonium [22]) and monocyclo five-membered ring systems (pyrrolidine-based ammonium [23]).

Among all available cycloalkyl ammoniums, the most important one is a bicyclo six-membered ring system, 1,4-diazabicyclo-[2.2.2]-octane (DABCO)-constructed ammonium, because it has been found to have even higher chemical stability than the traditional trimethyl benzyl ammonium [7]. Some cycloalkyl ammoniums (e.g., diazabicyclo- and piperazine-based ammoniums) have two nitrogen atoms that can be quaternized to ammonium, so that it is possible to perform chemical cross-linking by reacting with two haloalkyl groups from different polymer chains [35]. Generally speaking, the solubility and basicity of cycloalkyl ammonium hydroxides are similar to those of tetraalkyl ammonium ones. With the exception of DABCO-based ammonium, cycloalkyl ammoniums are questionable for HEM applications as some have shown much lower chemical stability than trimethyl benzyl ammonium.

6.4.1.3 Pyridinium

As the simplest conjugated cationic system, pyridinium was one of the first functional groups in both HEMs [25] and AEMs. Methyl pyridinium is the simplest conjugated cationic functional group used in HEMs. Pyridinium hydroxide is confirmed to be much less chemically stable than trimethyl benzyl ammonium hydroxide, limiting its use as a functional group for HEM applications. During degradation, pyridinium loses its positive charge through either a nucleophilic ring opening or nucleophilic addition–elimination mechanism [36]. The solubility of pyridinium hydroxide is similar to that of trimethyl benzyl ammonium, whereas the basicity of pyridinium hydroxide is considered much lower than that of trimethyl benzyl ammonium according to the very low hydroxide conductivity its HEMs offer even at high IEC (0.54 mS cm^{-1} hydroxide conductivity with 6.05 mmol g^{-1} theoretical IEC, or ~0.1 mS g cm^{-1} $mmol^{-1}$ specific conductivity [33]) (Table 6.2).

6.4.1.4 Guanidinium

Guanidinium is the second conjugated cationic functional group used in HEMs [26], the simplest form being pentamethyl benzyl guanidinium. Guanidinium-based HEMs show good solubility in lower alcohols [26]. Lower alcohols are water miscible and have low boiling points; so, as discussed in Section 6.2.4, guanidinium-functionalized polymers theoretically can be used as an ionomer in the electrodes. Guanidinium also offers flexibility in designing chemical structures as it has five customizable subgroups. Pentamethyl benzyl guanidinium hydroxide has been shown to be quite similar in basicity to trimethyl benzyl ammonium hydroxide, since their HEMs have very close specific conductivities (20 [34] versus 19 mS g cm^{-1} $mmol^{-1}$ [31] for guanidinium versus ammonium) (Table 6.2). In general, the chemical stability of guanidinium hydroxide has been found to be lower than that of trimethyl benzyl ammonium hydroxide.

6.4.1.5 Imidazolium

Imidazolium is another conjugated cationic functional group [28,37], with methyl benzyl imidazolium as the simplest example. Imidazolium-functionalized HEMs show good solubility in tetrahydrofuran [28], another low-boiling-point water-miscible solvent, and at the same time they are insoluble in alcohols (which are important fuels for HEMFCs). This particularly selective solubility not only makes imidazolium-functionalized polymers possible to use as ionomers but also allows alcohols to be used as fuels directly in HEMFC applications. The basicity of methyl benzyl imidazolium hydroxide is around half that of trimethyl benzyl ammonium hydroxide (specific conductivity: 8.4 [32] versus 19 mS g cm^{-1} $mmol^{-1}$ [31]) (Table 6.2). Generally, imidazolium systems are believed to be less chemically stable than ammonium ones due to a ring-opening degradation mechanism driven by the active hydrogen in the ring between the two nitrogen atoms [38].

6.4.2 Quaternary Phosphorus-Based Cationic Functional Groups

HEM functional groups are not limited to nitrogen atoms. A unique quaternary phosphonium system based on tris(2,4,6-trimethoxyphenyl) benzyl phosphonium has also been demonstrated [5,8,19,39]. While ordinary aliphatic or aromatic quaternary phosphonium hydroxides have very poor chemical stability, tris (2,4,6-trimethoxyphenyl) benzyl phosphonium hydroxide has been found to be very stable, largely because of the substantial charge decentralization offered by its nine strongly electron-donating methoxyl subgroups [5,8]. The chemical stability of tris(2,4,6-trimethoxyphenyl) benzyl phosphonium-functionalized HEMs has been shown to be much higher than that of trimethyl benzyl ammonium ones (e.g., the phosphonium can sustain much higher concentration of strong alkaline solution: 10 versus 2 M in a KOH solution treatment test for 2 days) [5].

Phosphonium HEMs were the first to be found to be soluble in low-boiling-point water-miscible solvents (e.g., lower alcohols) [8], which is necessary for ionomer applications. Phosphonium-based ionomers have been demonstrated to drastically improve cell performance in HEMFCs (3.5 times increase in peak power density) [8].

Tris(2,4,6-trimethoxyphenyl) benzyl phosphonium hydroxide shows the highest basicity ever reported. Its HEM has the highest specific hydroxide conductivity among all reported cationic functional group-based HEMs, typically about twice that of trimethyl benzyl ammonium and more than four times that of methyl imidazolium (39 [5], 19 [31], and 8.4 $mS\,g\,cm^{-1}\,mmol^{-1}$ [32] respectively, with the same polysulfone polymer matrix and homogeneous membrane structure in each case) (Table 6.2).

Tris(2,4,6-trimethoxyphenyl) benzyl phosphonium hydroxide functional group also has a greater dipole moment (3.07 D) than all other cationic hydroxides (1.32–2.20 D) [19]. This strong dipole moment is particularly important in achieving high dimensional stability through polarizing polymer chains, especially when combined with a high-electron-density polymer matrix (e.g., PPO) [19].

The disadvantage of such a phosphonium system may be that it has a high molecular weight, limiting the IEC to a moderate level.

6.5 Structure and Properties of Polymer Main Chain

The polymer matrix is the backbone of HEMs, and its chemical and physical structure profoundly impacts their properties.

6.5.1 Chemical Structure

The polymer matrices used in HEMs can be divided by chemical structure into two major categories: aromatic main-chain polymers and aliphatic main-chain

polymers (Table 6.3). Generally speaking, aromatic main-chain polymers are mechanically strong, chemically stable, and show very low gas/fuel permeability; whereas aliphatic main-chain polymers are more flexible, and their ability to reach ultrahigh molecular weights enables higher dimensional stability.

Table 6.3 Chemical structures of HEMs' polymer matrices.

Category	Example	
Aromatic main chain	Poly(aryl ether sulfones) [9,12,34,40–49]	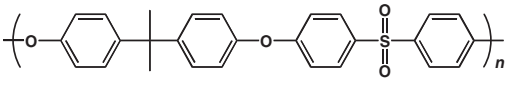
		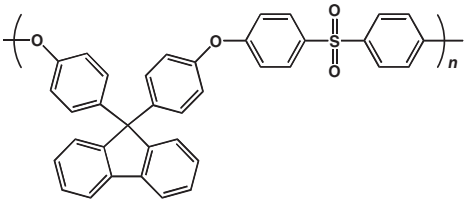
	Poly(aryl ether ketones) [50–52]	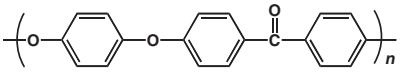
		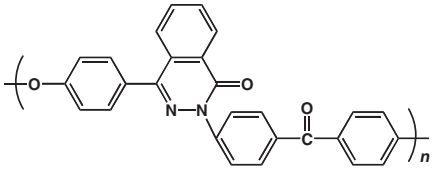
	Poly(aryl ethers) [10,53]	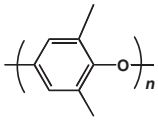
		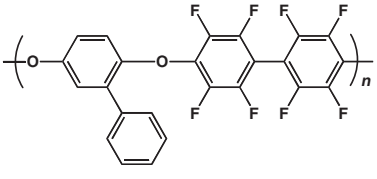

(*continued*)

Table 6.3 (*Continued*)

Category	Example	
	Poly(phenylenes) [54]	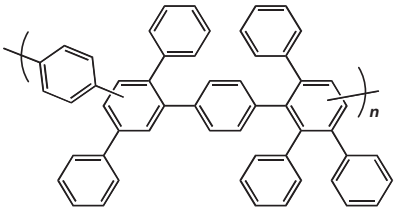
	Poly(aryl benzimidazoles) [29,55]	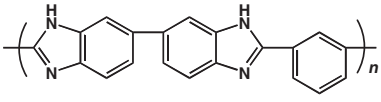
		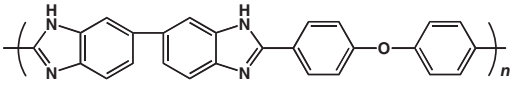
	Poly(aryl imides) [56]	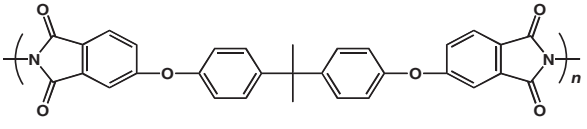
Aliphatic main chain	Benzene ring-containing [25,37,57–61]	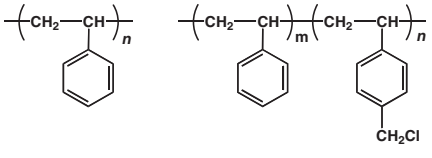
		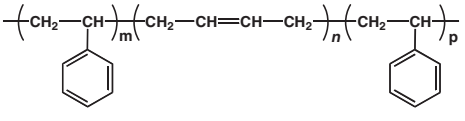
	Benzene ring-free [11,13–15,20,21,62–71]	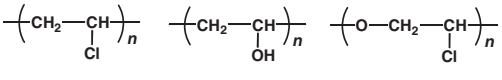
		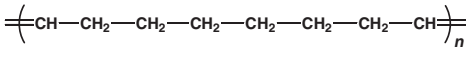
		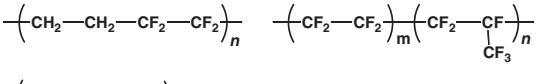
		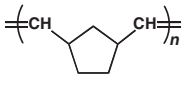

6.5.1.1 Aromatic Main-Chain Polymers

The aromatic main-chain polymer family includes poly(aryl ether sulfones), poly (aryl ether ketones), poly(aryl ethers), poly(phenylenes), poly(aryl benzimidazoles), and poly(aryl imides).

Belonging to the class of high-performance engineering polymers, poly(aryl ether sulfones) and poly(aryl ether ketones) are the two most frequently used polymer matrices in HEMs. They have high thermal stability, excellent chemical stability, outstanding mechanical strength, and good solubility in many organic solvents (necessary for chemical modification). Poly(aryl ethers) are similar to poly(aryl ether sulfones) and poly(aryl ether ketones), but they usually have higher electron density benzene rings owing to strong electron donation from more ether bonds, which offers better dimensional stability for their HEMs especially when a functional group with a large dipole moment (e.g., tris(2,4,6-trimethoxyphenyl benzyl quaternary phosphonium) is used [19]. On the other hand, their oxidative chemical stability is expected to decrease because of the activated benzene rings, and sometimes their solubility is also lowered due to the strong interaction among polymer chains.

By contrast, poly(phenylenes) are stable to chemical oxidation owing to their inactive benzene rings. However, they have poor flexibility because of the inherent rigidness of all-benzene ring architectures. Poly(aryl benzimidazoles) and poly(aryl imides) have also been used as polymer matrices in HEMs. Their biggest issue is poor chemical stability, because the benzimidazole and imide groups have been confirmed to hydrolyze irreversibly in alkaline media under certain conditions. Besides, poly(aryl benzimidazoles) also have very limited solubility in common solvents, rendering chemical modification difficult.

6.5.1.2 Aliphatic Main-Chain Polymers

The aromatic main-chain polymer family consists of benzene ring-containing aliphatic main-chain polymers and the benzene ring-free aliphatic main-chain polymers. Benzene ring-containing aliphatic polymers usually contain phenyl ethylene segments often derived from styrene. Compared with benzene ring-free polymers, benzene ring-containing aliphatic polymers offer higher thermal stability and greater mechanical strength, and the rings provide more options for chemical structure design. However, the active α-hydrogen in the phenyl ethylene segment is usually the weakest link in these HEMs, being especially sensitive to oxidation or substitution reactions, either of which leads to chemical degradation.

Benzene ring-free aliphatic polymers are more flexible and can reach much higher polymer molecular weight (helpful for increasing dimensional stability at a given IEC) than their benzene ring-containing counterparts. However, completely aliphatic structures yield poor mechanical strength and low thermal stability, and the large free volume in these membranes is expected to cause high gas/fuel permeability. Without careful design, attaching a cation to an aliphatic polymer may result in β-hydrogens on the main chain, which can cause severe degradation through chemical elimination mechanisms [72].

6.5.2 Sequential Structure

The polymer matrix can be sequenced in two ways: randomly or in blocks. A random polymer is made up of (the same or different) repeating units that occur in a completely random way. By contrast, a block polymer chain consists of different segments (or blocks), where each segment is composed of the same repeating unit and the segment adjacent to it is composed of a different repeating unit. In most cases, each type of block varies in hydrophilicity or hydrophobicity. Random polymers are more commonly used in HEMs. The random connection of repeating unit delivers a simple, homogeneous, and dense membrane.

Block polymers offer control over HEMs' microphase segregation [73], which if optimized properly can help increase ionic conductivity and decrease water uptake [74]. However, the block architecture sometimes brings challenging incompatibility problems among blocks in HEMs, potentially causing increased gas/fuel permeability and/or lowered mechanical strength. This incompatibility can be controlled to some extent by changing the lengths of blocks: increasing block length leads to deeper phase segregation but also more incompatibility, and vice versa [75]. Thus, there should be an optimal block length for a given block polymer system. The number of types of blocks (two for diblock, three for triblock, and so on) is another characteristic of block polymers. Using more types will bring more incompatibility problems, but at the same time it may also allow tuning interactions among different types of blocks.

6.6 Structure and Properties of Chemical Cross-Linking

Chemical cross-linking has been the most powerful method to prepare chemically reinforced HEMs with improved dimensional stability and solvent resistance. The chemical and physical structure of the linkage heavily impacts the properties and performance of cross-linked HEMs.

6.6.1 Chemical Structure

There are two types of chemical cross-linking linkages: benzene ring-based linkages and non-benzene ring-based linkages (Table 6.4). Aromatic linkages usually offer high mechanical strength and thermal stability owing to the robustness of benzene rings. They are compatible with aromatic polymer matrices and also show high chemical stability, especially when no β-hydrogens are present. On the other hand, the inclusion of benzene rings inevitably raises the molecular weight and size and decreases flexibility, which leads to lowered cross-linking

Table 6.4 Chemical structures of HEMs' chemical cross-linkages.

Category	Example	
Benzene ring-based linkage	Double-connection [37,55,66]	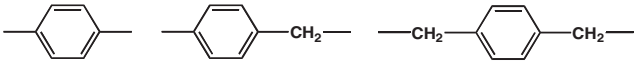
	Multiconnection [27,76]	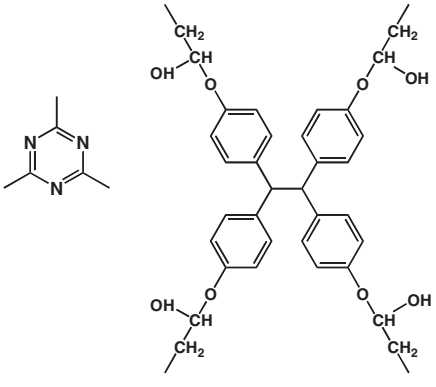
Non-benzene ring-based linkage	Carbon-based [10,35,39,48,49,77–81]	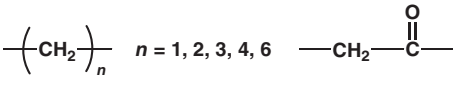
	Nitrogen-based [64,82]	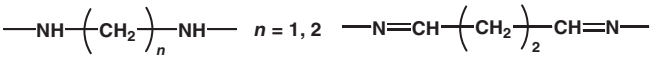
	Oxygen-based [65,67,83,84]	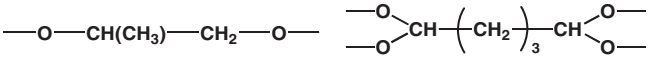
	Sulfur-based [21,85,86]	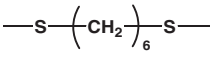
	Silicon-based [59,87–90]	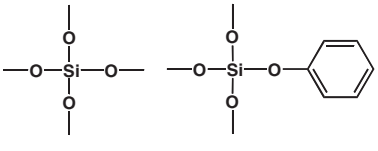

reactivity and decreased controllability. The rigidness of the introduced benzene rings may also cause the membrane's flexibility to decrease.

On the other hand, benzene ring-free linkages provide good flexibility, especially with a long cross-linking chain. Aliphatic linkages do not compromise IEC because they introduce relatively little additional molecular weight, and at the

same time the flexibility of aliphatic structures provides high cross-linking reactivity.

6.6.2 Physical Structure

Physical linkage structure impacts the properties and performance of cross-linked HEMs through the length, connection, and density of the linkage.

Long linkages usually bring good membrane flexibility but also lower materials compatibility, especially when the cross-linker and polymer chain are dissimilar in chemical structure. Short linkages provide better compatibility, as well as improved chemical stability by increasing the steric barrier to attack. For example, self-cross-linked HEMs with the shortest possible linkage, a single methylene, showed improved chemical and thermal stability [39,82].

The connection of linkage refers to the number of connections per linkage and the position of the linkage in polymer chain. Simple double-connection linkages, as well as multiconnection linkages such as triple- and quadruple-connection linkages, are possible. Double-connection linkages can be achieved by more accessible chemistry, but multiconnection linkages have an more powerful impact on HEMs' dimensional stability.

Within the polymer chain, the linkage may connect either to the polymer backbone or to the cationic functional group. Connecting directly to the functional group may improve chemical stability by protecting the cation, but, on the other hand, it will also restrict the cationic functional group's movement, hindering desirable microphase segregation and decreasing hydroxide conductivity.

Linkage density is an important parameter to practically tune the properties of cross-linked HEMs. At a given IEC, increasing linkage density translates directly to improved dimensional stability and mechanical strength, but it also reduces water uptake, thereby potentially lowering the hydroxide conductivity.

6.7 Prospective

HEMs will be a central research topic in the field of HEMFCs because their properties fundamentally impact HEMFCs' performance and durability. Designing/exploring cationic functional groups with higher basicity and stability is still of primary importance since they are the bottleneck for the entire HEMFC system. In addition, developing/deploying better chemical and physical cross-linking methods will be another critical direction especially for improving dimensional stability.

References

1 McLean, G.F., Niet, T., Prince-Richard, S., and Djilali, N. (2002) *International Journal of Hydrogen Energy*, **27**, 507–526.
2 Adams, L.A., Poynton, S.D., Tamain, C., Slade, R.C.T., and Varcoe, J.R. (2008) *ChemSusChem*, **1**, 79–81.
3 Varcoe, J.R., Slade, R.C.T., Wright, G.L., and Chen, Y.L. (2006) *Journal of Physical Chemistry B*, **110**, 21041–21049.
4 Lu, S.F., Pan, J., Huang, A.B., Zhuang, L., and Lu, J.T. (2008) *Proceedings of the National Academy of Sciences of the United States of America*, **105**, 20611–20614.
5 Gu, S., Cai, R., Luo, T., Jensen, K., Contreras, C., and Yan, Y.S. (2010) *ChemSusChem*, **3**, 555–558.
6 Yanagi, H. and Fukuta, K. (2008) *ECS Transactions*, **16**, 257–262.
7 Bauer, B., Strathmann, H., and Effenberger, F. (1990) *Desalination*, **79**, 125–144.
8 Gu, S., Cai, R., Luo, T., Chen, Z.W., Sun, M.W., Liu, Y., He, G.H., and Yan, Y.S. (2009) *Angewandte Chemie: International Edition*, **48**, 6499–6502.
9 Li, L. and Wang, Y.X. (2005) *Journal of Membrane Science*, **262**, 1–4.
10 Wu, L., Xu, T.W., Wu, D., and Zheng, X. (2008) *Journal of Membrane Science*, **310**, 577–585.
11 Clark, T.J., Robertson, N.J., Kostalik, H.A., Lobkovsky, E.B., Mutolo, P.F., Abruna, H. D., and Coates, G.W. (2009) *Journal of the American Chemical Society*, **131**, 12888–12889.
12 Zhou, J.F., Unlu, M., Vega, J.A., and Kohl, P.A. (2009) *Journal of Power Sources*, **190**, 285–292.
13 Danks, T.N., Slade, R.C.T., and Varcoe, J. R. (2002) *Journal of Materials Chemistry*, **12**, 3371–3373.
14 Herman, H., Slade, R.C.T., and Varcoe, J.R. (2003) *Journal of Membrane Science*, **218**, 147–163.
15 Varcoe, J.R. and Slade, R.C.T. (2006) *Electrochemistry Communications*, **8**, 839–843.
16 Schulze, A. and Gulzow, E. (2004) *Journal of Power Sources*, **127**, 252–263.
17 Wang, X., Li, M.Q., Golding, B.T., Sadeghi, M., Cao, Y.C., Yu, E.H., and Scott, K. (2011) *International Journal of Hydrogen Energy*, **36**, 10022–10026.
18 Jung, H.M., Fujii, K., Tamaki, T., Ohashi, H., Ito, T., and Yamaguchi, T. (2011) *Journal of Membrane Science*, **373**, 107–111.
19 Gu, S., Skovgard, J., and Yan, Y.S. (2012) *ChemSusChem*, **5**, 843–848.
20 Agel, E., Bouet, J., and Fauvarque, J.F. (2001) *Journal of Power Sources*, **101**, 267–274.
21 Stoica, D., Ogier, L., Akrour, L., Alloin, F., and Fauvarque, J.F. (2007) *Electrochimica Acta*, **53**, 1596–1603.
22 Jung, M.S.J., Arges, C.G., and Ramani, V. (2011) *Journal of Materials Chemistry*, **21**, 6158–6160.
23 Valade, D., Boschet, F., Roualdes, S., and Ameduri, B. (2009) *Journal of Polymer Science Part A: Polymer Chemistry*, **47**, 2043–2058.
24 Faraj, M., Elia, E., Boccia, M., Filpi, A., Pucci, A., and Ciardelli, F. (2011) *Journal of Polymer Science Part A: Polymer Chemistry*, **49**, 3437–3447.
25 Huang, A.B., Xiao, C.B., and Zhuang, L. (2005) *Journal of Applied Polymer Science*, **96**, 2146–2153.
26 Wang, J.H., Li, S.H., and Zhang, S.B. (2010) *Macromolecules*, **43**, 3890–3896.
27 Cao, Y.C., Wang, X., Mamlouk, M., and Scott, K. (2011) *Journal of Materials Chemistry*, **21**, 12910–12916.
28 Guo, M.L., Fang, J., Xu, H.K., Li, W., Lu, X.H., Lan, C.H., and Li, K.Y. (2010) *Journal of Membrane Science*, **362**, 97–104.
29 Thomas, O.D., Soo, K.J.W.Y., Peckham, T.J., Kulkarni, M.P., and Holdcroft, S. (2011) *Polymer Chemistry*, **2**, 1641–1643.
30 Juda, W. and Mcrae, W.A. (1950) *Journal of the American Chemical Society*, **72**, 1043–1044.
31 Pan, J., Lu, S.F., Li, Y., Huang, A.B., Zhuang, L., and Lu, J.T. (2010) *Advanced Functional Materials*, **20**, 312–319.
32 Zhang, F.X., Zhang, H.M., and Qu, C. (2011) *Journal of Materials Chemistry*, **21**, 12744–12752.

33 Matsuoka, K., Chiba, S., Iriyama, Y., Abe, T., Matsuoka, M., Kikuchi, K., and Ogumi, Z. (2008) *Thin Solid Films*, **516**, 3309–3313.

34 Kim, D.S., Labouriau, A., Guiver, M.D., and Kim, Y.S. (2011) *Chemistry of Materials*, **23**, 3795–3797.

35 Schmitt, F., Granet, R., Sarrazin, C., Mackenzie, G., and Krausz, P. (2011) *Carbohydrate Polymers*, **86**, 362–366.

36 Neagu, V., Bunia, I., and Plesca, I. (2000) *Polymer Degradation and Stability*, **70**, 463–468.

37 Lin, B.C., Qiu, L.H., Lu, J.M., and Yan, F. (2010) *Chemistry of Materials*, **22**, 6718–6725.

38 Ye, Y.S. and Elabd, Y.A. (2011) *Macromolecules*, **44**, 8494–8503.

39 Gu, S., Cai, R., and Yan, Y.S. (2011) *Chemical Communications*, **47**, 2856–2858.

40 Fang, J. and Shen, P.K. (2006) *Journal of Membrane Science*, **285**, 317–322.

41 Hibbs, M.R., Hickner, M.A., Alam, T.M., McIntyre, S.K., Fujimoto, C.H., and Cornelius, C.J. (2008) *Chemistry of Materials*, **20**, 2566–2573.

42 Wang, J.H., Zhao, Z., Gong, F.X., Li, S.H., and Zhang, S.B. (2009) *Macromolecules*, **42**, 8711–8717.

43 Tanaka, M., Koike, M., Miyatake, K., and Watanabe, M. (2010) *Macromolecules*, **43**, 2657–2659.

44 Yan, J.L. and Hickner, M.A. (2010) *Macromolecules*, **43**, 2349–2356.

45 Zhang, Q.A., Zhang, Q.F., Wang, J.H., Zhang, S.B., and Li, S.H. (2010) *Polymer*, **51**, 5407–5416.

46 Lee, K.M., Wycisk, R., Litt, M., and Pintauro, P.N. (2011) *Journal of Membrane Science*, **383**, 254–261.

47 Lin, B.C., Qiu, L.H., Qiu, B., Peng, Y., and Yan, F. (2011) *Macromolecules*, **44**, 9642–9649.

48 Park, J.S., Park, S.H., Yim, S.D., Yoon, Y.G., Lee, W.Y., and Kim, C.S. (2008) *Journal of Power Sources*, **178**, 620–626.

49 Ni, J., Zhao, C.J., Zhang, G., Zhang, Y., Wang, J., Ma, W.J., Liu, Z.G., and Na, H. (2011) *Chemical Communications*, **47**, 8943–8945.

50 Zhang, H.W. and Zhou, Z.T. (2008) *Journal of Applied Polymer Science*, **110**, 1756–1762.

51 Xiong, Y., Liu, Q.L., and Zeng, Q.H. (2009) *Journal of Power Sources*, **193**, 541–546.

52 Yan, X.M., He, G.H., Gu, S., Wu, X.M., Du, L.G., and Zhang, H.Y. (2011) *Journal of Membrane Science*, **375**, 204–211.

53 Zhou, J.F., Unlu, M., Anestis-Richard, I., Kim, H., and Kohl, P.A. (2011) *Journal of Power Sources*, **196**, 7924–7930.

54 Hibbs, M.R., Fujimoto, C.H., and Cornelius, C.J. (2009) *Macromolecules*, **42**, 8316–8321.

55 Henkensmeier, D., Kim, H.J., Lee, H.J., Lee, D.H., Oh, I.H., Hong, S.A., Nam, S. W., and Lim, T.H. (2011) *Macromolecular Materials and Engineering*, **296**, 899–908.

56 Wang, G.G., Weng, Y.M., Zhao, J., Chen, R.R., and Xie, D. (2009) *Journal of Applied Polymer Science*, **112**, 721–727.

57 Luo, Y.T., Guo, J.C., Wang, C.S., and Chu, D. (2010) *Journal of Power Sources*, **195**, 3765–3771.

58 Luo, Y.T., Guo, J.C., Wang, C.S., and Chu, D. (2011) *Macromolecular Chemistry and Physics*, **212**, 2094–2102.

59 Wu, Y.H., Wu, C.M., Xu, T.W., Yu, F., and Fu, Y.X. (2008) *Journal of Membrane Science*, **321**, 299–308.

60 Zhang, C.X., Hu, J., Cong, J., Zhao, Y.P., Shen, W., Toyoda, H., Nagatsu, M., and Meng, Y.D. (2011) *Journal of Power Sources*, **196**, 5386–5393.

61 Varcoe, J.R., Slade, R.C.T., and Lam How Yee, E. (2006) *Chemical Communications*, 1428–1429.

62 Valade, D., Boschet, F., and Ameduri, B. (2009) *Macromolecules*, **42**, 7689–7700.

63 Hong, J.H., Li, D., and Wang, H.T. (2008) *Journal of Membrane Science*, **318**, 441–444.

64 Hong, J.H. and Hong, S.K. (2010) *Journal of Applied Polymer Science*, **115**, 2296–2301.

65 Xiong, Y., Fang, J., Zeng, Q.H., and Liu, Q.L. (2008) *Journal of Membrane Science*, **311**, 319–325.

66 Robertson, N.J., Kostalik, H.A., Clark, T.J., Mutolo, P.F., Abruna, H.D., and Coates, G.W. (2010) *Journal of the American Chemical Society*, **132**, 3400–3404.

67 Wan, Y., Peppley, B., Creber, K.A.M., and Bui, V.T. (2010) *Journal of Power Sources*, **195**, 3785–3793.

68 Varcoe, J.R., Slade, R.C.T., Yee, E.L.H., Poynton, S.D., Driscoll, D.J., and Apperley, D.C. (2007) *Chemistry of Materials*, **19**, 2686–2693.

69 Ko, B.S., Sohn, J.Y., Nho, Y.C., and Shin, J. (2011) *Nuclear Instruments & Methods in Physics Research Section B: Beam Interactions with Materials and Atoms*, **269**, 2509–2513.

70 Zhang, F.X., Zhang, H.M., Ren, J.X., and Qu, C. (2010) *Journal of Materials Chemistry*, **20**, 8139–8146.

71 Kostalik, H.A., Clark, T.J., Robertson, N.J., Mutolo, P.F., Longo, J.M., Abruna, H.D., and Coates, G.W. (2010) *Macromolecules*, **43**, 7147–7150.

72 Varcoe, J.R. and Slade, R.C.T. (2005) *Fuel Cells*, **5**, 187–200.

73 Elabd, Y.A. and Hickner, M.A. (2011) *Macromolecules*, **44**, 1–11.

74 Peckham, T.J. and Holdcroft, S. (2010) *Advanced Materials*, **22**, 4667–4690.

75 Tanaka, M., Fukasawa, K., Nishino, E., Yamaguchi, S., Yamada, K., Tanaka, H., Bae, B., Miyatake, K., and Watanabe, M. (2011) *Journal of the American Chemical Society*, **133**, 10646–10654.

76 Zhou, J.F., Unlu, M., Anestis-Richard, I., and Kohl, P.A. (2010) *Journal of Membrane Science*, **350**, 286–292.

77 Ong, A.L., Saad, S., Lan, R., Goodfellow, R. J., and Tao, S.W. (2011) *Journal of Power Sources*, **196**, 8272–8279.

78 Wu, L. and Xu, T.W. (2008) *Journal of Membrane Science*, **322**, 286–292.

79 Wang, G.G., Weng, Y.M., Chu, D., Chen, R.R., and Xie, D. (2009) *Journal of Membrane Science*, **332**, 63–68.

80 Guo, T.Y., Zeng, Q.H., Zhao, C.H., Liu, Q. L., Zhu, A.M., and Broadwell, I. (2011) *Journal of Membrane Science*, **371**, 268–275.

81 Wang, G.H., Weng, Y.M., Zhao, J., Chu, D., Xie, D., and Chen, R.R. (2010) *Polymers for Advanced Technologies*, **21**, 554–560.

82 Pan, J., Li, Y., Zhuang, L., and Lu, J.T. (2010) *Chemical Communications*, **46**, 8597–8599.

83 Wan, Y., Peppley, B., Creber, K.A.M., Bui, V.T., and Halliop, E. (2008) *Journal of Power Sources*, **185**, 183–187.

84 Wang, E.D., Zhao, T.S., and Yang, W.W. (2010) *International Journal of Hydrogen Energy*, **35**, 2183–2189.

85 Sollogoub, C., Guinault, A., Bonnebat, C., Bennjima, M., Akrour, L., Fauvarque, J.F., and Ogier, L. (2009) *Journal of Membrane Science*, **335**, 37–42.

86 Stoica, D., Alloin, F., Marais, S., Langevin, D., Chappey, C., and Judeinstein, P. (2008) *Journal of Physical Chemistry B*, **112**, 12338–12346.

87 Wu, Y.H., Wu, C.M., Xu, T.W., Lin, X.C., and Fu, Y.X. (2009) *Journal of Membrane Science*, **338**, 51–60.

88 Wu, Y.H., Wu, C.M., Varcoe, J.R., Poynton, S.D., Xu, T.W., and Fu, Y.X. (2010) *Journal of Power Sources*, **195**, 3069–3076.

89 Singh, S., Jasti, A., Kumar, M., and Shahi, V.K. (2010) *Polymer Chemistry*, **1**, 1302–1312.

90 Tripathi, B.P., Kumar, M., and Shahi, V.K. (2010) *Journal of Membrane Science*, **360**, 90–101.

7
Materials for Microbial Fuel Cells

Yanzhen Fan and Hong Liu

7.1
Introduction

A microbial fuel cell (MFC) is a device that uses microbes to convert chemical energy stored in organic or inorganic matter into electrical energy. For nearly a century it has been known that bacteria can generate electrical current [1]. However, it is only within the last decade that MFCs have drawn much research attention for their potential applications in energy generation from wastewater [2], bioremediation, and powering remote sensors.

Figure 7.1 illustrates the essential components of an MFC: microbes, anode, cathode, and optional separator. Microbes oxidize organic or inorganic matter and release electrons and protons. The electrons flow through the circuit and combine with protons and oxygen (or other oxidants) on the cathode to form water and generate electrical current. The protons travel through the electrolyte solution, typically facilitated by proton carriers, such as phosphate or carbonate [3] ions, due to the near neutral pH condition required by the microbes.

Increasing power density and decreasing fabrication cost are two major challenges for the practical applications of MFCs, especially for wastewater treatment. While the electrochemical activity of the microbes is an important factor affecting power output, the materials of other essential components also play a critical role in determining the cost as well as the power output of MFCs. The properties of electrode materials, such as surface area, conductivity, stability, and hydrophobicity, have significant impact on microbial attachment, electrochemical reactions, and electron transfer and collection. Separators can also greatly affect the performance of MFCs due to the increase of internal resistance [4]. The remainder of this chapter will cover a brief introduction to various MFC configurations typically used in MFC studies, as well as common materials used for anodes, cathodes, and separators, with a focus on potential application in wastewater treatment. Existing problems with electrode materials in current MFCs are disclosed, and outlooks for future development are suggested.

Materials for Low-Temperature Fuel Cells, First Edition. Edited by Bradley Ladewig, San P. Jiang, and Yushan Yan.

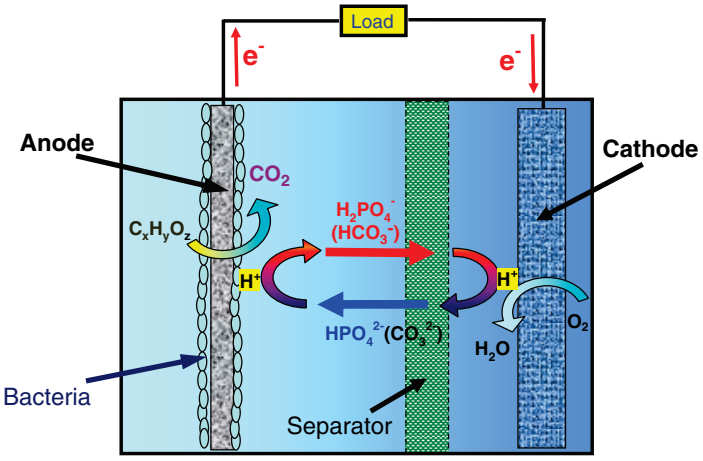

Figure 7.1 Diagram of an MFC, showing the anode with biofilm on the surface, the cathode, and the optional separator. The $H_2PO_4^-/HPO_4^{2-}$ ion pair accounts for the major mechanism for proton transfer in air cathode MFCs using phosphate buffer, while HCO_3^-/CO_3^{2-} is the major proton carrier for MFCs using bicarbonate buffer.

7.2 MFC Configuration

The most common MFC configurations used consist of either one or two chambers. In a two-chamber, or two-compartment, MFC, the bacteria in the anode chamber are separated from the cathode chamber by a membrane or a salt bridge. The cathodic oxidant can be oxygen through air sparging, where air is bubbled through water to provide dissolved oxygen to the electrode. This approach not only consumes a fair amount of energy but is also less efficient due to the low solubility and mass transfer rate of oxygen in water. Other oxidants, such as ferricyanide and permanganate [5], can greatly improve the MFC performance compared with the use of air [6]. The power generated from this type of MFC, however, is not sustainable because the oxidants are consumed in the cathodic reaction and needs to be replenished [7,8]. Oxygen, which is ubiquitous and virtually free, is probably the only oxidant widely available for practical MFC application.

In the single-chamber MFCs, an air cathode is commonly used with the anode at the opposite side of the chamber. Alternatively, the anode and cathode can be on the same side of the chamber if a membrane electrode assembly (MEA) or cloth electrode assembly (CEA) is used. Single-chamber MFCs can achieve much better performance than a two-chamber system due to the higher mass transfer rate and concentration of oxygen in air compared with water [3]. In a membrane-free single-chamber MFC, with the anode and cathode on opposite sides of the chamber, the biofilm developed on the cathode can function as a membrane to minimize oxygen diffusion into the anode chamber while allowing

efficient transport of protons/ions. Elimination of the membrane not only reduces the cost and complexity of MFCs but also increases the power density due to a decrease in internal resistance [3].

7.3 Anode Materials

Unlike the anodes of chemical fuel cells, which require catalysts to speed up the anodic reaction, the MFC anode mainly serves as current collector while providing a surface for biofilm development. In this configuration, the biofilm can function as the catalyst. Therefore, the anode should be constructed of material suitable for biofilm development as well as current collection.

Carbon-based materials are commonly used for the anode of MFCs due to their superior conductivity, chemical stability, biocompatibility, and versatility for creating a large surface area. Various carbon materials, including graphite rods [2], graphite plates [9], graphite foam [10], woven graphite, graphite felt [11], graphite granules [12], reticulated vitreous carbon (RVC) [13], granular activated carbon [14], carbon paper [15], carbon cloth [16], and graphite fiber brush [17], have been examined as anode electrodes for MFCs.

Non-carbon-based materials have also been explored for MFC anodes, including various metals, platinum [18], gold [19], titanium [11], stainless steel (SS) [20], and copper [13]. In spite of the fact that the conductivity of metals is normally higher than that of carbon materials, the performance of metal materials as MFC anodes is generally poor. Poor performance could be due to the relatively low surface area of metal electrodes and the less favorable surface properties for biofilm development compared with carbon electrodes. The high cost of Pt and Au materials impedes their large-scale applications. Attention should also be given to the corrosive nature and poisonous effects of some metals. For example, metals such as copper and stainless steel can be reactive as MFC anodes, which further limits the application of metals as anode materials in MFCs.

7.3.1 Solid Carbon Materials

Solid graphite plates, or rods, are the simplest form of MFC electrodes, which were commonly used in the early stages of MFC research because they are relatively inexpensive, easy to handle, and have a defined surface area [2]. A graphite disk anode embedded in marine sediment and a graphite disk cathode in overlying seawater were used in a sea-floor microbial fuel cell to generate electrical power *in situ* [14]. Graphite plates were commonly used in the laboratory in some pioneer MFC research [12,21]. Liu *et al.* used eight graphite rod anodes in a single-chamber air cathode MFC for generating electricity from wastewater [2]. The relatively smooth surface of solid graphite electrode makes it easier to calculate the surface area of the electrode. However, the smooth surface limits the

surface area available for biofilm development, thus limiting the maximum current density of the MFC anode. The maximum power density was only 26 mW m^{-2} for an MFC using graphite rods as anodes [2].

7.3.2 Granular Carbon Materials

Compared with solid carbon material, the surface area of granular carbon materials is significantly higher. Two types of granular carbon materials have been reported as MFC anodes: granular graphite [22] and granular activated carbon [23,24]. Using graphite as the anode material of a tubular MFC, Rabeay *et al.* achieved maximum power outputs of 90 and 66 W m^{-3} net anodic compartment for feed streams based on acetate and glucose, respectively [9]. You *et al.* reported similar maximum power density of 49 W m^{-3} with an upflow air cathode MFC using glucose as the substrate [25]. Higher power density (258 W m^{-3}) was achieved in a 6-MFC stack with sodium acetate as the substrate and potassium ferricyanide as the oxidant [24]. In spite of its higher surface area, granular activated carbon is less popular than granular graphite, probably due to its lower conductivity and thus lower maximum power density. The power densities of MFCs using granular activated carbon [23,26] are about one to two orders of magnitude lower than those using granular graphite.

7.3.3 Fiber Carbon Materials

Carbon fiber-based electrodes, including carbon fiber, carbon cloth, carbon/graphite felt, carbon paper, and graphite fiber brush, have arguably the best performance as MFC anodes due to their large surface area ratio, good conductivity, excellent physical strength and chemical stability, and favorable surface properties for biofilm development. Reimers *et al.* first reported the application of carbon fiber in a benthic microbial fuel cell to harvest energy from the marine sediment–seawater interface [21]. Liu *et al.* tested the performance of carbon paper and carbon cloth in air cathode microbial fuel cells [16,15]. Carbon paper electrodes exhibited lower performances, compared with carbon cloth, probably due to the lower surface area available for biofilm development. As a low profile carbon cloth, carbon mesh materials demonstrated similar or even better performance than carbon cloth anodes [27]. Carbon/graphite felt has also been widely used as a MFC anode [28,29]. Carbon felt exhibited higher performance compared with carbon paper due to a larger surface area, lower resistance, and open network of interwoven fibers [30]. Logan *et al.* designed a new graphite brush anode by winding graphite fibers around a twisted core consisting of two titanium wires [17]. The design achieved power densities of 73 W m^{-3} (based on the liquid volume) and 2400 mW m^{-2} when inoculated with wastewater. Under similar conditions, MFCs achieved up to 1430 mW m^{-2} (2.3 W m^{-3}) with a graphite brush anode compared with 600 mW m^{-2} with a plain carbon paper electrode.

To date, the highest power densities that have been generated so far are 6900 mW m^{-2} [31] and 1550 W m^{-3} [3] using carbon cloth anodes. The format of carbon cloth is probably the main reason for the high power density. Compared with the "brick" format of carbon felt or "cylinder" format of graphite brush, the "sheet" format of carbon cloth makes it easier to reduce the average distance between anode and cathode, thus greatly reducing the internal resistance [31] and increasing the surface area/volume ratio, producing significantly higher power densities.

7.3.4
Porous Carbon Materials

Porous carbon materials, including reticulated vitreous carbon, carbon sponge, and carbon foam, have also been tested in MFCs. RVC is a porous, rigid material of low density with an open structure and good electrical conductivity. Scott *et al.* compared the performance of carbon sponge, carbon cloth, carbon fiber, and reticulated vitreous carbon [22]. The MFC with the carbon sponge anode produced maximum power density of 55 mW m^{-2}, which was nearly twice that achieved with carbon cloth, and a hundred times higher than that with reticulated vitreous carbon (0.2 mW m^{-2}). Further comparison of graphite, sponge, paper, cloth, felt, fiber, foam, and RVC anode materials also demonstrated the poor performance of RVC, which might be related to the surface area available and concentration polarizations caused by the morphology of the material and the structure of the biofilm [32].

7.3.5
Modification of Anode Materials

Modification of anode materials can alter their surface properties, especially conductivity and biocompatibility, thus altering their performance as MFC anodes. The attachment of positively or negatively charged compounds to naturally occurring surfaces such as quartz and sand affects the adhesion of bacteria by altering the electrostatic attraction of the cells to the surface [33]. The treatment of a carbon cloth anode with ammonia gas increased the surface charge of the electrode and improved MFC performance [34]. Park and Zeikus constructed composites of graphite, metal (e.g., Fe^{3+} and Mn^{4+}), and mediator compounds (e.g., neutral red), and reported that current production was enhanced when an electron mediator (Mn^{4+} or neutral red) was incorporated into a graphite anode [35]. Lowy *et al.* [36] evaluated various modified graphite anodes, including graphite modified by adsorption of anthraquinone-1,6-disulfonic acid (AQDS) or 1,4-naphthoquinone (NQ), a graphite–ceramic composite containing $Mn^{2+}$and Ni^{2+}, and graphite modified with a graphite paste containing Fe_3O_4 or Fe_3O_4 and Ni^{2+}. It was found that these anodes possess between 1.5- and 2.2-fold greater kinetic activity compared with plain graphite.

The current production by *Shewanella putrefaciens* on gold electrodes coated with various alkanethiol self-assembled monolayers, having a carboxylic acid functional head group, were compared with that produced on glassy carbon electrodes [37]. It was revealed that current production correlated with monolayer molecular chain length and head group, with certain head groups enhancing electronic coupling to the bacteria, as a result of strong hydrogen bonding between the carboxylic acid groups and the cytochromes in the bacteria. This covalent linking functioned as an electrical connection between the bacteria and the electrode and the modified electrode produced significantly higher currents compared with glassy carbon. Polyethyleneimine was also used to bind the mediator (9,10-anthraquinone-2,6-disulfate) and *Geobacter sulfurreducens* to a graphite felt electrode, which showed a current density of $1.2\,\mathrm{mA\,cm^{-2}}$ [38].

Enhanced performance was also reported for anode modification with conductive polymers. A commonly used conductive polymer, polyaniline, can increase the current densities of MFC anodes. But it is also susceptible to microbial attack and degradation [39]. Schröder *et al.* [18] reported that a platinum electrode covered with polyaniline achieved a current density up to $1.5\,\mathrm{mA\,cm^{-2}}$ in an MFC. Modification of polyaniline can improve its performance and stability, such as fluorinated PANI [40], PANI/carbon nanotube (CNT) composite [41], and PANI/titanium dioxide composite [42].

Nanomaterials have also been used to improve the performance of MFC anodes. Recent studies have demonstrated that CNT-decorated anodes enhanced the power generation of MFCs [43,44]. The modification of a glassy carbon anode with carbon nanotubes increased the current density to $9.70 \pm 0.40\,\mu\mathrm{A\,cm^{-2}}$, a level 82 times greater than that of bare glassy carbon electrodes [45]. Graphite anodes decorated with Au nanoparticles produced current densities up to 20-fold higher than plain graphite anodes by *Shewanella oneidensis* MR-1, while those of Pd-decorated anodes with similar morphologies were 0.5–1.5 times higher than the control [46]. Multiwall carbon nanotube (MWNT) and polyelectrolyte polyethyleneimine (PEI) were employed to modify carbon paper electrodes utilizing a layer-by-layer (LBL) assembly technique, producing a 20% higher power density than the bare carbon paper anodes [47].

7.4 Cathode

The cathode is the main bottleneck of current MFC development. Development of high-performance, low-cost cathode material is critical for the successful application of MFC technology, especially for wastewater treatment. A typical air cathode includes a carbon base layer, a catalyst coating on the water facing side, and several diffusion layers (DLs) on the air-facing side [48].

7.4.1 Catalyst Binders

Binding agent, or binder, is often used in the preparation of cathodes to form a catalyst coating on the surface of the cathode substrate, or base layer. A solution of Nafion, a perfluroinated proton exchange resin, is widely used with Pt/C powder to form a paste, which is then applied by brushing or spraying onto carbon the cloth/paper base layer. However, the application of Nafion solution in preparing MFC cathodes should be reconsidered due to the following reasons. First, the Nafion solution is relatively expensive, which contributes a major portion of the total cost of MFC cathode. Second, the proton is mainly transported by anions, or pH buffer carriers, in the neutral condition of MFCs. Nafion as a proton, or cation, exchange resin may increase the ion mass transfer resistance, or polarization resistance, of the cathode. Simply replacing the Nafion solution with water improved the performance of the cathodes [49], although the long-term performance of a binder-free catalyst coating is not clear. The adverse effect of cation exchange functional groups was also demonstrated in a recent study [50]. The unsulfonated poly(phenylsulfone) binder, a nonionic hydrophobic polymer, showed the highest current in linear sweep voltammetry (LSV) tests and the lowest charge transfer resistance. The increase of sulfonate groups in the poly(phenylsulfone) binder from ion exchange capacities 0 to 2.54 meq/g resulted in a decreased current response in LSV tests and an increased charge transfer resistance from 8 to 23 Ω. It is proposed that the presence of sulfonate groups in the cathode binder impeded the oxygen reduction activity of the cathodes by adsorption of the sulfonate to catalytic sites and by impeding proton diffusion to the catalyst surface. These results suggest that the use of a nonionic binder is advantageous in an MFC cathode to facilitate charge transfer and stable performance in the neutral pH conditions found in MFCs [51]. The replacement of the Nafion binder with polytetrafluoroethylene (PTFE), however, reduced the maximum power densities [52]. Further tests showed that the increase of Nafion percentage in Nafion–PTFE mixture (from 0 to 100%) as catalyst binders increased the maximum power density (from 549 to 1060 $mW\,m^{-2}$) [53]. The relatively poor performance of PTFE as a binder might be due to its hydrophobicity. Increasing the hydrophilicity of polystyrene-*b*-polyethylene oxide binders enhanced the electrochemical response of the cathode and MFC power density by ~15%, compared with the hydrophobic PS–OH binder. The performance of an inexpensive hydrophilic neutral polymer, poly(bisphenol A-*co*-epichlorohydrin) (BAEH), was initially (after two cycles) worse (1360 and 630 $mW\,m^{-2}$ for 0.5 and 0.05 mg Pt cm^{-2}, respectively) than that of hydrophilic sulfonated Nafion binder (1980 and 1080 $mW\,m^{-2}$ for 0.5 and 0.05 mg Pt cm^{-2}, respectively). However, after long-term operation (22 cycles, 40 days), power production of each cell was similar (~1200 and 700–800 $mW\,m^{-2}$ for 0.5 and 0.05 mg Pt cm^{-2}, respectively) likely due to cathode biofouling that could not be completely reversed through physical cleaning [54].

7.4.2 Diffusion Layers

PTFE is widely used in diffusion layers to allow air breathing while preventing water leakage in air cathodes. A new and simplified approach for making cathodes for microbial fuel cells was developed by using metal mesh current collectors and inexpensive carbon/polymer, poly(dimethylsiloxane) (PDMS), diffusion layers [55]. The PDMS can limit oxygen transfer through the cathode and improve coulombic efficiency of MFCs. The low-cost design produced comparable power output and a much higher coulombic efficiency (80 versus 57% for carbon cloth cathode) [56].

7.4.3 Current Collector

Due to the relatively low current density in MFCs, there are normally no current collectors employed in cathodes using carbon cloth or carbon paper as a base material. Carbon cloth current collectors made of stainless steel can be integrated into MFC cathodes constructed of a reactive carbon black and Pt catalyst mixture and a poly(dimethylsiloxane) diffusion layer. It is shown here that the mesh properties of these cathodes can significantly affect performance. Cathodes made from the coarsest mesh (30 mesh) achieved the highest maximum power of $1616 \pm 25\,\mathrm{mW\,m^{-2}}$ (normalized to cathode projected surface area; $47.1 \pm 0.7\,\mathrm{W\,m^{-3}}$ based on liquid volume), while the finest mesh (120 mesh) had the lowest power density ($599 \pm 57\,\mathrm{mW\,m^{-2}}$). Electrochemical impedance spectroscopy showed that charge transfer and diffusion resistances decreased with increasing mesh opening size. In MFC tests, the cathode performance was primarily limited by reaction kinetics, and not mass transfer. Oxygen permeability increased with mesh opening size, accounting for the decreased diffusion resistance. At higher current densities, diffusion became a limiting factor, especially for fine mesh with low oxygen transfer coefficients. These results demonstrate the critical nature of the mesh size used for constructing MFC cathodes [57].

7.4.4 Cathode Fouling

Due to biofilm development and the complexity of medium solutions used in MFCs, the fouling of the cathode is a more serious issue than that for chemical fuel cells.

Kiely *et al.* operated microbial fuel cells for more than a year with individual endproducts of lignocellulose fermentation (acetic acid, formic acid, lactic acid, succinic acid, or ethanol) to investigate the long-term cathode performance and bacterial communities. Cathode performance degraded over time, as shown by an increase in power of up to 26% when the cathode biofilm was removed, and 118% using new cathodes [58]. For submerged air cathodes in two-chamber

MFCs, cathodic biofilm development and chemical scale accumulation can reduce oxygen diffusion through the cathode as well as the proton mass transfer, leading to a decrease in power generation during the long term. Thus, it is important to properly control the formation of chemical scale and biofilm on the cathode during long-term operation to obtain stable power generation in two-chamber MFCs [40].

7.4.5 Cathode Catalysts

Platinum is widely used in laboratory MFC systems as a cathode catalyst due to its high catalytic activity for oxygen reduction reaction. However, the high cost of platinum reduces the appeal of this approach. The near neutral pH condition also strongly affects the cathode performance and limits the power generation of MFCs. Extensive research efforts have been focused on improving the performance and reducing the cost of cathode materials [44,59,60].

7.4.5.1 Pt Cathode Modified with Nanomaterials

Nanomaterials, especially CNT, have been used to improve the performance of Pt cathodes. Thanks to the unique properties of CNTs, the performance of Pt cathodes can be greatly enhanced.

The current density of a single-wall carbon nanotube sheet electrode, with infused platinum nanoparticles as the cathode in a microbial fuel cell, was approximately an order of magnitude higher than that with an e-beam-evaporated platinum cathode. The enhancement of catalytic activity can be associated with the increase of the catalyst surface area in the active cathode layer [61]. In another study, MFCs with carbon nanotube mat cathodes produced a maximum power density of 329 $mW\,m^{-2}$, more than twice of that obtained with carbon cloth cathodes (151 $mW\,m^{-2}$) [62]. A similar twofold improvement was obtained by electrochemically depositing Pt nanoparticles on a CNT textile cathode for aqueous cathode MFCs, with only 19.3% Pt loading of a commercial Pt-coated carbon cloth cathode [63].

7.4.5.2 Cathode with Non-Pt Metal Catalyst

Various metals have been explored to replace Pt, including Fe, Co, Mn, and Pb. Among these metals, cobalt and iron are often used with tetramethoxyphenylporphyrin (TMPP) or phthalocyanine (Pc) to form metal macrocyclic complexes, which demonstrate performance comparable with Pt in neutral pH conditions. FePc supported on KJB carbon (FePc-KJB) produced a power density of 634 $mW\,m^{-2}$, which is higher than 593 $mW\,m^{-2}$ of Pt cathode and other cathodes with metal macrocyclic complexes, including CoTMPP, FeCoTMPP, CoPc, and FeCuPc [64]. The comparison of FePc and CoTMPP with platinum-based system demonstrated the potential of transition metal-based materials for substitution of the traditional cathode materials in microbial fuel cells [65]. Cheng *et al.* also demonstrated that the performance of

cathodes with CoTMPP is comparable with Pt cathodes, especially at current density above 0.6 mA cm^{-2} [52]. With a loading of 2 mg cm^{-2}, the maximum power density of MFCs with FePc-based cathode was 550–590 mW m^{-2}, which is comparable with that using a Pt-based carbon cloth cathode containing 0.5 mg Pt cm^{-2} [66]. The performance of metal macrocyclic complex catalysts is also affected by the chemical environment in microbial fuel cells. The limiting current density of pyrolyzed FePc and CoTMPP in galvanodynamic polarization experiments decreases from 1.5 to 0.6 mA cm^{-2} (pH 3.3, $E_{cathode} = 0$ V) when the buffer concentration is decreased from 500 to 50 mM [67]. High concentration of chloride ions may reduce the performance of Pt catalysts, while improving the performance of cathodes with CoTMPP [64].

Aelterman *et al.* demonstrated that it is possible to replace ferricyanide with an iron ethylenediaminetetraacetic acid (Fe-EDTA) catholyte [68]. Although the maximum power was 50% lower, no replenishment of the Fe-EDTA catholyte was needed. Simply pyrolyzing carbon mixed iron-chelated ethylenediaminetetraacetic acid (PFeEDTA/C) in an argon atmosphere may greatly improve its performance, with quaternary N-iron as the possible active site for the oxygen reduction reaction [48]. The MFC with a PFeEDTA/C cathode produced a maximum power density of 1122 mW m^{-2}, which was close to that with a Pt/C cathode (1166 mW m^{-2}) and which was stable during an operation period of 31 days.

Other non-Pt metal catalysts, including PbO_2 [69], MnO_2 [51,70], and Co [71], were also studied. However, their maximum power densities (normalized to the projected cathode surface area) were only about 100 mW m^{-2} or less, which is less than 10% of the power density that can be produced by high-performance air cathodes with Pt cathodes.

7.4.5.3 Carbon Cathodes

Carbon material, such as graphite plate and graphite felt, can be directly used as a cathode without any additional catalyst. Considering cathodes with high-performance Pt catalyst still limit the performance of MFCs, the current density of plain carbon cathodes is generally much lower than that with a catalyst. However, some recently developed carbon cathodes demonstrated performance comparable with that of Pt-catalyzed cathode.

Recent developments demonstrated the great potential of activated carbon as low-cost cathode material, which can be formed by cold pressing-activated carbon with a PTFE binder around a Ni mesh current collector. Such a cathode structure avoided the need for carbon cloth or a metal catalyst, and produced a cathode with high activity for oxygen reduction at typical MFC current densities [72]. Tests with the AC cathode produced a maximum power density of 1220 mW m^{-2}, compared with 1060 mW m^{-2} obtained by Pt-catalyzed carbon cloth cathode. Other carbon material, including activated carbon fiber felt [56] and HNO_3-treated carbon powder (Vulcan XC-72R) [73], also demonstrated good performance for oxygen reduction reaction in MFCs.

7.4.5.4 Conductive Polymers

Conductive polymers, such as ploypyrrole (PPy)/polyaniline (PANI) and mediator composites, show promising performance for the oxygen reduction reaction in MFCs. Modification of the anode and cathode of a dual-chamber MFC with PPy/anthraquinone-2,6-disulfonate (AQDS) composite boosts the maximum power density one order of magnitude to 823 mW cm^{-2}, which also increased the rate of H_2O_2 generation in the cathode chamber [74]. In another study, Prussian blue/polyaniline (PB/PANI)-modified cathode exhibited good electrocatalytical activity for oxygen reduction in an acidic electrolyte, demonstrating performance comparable with that of a ferricyanide cathode [75]. A cathode with polypyrrole/anthraquinone-2-sulfonate (PPy/AQS) conductive polymer on stainless steel mesh produced a maximum power density of 575 mW m^{-2} in a membraneless MFC [76].

7.4.5.5 Biocathodes

Laccase has been commonly used in cathodes of enzyme-based biofuel cells. Only recently, it was discovered that bacteria can also catalyze the oxygen reduction reaction in MFCs. Biocathode here refers to bacteria-based cathode.

Relatively low power/current density is the major obstacle for the application of biocathodes. Mass transfer calculations show that the transfer of oxygen poses a serious limitation to the use of dissolved oxygen as an electron acceptor in MFCs [77]. This limiting current density was calculated to be 0.848 A m^{-2} for a graphite plate biocathode, which is a factor of three times higher than the measured current density and an order of magnitude lower than what can be achieved by a Pt air cathode. However, a maximum current density of ~4 A m^{-2} was achieved using a tubular biocathode with carbon felt as the cathode material [78], corresponding to a maximum power density of 117 W m^{-3} (obtained by polarization at a 1 mV s^{-1} scan rate) or 83 W m^{-3} (obtained by changing external resistance). The cathode material and the fast catholyte flow rate (6 l h^{-1}, hydraulic retention time <0.4 min) might be the reasons for the improved oxygen mass transfer and the achievement of such a high current density. Slightly lower 68.4 W m^{-3} (obtained by polarization at a 1 mV s^{-1} scan rate) at a current density of 178.6 A m^{-3} was obtained by an MFC with a graphite fiber brush as the cathode material [79]. An MFC with an algae-grown cathode (*Chlorella vulgaris*) produced a maximum power density of 5.6 W m^{-3} [80]. A maximum current density of 1.0 mA m^{-2} was produced in another MFC using *C. vulgaris* at the cathode [81].

Although much work remains to be done to increase current density, biocathodes have drawn substantial research attention due to the low-cost and sustainable nature. Moreover, biocathodes can be used not only for oxygen reduction but also for many oxidized contaminates [82]. For example, Cr(VI) can be biologically reduced to $Cr(OH)_3$ precipitate in an MFC with a biocathode [83]. A maximum Cr(VI) reduction rate of 0.46 mg Cr(VI) g^{-1} VSS h^{-1} was achieved, which resulted in a current and power density of 123.4 mA m^{-2} and 55.5 mW m^{-2}, respectively.

7.5 Separators

The separator is an important component in a MFC, which physically separates the anode and cathode. A variety of separators have been explored for MFCs, including a salt bridge, cation exchange membrane (CEM), anion exchange membrane (AEM), bipolar membrane (BPM), microfiltration (MF) membrane, ultrafiltration (UF) membrane, and porous fabrics and porous materials.

In chemical fuel cells, membranes or other ion-conductive separators are needed to avoid fuel crossover while allowing charge carrying ion exchange between electrodes. In microbial fuel cells, however, the fuel crossover is no longer an issue because anodes and cathode use totally different catalysts, and thus fuel/substrate cannot be consumed at the cathode. Cation exchange membranes are still needed in two-chamber MFCs using ferricyanide as an electron acceptor to avoid the diffusion of toxic ferricyanide into the anode chamber while allowing the transfer of protons or other cations to the cathode chamber. For MFCs other than those using ferricyanide, anion [84] or bipolar [85] exchange membranes, nanoporous polymer filters [86], ultrafiltration membranes [84], and even J-cloth [87] could be better choices because they result in a relatively stable anolyte pH, which is critical for biological activity.

The main functions of separators in MFCs are to avoid the direct electric contact (short circuit) of anodes and cathodes and to reduce unwanted crossover of oxygen and other substances, while maintaining efficient proton mass transport through the separator. It is possible to replace/eliminate this expensive and complicated membrane system [87,15]. In a membrane-free air cathode microbial fuel cell system, the biofilm developed on the cathode can function as a membrane to minimize oxygen diffusion into the anode chamber while allowing efficient transport of protons/ions. The elimination of the membrane not only reduces the cost and complexity of MFCs but also increases the higher power density due to a decrease in internal resistance [3]. The active consumption of oxygen by the aerobic biofilm on the cathode can effectively reduce the oxygen diffusion through the biofilm. However, the biofilm also consumes substrate that results in low coulombic efficiency. The possible short circuit and increased oxygen diffusion limit the minimum electrode spacing to about 1–2 cm [88]. The relatively large electrode spacing not only contributes to the high internal resistance but also limits the ratio of the electrode surface area/volume and in turn the maximum volumetric power density. Therefore, separator is still needed if further reduction in electrode spacing is necessary.

7.5.1 Cation Exchange Membranes

Nafion membrane is widely used in MFC research, probably due to the popularity in PEM fuel cells. Nafion membrane is also called a proton exchange membrane for its preferential conduction of proton over other ions under acidic

condition. However, the charge balance in an MFC with Nafion or other CEM is achieved by the transportation of predominant cations, such as Na^+ and K^+, as the concentrations of these cations are typically 10^5 times higher than that of proton [89]. Due to the low efficiency in proton transportation through the membrane, the anodic pH increases while the cathodic pH decreases, which not only decreases the voltage output of the MFC but also inhibits the activity of anodic microbes and leads to cathode fouling. A low-cost alternative to Nafion membrane is CMI-7000 (Membranes International Inc.), which is also less permeable to oxygen than Nafion due to its thickness.

7.5.2 Anion Exchange Membranes

AEM generally perform better than CEM in MFCs because anions, such as phosphates and carbonates, can facilitate proton transport. In an MFC with AEM, pH buffers also work as proton carriers. The concentration of pH buffers used in MFCs is on the order of 0.1 M, which is 10^6 times higher than that of protons. The relatively higher concentration of proton carriers results in more efficient proton transfer through separators and higher power density [3]. Kim *et al.* reported higher maximum power density for AEM (610 mW m^{-2}) than by the Nafion (514 mW m^{-2}) and CEM (480 mW m^{-2}) [84]. The power density was further increased to 728 mW m^{-2} with AEM cathode and 200 mM PBS in a tubular MFC [90].

7.5.3 Biopolar Membranes

A bipolar membrane is a cation exchange membrane laminated together with an anion exchange membrane, through a catalytic intermediate layer (the "junction" layer) to accelerate the splitting of water into protons and hydroxide ions. Biopolar membranes were first applied in MFCs to combine with ferric iron reduction on a graphite electrode as an efficient cathode system [85]. Compared with AEM and CEM, BPM can suppress the transport of ions other than protons and hydroxide ions and thus reduce the pH difference between anode and cathode chambers. However, water splitting would increase polarization potential loss across the membrane. The loss was much larger than those of CEM and AEM (0.71 versus 0.27 and 0.32 V, respectively) in a bioelectrochemical system running on wastewater, in spite of the increased ability to transport protons and hydroxyl ions and to prevent pH increase in the cathode chamber [91].

7.5.4 Filtration Membranes

Filtration membranes, including UF and MF membranes, can be used as separators in MFCs. In addition to low cost, compared with ion exchange membrane,

the advantage of UF and MF membranes is that most of the ions can freely pass through the relatively large pores of the membranes, thus reducing the associated internal resistances and enhancing the MFC performance [92–95]. One major issue for the application of membranes in MFCs is oxygen crossover, especially for MFCs with membrane electrode assemblies [96]. An ideal separator should have the capacity to control oxygen crossover while facilitating proton transfer to the cathode. Oxygen crossover can be reduced by using membranes with a smaller pore size [97,98] or thicker membranes [99]. Unfortunately, materials that reduce oxygen crossover also decrease proton transport, reducing power generation.

7.5.5 Porous Fabrics

Porous fabrics can also accomplish the main functions of separators in MFCs, preventing short circuit and reducing oxygen diffusion. Thanks to the porous structure, fabrics allow efficient mass transfer of charge carrying ions, reducing internal resistance and enhancing power generation. In principle, any porous, nonconductive materials can be used as separators in MFCs. Basic requirements for the materials are nonconductive, durable, low-cost, high anion permeability and low oxygen permeability [87]. The oxygen crossover can be effectively suppressed by a simple cloth layer and developed biofilm, thus improving the coulombic efficiency. The coulombic efficiency improved by twofold compared with cathodes without the cloth layer (71 versus 35%) [87]. The cloth layer can also electrically isolate the anode from cathode, thus making it possible to reduce the electrode spacing to less than 1 mm and form a cloth electrode assembly structure. The CEA structure makes it possible to greatly reduce the internal resistance [31] and increase the surface/volume ratio, thus increasing the volumetric power density, of the MFC. A power density as high as 1550 $W\,m^{-3}$ (2770 $mW\,m^{-2}$) was achieved in an MFC with double CEAs using 0.2 M bicarbonate as buffer [3]. Thanks to its low cost and large variety, the balance between oxygen permeability and internal resistance can be optimized. However, the development of the biofilm should be well controlled to maintain its long-term stability.

7.6 Outlook

Although low power density and high material cost are still limiting the application of MFC technology, the power density of MFCs has been increased by several orders of magnitude in less than a decade [100]. Further improvement in power density and reduction in material cost are expected as a result of intensive research activities in this area.

With the rapid increase in the world population, about 7 billion today, water and energy are now growing expensive and are soon to be overwhelmed by insatiable demand. Microbial fuel cell technology, which uses microorganisms to catalyze the direct generation of electricity from biodegradable organic matter, provides a completely new approach for energy generation from wastewater and accomplishing wastewater treatment at the same time [101]. It has been known for nearly a century that bacteria can generate electrical current [1]. But only in the last few years, MFCs have drawn much attention and extensive research, especially after the demonstration of direct harvesting of electricity from wastewater [2].

Intensive research activities led to rapid improvement in MFC performance in the past decade. The power density of MFCs has been increased several orders of magnitude in <10 years. Until now, the highest reported power densities are on the order of 1 W m^{-2} and 1 kW m^{-3}, which are still about two to three orders of magnitude lower than those of chemical fuel cells. Further improvement in power density is necessary to make MFC technology competitive and commercially viable, which requires breakthroughs in low-cost and high-performance materials for MFCs.

The anode is a nonlimiting factor in the current stage of MFC development. Carbon cloth anode with mixed culture bacteria can at least produce a current density of 3 mA cm^{-2} while the current density for MFCs with equal sized electrodes is normally <1 mA cm^{-2}. The current commercial price for carbon cloth is about a few dozen dollars, which is expected to be reduced when large-scale application of this material in MFCs is possible. Further development of anode material should further reduce cost.

The cathode is a major limiting factor of MFCs, both in performance and in cost. Platinum is too expensive to be used in large-scale application. It is possible to find some cathode materials suitable for the neutral pH and relatively low current density. Activated carbon provides a good example of low-cost high-performance cathode materials. Special attention should be paid to searching high-performance oxygen reduction catalysts at a higher current density, for example, 2–3 mA cm^{-2}, to match the possible current density of anode.

Separators are often overlooked in MFC research, both in its cost and in its contribution to internal resistance. Ion exchange membranes are about a few hundred US dollars per square meter. The high cost and mediocre performance limit their potential commercial application in MFCs. While producing the highest reported volumetric power density, the cost of porous fabrics can be <1 US$ m^{-2}. Further optimization of thickness and control of biofilm development is needed.

Breakthroughs in MFC materials often lead to breakthroughs in reactor architecture and performance. New designs also call for new materials. The development of low-cost and high-performance electrode materials will greatly expand the application of MFCs.

References

1 Potter, M.C. (1911) Electrical effects accompanying the decomposition of organic compounds. *Proceedings of the Royal Society of London B: Biological Sciences*, **84**, 260–276.

2 Liu, H., Ramnarayanan, R., and Logan, B.E. (2004) Production of electricity during wastewater treatment using a single chamber microbial fuel cell. *Environmental Science & Technology*, **38** (7), 2281–2285.

3 Fan, Y., Hu, H., and Liu, H. (2007) Sustainable power generation in microbial fuel cells using bicarbonate buffer and proton transfer mechanisms. *Environmental Science & Technology*, **41** (23), 8154–8158.

4 Li, W.W., Sheng, G.P., Liu, X.W., and Yu, H.Q. (2011) Recent advances in the separators for microbial fuel cells. *Bioresource Technology*, **102** (1), 244–252.

5 You, S., Zhao, Q., Zhang, J., Jiang, J., and Zhao, S. (2006) A microbial fuel cell using permanganate as the cathodic electron acceptor. *Journal of Power Sources*, **162**, 1409–1415.

6 Oh, S.-E., Min, B., and Logan, B.E. (2004) Cathode performance as a factor in electricity generation in microbial fuel cells. *Environmental Science & Technology*, **38** (18), 4900–4904.

7 Pham, T.H., Jang, J.K., Chang, I.S., and Kim, B.H. (2004) Improvement of cathode reaction of a mediatorless microbial fuel cell. *Journal of Microbiology and Biotechnology*, **14** (2), 324–329.

8 Borole, A.P., Hamilton, C.Y., Aaron, D.S., and Tsouris, C. (2009) Investigating microbial fuel cell bioanode performance under different cathode conditions. *Biotechnology Progress*, **25** (6), 1630–1636.

9 Rabaey, K., Lissens, G., Siciliano, S.D., and Verstraete, W. (2003) A microbial fuel cell capable of converting glucose to electricity at high rate and efficiency. *Biotechnology Letters*, **25** (18), 1531–1535.

10 Chaudhuri, S.K. and Lovley, D.R. (2003) Electricity generation by direct oxidation of glucose in mediatorless microbial fuel cells. *Nature Biotechnology*, **21**, 1229–1232.

11 Ter Heijne, A., Hamelers, H.V.M., Saakes, M., and Buisman, C.J.N. (2008) Performance of non-porous graphite and titanium-based anodes in microbial fuel cells. *Electrochimica Acta*, **53** (18), 5697–5703.

12 Bond, D.R. and Lovley, D.R. (2003) Electricity production by *Geobacter sulfurreducens* attached to electrodes. *Applied and Environmental Microbiology*, **69**, 1548–1555.

13 Kargi, F. and Eker, S. (2007) Electricity generation with simultaneous wastewater treatment by a microbial fuel cell (MFC) with Cu and Cu-Au electrodes. *Journal of Chemical Technology and Biotechnology*, **82** (7), 658–662.

14 Tender, L.M., Reimers, C.E., Stecher, H.A., III, Holmes, D.E., Bond, D.R., Lowy, D.A., Pilobello, K., Fertig, S.J., and Lovley, D.R. (2002) Harnessing microbially generated power on the seafloor. *Nature Biotechnology*, **20** (8), 821–825.

15 Liu, H. and Logan, B.E. (2004) Electricity generation using an air-cathode single chamber microbial fuel cell in the presence and absence of a proton exchange membrane. *Environmental Science & Technology*, **38** (14), 4040–4046.

16 Liu, H., Cheng, S., and Logan, B.E. (2005) Production of electricity from acetate or butyrate using a single-chamber microbial fuel cell. *Environmental Science & Technology*, **39** (2), 658–662.

17 Logan, B.E., Cheng, S., Watson, V., and Estadt, G. (2007) Graphite fiber brush anodes for increased power production in air-cathode microbial fuel cells. *Environmental Science & Technology*, **41** (9), 3341–3346.

18 Schröder, U., Niessen, J., and Scholz, F. (2003) A generation of microbial fuel cells with current outputs boosted by more than one order of magnitude. *Angewandte Chemie: International Edition*, **115**, 2986–2989.

19 Richter, H., McKarthy, K., Nevin, K.P., Johnson, J.P., Rotello, V.M., and Lovley, D.R. (2008) Electricity generation by *Geobacter sulfurreducens* attached to gold electrodes. *Langmuir*, **24**, 4376–4379.

20 Dumas, C., Mollica, A., Féron, D., Basséguy, R., Etcheverry, L., and Bergel, A. (2007) Marine microbial fuel cell: use of stainless steel electrodes as anode and cathode materials. *Electrochimica Acta*, **53** (2), 468–473.

21 Reimers, C.E., Tender, L.M., Fertig, S.J., and Wang, W. (2001) Harvesting energy from the marine sediment–water interface. *Environmental Science & Technology*, **35**, 192–195.

22 Scott, K., Cotlarciuc, I., Hall, D., Lakeman, J.B., and Browning, D. (2008) Power from marine sediment fuel cells: the influence of anode material. *Journal of Applied Electrochemistry*, **38** (9), 1313–1319.

23 Jiang, D. and Li, B. (2009) Novel electrode materials to enhance the bacterial adhesion and increase the power generation in microbial fuel cells (MFCs). *Water Science & Technology*, **59** (3), 557–563.

24 Nam, J.-Y., Kim, H.-W., Lim, K.-H., and Shin, H.-S. (2010) Effects of organic loading rates on the continuous electricity generation from fermented wastewater using a single-chamber microbial fuel cell. *Bioresource Technology*, **101** (1 Suppl.), S33–S37.

25 You, S., Zhao, Q., Zhang, J., Liu, H., Jiang, J., and Zhao, S. (2008) Increased sustainable electricity generation in up-flow air-cathode microbial fuel cells. *Biosensors and Bioelectronics*, **23** (7), 1157–1160.

26 Nam, J.-Y., Kim, H.-W., and Shin, H.-S. (2010) Ammonia inhibition of electricity generation in single-chambered microbial fuel cells. *Journal of Power Sources*, **195** (19), 6428–6433.

27 Wang, X., Cheng, S., Feng, Y., Merrill, M.D., Saito, T., and Logan, B.E. (2009) The use of carbon mesh anodes and the effect of different pretreatment methods on power production in microbial fuel cells. *Environmental Science & Technology*, **43** (17), 6870–6874.

28 Park, D.H. and Zeikus, J.G. (1999) Utilization of electrically reduced neutral red by *Actinobacillus succinogenes*: physiological function of neutral red in membrane-driven fumarate reduction and energy conservation. *Journal of Bacteriology*, **181** (8), 2403–2410.

29 Kim, H.J., Park, H.S., Hyun, M.S., Chang, I.S., Kim, M., and Kim, B.H. (2002) A mediator-less microbial fuel cell using a metal reducing bacterium, *Shewanella putrefaciens*. *Enzyme and Microbial Technology*, **30** (2), 145–152.

30 In Ho, P., Gnana Kumar, G., Kim, A.R., Kim, P., and Suk Nahm, K. (2011) Microbial electricity generation of diversified carbonaceous electrodes under variable mediators. *Bioelectrochemistry*, **80** (2), 99–104.

31 Fan, Y., Sharbrough, E., and Liu, H. (2008) Quantification of the internal resistance distribution of microbial fuel cells. *Environmental Science & Technology*, **42** (21), 8101–8107.

32 Larrosa-Guerrero, A., Scott, K., Katuri, K.P., Godinez, C., Head, I.M., and Curtis, T. (2010) Open circuit versus closed circuit enrichment of anodic biofilms in MFC: effect on performance and anodic communities. *Applied Microbiology and Biotechnology*, **87** (5), 1699–1713.

33 Johnson, W.P. and Logan, B.E. (1996) Enhanced transport in porous media by sediment-phase and aqueous-phase natural organic matter. *Water Research*, **30** (4), 923–931.

34 Cheng, S. and Logan, B.E. (2007) Ammonia treatment of carbon cloth anodes to enhance power generation of microbial fuel cells. *Electrochemistry Communications*, **9**, 492–496.

35 Park, D.H. and Zeikus, J.G. (2003) Improved fuel cell and electrode designs for producing electricity from microbial degradation. *Biotechnology and Bioengineering*, **81**, 348–355.

36 Lowy, D., Tender, L.M., Zeikus, J.G., Park, D.H., and Lovley, D.R. (2006) Harvesting energy from the marine sediment–water interface II: kinetic activity of anode materials. *Biosensors and Bioelectronics*, **21**, 2058–2063.

37 Crittenden, S.R., Sund, C.J., and Sumner, J.J. (2006) Mediating electron transfer from bacteria to a gold electrode via a self-assembled monolayer. *Langmuir*, **22** (23), 9473–9476.

38 Adachi, M., Shimomura, T., Komatsu, M., Yakuwa, H., and Miya, A. (2008) A novel mediator-polymer-modified anode for microbial fuel cells. *Chemical Communications*, **7**, 2055–2057.

39 Niessen, J., Schröder, U., Rosenbaum, M., and Scholz, F. (2004) Fluorinated polyanilines as superior materials for electrocatalytic anodes in bacterial fuel cells. *Electrochemistry Communications*, **6**, 571–575.

40 Chung, K., Fujiki, I., and Okabe, S. (2011) Effect of formation of biofilms and chemical scale on the cathode electrode on the performance of a continuous two-chamber microbial fuel cell. *Bioresource Technology*, **102**, 355–360.

41 Qiao, Y., Li, C.M., Bao, S.J., and Bao, Q.L. (2007) Carbon nanotube/polyaniline composite as anode material for microbial fuel cells. *Journal of Power Sources*, **170**, 79–84.

42 Qiao, Y., Bao, S.J., Li, C.M., Cui, X.Q., Lu, Z.S., and Bao, J. (2008) Nanostructured polyaniline/titanium dioxide composite anode for microbial fuel cells. *ACS Nano*, **2**, 113–119.

43 Sharma, T., Leel Mohana Reddy, A., Chandra, T.S., and Ramaprabhu, S. (2008) Development of carbon nanotubes and nanofluids based microbial fuel cell. *International Journal of Hydrogen Energy*, **33**, 6749–6754.

44 HaoYu, E., Cheng, S., Scott, K., and Logan, B. (2007) Microbial fuel cell performance with non-Pt cathode catalysts. *Journal of Power Sources*, **171** (2), 275–281.

45 Peng, L., You, S.-J., and Wang, J.-Y. (2010) Carbon nanotubes as electrode modifier promoting direct electron transfer from *Shewanella oneidensis*. *Biosensors and Bioelectronics*, **25**, 1248–1251.

46 Fan, Y., Xu, S., Schaller, R., Jiao, J., Chaplen, F., and Liu, H. (2011) Nanoparticle decorated anodes for enhanced current generation in microbial electrochemical cells. *Biosensors and Bioelectronics*, **26** (5), 1908–1912.

47 Sun, J.-J., Zhao, H.-Z., Yang, Q.-Z., Song, J., and Xue, A. (2010) A novel layer-by-layer self-assembled carbon nanotube-based anode: preparation, characterization, and application in microbial fuel cell. *Electrochimica Acta*, **55**, 3041–3047.

48 Wang, L., Liang, P., Zhang, J., and Huang, X. (2011) Activity and stability of pyrolyzed iron ethylenediaminetetraacetic acid as cathode catalyst in microbial fuel cells. *Bioresource Technology*, **102** (8), 5093–5097.

49 Huang, Y., He, Z., and Mansfeld, F. (2010) Performance of microbial fuel cells with and without Nafion solution as cathode binding agent. *Bioelectrochemistry*, **79** (2), 261–264.

50 Saito, T., Merrill, M.D., Watson, V.J., Logan, B.E., and Hickner, M.A. (2010) Investigation of ionic polymer cathode binders for microbial fuel cells. *Electrochimica Acta*, **55** (9), 3398–3403.

51 Zhang, L.X., Liu, C.S., Zhuang, L., Li, W.S., Zhou, S.G., and Zhang, J.T. (2009) Manganese dioxide as an alternative cathodic catalyst to platinum in microbial fuel cells. *Biosensors and Bioelectronics*, **24**, 2825–2829.

52 Cheng, S., Liu, H., and Logan, B.E. (2006) Power densities using different cathode catalysts (Pt and CoTMPP) and polymer binders (Nafion and PTFE) in single chamber microbial fuel cells. *Environmental Science & Technology*, **40** (1), 364–369.

53 Wang, X., Feng, Y., Liu, J., Shi, X., Lee, H., Li, N., and Ren, N. (2010) Power generation using adjustable Nafion/PTFE mixed binders in air-cathode microbial fuel cells. *Biosensors and Bioelectronics*, **26** (2), 946–948.

54 Saito, T., Roberts, T.H., Long, T.E., Logan, B.E., and Hickner, M.A. (2011) Neutral hydrophilic cathode catalyst binders for microbial fuel cells. *Energy & Environmental Science*, **4** (3), 928–934.

55 Zhang, F., Saito, T., Cheng, S., Hickner, M.A., and Logan, B.E. (2010) Microbial

fuel cell cathodes with poly (dimethylsiloxane) diffusion layers constructed around stainless steel mesh current collectors. *Environmental Science & Technology*, **44** (4), 1490–1495.

56 Deng, Q., Li, X., Zuo, J., Ling, A., and Logan, B.E. (2010) Power generation using an activated carbon fiber felt cathode in an upflow microbial fuel cell. *Journal of Power Sources*, **195** (4), 1130–1135.

57 Zhang, F., Merrill, M.D., Tokash, J.C., Saito, T., Cheng, S., Hickner, M.A., and Logan, B.E. (2011) Mesh optimization for microbial fuel cell cathodes constructed around stainless steel mesh current collectors. *Journal of Power Sources*, **196** (3), 1097–1102.

58 Kiely, P.D., Rader, G., Regan, J.M., and Logan, B.E. (2011) Long-term cathode performance and the microbial communities that develop in microbial fuel cells fed different fermentation endproducts. *Bioresource Technology*, **102** (1), 361–366.

59 Lefebvre, O., Al-Mamun, A., Ooi, W.K., Tang, Z., Chua, D.H.C., and Ng, H.Y. (2008) An insight into cathode options for microbial fuel cells. *Water Science & Technology*, **57** (12), 2031–2037.

60 Harnisch, F. and Schröder, U. (2010) From MFC to MXC: chemical and biological cathodes and their potential for microbial bioelectrochemical systems. *Chemical Society Reviews*, **39** (11), 4433–4448.

61 Sanchez, D.V.P., Huynh, P., Kozlov, M.E., Baughman, R.H., Vidic, R.D., and Yun, M. (2010) Carbon nanotube/platinum (Pt) sheet as an improved cathode for microbial fuel cells. *Energy & Fuels*, **24** (11), 5897–5902.

62 Wang, H., Wu, Z., Plaseied, A., Jenkins, P., Simpson, L., Engtrakul, C., and Ren, Z. (2011) Carbon nanotube modified air-cathodes for electricity production in microbial fuel cells. *Journal of Power Sources*, **196** (18), 7465–7469.

63 Xie, X., Pasta, M., Hu, L., Yang, Y., McDonough, J., Cha, J., Criddle, C.S., and Cui, Y. (2011) Nano-structured textiles as high-performance aqueous cathodes for microbial fuel cells. *Energy & Environmental Science*, **4** (4), 1293–1297.

64 Wang, X., Cheng, S., Zhang, X., Li, X.-Y., and Logan, B.E. (2011) Impact of salinity on cathode catalyst performance in microbial fuel cells (MFCs). *International Journal of Hydrogen Energy*, **36** (21), 13900–13906.

65 Zhao, F., Harnisch, F., Schröder, U., Scholz, F., Bogdanoff, P., and Herrmann, I. (2005) Application of pyrolysed iron(II) phthalocyanine and CoTMPP based oxygen reduction catalysts as cathode materials in microbial fuel cells. *Electrochemistry Communications*, **7** (12), 1405–1410.

66 Birry, L., Mehta, P., Jaouen, F., Dodelet, J.-P., Guiot, S.R., and Tartakovsky, B. (2011) Application of iron-based cathode catalysts in a microbial fuel cell. *Electrochimica Acta*, **56** (3), 1505–1511.

67 Zhao, F., Harnisch, F., Schröder, U., Scholz, F., Bogdanoff, P., and Herrmann, I. (2006) Challenges and constraints of using oxygen cathodes in microbial fuel cells. *Environmental Science & Technology*, **40** (17), 5193–5199.

68 Aelterman, P., Versichele, M., Genettello, E., Verbeken, K., and Verstraete, W. (2009) Microbial fuel cells operated with iron-chelated air cathodes. *Electrochimica Acta*, **54** (24), 5754–5760.

69 Morris, J.M., Jin, S., Wang, J.Q., Zhu, C.Z., and Urynowicz, M.A. (2007) Lead dioxide as an alternative catalyst to platinum in microbial fuel cells. *Electrochemistry Communications*, **9**, 1730–1734.

70 Zhuang, L., Zhou, S., Wang, Y., Liu, C., and Geng, S. (2009) Membrane-less cloth cathode assembly (CCA) for scalable microbial fuel cells. *Biosensors and Bioelectronics*, **24** (12), 3652–3656.

71 Lefebvre, O., Ooi, W.K., Tang, Z., Abdullah-Al-Mamun, Md., Chua, D.H.C., and Ng, H.Y. (2009) Optimization of a Pt-free cathode suitable for practical applications of microbial fuel cells. *Bioresource Technology*, **100** (20), 4907–4910.

72 Zhang, F., Cheng, S., Pant, D., Bogaert, G.V., and Logan, B.E. (2009) Power generation using an activated carbon and metal mesh cathode in a microbial fuel

cell. *Electrochemistry Communications*, **11** (11), 2177–2179.
73 Duteanu, N., Erable, B., Senthil Kumar, S.M., Ghangrekar, M.M., and Scott, K. (2010) Effect of chemically modified Vulcan XC-72R on the performance of air-breathing cathode in a single-chamber microbial fuel cell. *Bioresource Technology*, **101** (14), 5250–5255.
74 Feng, C., Li, F., Liu, H., Lang, X., and Fan, S. (2010) A dual-chamber microbial fuel cell with conductive film-modified anode and cathode and its application for the neutral electro-Fenton process. *Electrochimica Acta*, **55** (6), 2048–2054.
75 Fu, L., You, S.-J., Zhang, G.-Q., Yang, F.-L., Fang, X.-H., and Gong, Z. (2011) PB/PANI-modified electrode used as a novel oxygen reduction cathode in microbial fuel cell. *Biosensors and Bioelectronics*, **26** (5), 1975–1979.
76 Feng, C., Wan, Q., Lv, Z., Yue, X., Chen, Y., and Wei, C. (2011) One-step fabrication of membraneless microbial fuel cell cathode by electropolymerization of polypyrrole onto stainless steel mesh. *Biosensors and Bioelectronics*, **26** (9), 3953–3957.
77 Ter Heijne, A., Strik, D.P.B.T.B., Hamelers, H.V.M., and Buisman, C.J.N. (2010) Cathode potential and mass transfer determine performance of oxygen reducing biocathodes in microbial fuel cells. *Environmental Science & Technology*, **44** (18), 7151–7156.
78 Clauwaert, P., van derHa, D., Boon, N., Verbeken, K., Verhaege, M., Rabaey, K., and Verstraete, W. (2007) Open air biocathode enables effective electricity generation with microbial fuel cells. *Environmental Science & Technology*, **41** (21), 7564–7569.
79 You, S.-J., Ren, N.-Q., Zhao, Q.-L., Wang, J.-Y., and Yang, F.-L. (2009) Power generation and electrochemical analysis of biocathode microbial fuel cell using graphite fibre brush as cathode material. *Fuel Cells*, **9** (5), 588–596.
80 Wang, X., Feng, Y., Liu, J., Lee, H., Li, C., Li, N., and Ren, N. (2010) Sequestration of CO_2 discharged from anode by algal cathode in microbial carbon capture cells (MCCs). *Biosensors and Bioelectronics*, **25** (12), 2639–2643.
81 Mitra, P. and Hill, G.A. (2011) Continuous microbial fuel cell using a photoautotrophic cathode and a fermentative anode. *The Canadian Journal of Chemical Engineering*, **90** (4), 1006–1010.
82 Clauwaert, P., Rabaey, K., Aelterman, P., DeSchamphelaire, L., Pham, T.H., Boeckx, P., Boon, N., and Verstraete, W. (2007) Biological denitrification in microbial fuel cells. *Environmental Science & Technology*, **41**, 3354–3360.
83 Tandukar, M., Huber, S.J., Onodera, T., and Pavlostathis, S.G. (2009) Biological chromium(VI) reduction in the cathode of a microbial fuel cell. *Environmental Science & Technology*, **43** (21), 8159–8165.
84 Kim, J.R., Oh, S.-E., Cheng, S., and Logan, B.E. (2007) Power generation using different cation, anion and ultrafiltration membranes in microbial fuel cells. *Environmental Science & Technology*, **41** (3), 1004–1009.
85 Ter Heijne, A., Hamelers, H.V.M., De Wilde, V., Rozendal, R.A., and Buisman, C.J.N. (2006) A bipolar membrane combined with ferric iron reduction as an efficient cathode system in microbial fuel cells. *Environmental Science & Technology*, **40** (17), 5200–5205.
86 Biffinger, J.C., Pietron, J., Ray, R., Little, B., and Ringeisen, B.R. (2007) A biofilm enhanced miniature microbial fuel cell using *Shewanella oneidensis* DSP10 and oxygen reduction cathodes. *Biosensors and Bioelectronics*, **22** (8), 1672–1679.
87 Fan, Y., Hu, H., and Liu, H. (2007) Enhanced coulombic efficiency and power density of air-cathode microbial fuel cells with an improved cell configuration. *Journal of Power Sources*, **171** (2), 348–354.
88 Cheng, S., Liu, H., and Logan, B.E. (2006) Increased power generation in a continuous fow MFC with advective flow through the porous anode and reduced electrode spacing. *Environmental Science & Technology*, **40** (7), 2426–2432.

89 Rozendal, R.A., Hamelers, H.V.M., and Buisman, C.J.N. (2006) Effects of membrane cation transport on pH and microbial fuel cell performance. *Environmental Science & Technology*, **40**, 5206–5211.

90 Zuo, Y., Cheng, S., and Logan, B.E. (2008) Ion exchange membrane cathodes for scalable microbial fuel cells. *Environmental Science & Technology*, **42** (18), 6967–6972.

91 Rozendal, R.A., Sleutels, T.H.J.A., Hamelers, H.V.M., and Buisman, C.J.N. (2008) Effect of the type of ion exchange membrane on performance, ion transport, and pH in biocatalyzed electrolysis of wastewater. *Water Science & Technology*, **57**, 1757–1762.

92 Zuo, Y., Cheng, S., Call, D., and Logan, B.E. (2007) Tubular membrane cathodes for scalable power generation in microbial fuel cells. *Environmental Science & Technology*, **41** (9), 3347–3353.

93 Kim, J.R., Premier, G.C., Hawkes, F.R., Dinsdale, R.M., and Guwy, A.J. (2009) Development of a tubular microbial fuel cell (MFC) employing a membrane electrode assembly cathode. *Journal of Power Sources*, **187** (2), 393–399.

94 Sun, J., Hu, Y., Bi, Z., and Cao, Y. (2009) Improved performance of air-cathode single-chamber microbial fuel cell for wastewater treatment using microfiltration membranes and multiple sludge inoculation. *Journal of Power Sources*, **187** (2), 471–479.

95 Sun, J., Hu, Y.-Y., Bi, Z., and Cao, Y.-Q. (2009) Simultaneous decolorization of azo dye and bioelectricity generation using a microfiltration membrane air-cathode single-chamber microbial fuel cell. *Bioresource Technology*, **100** (13), 3185–3192.

96 Butler, C.S. and Nerenberg, R. (2010) Performance and microbial ecology of air-cathode microbial fuel cells with layered electrode assemblies. *Applied Microbiology and Biotechnology*, **86** (5), 1399–1408.

97 Zhang, X., Cheng, S., Huang, X., and Logan, B.E. (2010) The use of nylon and glass fiber filter separators with different pore sizes in air-cathode single-chamber microbial fuel cells. *Energy & Environmental Science*, **3** (5), 659–664.

98 Hou, B., Sun, J., and Hu, Y.-Y. (2011) Simultaneous Congo red decolorization and electricity generation in air-cathode single-chamber microbial fuel cell with different microfiltration, ultrafiltration and proton exchange membranes. *Bioresource Technology*, **102** (6), 4433–4438.

99 Watson, V.J., Saito, T., Hickner, M.A., and Logan, B.E. (2011) Polymer coatings as separator layers for microbial fuel cell cathodes. *Journal of Power Sources*, **196** (6), 3009–3014.

100 Logan, B.E. and Regan, J.M. (2006) Microbial fuel cells: challenges and applications. *Environmental Science & Technology*, **40**, 5172–5180.

101 Logan, B.E., Aelterman, P., Hamelers, B., Rozendal, R., Schröeder, U., Keller, J., Freguiac, S., Verstraete, W., and Rabaey, K. (2006) Microbial fuel cells: methodology and technology. *Environmental Science & Technology*, **40** (17), 5181–5192.

8
Bioelectrochemical Systems

Falk Harnisch and Korneel Rabaey

8.1
Bioelectrochemical Systems and Bioelectrocatalysis

A bioelectrochemical system (BES) exploits biological catalysts for anode and/or cathode reactions, or both. In this regard, "bioelectrocatalysts" can be defined as moieties of biological origin leading to an increase of the rate constant of a given electrode reaction and a corresponding decrease of its overpotential. As depicted in Figure 8.1, three different classes of bioelectrocatalysts can be distinguished, ranging from single enzymes (e.g., dehydrogenases [1]) or enzyme arrays and organelles (e.g., mitochondria [2,3]) to entire living microbial cells. The latter, referred to as microbial bioelectrocatalysts, have attracted increasing attention in the past years, as they offer appealing advantages: They are self-reproducing, can catalyze multielectron reaction steps often with high specificity, and are able to transform complex substrates or mixtures thereof. This chapter will focus on these microbial bioelectrocatalysts.

First we will discuss the similarities and differences between conventional chemical and microbial bioelectrocatalysts. Subsequently, the principal mechanisms of the extracellular electron transfer (EET) and the technology aiming at their exploitation will be introduced. Finally, the biological and electrochemical methods that allow the analysis of the microbial electron transfer and identification of the respective mediators, proteins, and microorganisms will be addressed.

8.2
On the Nature of Microbial Bioelectrocatalysis

Microbial bioelectrocatalysts are living cells. As a consequence, they need a certain amount of energy for their maintenance and proliferation. Cells use energy gained to produce ATP and NAD(P)H, the two main energy carriers. In order to generate these, they need to build up internal potential gradients, which externally lead to a loss of useful potential. In the context of bioelectrocatalysis, this

Materials for Low-Temperature Fuel Cells, First Edition. Edited by Bradley Ladewig, San P. Jiang, and Yushan Yan.

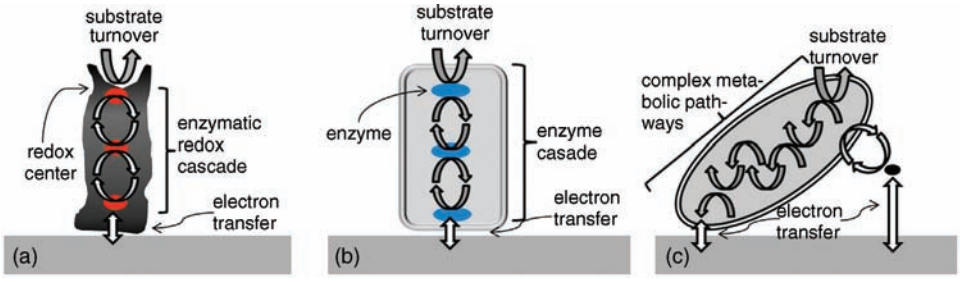

Figure 8.1 Types of bioelectrocatalysts (a) enzymes, (b) organelles, and (c) microorganisms.

share of energy is usually extracted from a part of the energetic difference between electron donor and electron acceptor of the catalyzed reaction. This will be discussed using the example of an anodic, acetate oxidizing biofilm. In a typical anodic biofilm, operated at 0.400 V (provided versus SHE, as all potentials in this chapter, if not indicated otherwise) and dominated by *Geobacter* species, the net reaction of the acetate oxidation is as follows:

$$C_2H_4O_2 + 2H_2O \rightarrow 2CO_2 + 8H^+ + 8e^- \tag{8.1}$$

(Note that reaction (8.1) and all following reactions and derived equations are, for simplicity reasons, based on the neutral species.)

The biological standard potential of the acetate/CO_2–redox couple is $E^{0'} = -0.290$ V; it needs to be noted that potentials may vary substantially based on the local concentrations of the substrate and the oxidation/reduction products [4]. Thus, the maximum extractable voltage difference, ΔE, for the described scenario is 0.690 V, which is equivalent to an energy difference of maximum 66.6 kJ mol^{-1} of transferred electrons ($\Delta G_{max} = 66.6$ kJ $mol_{e^-}^{-1}$ according to $\Delta G = -nF\Delta E$). However, the microorganisms do not transfer the electron at a potential of −0.290 V to the anode, but at roughly −0.150 V (versus SHE, equivalent to −0.350 V versus Ag/AgCl). As a consequence, the potential difference between the terminal electron shuttle and the anode is maximal 0.550 V. The real maximum energy gain per electron for the microbial bioelectrocatalytic acetate oxidation is thus $\Delta G_{real} = 53.1$ kJ $mol_{e^-}^{-1}$. From the microorganism perspective, the remaining energy share is $\Delta G_{microbio} = 13.5$ kJ $mol_{e^-}^{-1}$ per electron and this can potentially be exploited for growth. All known microbial bioelectrocatalysts extract a certain share of the energy difference between electron donor and acceptor, which is actually the driving force for their setup from the biological perspective. Thus, strictly speaking, the term "bioelectrocatalysis" might not be entirely correct, but it is conveniently used in literature and in this chapter.

When comparing the microbial bioelectrocatalyst with a conventional, noble metal-based electrocatalyst for low-temperature fuel cells, it appears that the aforementioned energetic disadvantage could be compensated by a number of advantages (Table 8.1).

Table 8.1 Operating conditions of a microbial bioelectrocatalyst and an electrocatalyst in a low-temperature fuel cell.

Parameter	Conventional electrocatalyst	Microbial bioelectrocatalyst
Operating temperature	Room temperature to high temperatures	Observed 15–75 °C
Fuel, "substrate"	Simple molecules, for example, H_2, methanol	From simple to complex, mixed substrates
Purity	Pure substrates required	No purity required
Longevity	Limited, corrosion	Self-regenerating
Costs	Considerable	Negligible
Process rate	Fast (several A m^{-2} level)	Medium (A m^{-2} level)
Catalyst volume	Small (nm size)	Considerable (single cells micrometer level, biofilms 10–50 μm)
Medium requirements	Typically pure water or solvent	Water-based mixture containing nutrients (N, P, trace elements) and vitamins
Selectivity	Often low	Potentially high, up to 100%

8.3 Microbial Electron Transfer Mechanisms

As already discussed, microorganisms extract a certain share of energy for their living from the maximum theoretically exploitable energetic difference. In case of anodic bioelectrocatalysis, the energy difference is situated between the microbial substrate, that is, the fuel, and the potential of the terminal electron transfer site. Furthermore, and like in conventional electrocatalytic systems [5], several energetic losses at the bioelectrocatalyst–electrode interface occur (Figure 8.2).

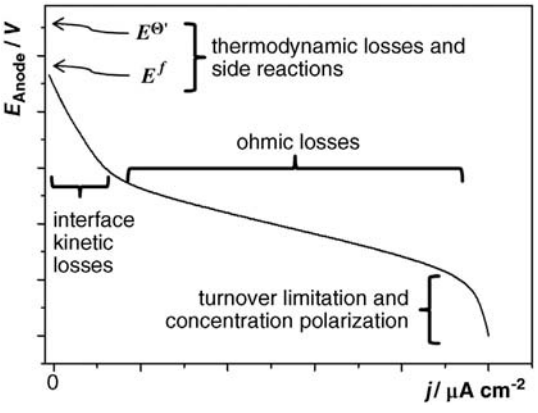

Figure 8.2 Polarization curve of a microbial bioanode. The deviation between biological standard potential and the measured formal potential at open circuit is indicated as well as the different losses during electrode polarization from open circuit to maximum current.

As shown in Figure 8.2, these losses include thermodynamic as well as kinetic losses, losses due to the microbial metabolism, and the electron transfer kinetics at the electrode interface; see for example, Refs [6,7] for a detailed treatise. In the following, the electron transfer pathways between microorganisms and electrodes will be discussed. Noteworthy, this discussion will mainly focus on bioelectrocatalytic anodes, that is, the electrode is used as an electron acceptor, as only very little is known about the mechanisms at microbial biocathodes [8].

From its first description in 1911 by Potter [9] until the mid-1990s, it was believed and generally acknowledged that exogenous, artificial redox substances are needed to facilitate reversible electron shuttles between the microorganism and the electrode. These mediators were often toxic organic dyes like neutral red [10] or methylene blue. However, the addition of these endogenous substances is not necessary [11], and we are now starting to understand both the mechanisms of direct electron transfer (DET) (see Section 8.3.1) and mediated electron transfer (MET) based on primary and secondary metabolites rather than via addition of redox mediators (MET) (see Section 8.3.2).

8.3.1
Direct Electron Transfer

Common to DET mechanisms is the necessity of some form of physical contact between the microorganism and the terminal electron acceptor. As Figure 8.3 shows, two possibilities of DET can be distinguished: DET via membrane-bound redox proteins and DET via bacterial pili – so-called "nanowires." Recent research indicates that these options likely occur in conjunction, and are mutually dependent to achieve high electron transfer rates.

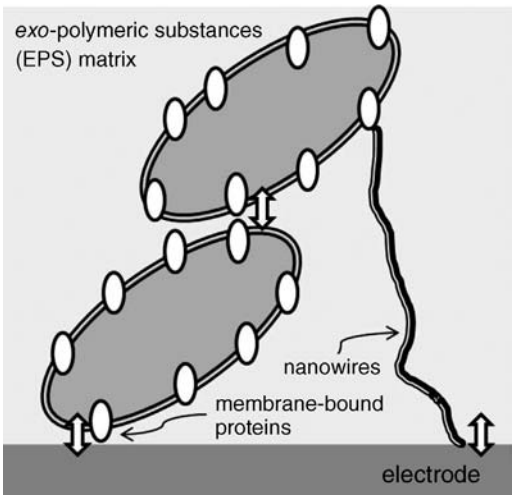

Figure 8.3 Sketch of DET via membrane-bound DET proteins and nanowires to the electrode and between the bacteria.

Direct transfer via membrane proteins at first glance appears to be the most straightforward electron transfer pathway, the whole bacterial cell is positioned adjacent to the anode and tunnels its electrons through the bacterial membrane. DET using membrane-bound enzymes is ascribed to a number of microorganisms, most prominently *Geobacter* [12] and *Shewanella* species. Whereas *Geobacter* species carry a wide variety of c-type cytochromes with limited individual potential bandwidth and which can be expressed under different circumstances to achieve this electron transfer [13], *Shewanella oneidensis* appears to mainly use a multiheme complex MtrCAB that has a broad potential range (a good overview on this complex can be found in Ref. [14]). Interestingly, considerably higher current densities are achieved with *Geobacter* relative to other described species, demonstrating that its approach makes it ideally suited for microbial bioelectrocatalysis. Interestingly, whereas for only monolayer biofilm forming species like *Rhodoferax* the current densities seem to be severely limited (e.g., $3\,\mu A\,cm^{-2}$) [15], other species can produce significant higher current densities and this relates to the fact that biofilms containing many layers of cells form on anodes. This highlights that direct electron transfer is only one of the means for current formation.

In 2005, it was first described that microorganisms express pili or pilus-like structures in conditions relevant for EET. It was shown that these structures, "nanowires," are conductive in the transversal direction [16,17] and more recently in the longitudinal direction [18,19]. These nanowires would allow the microorganism to connect its membrane-bound terminal electron shuttle (e.g., a cytochrome) via conductive pili to the terminal electron acceptor (see Figure 8.3) [16,17]. This strategy was reported to increase the achievable current density by orders of magnitude compared with the above-described DET using membrane-bound proteins, with the presently maximum achieved geometric current density of $3\,mA\,cm^{-2}$ (see also Table 8.2) [20]. Many mechanistic questions on this electron transfer pathway and on the role of the complex biofilm matrix remain to be addressed [21]. It is important to note here that current density depends not just on the presence of the nanowires but is also intricately linked to the expression of cytochromes both associated with the bacterial membrane and released in the biofilm [22,23]. It is possible that these cytochromes allow electron transfer from the nanowires to the electrode, whereas the nanowires provide the transport from the cell to the electrode surface.

Whereas the mediated electron transfer, for example, via the oxidation of primary metabolites, can be realized with cell suspensions (see later) without any direct interaction of the living cell and the electrode material, an attachment of the bacterial cells (or its appendices) to an electrode surface is compulsory for the direct electron transfer. This attachment is not necessarily permanent, some bacterial species possess a directed motility toward prospective electron acceptors such as electrodes allowing a DET of suspended cells [24]. Furthermore, there is growing evidence that the matrix of exopolymeric substances (EPS) may also play an important role in the microbial electron transfer [25].

Table 8.2 Selected studies on different electrode materials and the associated maximum current densities per projected surface area at maximum power.

Anode material	Microbial source	Substrate	j_{max} ($\mu A\,cm^{-2}$)	Reference
Glassy carbon	*Geobacter*	Acetate	100	[56]
Graphite fiber brush	Preacclimated MFC	Acetate	800	[57]
Polycrystalline carbon	Wastewater	Acetate	920	[55]
Carbon paper	Wastewater	Acetate	1350	[55]
Polyaniline on graphite felt	Rice paddy field soil	Starch, peptone, and fish extract	2400	[58]
Electrospun carbon fiber mats	Wastewater	Acetate	3000	[20]

The actual operation conditions, for example, temperature, differ among the studies.

8.3.2 Mediated Electron Transfer (MET)

Mediated electron transfer can be realized either by primary or by secondary microbial metabolites [26], both concepts are summarized in Figure 8.4. Whereas the latter substances are used for a reversible shuttling of electrons, primary metabolites are mostly irreversibly oxidized. Depending on the origin of the shuttling compounds, one can distinguish endogenous and exogenous shuttles.

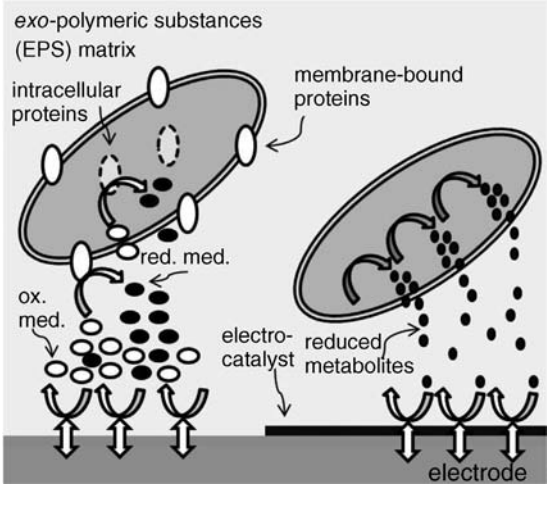

Figure 8.4 MET mechanisms.

8.3.2.1 MET Based on Secondary Metabolites

Whereas artificially added exogenous redox shuttles were used at the onset of EET research [27], the electron transfer via microbially synthesized secondary metabolites is increasingly studied. Secondary metabolites are synthesized by the bacteria not using the main catabolic metabolic pathways, therefore, their synthesis is an energetic investment of the bacteria. These compounds, for example, pycocyanine [28] or 2-amino-3-carboxy-1,4-naphthoquinone [29], allow the electron transfer within thicker biofilms (and even between planktonic cells and the anode) and thus lead to an increase of the performance of microbial fuel cell (MFC) anodes. This electron transfer pathway has been reported for a few single species (e.g., *Pseudomonas* sp.) [30] and for microbial biofilms from natural inoculi. Interestingly, there is increasing evidence that distinct shuttle compounds can not only be used by microorganism of the same species they were synthesized by but also (and even more effective) by other microbial species [30]. In this context of complex bacterial interaction, it is further observed that the electron shuttle compounds may also act as signaling substances for microbial communication, for example, quorum sensing [31]. Finally, it can be considered that some compounds, such as humic substances, can be the result of microbial degradation and used by a lots of other organisms in the natural environment and in the laboratory in the context of EET [32].

8.3.2.2 MET Based on Primary Metabolites

Primary metabolites are directly linked to the microbial catabolic (in case of anodic biofilms) metabolism and thus mainly derive from microbial anaerobic respiration as well as fermentation, with key examples being hydrogen and sulfide. These compounds are mostly "waste products" from the microorganism's perspective and serve the purpose of adjusting the intracellular redox balance. For their exploitation at the anode of microbial BESs, these compounds have to be oxidized at an electrocatalytic electrode surface. This anode concept has been used for the oxidation of hydrogen produced during glucose fermentation on a platinum polymer-based sandwich electrode. In a subsequent step, these noble metal-free materials were replaced by noble metal-free electrode electrocatalysts allowing the oxidation of not only H_2 but also low-molecular organic acids such as formate and lactate [33–35]. Furthermore, the exploitation of sulfur species [36–38] can be classified within this electron transfer concept, although it needs to be noted that sulfur species can be reversibly cycled over sulfide/sulfur in BESs [39].

8.4 From Physiology to Technology: Microbial Bioelectrochemical Systems

Based on the initial findings of Potter [9,40], the possibility to produce electricity from microbial decomposition was intermittently studied during the twentieth century. The first increase in research efforts was at the time of the NASA

Apollo program, focusing on the exploitation of human feces and urine [41,42]. The attention, however, decreased after photovoltaics provided an excellent electric energy source for space ships. Initiated by Wilkinson, bioelectrocatalytic electricity generation for autonomous robots, so-called gastrobots, was investigated in the 1990s [43]. Based on the discovery of self-formation of electrocatalytic biofilms from even complex natural sources such as wastewater [11,44,45] and driven by the awareness that the systems allow the exploitation of low-value biomasses (see Section 8.4.1 for details) [26], the research efforts were accelerated. For a long time, the sole application purpose of these systems was as MFCs (see Figure 8.5a) [46]. One of the most important developments of the past period was the introduction of new application goals starting with the redirection of microbial fermentations [47,48] and microbially assisted hydrogen production in 2005 [49]. Since then, numerous application concept and niches, including bioremediation cells [50], microbial desalination cells [51], photobioelectrochemical cells [52], and many more [7] evolved. These are now summarized as microbial bioelectrochemical systems [53]. A new avenue is microbial electrosynthesis [54]. Here microorganisms are used not only at the anode, as already described but also at the cathode for the upgrading and synthesis of value-added chemicals; the principal of a microbial electrosynthesis cell is depicted in Figure 8.5b.

In most cases, BESs make use of biofilms attached to the electrodes to achieve the bioelectrocatalysis. Thus, the electrode plays a dual role, as substrate for biofilm formation as well as suitable surface for electron exchange with the cells or terminal electron shuttles. Consequently, its microbially accessible surface area –

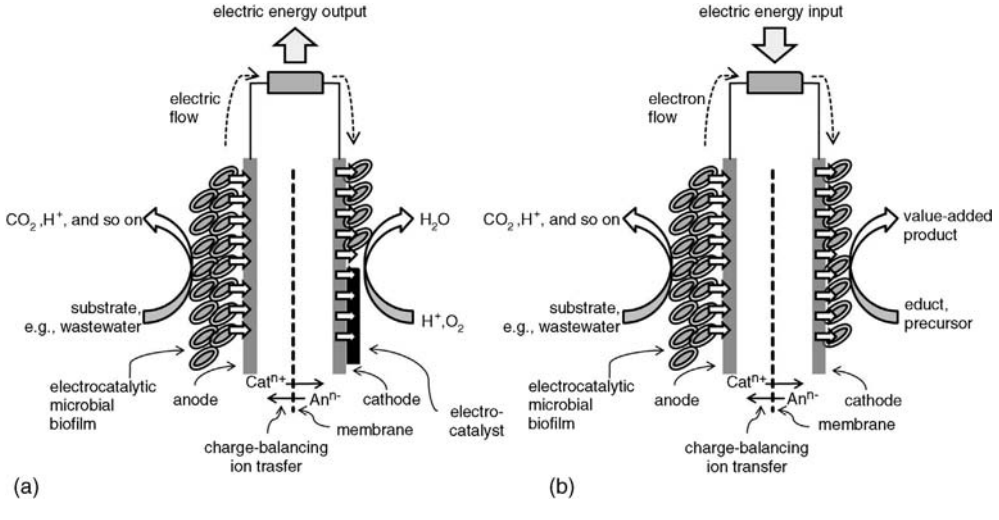

Figure 8.5 Example sketches of (a) a microbial fuel cells and (b) a microbial electrosynthesis cell to convert wastewater at the anode and produce biochemicals at the cathode.

which is neither equivalent with its geometric area nor its real surface area determined by gas-absorption [55] – predetermines the overall biofilm formation. To date, there has been no precise determination of this biologically relevant surface. Table 8.2 gives an overview of selected electrode materials and the respectively achieved maximum geometric current densities using electroactive microbial biofilms.

Noteworthy, from a wastewater engineering point of view, the coulombic efficiency and related organics removal is often considered the more relevant parameter relative to optimized geometric current densities. Therefore, 3D electrode materials such as graphite granules are often used in this context [59]. In this regard, the usage of volumetric current densities, for example, in A per cubic meter reactor volume, rather than per electrode, surface area is convenient. However, any reporting should still include the surface-based conversion as the key cost of a system is determined by the membrane electrode assembly (MEA) it requires [60].

8.5 Application Potential of BES Technology

BESs have seen a tremendous increase in possible applications in the past years. The key focus until 2005 was on energy generation via MFCs [26,61]. As energy is a low-value commodity, except from niche applications, such as remote power production, bringing MFCs to practice will require (very) low-cost reactor systems with still adequate performance and within acceptable reactor volumes [62]. Furthermore, it will require that the wastewater is effectively treated with lower sludge production, in a configuration that also considers the need to remove nutrients. Exept from these cost considerations are systems such as sediment fuel cells powering remote applications [63], as well as MFCs deployed at forward-operating bases from the military.

Considering the value of electrical energy, pathways that produce value-added products appear to deliver a better return. Hydrogen gas brings moderate values [64], while products such as caustic soda [65] and hydrogen peroxide [66] allow more sophisticated reactor systems while still remaining competitive and without requiring full wastewater treatment. The future prospect of producing biochemicals further opens up new opportunities particularly for medium-value commodities within the biorefinery market [54]. Nevertheless, the cost of the systems will in many cases require secondary benefits such as salt removal to be competitive [51].

Wholly different cases are BESs for bioremediation and biosensing. In the context of bioremediation, BESs have delivered hereto unseen control of degradation or immobilization processes, for example, nitrobenzene [67] and uranium [68]. Similarly, BESs can simultaneously provide sensing abilities and power supply for remote sensors.

8.6
Characterization of BESs and Microbial Bioelectrocatalysts

The characterization of microbial bioelectrocatalysts and development of methods and techniques are therefore one of the most active and vital fields. One might distinguish two different types of methods (i) electrochemical methods (see Section 8.5.1) and (ii) biological methods (see Section 8.5.2). Whereas the former generally focus on the identification and characterization of the electron transfer, the latter are devoted to the identification, analysis, and spatial distribution of the bioelectrocatalytic cells and their environment.

8.6.1
Electrochemical Methods

8.6.1.1 Polarization Curves

One of the most widespread electrochemical techniques is the use of polarization curves on individual electrodes or entire BESs. This has been particularly popular for microbial fuel cells as a means to establish maximum power. Figure 8.6 shows an exemplary polarization curve of the cell potential of a microbial fuel cell as well as the derived power curve. From the engineering perspective, these polarization and power curves can provide important information on the limitation and bottlenecks within a certain BES device, for example, its total internal resistance and maximum power point. However, as shown in Figure 8.2, polarization curves of individual electrodes may provide further information on the bioelectrocatalysis and potential bottlenecks. Very important when recording these polarization curves is to adopt an appropriate scan rate to avoid power or current overshoots.

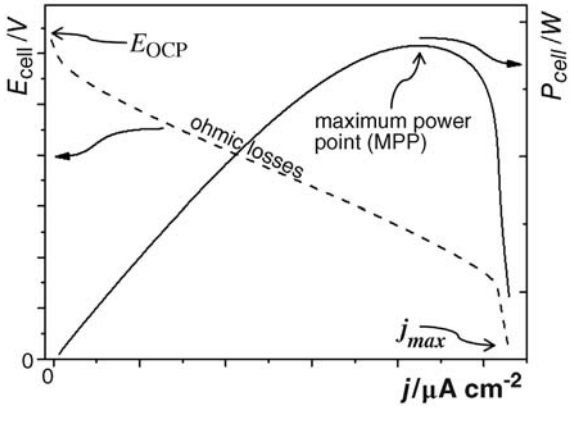

Figure 8.6 Fuel cell polarization and power curve. Characteristic points and generally derived information are indicated.

8.6.1.2 **Voltammetry**

In order to analyze the bioelectrocatalytic microbial electron transfer mechanisms in detail, voltammetric techniques can be exploited. These include, among other methods such as squarewave voltammetry, mostly cyclic voltammetry [69–71]. Figure 8.7 shows the non-turnover and turnover cyclic voltammetric curves of an anodic, *Geobacteraceae*-dominated [72] biofilm fed with acetate as electron source. Figure 8.7a shows the cyclic voltammetric curve of this anodic biofilm for non-turnover, that is, substrate-depleted conditions. One can clearly identify four oxidation–reduction couples, representing possible electron transfer sites. The respective formal potentials of these are indicated in the figure and denominated E_1^f to E_4^f. The corresponding CV for turnover conditions, that is, in the presence of the electron donor acetate, shows a typical (bio)electrocatalytic s-shape (Figure 8.7b). Interestingly, the first derivative (shown in the inset of Figure 8.7b) reveals clearly that only E_2^f and E_3^f are associated with the bacterial electron transfer, whereas E_1^f and E_4^f are not related to the bioelectrocatalytic activity. This means that the electrons gained from acetate are transferred to the anode at a potential of about −0.350 V (versus Ag/AgCl, equal to −0.150 V versus SHE) (see Section 8.2). It has to be mentioned that the in-depth kinetic and thermodynamic analysis of electrochemical data, including rate constant and so on, need new models and procedures (see Ref. [73] for kinetics), as due to the high complexity of these biofilms, "traditional models" from molecule or enzyme electrochemistry cannot readily be applied.

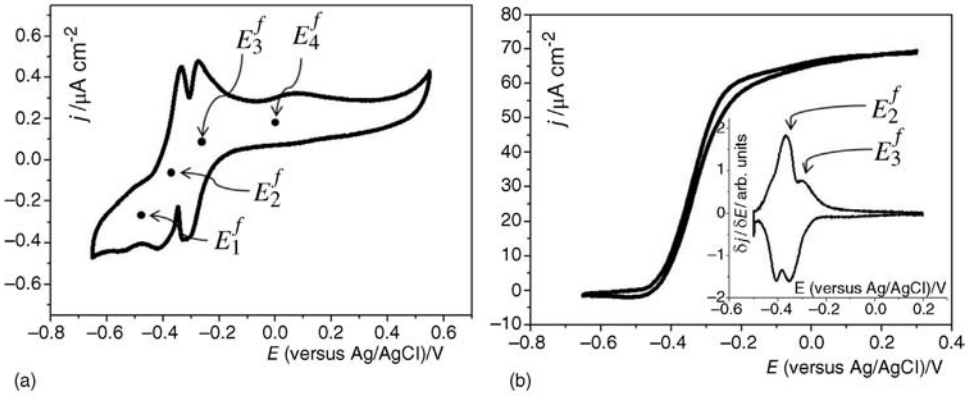

Figure 8.7 (a) CV of a *Geobacter* biofilm grown at 0.2 V versus Ag/AgCl on a graphite rod electrode in substrate depleted (non-turnover) conditions E_1^f to E_4^f indicates formal potentials of the four detected redox couples of the biofilm. (b) CV of the same biofilm in the presence of acetate (turnover conditions); the inset shows the first derivative of the CV curves and clearly reveals that only E_2^f and E_3^f are associated with the bacterial electron transfer (scan rate in all cases 1 mV s^{-1}). Data according to Ref. [69].

8.6.1.3 Spectroelectrochemical and Further Techniques

As already discussed, dynamic electrochemical techniques, such as cyclic voltammetry, can be exploited for the thermodynamic and – in a so far limited frame – kinetic analyses of bioelectrocatalytic electrodes. However, the identification of the underlying redox species is not possible by pure electrochemical means. Whereas mediators might be identified by purification from solution and subsequent spectroscopic characterization [28], this is often not possible for mediators, present only in low concentrations, and even more for direct electron transfer proteins. Here a combined spectroscopic and electrochemical analyses – the so-called spectroelectrochemistry – can provide the desired information. First, spectroelectrochemcial experiments on electroactive microorganism were performed on suspended cells of *Geobacter* using attenuated total reflectance surface-enhanced infrared absorption spectroscopy (ATR-SEIRAS) [74], followed by studies using UV/vis evanescent field wave spectroscopy [75], both allowing the general identification of cytochromes as redox active proteins. The first spectroelectrochemical study on living anodic biofilms (*in situ*), using surface-enhanced Raman resonance scattering (SERRS), allowed the exact identification of the catalytic center of the transmembrane protein of *Geobacter*-denominated biofilms as a six-coordinated low-spin heme with two histidine groups serving as axial ligands [76].

Further techniques that are exploited for full BES and individual electrode studies include electrochemical impedance spectroscopy [77], current interrupt method [78], Tafel plots [79], and others.

8.6.2 Biological Methods

Over the years, a vast array of microbial and molecular biotechnological methods have been applied particularly to the study of anodic biofilms. Due to the high diversity of methods and rapid progress in their development, no comprehensive overview can be provided, hence in the following a snapshot on the latest results will be shown for illustration.

For the analysis of microbial communities on electrode surfaces, many approaches exist and the method used evidently depends on the questions asked. It is not unreasonable to state that high-throughput sequencing-based methods provide the best level of information; however, at this point the cost may not always be justified by the questions. Once the community data are collected, more information can be derived than simple composition by calculating diversity-related parameters as outlined in Ref. [80]. It is important to note that a DNA-based analysis does not provide information on activity, and that typical 16SrRNA gene-based community analyses do not provide effective information on metabolic, and thus bioelectrocatalytic, potential of a certain microbial species or mixed culture. Here, the combinations of transcriptomics and proteomics, potentially in conjunction with deletion mutants or *in situ* imaging via for example, NanoSIMS, are required in future.

A key point to highlight is that biofilms on electrodes are three-dimensional structures of many micrometers thickness, and should be studied as such. While typical molecular analyses provide pooled information on the biofilm composition/activity, it is clear that the conditions vary along the biofilm leading to stratification [81]. This stratification can be evident through different types of organisms in mixed population systems, or through changes in transcriptome/proteome for pure culture systems. For microbial populations, analyses such as confocal laser scanning microscopy (CLSM) in combination with fluorescence *in situ* hybridization (FISH) are thus an essential part of community analysis [82]. For pure cultures, *in situ* imaging of specific genes or even biofilm subsampling is necessary to understand stratification [83].

Within the realm of these approaches, immunogold labeling can be of great value to address questions about electron transfer. For example, it was established that cytochromes can be associated with nanowires [17], and that in *Geobacter* biofilms OmcZ is a released cytochrome accumulating near the electrode surface [84]. From this it was hypothesized that it performed the role of a catalyst for transferring electrons from the nanowire to the electrode surface.

In a broader context, the importance of nowadays commonplace imaging techniques such as SEM and TEM cannot be underestimated to understand the architecture of electroactive biofilms. The required sample preparation – and thus possible destruction of the native biofilm state – has to be approached very carefully.

8.7 Conclusions

The field of BESs is rapidly expanding, leading to a vast array of applications in bioenergy, bioproduction, bioremediation, and biosensing. Due to the multidisciplinary nature of this technology, new developments need to integrate techniques from various disciplines while still providing the necessary quality for data reporting in every particular subfield. The following are the critical bottlenecks toward further development:

1) A better understanding and engineering of the electrode–cell interface.
2) The development of novel, cost-effective materials (electrodes, membranes, etc.) enabling to sustain electroactive biofilms.
3) The establishment of appropriate process parameters and characteristics (e.g., reactor geometries) to reach sufficient production, and respectively the removal levels.
4) The study and engineering of the microbial electrocatalyst toward increased versatility, robustness, and effectivity.

Besides providing perspectives for application, this chapter will also lead to a better understanding of the functioning of microorganisms in the natural and engineered environment.

Acknowledgments

F.H. gratefully acknowledges the support by the DAAD (postdoctoral scholarship) and the receipt of an Australia award – Endeavor Research Fellowship. K.R. acknowledges support from the Australian Research Council (DP0879245), the University of Queensland (Center for Microbial Electrosynthesis), and Bijzonder Onderzoeks Fonds UGent (BOF10/MRP/005).

References

1 Cracknell, J.A., Vincent, K.A., and Armstrong, F.A. (2008) Enzymes as working or inspirational electrocatalysts for fuel cells and electrolysis. *Chemical Reviews*, **108**, 2439–2461.
2 Moehlenbrock, M.J., Toby, T.K., Waheed, A., and Minteer, S.D. (2010) Metabolon catalyzed pyruvate/air biofuel cells. *Journal of the American Chemical Society*, **132**, 6288–6289.
3 Arechderra, R. and Minteer, S.D. (2008) Organelle-based biofuel cells: immobilized mitochondria on carbon paper electrodes. *Electrochimica Acta*, **53**, 6698–6703.
4 Madigan, M.T., Martink, J.M., and Parker, J. (1999) *Brock Biology of Microorganisms*, Prentice Hall International, Inc.
5 Katz, E., Shipway, A.N., and Willner, I. (2003) Biochemical fuel cells, in *Handbook of Fuel Cells: Fundamentals, Technology and Applications* (eds W. Vielstich, H.A. Gasteiger, and A. Lamm), John Wiley & Sons, Inc., Hoboken.
6 Schröder, U. and Harnisch, F. (2010) Electrochemical losses defining BES performance, in *Bioelectrochemical Systems: From Extracellular Electron Transfer to Biotechnological Application* (eds K. Rabaey, L. Angenent, U. Schröder, and J. Keller), IWA Publishing, London.
7 Harnisch, F. and Schröder, U. (2010) From MFC to MXC: chemical and biological cathodes and their potential for microbial bioelectrochemical systems. *Chemical Society Reviews*, **39**, 4433–4448.
8 Rosenbaum, M., Aulenta, F., Villano, M., and Angenent, L.T. (2011) Cathodes as electron donors for microbial metabolism: Which extracellular electron transfer mechanisms are involved? *Bioresource Technology*, **102** (1), 324–333.
9 Potter, M.C. (1912) Electrical effects accompanying the decomposition of organic compounds. *Proceedings of the Royal Society B: Biological Sciences*, **84**, 260–276.
10 Park, D.H. and Zeikus, J.G. (2000) Electricity generation in microbial fuel cell using neutral red as an electronophore. *Applied and Environmental Microbiology*, **66** (4), 1292–1297.
11 Kim, B.H., Park, D.H., Shin, P.K., Chang, I.S., and Kim, H.J. (1999) Mediator-less biofuel cell.
12 Lovley, D.R. (2008) The microbe electric: conversion of organic matter to electricity. *Current Opinion in Biotechnology*, **19**, 1–8.
13 Lovley, D.R. (2006) Bug juice: harvesting electricity with microorganisms. *Nature Reviews Microbiology*, **4**, 497–508.
14 Hartshorne, R.S., Reardon, C.L., Ross, D., Nuester, J., Clarke, T.A., Gates, A.J., Mills, P.C., Fredrickson, J.K., Zachara, J.M., Shi, L., Beliaev, A.S., Marshall, M.J., Tien, M., Brantley, S., Butt, J.N., and Richardson, D.J. (2009) Characterization of an electron conduit between bacteria and the extracellular environment. *Proceedings of the National Academy of Sciences of the United States of America*, **106** (52), 22169–22174.
15 Chaudhuri, S.K. and Lovley, D.R. (2003) Electricity generation by direct oxidation of glucose in mediatorless microbial fuel cells. *Nature Biotechnology*, **21** (10), 1229–1232.
16 Reguera, G., McCarthy, K.D., Mehta, T., Nicoll, J.S., Tuominen, M.T., and Lovley, D.R. (2005) Extracellular electron transfer

via microbial nanowires. *Nature*, **435**, 1098–1101.

17 Gorby, Y.A., Yanina, S., McLean, J.S., Rosso, K.M., Moyles, D., Dohnalkova, A., Beveridge, T.J., Chang, I.S., Kim, B.H., Kim, K.S., Culley, D.E., Reed, S.B., Romine, M.F., Saffarini, D.A., Hill, E.A., Shi, L., Elias, D.A., Kennedy, D.W., Pinchuk, G., Watanabe, K., Ishii, S.I., Logan, B., and Nealson, K.H., and Fredrickson, J.K. (2006) Electrically conductive bacterial nanowires produced by *Shewanella oneidensis* strain MR-1 and other microorganisms. *Proceedings of the National Academy of Sciences of the United States of America*, **103**, 11358–11363.

18 Malvankar, N.S., Vargas, M., Nevin, K.P., Franks, A.E., Leang, C., Kim, B.-C., Inoue, K., Mester, T., Covalla, S.F., Johnson, J.P., Rotello, V.M., and Tuominen, M.T., and Lovley, D.R. (2011) Tunable metallic-like conductivity in microbial nanowire networks. *Nature Nanotechnology*, **6** (9), 573–579.

19 El-Naggar, M.Y., Wanger, G., Leung, K.M., Yuzvinskya, T.D., Southame, G., Yang, J., Lau, W.M., Nealson, K.H., and Gorby, Y.A. (2010) Electrical transport along bacterial nanowires from *Shewanella oneidensis* MR-1. *Proceedings of the National Academy of Sciences of the United States of America*, **107** (42), 18127–18131.

20 Chen, S., Hou, H., Harnisch, F., Patil, S.A., Carmona-Martinez, A.A., Agarwal, S., Zhang, Y., Sinha-Ray, S., Yarin, A.L., Greiner, A., and Schröder, U. (2011) Electrospun and solution blown three-dimensional carbon fiber nonwovens for application as electrodes in microbial fuel cells. *Energy & Environmental Science*, **4**, 1417–1421.

21 Cao, B.E.A. (2011) Extracellular polymeric substances from Shewanella sp. HRCH-1 biofilms: characterization by infrared spectroscopy and proteomics. *Environmental Microbiology*, **13** (4), 1018–1031.

22 Nevin, K.P., Kim, B.-C., Glaven, R.H., Johnson, J.P., Woodard, T.L., Methé, B.A., DiDonato, R.J.J., Covalla, S.F., Franks, A.E., Liu, A., and Lovley, D.R. (2009) Anode biofilm transcriptomics reveals outer surface components essential for high density current production in *Geobacter sulfurreducens* fuel cells. *PLoS One*, **4** (5), e5628.

23 Mehta, T., Coppi, M.V., Childers, S.E., and Lovley, D.R. (2005) Outer membrane *c*-type cytochromes required for Fe(III) and Mn(IV) oxide reduction in *Geobacter sulfurreducens*. *Applied and Environmental Microbiology*, **71** (12), 8634–8641.

24 Harris, H.W., El-Naggar, M.Y., Bretschger, O., Ward, M.J., Romine, M.F., Obraztsova, A.Y., and Nealson, K.H. (2010) Electrokinesis is a microbial behavior that requires extracellular electron transport. *Proceedings of the National Academy of Sciences of the United States of America*, **107** (1), 326–331.

25 Magnuson, T.S. (2011) How the xap locus put electrical "Zap" in *Geobacter sulfurreducens* biofilms. *Journal of Bacteriology*, **193** (5), 1021–1022.

26 Rabaey, K. and Verstraete, W. (2005) Microbial fuel cells: novel biotechnology for electricity generation. *Trends in Biotechnology*, **23** (6), 291–298.

27 Schröder, U. (2007) Anodic electron transfer mechanisms in microbial fuel cells and their energy efficiency. *Physical Chemistry Chemical Physics*, **9**, 2619–2629.

28 Rabaey, K., Boon, N., Verstraete, W., and Höfte, M. (2005) Microbial phenazine production enhances electron transfer in biofuel cells. *Environmental Science & Technology*, **39** (9), 3401–3408.

29 Hernandez, M.E., Kappler, A., and Newman, D.K. (2004) Phenazines and other redox-active antibiotics promote microbial mineral reduction. *Applied and Environmental Microbiology*, **70** (2), 921–928.

30 Pham, T.H., Boon, N., Aelterman, P., Clauwaert, P., De Schamphelaire, L., Vanhaecke, L., De Maeyer, K., Höfte, M., and Verstraete, W., and Rabaey, K. (2008) Metabolites produced by *Pseudomonas* sp. enable Gram positive bacterium to achieve extracellular electron transfer. *Applied Microbiology and Biotechnology*, **77**, 1119–1129.

31 Venkataraman, A., Rosenbaum, M., Arends, J.B.A., Halitschke, R., and Angenent, L.T. (2010) Quorum sensing regulates electric current generation of *Pseudomonas aeruginosa* PA14 in bioelectrochemical systems.

Electrochemistry Communications, **12** (3), 459–462.

32 Benz, M., Schink, B., and Brune, A. (1998) Humic acid reduction by *Propionibacterium freudenreichii* and other fermenting bacteria. *Applied and Environmental Microbiology*, **64** (11), 4507–4512.

33 Harnisch, F., Schröder, U., Quaas, M., and Scholz, F. (2008) Electrocatalytic and corrosion behaviour of tungsten carbide in pH neutral electrolytes. *Applied Catalysis B: Environmental*, **87**, 63–69.

34 Rosenbaum, M., Zhao, F., Quaas, M., Wulff, H., Schröder, U., and Scholz, F. (2007) Evaluation of catalytic properties of tungsten carbide for the anode of microbial fuel cells. *Applied Catalysis B: Environmental*, **74**, 262–270.

35 Rosenbaum, M., Zhao, F., Schröder, U., and Scholz, F. (2006) Interfacing electrocatalysis and biocatalysis using tungsten carbide: a high performance noble-metal-free microbial fuel cell. *Angewandte Chemie: International Edition*, **45**, 6658–6661.

36 Rabaey, K., van den Sompel, K., Maignien, L., Boon, N., Aelterman, P., Clauwaert, P., de Schamphelaire, L., Pham, H.T., Vermuelen, J., Verhaege, M., and Lens, P., and Verstraete, W. (2006) Microbial fuel cells for sulfide removal. *Environmental Science & Technology*, **40**, 5218–5224.

37 Zhao, F., Rahunen, N., Varcoe, J.R., Roberts, A.J., Avignone-Rossa, C., Thumser, A.E., and Slade, R.C.T. (2009) Factors affecting the performance of microbial fuel cells for sulfur pollutants removal. *Biosensors & Bioelectromagnetics*, **24** (7), 1931–1936.

38 Zhao, F., Rahunen, N., Varcoe, J.R., Chandra, A., Avignone-Rossa, C., Thumser, A.E., and Slade, R.C.T. (2008) Activated carbon cloth as anode for sulfate removal in a microbial fuel cell. *Environmental Science & Technology*, **42** (13), 4971–4976.

39 Dutta, P.K., Keller, J., Yuan, Z.G., Rozendal, R.A., and Rabaey, K. (2009) Role of sulfur during acetate oxidation in biological anodes. *Environmental Science & Technology*, **43**, 3839–3845.

40 Potter, M.C. (1931) Measurement of the electricity liberated during the downgrade reactions of organic compounds. *Nature*, **127** (3206), 554–555.

41 Bean, R.C., Inami, Y.H., Basford, P.R., Boyer, M.H., Shepherd, W.C., Walwick, E.R., and Kay, R.E. (1964) Study of the fundamental principles of bio-electrochemistry. NASA Final Technical Report (NASA N64-25906), p. 107.

42 Canfield, J.H., Goldner, B.H., and Lutwack, R. (1963) Utilization of human wastes as electrochemical fuels. NASA Technical Report (N66 23679), p. 63.

43 Wilkinson, S. (2000) "Gastrobots"-benefits and challenges of microbial fuel cells in food powered robot. *Autonomous Robots*, **9**, 99–111.

44 Kim, B., Chang, I., Hyun, M., Kim, H., and Park, H. (2001) An electrochemical method for enrichment of microorganism, a biosensor for analysing organic substance and BOD.

45 Rabaey, K., Boon, N., Siciliano, S.D., Verhaege, M., and Verstraete, W. (2004) Biofuel cells select for microbial consortia that self-mediate electron transfer. *Applied and Environmental Microbiology*, **70** (9), 5373–5382.

46 Rabaey, K., Angenent, L., Schröder, U., and Keller, J. (eds) (2010) *Bioelectrochemical Systems: From Extracellular Electron Transfer to Biotechnological Application*, IWA Publishing, London.

47 Emde, R. and Schink, B. (1990) Enhanced propionate formation by *Propionibacterium freudenreichii* subsp. *freudenreichii* in a 3-electrode amperometric culture system. *Applied and Environmental Microbiology*, **56**, 2771–2776.

48 Hongo, M. and Iwahara, M. (1979) Electrochemical studies on fermentation. 1. Application of electro-energizing method to L-glutamic acid fermentation. *Agricultural and Biological Chemistry*, **43**, 2075–2081.

49 Rozendal, R. and Buisman, C.J.N. (2005) Process for producing hydrogen. Patent WO2005005981.

50 Aulenta, F., Canosa, A., De Roma, L., Reale, P., Panero, S., and Rossetti, S., and Majone, M. (2009) Influence of mediator immobilization on the electrochemically

assisted microbial dechlorination of trichloroethene (TCE) and *cis*-dichloroethene (*cis*-DCE). *Journal of Chemical Technology and Biotechnology (Oxford, Oxfordshire: 1986)*, **84**, 864–870.

51 Cao, X., Huang, X., Liang, P., Xiao, K., Zhou, Y., Zhang, X., and Logan, B.E. (2009) A new method for water desalination using microbial desalination cells. *Environmental Science & Technology*, **43** (18), 7148–7152.

52 Rosenbaum, M., He, Z., and Angenent, L. (2010) Light energy to bioelectricity: photosynthetic microbial fuel cells. *Current Opinion in Biotechnology*, **21**, 259–264.

53 Rabaey, K., Rodríguez, J., Blackall, L., Keller, J., Batstone, D., Verstraete, W., and Nealson, K.H. (2007) Microbial ecology meets electrochemistry: electricity driven and driving communities. *ISME Journal*, **1** (1), 9–18.

54 Rabaey, K. and Rozendal, R.A. (2010) Microbial electrosynthesis: revisiting the electrical route for microbial production. *Nature Reviews Microbiology*, **8**, 706–716.

55 Liu, Y., Harnisch, F., Schröder, U., Fricke, K., Climent, V., and Feliu, J.M. (2010) The study of electrochemically active mixed culture microbial biofilms on different carbon-based anode materials. *Biosensors & Bioelectronics*, **25**, 2167–2171.

56 Katuri, K.P., Kavanagh, P., Rengaraj, S., and Leech, D. (2010) *Geobacter sulfurreducens* biofilms developed under different growth conditions on glassy carbon electrodes: insights using cyclic voltammetry. *Chemical Communications*, **46**, 4758–4760.

57 Logan, B.E., Cheng, S., Watson, V., and Estadt, G. (2007) Graphite fiber brush anodes for increased power production in air-cathode microbial fuel cells. *Environmental Science & Technology*, **41**, 3341–3346.

58 Zhao, Y., Watanabe, K., Nakamura, R., Mori, S., Liu, H., Ishii, K., and Hashimoto, K. (2010) Three-dimensional conductive nanowire networks for maximizing anode performance in microbial fuel cells. *Chemistry: A European Journal*, **16**, 4982–4985.

59 Rabaey, K., Clauwaert, P., Aelterman, P., and Verstraete, W. (2005) Tubular microbial fuel cells for efficient electricity generation. *Environmental Science & Technology*, **39** (20), 8077–8082.

60 Foley, J.M., Rozendal, R.A., Hertle, C.K., Lant, P.A., and Rabaey, K. (2010) Life cycle assessment of high-rate anaerobic treatment, microbial fuel cells, and microbial electrolysis cells. *Environmental Science & Technology*, **44** (9), 3629–3637.

61 Logan, B.E., Hamelers, B., Rozendal, R., Schröder, U., Keller, J., Freguia, S., Aelterman, P., Verstraete, W., and Rabaey, K. (2006) Microbial fuel cells: methodology and technology. *Environmental Science & Technology*, **40** (17), 5181–5191.

62 Rozendal, R.A., Hamelers, H.V.M., Rabaey, K., Keller, J., and Buisman, C.J.N. (2008) Towards practical implementation of bioelectrochemical wastewater treatment. *Trends in Biotechnology*, **26** (8), 450–459.

63 Tender, L.M., Reimers, C.E., Stecher, H.A., Holmes, D.E., Bond, D.R., and Lovley, D.R. (2002) Harnessing microbially generated power on the seafloor. *Nature Biotechnology*, **20**, 821–825.

64 Logan, B.E., Call, D., Cheng, S., Hamelers, H.V.M., Sleutels, T.H.J.A., Jeremiasse, A.W., and Rozendal, R.A. (2008) Microbial electrolysis cells for high yield hydrogen gas production from organic matter. *Environmental Science & Technology*, **42**, 8630–8640.

65 Rabaey, K., Bützer, S., Brown, S., Keller, J., and Rozendal, R.A. (2010) High current generation coupled to caustic production using a lamellar bioelectrochemical system. *Environmental Science & Technology*, **44** (11), 4315–4321.

66 Rozendal, R., Leone, E., Keller, J., and Rabaey, K. (2009) Efficient hydrogen peroxide generation from organic matter in a bioelectrochemical system. *Electrochemistry Communications*, **11** (9), 1752–1755.

67 Mu, Y., Rozendal, R.A., Rabaey, K., and Keller, J. (2009) Nitrobenzene removal in bioelectrochemical systems. *Environmental Science & Technology*, **43**, 8690–8695.

68 Gregory, K.B. and Lovley, D.R. (2005) Remediation and recovery of uranium from contaminated subsurface

environments with electrodes. *Environmental Science & Technology*, **39**, 8943–8947.

69 Fricke, K., Harnisch, F., and Schröder, U. (2008) On the use of cyclic voltammetry for the study of anodic electron transfer in microbial fuel cells. *Environmental Science & Technology*, **1** (1), 144–147.

70 Marsili, E., Rollefson, J.B., Baron, D.B., and Hozalski, R.M., and Bond, D.R. (2008) Microbial biofilm voltammetry: direct electrochemical characterization of catalytic electrode-attached biofilm. *Applied and Environmental Microbiology*, **74** (23), 7329–7337.

71 Srikanth, S., Marsili, E., Flickinger, M., and Bond, D.R. (2007) Electrochemical characterization of *Geobacter sulfurreducens* cells immobilized on graphite paper electrodes. *Biotechnology and Bioengineering*, **99** (5), 1065–1073.

72 Harnisch, F., Koch, C., Patil, S.A., Hübschmann, T., Müller, S., and Schröder, U. (2011) Revealing the electrochemically driven selection in natural community derived microbial biofilms using flow-cytometry. *Energy & Environmental Science*, **4** (4), 1265–1267.

73 Torres, C.I., Marcus, A.K., Lee, H.-S., Parameswaran, P., Krajmalnik-Brown, R., and Rittmann, B.E. (2010) A kinetic perspective on extracellular electron transfer by anode-respiring bacteria. *FEMS Microbiology Reviews*, **34**, 3–17.

74 Busalmen, J.P., Esteve-Nunez, A., Berná, A., and Feliu, J.M. (2008) C-type cytochromes wire electricity-producing bacteria to electrodes. *Angewandte Chemie*, **47**, 4874–4877.

75 Nakamura, R., Ishii, K., and Hashimoto, K. (2009) Electronic absorption spectra and redox properties of C type cytochromes in living microbes. *Angewandte Chemie*, **121**, 1634–1636.

76 Millo, D., Harnisch, F., Patil, S.A., Ly, K.H., Schröder, U., and Hildebrandt, P. (2011) *In situ* spectroelectrochemcial investigation of electrocatalytic microbial biofilms by surface-enhanced resonance Raman spectroscopy. *Angewandte Chemie: International Edition*, **50**, 2625–2627.

77 He, Z. and Mansfeld, F. (2009) Exploring the use of electrochemical impedance spectroscopy in microbial fuel cell studies. *Energy & Environmental Science*, **2**, 215–219.

78 Schröder, U. and Harnisch, F. (2009) Electrochemical losses defining BES performance, in *Bioelectrochemical Systems: From Extracellular Electron Transfer to Biotechnological Application* (eds K. Rabaey, L. Angenent, U. Schröder, and J. Keller), International Water Association.

79 Lowy, D.A. (2010) Importance of Tafel plots in the investigation of bioelectrochemical systems, in *Bioelectrochemical Systems: From Extracellular Electron Transfer to Biotechnological Application* (eds K. Rabaey, L. Angenent, U. Schröder, and J. Keller), IWA.

80 Marzorati, M., Wittebolle, L., Boon, N., Daffonchio, D., and Verstraete, W. (2008) How to get more out of molecular fingerprints: practical tools for microbial ecology. *Environmental Microbiology Reports*, **10**, 1571–1581.

81 Franks, A.E., Nevin, K.P., Glaven, R., and Lovely, D.R. (2010) A novel approach for spatial analysis of global gene expression within a *Geobacter sulfurreducens* current-producing biofilm. *The ISME Journal*, **4** (4), 509–519.

82 Read, S.T., Dutta, P., Bond, P.L., Keller, J., and Rabaey, K. (2010) Initial development and structure of biofilms on microbial fuel cell anodes. *BMC Microbiology*, **10**, 98.

83 Franks, A.E., Nevin, K.P., Glaven, R.H., and Lovley, D.L. (2010) Microtoming coupled to microarray analysis to evaluate the spatial metabolic status of *Geobacter sulfurreducens* biofilms. *ISME Journal*, **4**, 509–519.

84 Inoue, K., Leang, C., Franks, A.E., Woodard, T.L., Nevin, K.P., and Lovley, D.R. (2010) Specific localization of the c-type cytochrome OmcZ at the anode surface in current-producing biofilms of *Geobacter sulfurreducens*. *Environmental Microbiology Reports*, **3** (2), 211–217.

9
Materials for Microfluidic Fuel Cells

Seyed Ali Mousavi Shaegh and Nam-Trung Nguyen

9.1
Introduction

The demand for ever-increasing capabilities and longer run times for portable electronic devices has led to the recent surge of research and development of high energy density power sources. Numerous investigations have focused only on batteries to increase the power density. But the recent progress in battery technology cannot fill the so-called power gap between the power sources and power consumers, which is expected to grow faster in the coming years [1].

In addition, the emergence of the networks of wireless and off-the-grid sensors, which can be deployed for biological, environmental, military, and security monitoring, has opened a new market for robust and reliable power sources with long empowering times. Moreover, realization/development of new devices such as small unmanned aerial vehicles (UAVs) or intelligent insect-sized robots and smart bugs [2] is tied to existence of small power sources.

The energy density of metal hydrides, for example, $NaBH_4$, methanol, and most hydrocarbon fuels, are higher than the competitive battery technologies [3]. Microfuel cell technology can be considered as a suitable power source for the applications already mentioned. Micro fuel cells can be implemented in a hybrid system in connection to a rechargeable (secondary) battery to improve the flexibility and reliability of the whole system. A micro fuel cell system is generally comprised of a fuel cell engine, auxiliary systems, a fuel tank, and an oxidant container. These cells can outperform batteries if the ratio of fuel to fuel cell engine volume is maximized and the power consumption of their auxiliary devices for fuel or oxidant delivery and regulating the engine power is significantly reduced [3].

Because of the higher energy density and better safety of liquid fuels compared with gaseous hydrogen, the types of fuel cell under active development usually includes direct methanol fuel cells (DMFCs) [4], direct formic acid fuel cells (DFAFCs) [5], proton exchange fuel cells (PEMFCs) run by hydrogen generated from metal hydride [6], and membraneless microfluidic fuel cells [7].

Materials for Low-Temperature Fuel Cells, First Edition. Edited by Bradley Ladewig, San P. Jiang, and Yushan Yan.

To downsize the conventional PEM fuel cells into micro PEM fuel cells several design and operational considerations must be taken into account. Proton exchange membrane, usually made of Nafion®, as the heart of the PEM fuel cells needs specific conditioning to provide enough water for proton conductivity. The dynamic conditions of cell operation add further complexity to fuel cell engine and auxiliary systems. In addition, membrane swelling and shrinkage, due to the water uptake and retention of the nanoporous structure of Nafion, can be problematic for fuel cell packaging. Furthermore, the current fabrication technologies for micro fuel cells are a combination of microfabrication techniques for making channels or electrodes such as laser machining on PMMA [8], silicon etching [9], and conventional methods and materials for making membrane electrode assembly (MEA). Therefore, there is a mismatch between the required material and the fabrication processes, as well as between the micro feature size of the micro fuel cells and the available technologies. Many investigations were carried out to address this mismatch by introducing new materials to fabricate the fuel cell in a monolithic platform. An example is making a proton conductive membrane in porous silicon, which is compatible with microfabrication technologies [1,10,11].

In parallel to the microelectromechanical systems (MEMS)-based approaches for miniaturizing of conventional power sources, micro/nanofluidics can provide new approaches for energy conversion systems [12] and take advantage of the specific phenomena that emerge by downsizing the fluidic systems.

The absence of instability due to the convective mass transport in laminar flows at low Reynolds numbers allows many streams containing different substances with dissimilar concentrations flow through a microchannel in a side-by-side configuration. Depending on the Péclet number, an indication of relative importance of convection to diffusion, liquid streams can travel down the channel separately. Diffusive mixing of two streams across the liquid–liquid interface results in a concentration gradient. By exploiting the property of such controlled microfluidic interface, different applications such as extraction and separation of molecules [13–15], microfabrication and patterning at the interface of the streams in a microchannel [16], and micro-optofluidic lenses have been achieved [17].

Ferrigno *et al.* [18] proposed the concept of membraneless fuel cell based on the lamination of two streams in a microchannel. As shown in Figure 9.1, the two streams of oxidant and fuel are introduced into a microchannel with integrated electrodes as active area for electrochemical reactions and current collection. Both anolyte and catholyte have supporting liquid electrolyte to facilitate ion conduction across the channel. Ions from oxidized fuel or reduced oxidant travel across the channel by migration and concentration gradient, while the electrons reach the cathode side through an external circuit (Figure 9.1).

Since fuel and oxidant streams flow down the channel in a parallel manner, the necessity for the presence of a membrane as a separator of two streams is eliminated [18]. Interdiffusion zone between two streams is restricted to an interfacial width at the center of the channel. To avoid the effects of fuel and

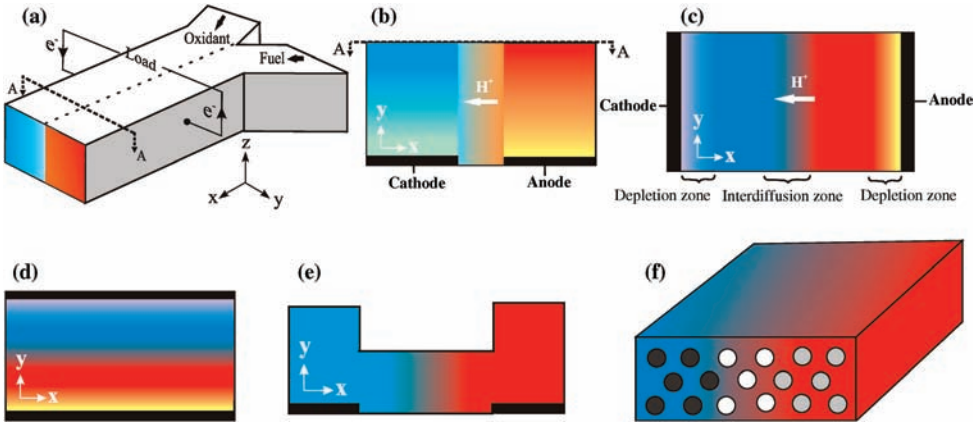

Figure 9.1 Flow-over designs. (a) Schematic sketch of LFFC with side-by-side streaming in a Y-shape channel. (b) A–A cross section of the channel, schematic sketch of configuration of both electrodes at bottom wall. (c) Cross section of channel showing depletion boundary layers over anode and cathode and interdiffusion zone at the liquid–liquid interface with vertical electrodes on side walls. (d) Cross section of channel with top–bottom electrodes configuration. (e) Cross section of channel with both electrodes on bottom wall in a grooved channel. (f) Cross section of channel with graphite rods as electrodes. Reproduced with permission from Ref. [19]. Copyright 2011, Elsevier.

oxidant crossover, the electrode-to-electrode spacing should be optimized while ohmic losses across the channel and pumping energy through the channel are kept minimum.

In this chapter, the fundamentals of the membraneless laminar flow-based fuel cells (LLFCs) operation are first explained. Then, design and exploited fabrication technologies of membraneless LFFCs and the effect of flow architectures of electrodes and their arrangements on cell performance are discussed. Subsequently, reader can find more details about the proposed fuels, oxidants, and electrolytes for membraneless LLFCs. Finally, some discussions on material constraints and selections are provided.

Investigations have proved that membraneless LFFCs can provide an appropriate platform for biofuel cells [20]. Biofuel cells are beyond the scope of this chapter, but they can benefit from the technology development explained here. To gain more knowledge about the design considerations and performance-limiting factors of membraneless LFFCs, readers are advised to study available review articles [7,20].

9.2 Fundamentals

Membraneless LFFCs follow the basic electrochemical principles of membrane-based fuel cells. The main difference is that the role of membrane as a charge

transport media and as a separator of electrodes is represented by creating a confined liquid–liquid interface in a microchannel. Usually, microchannels are defined as channels with characteristic dimension <1 mm and >1 μm [21], and fluid manipulation inside microchannels is known as microfluidics. Fundamentals and applications of microfluidics can be found in [22].

With a scale factor of R, the ratio of surface to volume is $\left((R^2/R^3) = R^{-1}\right)$, which decreases with miniaturization. Microfluidic systems can harness the scale dependence of interface properties to exploit a broad series of applications [23]. As fluidic systems are reduced in size, laminar flow regime at low Reynolds numbers is established. In this case, surface-based effects, including surface tension or viscosity, can dominate over volume-based effects, offering new microscale phenomena, for instance, confined liquid–liquid interface in a microchannel with colaminar streams can be achieved.

Due to the continuum and laminar nature of liquids in microchannels [21], mass conservation for fluid flows obeys the continuity equation:

$$\frac{\partial \rho}{\partial t} + \nabla \cdot (\rho \vec{u}) = 0 \tag{9.1}$$

while fluid density (ρ) is constant, it leads to the incompressible flow condition, $\nabla \cdot \vec{u} = 0$. The Navier–Stokes equations can be solved to determine the three-dimensional velocity field ($\vec{u}$):

$$\rho\left(\frac{\partial \vec{u}}{\partial t} + \vec{u} \cdot \nabla \vec{u}\right) = -\nabla p + \mu \nabla^2 \vec{u} + \vec{f} \tag{9.2}$$

where p is the representative of pressure and $\vec{f}$ includes the body forces per unit volume.

As shown in Figure 9.1a, after two separate streams including fuel and oxidant are introduced into the channel, they come into contact to create a parallel colaminar flow in the channel with a liquid–liquid interface. This interface takes action as a separator of fuel and oxidant streams. Current collectors and electrodes with appropriate catalyst layer on the surface are fabricated on channel walls where the electrochemical reactions take place. To obtain charge transport between two electrodes, both fuel and oxidant solutions should contain ionic conductivity, which is obtained by adding supportive electrolyte to both streams. The supporting electrolyte contains hydroxide or hydronium ions such as diluted solutions of potassium hydroxide or sulfuric acid.

For a fuel–oxidant configuration shown in Equation 9.3 at a given temperature and pressure, the theoretical equilibrium open-circuit potential of a given oxidation–reduction reaction within the cell is determined by Equation 9.4 known as Nernst equation:

$$\nu_A A + \nu_B B \leftrightarrow \nu_c C + \nu_D D \tag{9.3}$$

$$E^0(T,P) = E^0 + \frac{R_u T}{nF} \ln\left[\left(\frac{a_A^{\nu_a} a_B^{\nu_B}}{a_c^{\nu_c} a_D^{\nu_D}}\right)\right] \tag{9.4}$$

where E^0 is the equilibrium potential at standard state and a is the activity of each species. For aqueous species, activity is estimated by the concentration. Since there is no membrane between the fuel and oxidant streams, pH of the two streams can be modified individually to increase the half-cell potentials. The theoretical cell potential is degraded by the anodic and cathodic activation losses ($\eta_{a,a}$, $\eta_{a,c}$), ohmic losses (η_r), anodic and cathodic mass transport losses ($\eta_{m,a}$, $\eta_{m,c}$), and other losses η_x:

$$E_{cell} = E^0(T,P) - \eta_{a,a} - \left|\eta_{a,c}\right| - \eta_r - \eta_{m,a} - \left|\eta_{m,c}\right| - \eta_x \tag{9.5}$$

Here, η_x represents the crossover effect of fuel/oxidizer through the electrolyte to the opposite electrode or internal short circuits in the cell that is responsible for more departure of theoretical equilibrium open-circuit potential from Nernst equilibrium voltage.

Due to the sluggish electrooxidation reactions of aqueous liquids such as formic acid and methanol, the activation losses are generally higher than a hydrogen-fed PEM fuel cell and the cell potential drops more rapidly.

Ohmic losses are mainly attributed to the electrolyte ionic resistivity ($R_{electrolyte}$) and the external resistance of electrodes and connections ($R_{external}$) when current (i) is drawn from the cell:

$$\eta_r = i \cdot \left(R_{electrolyte} + R_{external}\right) \tag{9.6}$$

Ohmic resistance of the supporting electrolyte for charge transport between electrodes depends on anode-to-cathode spacing as charge transport length (d), cross-sectional area of charge transport (A), and the ionic conductivity (σ):

$$R_{electrical} = \frac{d}{\sigma A} \tag{9.7}$$

Typical bulk through-plane conductivity of Nafion as proton exchange membrane is around $0.1\,S\,cm^{-2}$ at 100% relative humidity (RH) and room temperature [24] with typical membrane thickness of 50–200 μm. In contrast, the conductivity of 0.5 M sulfuric acid as a common supporting electrolyte is on the order of $0.2\,S\,cm^{-2}$. Anode to cathode spacing in a membraneless LFFC generally ranges from 0.5 to 1.5 mm, which results in higher total ohmic losses rather than PEM fuel cells.

Low concentration of oxidant or fuel is the main source of mass transfer losses. Mass transfer losses have significant role in degradation of cell potential at high current densities while a cell is operating at low flow rates due to slow replenishment of depletion layer over the electrodes.

While the electrochemical reactions occur, fuel and oxidant are consumed over the corresponding electrodes to generate current. Current density distribution is estimated for simulations by Butler–Volmer equation as a function of volumetric exchange current of a given electrode (i_0) at reference concentration ($C_{i,ref}$):

$$J_0 = i_0\left(\frac{C_i}{C_{i,ref}}\right)^{\beta_i}\left[\exp\left(\frac{\alpha_a F\eta}{R_u T}\right) - \exp\left(-\frac{\alpha_c F\eta}{RT}\right)\right] \tag{9.8}$$

Here, C_i is the species concentration "i" that refers to fuel or oxidant, and β_i is the reaction order of species for the elementary charge transfer step. α_a and α_c are the anodic and cathodic charge transfer coefficients, R is the universal constant, and T is the operating temperature. F is the Faraday's constant and η is the surface overpotential:

$$\eta = \phi_s - \phi_e - E^0(T, P) \tag{9.9}$$

where φ_s and φ_e are the potential of electrode and electrolyte. The species concentration distribution over the electrodes is governed by diffusion–convection transport, and can be calculated by solving mass conservation equation:

$$\nabla.(-D_i \nabla C_i + C_i \vec{u}) = S_i \tag{9.10}$$

where D_i is the diffusion coefficient of species "i" and S_i is the net rate of change of species "i" by electrochemical reactions over anode and cathode, and represents the rate of consumed species per cubic meter:

$$S_i = \frac{J_0}{nF} \tag{9.11}$$

Increasing flow rate of fuel/oxidant accelerates the replenishment of the depletion zone over the electrodes and develops the maximum cell current and power density at the expense of low fuel utilization. Fuel utilization is defined as

$$\varepsilon_{\text{fuel}} = \frac{J}{nF\nu_{\text{fuel}}} \tag{9.12}$$

where ν_{fuel} represents the rate at which fuel is supplied to the fuel cell with a unit of mol s^{-1}. Low fuel utilization may dictate the implementation of a recycling fuel/oxidant system for practical applications, which makes the whole fuel cell system complicated.

9.3 Membraneless LFFC Designs and the Materials in Use

The interface between two streams with supporting electrolytes represents a virtual membrane by providing (i) an ion conductive media with (ii) effective controlled mixing of reactants across the cell. In brief, membraneless LFFCs can benefit from the following advantages of microfluidics:

a) Membrane is eliminated, thus reducing the size of the cell and enhancing the flexibility in cell design and fabrication including miniaturization [18,25].
b) Since both streams flow through a single channel, some design considerations for fuel and oxidant delivery systems are eliminated, simplifying sealing and packaging requirements. Furthermore, the composition of fuel and oxidant streams can be tailored individually to maximize reaction kinetics at anode and cathode [26].

c) Membrane-related issues such as water management, membrane fouling, and damaging partially disappear [18,27]. Unlike the PEMFCs, there is no Pt dissolution in polymeric membranes. Since both streams contain liquid electrolyte, the precise establishment of the interface among the electron conductor, charge transport media, and pathways for reactants feeding, which is known as the triple-phase boundary, is easier than PEMFCs.
d) Membraneless LFFC as a power source is compatible with other microfluidic systems such as lab-on-chip devices.

Flow architecture of streams has significant effects on the performance of membraneless LFFC. Depending on the architecture/structure of the implemented electrodes, membraneless LFFC are categorized into (i) flow-over type with planar electrodes, (ii) flow-through type with three-dimensional porous electrodes, and (iii) membraneless LFFC with air-breathing cathode. All designs exploit common fuels and oxidants and can be fabricated by conventional fabrication methods with the same level of precision. All designs can use either alkaline or acidic electrolytes.

Table 9.1 lists the materials and electrocatalysts used for the fabrication of fuel cells. Different materials and processing considerations must be taken into account to fabricate a reliable fuel cell. The design considerations are as follows [28]:

a) Carrier substrate to form the channel and the desired geometry.
b) Structure of the catalyst and its deposition method on the supporting substrate of the catalyst.
c) Assembly method of the electrodes and channel structures to provide a liquid-tight sealed cell with interfaces to instrumentation and fuel/oxidant delivery systems.

As shown in Figure 9.1, a membraneless LFFC basically consists of a main microchannel that can be capped between liquid-tight support structure(s). The colaminar flows in the channel come into contact in two configurations: side-by-side streaming and vertically layered streaming. For side-by-side streaming with vertical fuel–oxidant interface and vertically layered streaming with horizontal liquid–liquid interface, electrodes are positioned on bottom walls (Figure 9.1b), side walls (Figure 9.1c), and top and bottom walls (Figure 9.1d). In addition, the electrodes can be positioned in grooved channels (Figure 9.1e) to control bubble generation or an array of electrodes can be implemented in a single channel (Figure 9.1f).

As shown in Figure 9.1, flow-over designs generally provide streaming of fuel and oxidant over planar electrodes. Only a fraction of fuel and oxidant streams adjacent to the catalyst layer participate in electrocatalytic reactions. Due to the lack of effective convective mass transport, a depletion boundary layer with low concentration of reactant grows over both electrodes. To enhance fuel utilization in flow-over designs, an improved design of electrodes was implemented in the

Table 9.1 Overview of the materials for microfluidic fuel cell devices.

Design	Fuel/oxidant	Electrolyte	Anode catalyst	Cathode catalyst	Channel	Current collector
Ferrigno *et al.* [18]	Vanadium (II) redox species (1 M) Vanadium (V) redox species (1 M)	Sulfuric acid (25%)	Bare	Bare	PDMS/SU8	Carbon on deposited Au by E-beam evaporator
Kjeang *et al.* [27]	Vanadium (II) redox species (1–2 M) Vanadium (V) redox species (1–2 M)	Sulfuric acid (1–2 M)	Bare	Bare	PDMS/Derlin	Graphite rod as electrodes
Kjeang *et al.* [29]	Vanadium(II) redox species (2 M) Vanadium(V) redox species (2 M)	Sulfuric acid (2 M)	Bare	Bare	PDMS	Toray carbon paper as electrodes
Kjeang *et al.* [30]	Vanadium(II) redox species (2 M) Vanadium(V) redox species (2 M)	Sulfuric acid (4 M)	Bare	Bare	PDMS	Toray carbon paper as porous flow-through electrodes-current collectors
Tominaka *et al.* [25]	Methanol Air	Sulfuric acid (0.5 M) or sodium sulfate (0.5 M)	Electrodeposited Pt–Ru alloy	Electrodeposited Pd–Co alloy as selective catalyst for O_2 electroreduction	Silicon	200 nm Au on 30 nm Ti using E-beam evaporation
Morales-Acosta *et al.* [31]	Formic acid (0.1, 0.5 M) Dissolved O_2	H_2SO_4	0.7 mg cm^{-2} Pd supported on MWCNT or 1.9 mg cm^{-2} Pd supported on V XC-72	1.9 mg cm^{-2} Pd on V XC-72	1 mm PMMA	V XC-72 as current collector

Jayashree *et al.* [32]	Formic acid (1 M) Air	Sulfuric acid (0.5 M)	10 mg cm^{-2} Pd black nanoparticles painted on graphite	0.35 mg cm^{-2} Pt with additional 2 mg cm^{-2} Pt on Toray carbon paper as air-breathing cathode	2 mm thick PMMA	Graphite plate for anode side
Jayashree *et al.* [33]	Methanol (1 M) Air	Sulfuric acid (0.5 M) or potassium hydroxide (1 M)	10 mg cm^{-2} Pt-Ru 50:50 atom wt% alloy painted on graphite	0.35 mg cm^{-2} Pt with additional 2 mg cm^{-2} Pt painted on Toray carbon paper as air-breathing cathode	2 mm thick PMMA	Graphite plate for anode side
Brushett *et al.* [34]	Formic acid (1 M) Methanol (1 M) Ethanol (1 M) Sodium borohydride (1 M) Hydrazine (3 M) Air	Sulfuric acid (0.5 M) or potassium hydroxide (1 M)	Pd black Pt/Ru black Pt/Ru black Pt black Pt/C, 10 mg cm^{-2} for all catalysts, painted on graphite	2 mg cm^{-2} Pt black painted on Toray carbon paper as air-breathing cathode	2 mm thick PMMA	Graphite plate for anode side
Whipple *et al.* [35]	Methanol (0.1–15 M) Air	H_2SO_4 (0.5 M)	10 mg cm^{-2} Pt/Ru on carbon paper	2 mg cm^{-2} Pt black or Ru_xSe_y as methanol tolerant catalyst painted on Toray carbon paper as air-breathing cathode	2 mm thick PMMA	Graphite plate for anode side
Hollinger *et al.* [36]	Methanol (0.063, 0.125, 0.25, 1 M) Air, O_2	H_2SO_4 (1 M)	10 mg cm^{-2} Pt/Ru 50:50 atom wt% on carbon paper	2 mg cm^{-2} Pt-C 50:50 wt% alloy brushed on Sigracet carbon paper as air-breathing cathode with a thin layer of Nafion on catalyst layer	150 μm Kapton sheet at both sides of a polycarbonate separator	Graphite plate for anode side

(*continued*)

Table 9.1 (*Continued*)

Design	Fuel/oxidant	Electrolyte	Anode catalyst	Cathode catalyst	Channel	Current collector
Mitrovski and Nuzzo [37]	H_2 Air	Sulfuric acid (5 M) or sodium hydroxide (2.5 M)	Electrodeposited Pt or electrodeposited Pd on 100 nm of Pt	Electrodeposited Pt or electrodeposited Pd on 100 nm of Pt	PDMS	100 nm Pt on 15 nm of titanium deposited by E-beam evaporation
Mitrovski *et al.* [38]	Hydrogen Oxygen	Sulfuric acid (0.1 M) or sodium hydroxide (0.1and 1 M)	Electrodeposited Pt or electrodeposited Pd on 100 nm of Pt	Electrodeposited Pt or electrodeposited Pd on 100 nm of Pt	PDMS	100 nm Pt on 15 nm of titanium deposited by E-beam evaporation
Li *et al.* [39]	Formic acid (0.5 M) Dissolved O_2 or hydrogen peroxide (0.01 M)	Sulfuric acid (0.1 M)	Supported Pt–Ru 50:50 wt% wet sprayed on Au	Pt black nanoparticle wet-sprayed on Au	PMMA	Sputtered Au
Mousavi Shaegh *et al.* [40]	Formic acid (1 M) Air	Sulfuric acid (0.5 M)	Pd black	Pt black nanoparticles	PMMA	Toray carbon paper
Choban *et al.* [41]	HCOOH (2.1 M) Dissolved O_2	Sulfuric acid (0.5 M)	Pt black using electrodeposition	Pt black using electrodeposition	PDMS/ Polyurethane	Sputtered 25–150 nm Au on 2.8–5 nm Cr
Choban *et al.* [26]	Methanol (1 M) Dissolved O_2	Sulfuric acid or potassium hydroxide (1 M)	Unsupported Pt/Ru 50:50 wt % alloy nanoparticles	Unsupported Pt black nanoparticles	Graphite/poly carbonate slabs	Graphite plate
Choban *et al.* [42]	Methanol (1 M) Dissolved O_2	Sulfuric acid (0.5 M)	2–4 mg cm^{-2} of unsupported Pt/Ru 50:50% wt % alloy or 50:50 mixture of unsupported Pt nanoparticles and unsupported Ru nanoparticles or unsupported Pt nanoparticles applied drop-wise on graphite plate	2-4 mg cm^{-2} of unsupported Pt nanoparticles applied drop wise on graphite	Graphite/poly-carbonate slabs	Graphite plate as current collector

Cohen *et al.* [28]	Formic acid (0.5 M) Dissolved O_2	Sulfuric acid (0.1 M)	20 nm of Ta and 50 nm of Pt or 50 nm Ta and 100 nm Pt on 200 nm Cr evaporated on polyimide film (Kapton®)	20 nm of Ta and 50 nm of Pt or 50 nm Ta and 100 nm Pt on 200 nm Cr evaporated on Kapton	Silicon	Integrated with catalyst layer
Cohen *et al.* [43]	Dissolved H_2 Dissolved O_2	Potassium hydroxide (0.1 M) or sulfuric acid (0.1 M)	50 nm of Ta and 50 nm of Pt evaporated on Kapton	50 nm of Ta and 50 nm of Pt evaporated on Kapton	Silicon	Integrated with catalyst layer
López-ontesinos *et al.* [44]	Formic acid (1 M) Potassium permanganate (60 mM, 144 mM)	Sulfuric acid (0.5 M)	Electrodeposited Pd on Cr/Au	None (bare)	Silicon	Cr/Au
Hasegawa *et al.* [45]	Hydrogen peroxide (0.75 M) Hydrogen peroxide (0.75 M)	Sodium hydroxide (0.75 M) sulfuric acid (0.375 M)	Sputtered Pt	Sputtered Pt	Glass	Integrated with catalyst layer
Sun *et al.* [46]	Formic acid (2.1 M) Potassium permanganate (0.144 M)	Sulfuric acid (0.5 M)	40 nm of Pt on 5 nm of Ti by E-beam evaporation	40 nm of Pt on 5 nm of Ti by E-beam evaporation	PDMS	Integrated with catalyst layer
Kjeang *et al.* [47]	Formic acid (1 M) Hydrogen peroxide (1–3 M)	Phosphate (1–3 M; pH 6–8) Phosphate (1–2 M; pH 0–1)	Electrodeposited Pd on Au	Electrodeposited Pt on Au	PDMS	100 nmAu
Kjeang *et al.* [48]	Formic acid (1.2 M) Sodium hypochlorite (0.67 M)	Sodium hydroxide (2.8 M)	Electrodeposited Pd on carbon paper	Electrodeposited Pd on carbon paper	PDMS	Toray carbon paper

(*continued*)

Table 9.1 (*Continued*)

Design	Fuel/oxidant	Electrolyte	Anode catalyst	Cathode catalyst	Channel	Current collector
Salloum *et al.* [49]	Formic acid (0.04 M) Potassium permanganate (0.01 M)	Sulfuric acid (0.5–1 M)	Pt black nanoparticles	Pt black nanoparticles	PMMA	Toray carbon paper
Sung and Choi [50]	Methanol (2 M) Hydrogen peroxide (0.05 M)	Potassium hydroxide (0.2 M)	Electrodeposited nickel hydroxide on 20 nm of Cr and 300 nm of Au	Electrodeposited silver oxide on 20 nm of Cr and 300 nm of Au	Glass	Cr/Au

channel to provide more active area for electrochemical reactions, as shown in Figure 9.1f. The graphite rods at the center of the channel are electrically insulated [27].

9.3.1 Flow Architecture and Fabrication of Flow-Over Design

Generally, electrodes including the catalyst and current collectors are implemented at two sides of a channel. In some designs of membraneless LFFCs with side-by-side colaminar flows, the channel structure is fabricated using poly dimethylsiloxane (PDMS) replica molding and then sealed to a solid substrate with electrodes [47,48]. PDMS molding takes advantage of soft lithography-based procedures [51]. Soft lithography is a direct pattern transfer techniques. The term "soft" refers to an elastomeric stamp with patterned relief structures on its surface. Soft lithography includes two basic techniques for transferring the micropatterns: microcontact printing and replica molding. Replica molding is generally used for making the microchannels. This technique starts with the deposition of a thin layer of photoresist such as SU8 on silicon wafer or glass slide using spin coating. The thickness of a photoresist layer with a given viscosity is determined by the rotational speed and the extent of spin coating. The thickness layer defines the channel depth on PDMS. To stabilize the photoresist on the substrate, it is baked on a hot plate or in an oven at moderate temperature (70–90 °C). The pattern of the channel should be printed on a mask made of plastic or glass depending on the finest feature size. This photomask and the substrate are aligned and then exposed to UV light for a certain exposure time. For a negative photoresist like SU8, during the UV exposure, the exposed parts are cross-linked and then stabilized for the duration of postexposure bake. Then, the substrate is immersed in a developing solution and the unexposed parts are removed and a master is remained on the wafer, which can be used for several replica molding. A soft polymer such as PDMS, a mixture of base resin and curing agent, is poured on the master, followed by degassing in a vacuum chamber and baking in an oven or over a hot plate for several hours. After baking, the channel structure is removed from the master. The channel open area can be sealed by bonding glass or PDMS reversibly or irreversibly. O_2 plasma treatment of the channel and glass or PDMS as sealing substrate results in an irreversible bond. In addition, O_2 plasma treatment makes both surfaces hydrophilic and improves the wetability of the channel.

Several characteristics make PDMS useful for making microfluidic devices, including easy fabrication (rapid prototyping, sealing, and interfacing with the user), transparency in the UV-visible regions, chemical inertness, low polarity, low electrical conductivity, and elasticity and low-cost fabrication [52].

Due to the relatively high solubility and permeability of hydrogen and oxygen in PDMS ($D_{H_2} = 1.4 \times 10^{-4}$ cm^2 s^{-1} and $D_{H_2} = 34 \times 10^{-5}$ cm^2 s^{-1} at 35 °C) [53], gas reactants can be supplied through thin layers of PDMS to a pair of electrodes separated by a channel containing sulfuric acid or sodium hydroxide as electrolyte

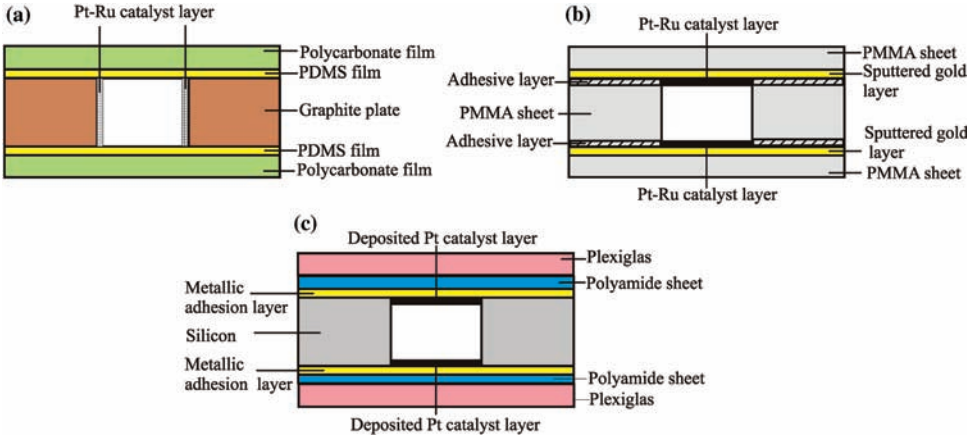

Figure 9.2 Carrier substrate with configuration of different layers of membraneless LFFCs. (a) Vertical electrodes with vertical liquid–liquid interface. (b) PMMA-based membraneless LFFC with horizontal electrodes. (c) Silicon-based microchannel for membraneless LFFC with horizontal flow-over electrodes. Reproduced with permission from Ref. [19]. Copyright 2011, Elsevier.

[37,38]. Using this concept, the achieved power densities of the cells running on dissolved hydrogen/oxygen [38] and hydrogen/air [37] were around 0.7 mW cm^{-2} as restricted by permeation rate of dissolved hydrogen through PDMS.

Graphite can be used as substrate to make the channel. Choban *et al.* [26] used graphite as substrate to serve three functions: current collector, catalyst support structure, and edificial element. As shown in Figure 9.2a, the graphite plates are placed side-by-side with a specific spacing that determines the width of the channel. Before assembling, the catalyst ink is applied to the graphite plates. To seal the channel, 1 mm thick polycarbonate slabs with thin films of PDMS were used as gasket.

Polymethylmethacrylate (PMMA) is another polymeric material frequently employed for microfluidics and micro fuel cells [4]. PMMA is one of the thermoplastic polymers that is usually linearly linked and can be softened by applying heat at above the glass transition temperature [8]. PMMA has a noncrystalline structure with 92% light transmittance in the visible spectrum. This material also has other excellent properties such as low frictional coefficient, high chemical resistance, and good electrical insulation. All these features and properties make PMMA a good substrate for microfluidic devices, especially for those involved in chemical applications [8].

A PMMA substrate can be micromachined in many ways, such as X-ray exposure and subsequent developing, hot embossing, and laser machining [8]. For laser machining, the cross section of the microchannel depends on the shape of the laser beam, its moving speed, the laser power, and the thermal diffusivity of substrate material. The energy of the laser beam has a Gaussian distribution that creates a Gaussian-shaped channel cross section in PMMA as a substrate [8].

Li *et al.* [39] used infrared CO_2 laser to engrave channels in PMMA to fabricate a membraneless fuel cell. Three PMMA sheets were used to create the channel (Figure 9.2b). A slit is produced in the 1 mm middle sheet using laser and is sandwiched between the top and bottom PMMA stencils using an adhesive layer. The bottom layer works as the electrode support and liquid sealing plate. A 100 nm gold layer was sputtered on the surface of the PMMA sheet to reduce the contact resistance. This gold layer acts as the current collector. The surface of the PMMA sheets was mechanically treated with fine sandpaper (1200 grit) to improve the surface roughness and to improve the adhesion of the gold layer to the substrate. Outlet and inlet holes were machined on the top PMMA piece. Pt-Ru and Pt catalyst ink were wet sprayed on the gold layer to make anode and cathode, respectively, with a loading of 4.5 mg cm^{-2}.

Rigid microchannels are also fabricated in silicon using a photolithography process [28,43]. Since silicon is stable against thermal deformation, silicon channels and substrates can be used to investigate temperature-dependent fuel cell oxidation and performance [28]. As shown in Figure 9.3c, platinum was deposited on the metallic adhesion layer using E-beam evaporation technique. The conductivity of the deposited metallic thin film as current collector depends on the thickness and the deposition process and the rate of deposition. To find a deeper understanding of thin-film materials and the corresponding processes for microfabrication, readers can refer to Ref. [54]. By exploiting the standard photolithography for silicon processing, the design can benefit from the ease of fabrication where parameters can be varied and optimization of microchannel dimension can be carried out precisely [28]. However, the whole fabrication process may be more expensive than other polymer-compatible processes.

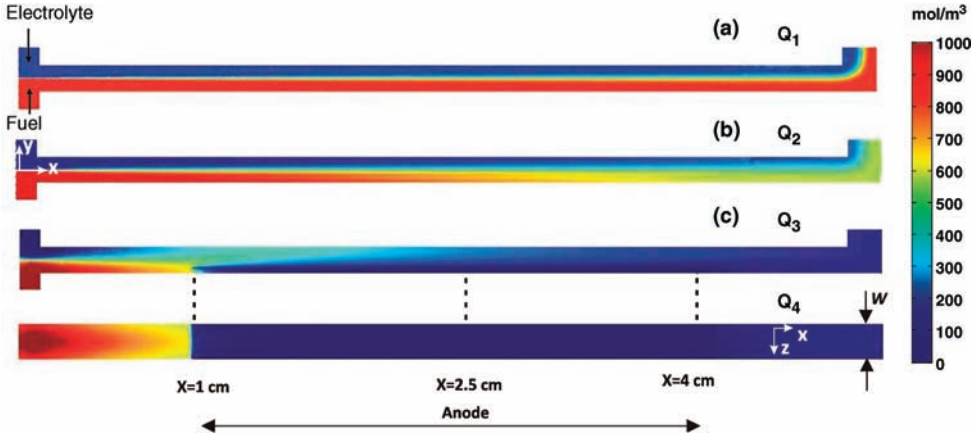

Figure 9.3 Numerical simulation of formic acid concentration in a membraneless LFFC with flow-over anode with inlet concentration of 1 M. (a) $Q_1 = 500\ \mu l\ min^{-1}$, with maximum current density of 68 mA cm^{-2}. (b) $Q_2 = 100\ \mu l\ min^{-1}$, with maximum current density of 58 mA cm^{-2}. (c) $Q_3 = 10\ \mu l\ min^{-1}$, with maximum current density of 40 mA cm^{-2}. Reproduced with permission from Ref. [40]. Copyright 2010, IOP.

To fabricate the channel in silicon, the pattern of the channel is transferred on the silicon wafer that was covered by a layer of photoresist to make a sacrificial layer. The undesired parts of the sacrificial layer are removed in the developing process. The open area allows silicon etching to create the channel. It is worthy to note that silicon is compatible with a variety of fabrication processes, including epitaxy, sputtering, chemical, and physical vapor deposition, to deposit desired layers on silicon or make thin-film current collectors and electrodes. Dry and wet chemical etchings can be used to make complex channel geometries, and electrochemical etching can be used to make porous silicon. Readers are encouraged to refer to Refs [54,55] to find more details about silicon-based fabrication processes.

Because of the ongoing electrooxidation of fuel and electroreduction of oxidant over anode and cathode, fuel and oxidant concentrations through the channel decrease. Due to the lack of convective mass transport to replenish fresh reactants to the catalytic active area, a depletion boundary layer over the catalyst-covered electrodes is formed [40], as shown in Figure 9.3.

If effective replenishment of the depletion layer does not exist, the reactant concentration over the active area of electrodes drops dramatically. In this case, only the first few millimeters of the electrode contribute the most to current collection [56] limiting the electrode length. In addition, to control diffusive mixing and consequent parasitic losses, the length of the channel must be restricted [57].

The idea of passive control of depletion layer to develop the maximum current density without using additional power-triggered investigations on the effect of multiple consecutive electrodes on the current density and fuel utilization [58,59]. Lim *et al.* [58] proposed that each electrode can be made of an array of microelectrodes. Splitting the length of an electrode into two or more sections to make shorter electrodes with spacing equal to three times of their length can avoid the continuous increase in thickness of the depleted layer. Thus, a 25% increase in maximum power density in comparison with a single-electrode device with identical active area was achieved.

9.3.2
Flow Architecture and Fabrication of Flow-Through Design

In a flow-through design, the reactant streams pass through a three-dimensional porous electrode including the catalytic active area, as shown in Figure 9.4. Salloum *et al.* [49] proposed a convective flow membraneless LFFC with porous disk electrodes (Figure 9.4a). The carrier substrate was fabricated using PMMA. Formic acid in sulfuric acid as fuel stream was introduced through an inlet from the center of the disk and made to undergo oxidation through the carbon paper covered by catalyst nanoparticles as its porous anode. Oxidant stream, potassium permanganate in sulfuric acid, was introduced concentrically through a ring of inlets. Oxidant was reduced and then mixed with the oxidized fuel, and a 2 mm gap between the anode and the cathode prevented short circuit due to backflow of oxidant.

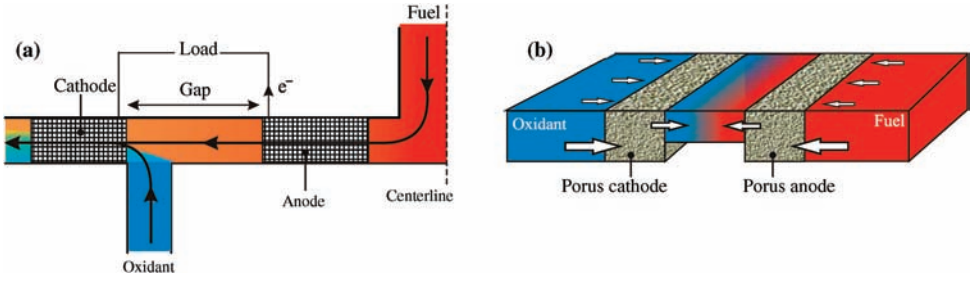

Figure 9.4 Flow-through designs. (a) Radial flow architecture for a membraneless LFFC. (b) 3D porous electrodes with so-called "multiple inlets" concept. Reproduced with permission from Ref. [19]. Copyright 2011, Elsevier.

Ion transport induced by convective transport effects increases the fuel utilization up to 58% and enables control of fuel and oxidant flow rate independently. Experimental results indicated that by increasing the fuel flow rates, fuel utilization is decreased from 58% at 100 μl min^{-1} to 4% at 5 ml min^{-1}. Increasing the concentration of sulfuric acid as supporting electrolyte increases the maximum power density from ~1.5 to ~3 mW cm^{-2} due to decreasing charge transport losses.

The concept of the so-called "multiple inlets" was developed in Sinton's group [30]. A flow-through design was proposed without imposing fluidic networks of inlets for adding fresh reactants. The whole cell is fabricated in PDMS. As schematically shown in Figure 9.4b, hydrophilic porous fiber-based carbon paper, with the main application for making gas diffusion media in PEMFC, was cut in strip shape and placed in two compartments. High porosity of carbon paper, ~78% (HGP-H 90 from Toray), provides large surface area for electrochemical reactions and enhanced the fuel utilization due to the improved diffusive/convective mass transport [30]. Running the cell on all-vanadium redox species, peak power density of 131 mW cm^{-2} was obtained at a flow rate of 300 μl min^{-1}.

9.3.3
Flow Architecture and Fabrication of LFFC with Air-Breathing Cathode

Mass transfer and diffusivity of dissolved oxygen as an oxidant in aqueous media (2×10^{-5} cm^2 s^{-1}) limit the performance of membraneless LFFCs running on dissolved oxygen. In addition, low concentration of dissolved oxygen in aqueous media (2–4 mM) cannot sufficiently provide reactant for replenishment of depletion boundary layer over the cathode. Exploiting a gas diffusion electrode (GDE) on a side wall of the channel facilitates the cell to access the high concentration of oxygen in air (10 mM) with a diffusivity four order of magnitude higher than that in aqueous media (0.2 cm^2 s^{-1}).

Proof of concept of membraneless LFFC with air-breathing cathode was proposed by Kenis' research group in 2005 [32]. As shown in Figure 9.5a and b, GDE, made of Toray carbon paper covered by catalyst ink containing platinum

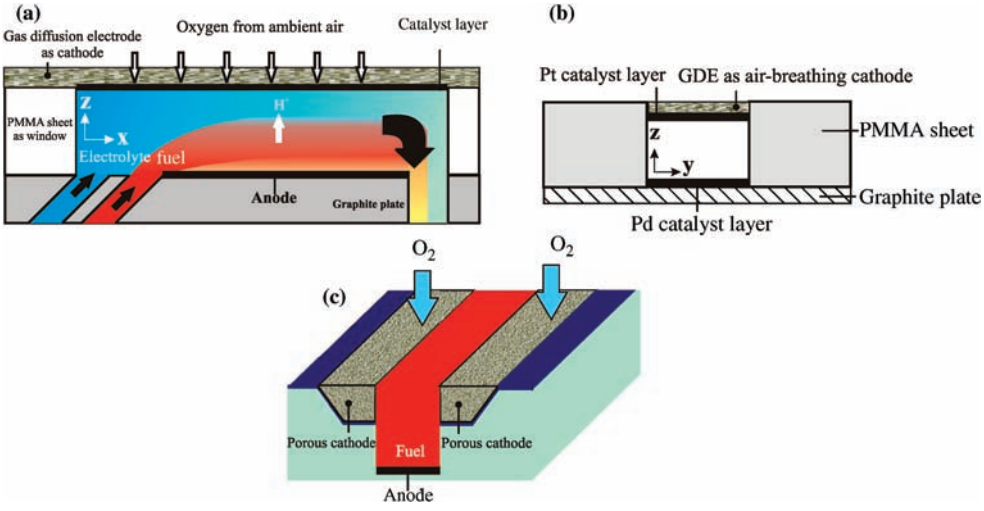

Figure 9.5 Membraneless LFFCs with air-breathing cathodes. (a) Schematic illustration for the arrangement of fuel and electrolyte streams in the channel. Adapted from Ref. [32]. (b) Cross section and carrier substrate of the channel depicted in part (a). (c) Monolithic design with air-breathing cathode. Reproduced with permission from Ref. [19]. Copyright 2011, Elsevier.

black nanoparticles, was implemented at the top wall as air-breathing cathode. The channel was made by PMMA, which is glued to a graphite plate covered with palladium black nanoparticles as a flow-over anode.

Since the oxidant stream is eliminated in this design, a stream of electrolyte is needed to separate fuel stream from direct exposure to the cathode, thus avoiding fuel crossover losses and catalyst poisoning. 1 M formic acid was used as fuel while 0.5 M sulfuric acid available in both fuel and electrolyte streams facilitated proton conduction across the channel. In this case, a peak current density of 130 mA cm^{-2}, a power density of 26 mW cm^{-2}, and a maximum power output of 16 mW were achieved for 300 ml min^{-1} at a fuel-to-electrolyte flow rate ratio of 1:1. Anode and cathode potentials obtained using a reference electrode revealed that oxygen concentration is not the source of limiting performance for an air-breathing membraneless LFFC [33].

Tominaka *et al.* [25] reported a monolithic design for running on methanol. The whole cell, which is a reservoir with open top, was fabricated in silicon as a monolithic structure that omits the electrolyte stream to separate fuel stream from the cathode. Palladium–cobalt (Pd–Co) alloy was electrodeposited on a thin layer of gold and worked as the electrode/current collector. In this design with full passive fuel and oxidant delivery systems, oxygen is taken through a porous cathode. A 2 M methanol solution containing a sulfuric acid as supporting electrolyte is dropped onto the end of the microchannel. Open-circuit voltage and net maximum power of this fuel cell reached 0.5 V and 1.4 μW, respectively.

9.3.4
Performance Comparison

To provide a quantitative performance comparison, performance of different membraneless LFFCs based on the three electrode designs is reviewed in Tables 9.2 and 9.3.

Since fuel type has significant effects on cell kinetics, only membraneless LFFCs running on formic acid or methanol is discussed for comparison. Table 9.2 provides some design features of the maximum power density of three different flow architectures running on formic acid or methanol.

Table 9.3 shows that the order of magnitude for the power density of membraneless LFFCs running on formic acid or methanol for flow-over design ranges from 0.1 to 1 $mW\,cm^{-2}$, and for flow-through design from 1 to 10 $mW\,cm^{-2}$. The low performance of flow-over designs is mainly attributed to low oxidant concentration at catholyte and the growth of depletion layer over electrodes. The development of performance for flow-through design is associated with enhancement of catalytic reaction through porous and 3D electrodes with effective replenishment of reactant over active sites. The main reason for higher performance of membraneless LFFCs with air breathing is the higher rate of oxygen transport to cathode from ambient air. Since oxygen is provided from air through GDE, the oxygen concentration over the active site of the cathode is almost constant, thus enhancing the current generation.

9.4
Fuel, Oxidant, and Electrolytes

9.4.1
Fuel Types

Membraneless LFFCs have a wide range of fuel options. With respect to fuel and oxidant selection, there are many fuels available including hydrogen (H_2) [37,43,60], methanol (CH_3OH) [26,33], ethanol (C_2H_5OH) [34], formic acid [28,46], hydrogen peroxide (H_2O_2) [45], vanadium redox species [18,29], sodium borohydride ($NaBH_4$) [34], and hydrazine (N_2H_4) [34].

Among such aqueous fuels, formic acid and methanol with energy densities of 2.08 and 4.69 $kWh\,l^{-1}$ attracted more attention for the use in membraneless LFFCs due to the ease of access and well-studied electrocatalysis. A formic acid/O_2 fuel cell has a high theoretical electromotive force of 1.45 V, while the corresponding value of methanol is 1.2 V.

Cohen *et al.* [28] tested a membraneless LFFC run by formic acid as fuel with platinum as catalyst to oxidize formic acid in combination with dissolved oxygen:

$$HCOOH \rightarrow 2H^+ + 2e^- + CO_2, \quad E^0 = 0.22\,V \tag{9.13}$$

$$4H^+ + O_2 + 4e^- \rightarrow 2H_2O, \quad E^0 = 1.23\,V \tag{9.14}$$

Table 9.2 Performance of LFFCs running on formic acid or methanol.

Design	Fuel/oxidant	Electrolyte	Electrode structure	Maximum current density ($mA\ cm^{-2}$)	Maximum power density ($mW\ cm^{-2}$)	Design features
Choban *et al.* [26]	Methanol (1 M) Dissolved oxygen	Sulfuric acid or potassium hydroxide (1 M)	Flow-over	40	12	Mixed media operation
Choban *et al.* [42]	Methanol (1 M) Dissolved O_2	Sulfuric acid (0.5 M)	Flow-over	8	2.8	—
Cohen *et al.* [28]	Formic acid (0.5 M) Dissolved O_2	Sulfuric acid (0.1 M)	Flow-over	1.5	0.18	Stackable microchannels
Choban *et al.* [41]	Formic acid (2.1 M) Dissolved oxygen	Sulfuric acid (0.5 M)	Flow-over	0.8	0.17	
Li *et al.* [39]	Formic acid (0.5 M) Dissolved O_2	Sulfuric acid (0.1 M)	Flow-over	1.5	0.58	Laser-machined
Morales-Acosta *et al.* [31]	Formic acid (0.1, 0.5 M) Dissolved oxygen	Sulfuric acid	Flow-over	11.5	3.3	Pd/MWCNTs as catalyst
Salloum *et al.* [49]	Formic acid (0.04 M) Potassium permanganate (0.01 M)	Sulfuric acid (0.5–1 M)	Flow-through	5	2.8	Sequential radial flow
Kjeang *et al.* [48]	Formic acid (1.2 M) Sodium hypochlorite (0.67 M)	Sodium hydroxide (2.8 M)	Flow-through	230	52	3D structure of electrodes

Jayashree *et al.* [32]	Formic acid (1 M) Air	Sulfuric acid (0.5 M)	Air breathing	130	26	—
Jayashree *et al.* [33]	Methanol (1 M) Potassium hydroxide (1 M) Air	Sulfuric acid (0.5 M)	Air breathing	120	17	—
Brushett *et al.* [34]	HCOOH (1 M) Air	Sulfuric acid (0.5 M) or potassium hydroxide (1 M)	Air breathing	130	26	—
Hollinger *et al.* [36]	Methanol (1 M) O_2	Sulfuric acid (1 M)	Air breathing	655	70	Methanol @ 80 C with O_2 feed to the cathode
Whipple *et al.* [35]	Methanol (0.1–15 M) Air	Sulfuric acid (0.5 M)	Air breathing	62	4	Using Ru_xSe_y as methanol-tolerant catalyst for cathode

Reproduced with permission from Ref. [19]. Copyright 2011, Elsevier.

Table 9.3 Design features of three different flow architecture with maximum running by formic acid or methanol.

Reference	Maximum power density ($mW\,cm^{-2}$)	Design features and comments
	Flow-over electrode	
Choban *et al.* [26]	12 at flow rate of $3\,ml\,min^{-1}$ per inlet flow	Side-by-side streaming, Y shape, channel length = 29 mm, channel height = 1 mm, and channel width = 0.75 mm, Pt/Ru and Pt black nanoparticles in Nafion-based ink solution applied to graphite plate as anode and cathode, fuel utilization <10%
	Flow-through electrode	
Kjeang *et al.* [48]	52 at 0.4 V and flow rate of $60\,\mu l\,min^{-1}$ per inlet	Side-by-side streaming, T shape, channel length = 12 mm, channel height = 0.3 mm, channel width = 3 mm, electrodeposited Pd and Au on carbon paper strips to make flow-through anode and cathode, fuel utilization of 85% at peak power density and 100% at lower voltages
	Air-breathing electrode	
Hollinger *et al.* [36]	70 at flow rate of $0.3\,ml\,min^{-1}$ per inlet	Vertically layered streaming, T shape, channel length = 48 mm, channel width = 3.3 mm, Pt/Ru and Pt nanoparticles in Nafion-based ink solution brushed on carbon paper as electrodes, graphite plates as current collectors, implementing of nanoporous separator at the fuel–electrolyte interface, running at 80 °C with O_2 supply of 50 sccm, hot-pressed thin film of Nafion over cathode to alleviate fuel crossover effects

Reproduced with permission from Ref. [19]. Copyright 2011, Elsevier.

However, there are some disadvantages of using formic acid, for example, CO poisoning of the Pt catalyst; the system is easily controlled and the cell has a large open-circuit potential and high electrochemical efficiency [28].

Usually, vanadium redox couples dissolved in a supporting electrolyte, such as sulfuric acid, V^{2+}/V^{3+} as anolyte and VO_2^+/VO^{2+} as catholyte, are used to form all-vanadium fuel/oxidant system for membraneless LFFCs [18,27,30,61]. A membraneless LFFC can operate based on the following anodic and cathodic redox reactions and the standard electrode potential [30]:

$$V^{3+} + e^- = V^{2+}, \quad E^0 = -0.496\,V \text{ versus SCE} \tag{9.15}$$

$$VO_2^+ + 2H + e \rightleftarrows VO^{2+} + H_2O, \quad E^0 = 0.750\,V \text{ versus SCE} \tag{9.16}$$

The advantages of this redox combination for microfluidic fuel cells [20,30] are (i) providing the well-balanced electrochemical half-cells in terms of reaction rates and transport characteristics, (ii) having high solubility and ability of having

relatively high redox concentration up to 5.4 M, (iii) having a high open-circuit voltage (up to ~1.7 V at uniform pH) due to the presence of large difference in formal redox potentials, and (iv) utilization of bare carbon electrodes without precious metal catalyst to facilitate the reactions.

The energy density of a vanadium redox fuel cell is limited by the solubility of the vanadium redox species. To address this situation, a new alkaline microfluidic fuel cell was demonstrated by Kjeang *et al.* [48], based on formic acid and hypochlorite oxidant. The reactant solutions are obtained from formic and sodium hypochlorite, both of which are available and stable as highly concentrated liquids, leading to a fuel cell system with high overall energy density. Formate ($HCOO^-$) oxidation and hypochlorite reduction were established in alkaline media on porous Pd and Au electrodes, respectively. The results indicate the rapid kinetics at low overpotentials while preventing gaseous CO_2 formation by carbonate absorption.

Brushett *et al.* [34] utilized 3 M hydrazine as fuel with 0.5 M of sulfuric acid as electrolyte in an air-breathing flow architecture. For this hydrazine membraneless LFFC, maximum power density of 80 mW cm^{-2} was achieved at room temperature, while the anode catalyst loading was 1 mg cm^{-2} supported by Pt and the fuel/electrolyte flow rate was 0.3 ml min^{-1}. Moreover, with the same operating conditions as mentioned earlier, hydrazine was tested with oxygen delivery method at a flow rate of 50 sccm instead of quiescent air. No considerable improvement was achieved in peak power density and maximum current density, which indicates that this membraneless LFFC configuration is not restricted by oxygen transport.

This direct hydrazine acidic membraneless LFFC can be a promising microscale power source for applications where the safety is not a major concern. The theoretical open-circuit potential of a hydrazine/O_2 fuel cell is 1.56 V. In addition, the end products of complete electrooxidation of hydrazine/O_2 are nitrogen gas and water, which can enable the hydrazine fuel cells to be eco-friendly zero-emission energy convertors [34]. Also, Brushett *et al.* [34] used 1 M sodium borohydride in 1 M KOH as fuel on Pt anode. However, sodium borohydride with energy density of 9.29 kWh kg^{-1} is unstable in acidic media, but highly stable in alkaline media. Peak power density of 101 mW cm^{-2} was recorded when both fuel and electrolyte stream (1 M KOH) flow at 0.3 ml min^{-1} with air-breathing cathode. This high performance is mainly credited to the improved electrocatalytic activity of Pt toward the oxidation of the borohydride anions.

9.4.2 Oxidant Types

Oxidants can be dissolved oxygen in aqueous form [26,39,42,62], air [25,32–35], hydrogen peroxide [45,47], vanadium redox species [18,27,29], potassium permanganate [46,49], and sodium hypochlorite [48].

Basically, the cathodic half-cell electrokinetics is slower than the anodic one. The oxygen reduction reaction (ORR) is sluggish. Completion of ORR requires

many individual steps and significant molecular reorganization, so the majority of activation overvoltage loss takes place at the cathode. At standard temperature and pressure (298 K, 1 atm) the exchange current densities (i_0) for ORR on Pt is six orders of magnitude lower than that of the hydrogen oxidation reaction (HOR). When the dissolved oxygen is used as oxidant, the slow electrokinetic reactions in the cathode are coupled with low oxygen concentration resulting in low power density. For improving the mass transport limitation of dissolved oxygen in electrolyte, alternative oxidants soluble at higher concentration than dissolved oxygen can be used.

The few fuel cell designs using liquid oxidants have generally more power output. Choban *et al.* [62] replaced oxygen saturated in 0.5 M sulfuric acid by 0.144 M potassium permanganate as oxidant and used 2.1 M formic acid as fuel. The results showed that the cell operation using potassium permanganate develops a current density with one order of magnitude higher due to the higher solubility of potassium permanganate in aqueous media [41].

Li *et al.* [39] utilized saturated oxygen in 0.1 M H_2SO_4 solution as oxidant with 0.5 M HCOOH in 0.1 M H_2SO_4 solution as fuel. The maximum power density of 0.58 mW cm^{-2} was caused by insufficient supply of oxygen from oxidant stream to the cathode.

Also, gaseous air was used as oxidant in air-breathing configurations [32–34,40]. Since the concentration of oxygen in air (0.2 cm^2 s^{-1}) is four orders of magnitude higher than in aqueous media (2×10^{-5} cm^2 s^{-1}) [32], the air cathode designs can provide higher maximum power density and power output.

9.4.3 Electrolyte Types

In most membraneless LFFC designs, fuel and oxidant are dissolved in electrolyte and then usually introduced into the channel using syringe pumps. The main reason for adding electrolyte to streams is to enhance the ionic conduction to decrease the ohmic losses across the distance between the anode and cathode. As an example, by adding sulfuric acid to both streams in a membraneless LFFC, a source of protons closer to cathode is provided and because of the proton consumption at cathode a gradient of protons is maintained [62]. Experimental results of Choban *et al.* [62] revealed that by using 0.5 M sulfuric acid as supporting electrolyte, a maximum current density of 0.9 mW cm^{-2} was obtained, while the maximum current density of the LFFC with water as electrolyte was just 0.2 mW cm^{-2} at the maximum volumetric flow rate of 0.8 ml min^{-1}.

Lack of the membrane allows the cell to operate in both acidic and alkaline media, as well as under "mixed-media" where the cathode is in acidic and anode is in alkali media, or vice versa [26]. This media flexibility enables the designer to tailor the composition of cathode and anode streams individually to optimize the individual electrode kinetics as well as the overall cell potential [26]. Furthermore, one has the freedom to run the membraneless LFFC in all-acidic, all-alkaline, or in a mixed-media mode.

The pH of the electrolyte is effective on the reaction kinetics at the individual electrodes and the electrode potential at which oxidation or reduction takes place [26]. Electrolyte is typically a strong acid or a strong base, such as sulfuric acid or potassium hydroxide, which include highly mobile hydronium or hydroxide ions, respectively [20]. Typically, operation of fuel cell in alkaline media can develop the electrooxidation of the catalyst-poisoning carbon monoxide species on the anode and the kinetics of ORR is improved at the cathode [26]. However, in membrane-based fuel cells, due to the potential of carbonate formation resulting in clogging the membrane, the long-term stability is restricted and limits the use of these alkali-compatible membranes for liquid fuel cell operations [26].

Bruhsett *et al.* [34] examined the performance of air-breathing membraneless LFFC operated with ethanol and methanol under acidic (H_2SO_4) and alkaline (KOH) conditions. Methanol and ethanol showed improved open-circuit potential and maximum power density in alkaline media (1.2 and 0.7 V, 17.2 and 12.1 mW cm^{-2}) compared with acidic conditions (0.93 and 0.41 V, 11.8 and 1.9 mW cm^{-2}). The improved performance in alkaline media was the result of the enhanced alcohol oxidation kinetics and oxygen reduction kinetics compared with acidic media.

Choban *et al.* [26] investigated the acidic (H_2SO_4), alkaline (KOH), and acidic/alkaline media on the cell potential and power output of a membraneless LFFC running on 1 M methanol and dissolved oxygen. The results indicate that the process in both acidic and alkaline media is cathode limited, which can be attributed to the low oxygen concentration in solution. The oxygen solubility in acidic media is about 1 mM, while the oxygen solubility in alkaline media is approximately 25% lower, resulting in earlier drop in performance in the I–V curve [26]. Also, there is no issue with carbonate formation in their work due to the immediate removal of any formed carbonates from the system by the flowing streams.

In the case of acidic anode stream combined with an alkaline cathode stream, the maximum theoretical OCP is 0.38 V, but an OCP <0.1 V is observed due to the overpotentials on the cathode and anode. In other words, the energy liberated in the methanol oxidation and oxygen reduction reactions is mostly used by water ionization reaction. In this configuration, the electrolytic reaction combined with a galvanic reaction is incapable of producing a large amount of energy [26].

In the case of alkaline anode and acidic cathode, the combination of two galvanic reactions in this configuration yields a desirable high theoretical OCP of 2.04 V. However, the practical OCP is 1.4 V due to the slow kinetics of oxygen reduction and methanol oxidation. Also the power density of mixed media is higher than those obtained for all-acidic and all-alkaline membraneless LFFC experiments.

Most of the observed extra power density for the mixed media configuration is supplied by the electrochemical acid–base neutralization reaction where protons are reduced on the cathode and hydroxide ions are consumed, in methanol oxidation at the cathode. So, the consumption of H_2SO_4 and KOH must be taken into account while comparing the different membraneless LFFC configurations.

While the cell runs under alkaline anode with acidic cathode conditions, both OH^- and H^+ are consumed at the anode and cathode at a rate of six for each molecule of methanol. The maximum theoretical energy density (based on the reaction of 1 M of methanol with ambient oxygen, consuming 6 equiv of H_2SO_4 and KOH) is 495 Wh kg^{-1}, much lower than the theoretical value for the all-alkaline and all-acidic LFFC in which only methanol is consumed (6000 Wh kg^{-1}) [26].

Hasegawa *et al.* [45] utilized the mixed media approach to operate a microfluidic fuel cell on hydrogen peroxide as both fuel and oxidant, in alkaline (NaOH) and acidic (H_2SO_4) media, respectively. This design produced relatively high power densities up to 23 mW cm^{-2}. The drawback of this design is the spontaneous decomposition of hydrogen peroxide on the cathode and associated bubble generation due to oxygen gas evolution that may disturb the colaminar flow interface.

The overall reaction of this design is

$$H_2O_2(aq) + HO_2^-(aq) + 2H^+(aq) + OH^-(aq) \rightarrow O_2 + 3H_2O \qquad (9.17)$$

which involves the disproportionation reaction of H_2O_2 together with the combination of H^+ and OH^- ions. SO_4^{2-} ion neutralizes Na^+ ion electrically at the acidic/alkaline bipolar electrolyte interface so that the reaction of 9.17 proceeds continuously. Consequently, the products of this fuel cell type are water, oxygen, and salt.

9.5 Conclusions

This chapter discusses the design, fabrication technology, and performance of membraneless LFFCs. Innovative designs including new flow architectures and electrode arrangements in the channel using new materials are under development to increase the performance of single cell and the fuel utilization in single pass. To generate enough power for practical applications, stacking is inevitable. Commercialization aspects, including cost and durability, reveal a huge research potential for the development of alternative materials besides the innovative fluidic design and optimization for stacking of membraneless LFFCs. Optimal choice of fuel and oxidant should be addressed as well. Novel electrodes and current collectors with high electrical conductivity and long-term durability must be developed and explored according to acidic or basic medium of the cell. Also, the combined area-specific resistivity (ASR) of the cell components, including electrolyte, anode, and cathode, should be decreased to provide high power densities. Graphite is resistant to corrosion unlike most metallic materials, but its micromachining may increase the total cost. In terms of electrocatalyst, membraneless LFFCs can generally benefit from the advancements in electrocatalyst materials for instance poisoning tolerant nanocatalysts for direct liquid fuel cells. The whole fuel cell system should be run on very low power consumption of in a passive scheme. Microfabrication and microfluidic technologies can provide passive or very low power consumption fuel/oxidant delivery systems.

References

1 Moghaddam, S., Pengwang, E., Jiang, Y.B., Garcia, A.R., Burnett, D.J., Brinker, C.J., Masel, R.I., and Shannon, M.A. (2010) An inorganic–organic proton exchange membrane for fuel cells with a controlled nanoscale pore structure. *Nat Nano*, **5** (3), 230–236.

2 Moghaddam, S. *et al.* (2010) An enhanced microfluidic control system for improving power density of a hydride-based micro fuel cell. *Journal of Power Sources*, **195** (7), 1866–1871.

3 Moghaddam, S. *et al.* (2008) A self-regulating hydrogen generator for micro fuel cells. *Journal of Power Sources*, **185** (1), 445–450.

4 Nguyen, N.T. and Chan, S.H. (2006) Micromachined polymer electrolyte membrane and direct methanol fuel cells: a review. *Journal of Micromechanics and Microengineering*, **16** (4), R1–R12.

5 Ha, S., Dunbar, Z., and Masel, R.I. (2006) Characterization of a high performing passive direct formic acid fuel cell. *Journal of Power Sources*, **158** (1), 129–136.

6 Moghaddam, S. *et al.* (2010) An enhanced microfluidic control system for improving power density of a hydride-based micro fuel cell. *Journal of Power Sources*, **195** (7), 1866–1871.

7 Mousavi Shaegh, S.A., Nguyen, N.T., and Chan, S.H. (2011) A review on membraneless laminar flow-based fuel cells. *International Journal of Hydrogen Energy*, **36** (9), 5675–5694.

8 Chan, S.H., Nguyen, N.T., Xia, Z., and Wu, Z. (2005) Development of a polymeric micro fuel cell containing laser-micromachined flow channels. *Journal of Micromechanics and Microengineering*, **15** (1), 231–236.

9 Kelley, S.C., Deluga, G.A., and Smyrl, W. H. (2000) A miniature methanol/air polymer electrolyte fuel cell. *Electrochemical and Solid-State Letters*, **3** (9), 407–409.

10 Pichonat, T., Gauthier-Manuel, B., and Hauden, D. (2004) A new proton-conducting porous silicon membrane for small fuel cells. *Chemical Engineering Journal*, **101** (1–3), 107–111.

11 Gold, S., Chu, K.-L., Lu, C., Shannon, M.A., and Masel, R.I. (2004) Acid loaded porous silicon as a proton exchange membrane for micro-fuel cells. *Journal of Power Sources*, **135** (1–2), 198–203.

12 Pennathur, S., Eijkel, J.C.T., and van denBerg, A. (2007) Energy conversion in microsystems: is there a role for micro/nanofluidics? *Lab on a Chip*, **7** (10), 1234–1237.

13 Brody, J.P. and Yager, P. (1997) Diffusion-based extraction in a microfabricated device. *Sensors and Actuators A: Physical*, **58** (1), 13–18.

14 Surmeian, M., Slyadnev, M.N., Hisamoto, H., Hibara, A., Uchiyama, K., and Kitamori, T. (2002) Three-layer flow membrane system on a microchip for investigation of molecular transport. *Analytical Chemistry*, **74** (9), 2014–2020.

15 Weigl, B.H. and Yager, P. (1999) Microfluidic diffusion-based separation and detection. *Science*, **283** (5400), 346–347.

16 Kenis, P.J.A., Ismagilov, R.F., and Whitesides, G.M. (1999) Microfabrication inside capillaries using multiphase laminar flow patterning. *Science*, **285**, 83–85.

17 Song, C., Nguyen, N.T., Tan, S.H., and Asundi, A.K. (2009) Modelling and optimization of micro optofluidic lenses. *Lab on a Chip*, **9**, 1178–1184.

18 Ferrigno, R., Stroock, A.D., Clark, T.D., Mayer, M., and Whitesides, G.M. (2002) Membraneless vanadium redox fuel cell using laminar flow. *Journal of the American Chemical Society*, **124** (44), 12930–12931.

19 Mousavi Shaegh, S.A., Nguyen, N.T., and Chan, S.H. (2011) A review on membraneless laminar flow-based fuel cells. *International Journal of Hydrogen Energy*, **36** (9), 5675–5694.

20 Kjeang, E., Djilali, N., and Sinton, D. (2008) Microfluidic fuel cells: a review. *Journal of Power Sources*, **186** (2), 353–369.

21 Sharp, K.V., Adrian, R.J., Santiago, J.G., and Molho, J.I. (2002) Liquid flows in microchannels, in *CRC Handbook of MEMS* (ed. M. Gad-el-Hak), CRC Press, New York, 6-1–6-38.

22 Nguyen, N.T. and WEreley, S.T. (2006) *Fundamentals and Applications of Microfluidics*, Artech House, Inc.

23 Atencia, J. and Beebe, D.J. (2005) Controlled microfluidic interfaces. *Nature*, **437** (7059), 648–655.

24 Mench, M.M. (2008) *Fuel Cell Engines*, John Wiley & Sons, Inc., New Jersey.

25 Tominaka, S., Ohta, S., Obata, H., Momma, T., and Osaka, T. (2008) On-chip fuel cell: micro direct methanol fuel cell of an air-breathing, membraneless, and monolithic design. *Journal of the American Chemical Society*, **130** (32), 10456–10457.

26 Choban, E.R., Spendelow, J.S., Gancs, L., Wieckowski, A., and Kenis, P.J.A. (2005) Membraneless laminar flow-based micro fuel cells operating in alkaline, acidic, and acidic/alkaline media. *Electrochimica Acta*, **50** (27), 5390–5398.

27 Kjeang, E., McKechnie, J., Sinton, D., and Djilali, N. (2007) Planar and three-dimensional microfluidic fuel cell architectures based on graphite rod electrodes. *Journal of Power Sources*, **168** (2), 379–390.

28 Cohen, J.L., Westly, D.A., Pechenik, A., and Abruña, H.D. (2005) Fabrication and preliminary testing of a planar membraneless microchannel fuel cell. *Journal of Power Sources*, **139** (1–2), 96–105.

29 Kjeang, E., Proctor, B.T.M., Brolo, A.G., Harrington, D.A., Djilali, N., and Sinton, D. (2007) High-performance microfluidic vanadium redox fuel cell. *Electrochimica Acta*, **52** (15), 4942–4946.

30 Kjeang, E., Michel, R., Harrington, D.A., Djilali, N., and Sinton, D. (2008) A microfluidic fuel cell with flow-through porous electrodes. *Journal of the American Chemical Society*, **130** (12), 4000–4006.

31 Morales-Acosta, D., Rodríguez, G., Godinez, H., Luis, A., and Arriaga, L.G. (2010) Performance increase of microfluidic formic acid fuel cell using Pd/MWCNTs as catalyst. *Journal of Power Sources*, **195** (7), 1862–1865.

32 Jayashree, R.S., Gancs, L., Choban, E.R., Primak, A., Natarajan, D., Markoski, L.J., and Kenis, P.J.A. (2005) Air-breathing laminar flow-based microfluidic fuel cell. *Journal of the American Chemical Society*, **127** (48), 16758–16759.

33 Jayashree, R.S., Egas, D., Spendelow, J.S., Natarajan, D., Markoski, L.J., and Kenis, P.J.A. (2006) Air-breathing laminar flow-based direct methanol fuel cell with alkaline electrolyte. *Electrochemical and Solid-State Letters*, **9** (5), A252–A256.

34 Brushett, F.R., Jayashree, R.S., Zhou, W.P., and Kenis, P.J.A. (2009) Investigation of fuel and media flexible laminar flow-based fuel cells. *Electrochimica Acta*, **54** (27), 7099–7105.

35 Whipple, D.T., Jayashree, R.S., Egas, D., Alonso-Vante, N., and Kenis, P.J.A. (2009) Ruthenium cluster-like chalcogenide as a methanol tolerant cathode catalyst in air-breathing laminar flow fuel cells. *Electrochimica Acta*, **54** (18), 4384–4388.

36 Hollinger, A.S., Maloney, R.J., Jayashree, R.S., Natarajan, D., Markoski, L.J., and Kenis, P.J.A. (2010) Nanoporous separator and low fuel concentration to minimize crossover in direct methanol laminar flow fuel cells. *Journal of Power Sources*, **195** (11), 3523–3528.

37 Mitrovski, S.M. and Nuzzo, R.G. (2006) A passive microfluidic hydrogen-air fuel cell with exceptional stability and high performance. *Lab on a Chip*, **6** (3), 353–361.

38 Mitrovski, S.M., Elliott, L.C.C., and Nuzzo, R.G. (2004) Microfluidic devices for energy conversion: planar integration and performance of a passive, fully immersed H_2-O_2 fuel cell. *Langmuir*, **20** (17), 6974–6976.

39 Li, A., Chan, S.H., and Nguyen, N.T. (2007) A laser-micromachined polymeric membraneless fuel cell. *Journal of Micromechanics and Microengineering*, **17**, 1107–1113.

40 Mousavi Shaegh, S.A., Nguyen, N.T., and Chan, S.H. (2010) An air-breathing laminar flow-based formic acid fuel cell with porous planar anode: experimental and numerical investigations. *Journal of Micromechanics and Microengineering*, **20**, 12.

41 Choban, E.R. *et al.* (2004) Microfluidic fuel cell based on laminar flow. *Journal of Power Sources*, **128** (1), 54–60.

42 Choban, E.R., Waszczuk, P., and Kenis, P.J.A. (2005) Characterization of limiting

factors in laminar flow-based membraneless microfuel cells. *Electrochemical and Solid-State Letters*, **8** (7), A348–A352.

43 Cohen, J.L., Volpe, D.J., Westly, D.A., Pechenik, A., and Abruña, H.D. (2005) A dual electrolyte H_2/O_2 planar membraneless microchannel fuel cell system with open circuit potentials in excess of 1.4V. *Langmuir*, **21** (8), 3544–3550.

44 López-Montesinos, P.O. *et al.* (2011) Design, fabrication, and characterization of a planar, silicon-based, monolithically integrated micro laminar flow fuel cell with a bridge-shaped microchannel cross-section. *Journal of Power Sources*, **196** (10), 4638–4645.

45 Hasegawa, S., Shimotani, K., Kishi, K., and Watanabe, H. (2005) Electricity generation from decomposition of hydrogen peroxide. *Electrochemical and Solid-State Letters*, **8** (2), A119–A121.

46 Sun, M.H., Velve Casquillas, G., Guo, S.S., Shi, J., Ji, H., Ouyang, Q., and Chen, Y. (2007) Characterization of microfluidic fuel cell based on multiple laminar flow. *Microelectronic Engineering*, **84** (5–8), 1182–1185.

47 Kjeang, E., Brolo, A.G., Harrington, D.A., Djilali, N., and Sinton, D. (2007) Hydrogen peroxide as an oxidant for microfluidic fuel cells. *Journal of the Electrochemical Society*, **154** (12), B1220–B1226.

48 Kjeang, E., Michel, R., Harrington, D.A., Sinton, D., and Djilali, N. (2008) An alkaline microfluidic fuel cell based on formate and hypochlorite bleach. *Electrochimica Acta*, **54** (2), 698–705.

49 Salloum, K.S., Hayes, J.R., Friesen, C.A., and Posner, J.D. (2008) Sequential flow membraneless microfluidic fuel cell with porous electrodes. *Journal of Power Sources*, **180** (1), 243–252.

50 Sung, W. and Choi, J.-W. (2007) A membraneless microscale fuel cell using non-noble catalysts in alkaline solution. *Journal of Power Sources*, **172** (1), 198–208.

51 Xia, Y.N. and Whitesides, G.M. (1998) Soft lithography. *Annual Review of Materials Science*, **28** (1), 153–184.

52 Lee, J.N., Park, C., and Whitesides, G.M. (2003) Solvent compatibility of poly (dimethylsiloxane)-based microfluidic devices. *Analytical Chemistry*, **75** (23), 6544–6554.

53 Merkel, T.C., Bondar, V.I., Nagai, K., Freeman, B.D., and Pinnau, I. (2000) Gas sorption, diffusion, and permeation in poly (dimethylsiloxane). *Journal of Polymer Science, Part B: Polymer Physics*, **38** (3), 415–434.

54 Franssila, S. (2010) *Introduction to Microfabrication*, 2nd edn, John Wiley & Sons, Inc., Hoboken, NJ.

55 Madou, M.J. (2002) *Fundamental of Microfabrication: The Science of Miniaturization*, 2nd edn, CRC Press, Boca Raton, FL.

56 Jayashree, R.S., Yoon, S.K., Brushett, F.R., Lopez-Montesinos, P.O., Natarajan, D., Markoski, L.J., and Kenis, P.J.A. (2010) On the performance of membraneless laminar flow-based fuel cells. *Journal of Power Sources*, **195** (11), 3569–3578.

57 Hayes, J.R., Engstrom, A.M., and Friesen, C. (2008) Orthogonal flow membraneless fuel cell. *Journal of Power Sources*, **183** (1), 257–259.

58 Lim, K.G., Palmore, G., and Tayhas, R. (2007) Microfluidic biofuel cells: the influence of electrode diffusion layer on performance. *Biosensors and Bioelectronics*, **22** (6), 941–947.

59 Lee, J., Lim, K.G., Palmore, G.T.R., and Tripathi, A. (2007) Optimization of microfluidic fuel cells using transport principles. *Analytical Chemistry*, **79** (19), 7301–7307.

60 Mitrovski, S.M., Elliott, L.C.C., and Nuzzo, R.G. (2004) Microfluidic devices for energy conversion: Planar integration and performance of a passive, fully immersed H2-O2 fuel cell (Supporting Information). *Langmuir*, **20** (17), 6974–6976.

61 Salloum, K.S. and Posner, J.D. (2010) Counter flow membraneless microfluidic fuel cell. *Journal of Power Sources*, **195** (19), 6941–6944.

62 Choban, E.R., Markoski, L.J., Wieckowski, A., and Kenis, P.J.A. (2004) Microfluidic fuel cell based on laminar flow. *Journal of Power Sources*, **128** (1), 54–60.

10
Progress in Electrocatalysts for Direct Alcohol Fuel Cells

Luhua Jiang and Gongquan Sun

10.1
Introduction

Proton exchange membrane fuel cells (PEMFCs) attract more and more interest as promising power sources for automobiles and stationary and portable applications owing to its inherent properties such as quietness, being environmentally benign, compact system, easy start-up and shutdown, and high power density [1–5]. If the anode of a PEMFC is fed with alcohols, it is called direct alcohol fuel cell (DAFC). DAFCs have been developed since 1960s [6] owing to its advantages in fuel storage, transport, and so on. Among all the investigated possible liquid fuels [7–16], methanol and ethanol are the most potential ones for their relatively simple structure and higher oxidation activity. Until now, focus has been mainly on methanol because it does not require a C−C bond cleavage. An excellent methanol oxidation catalyst is characterized by both dehydrogenation at low temperatures and removal of the methanol oxidation residues such as CO-like species. In order to improve the activity of Pt, different promoters such as Ru [17–20], Sn [21–25], W [26,27], and Mo [28,29] have been adopted to enhance the activity of Pt toward methanol oxidation reaction (MOR) and weaken CO-like species produced on Pt active sites. Until now, PtRu alloy is considered to be the most effective one as explained by the famous bifunctional mechanism [18]. For ethanol, the complete electrooxidation is relatively difficult because it includes the cleavage of C−C bond. So a good ethanol oxidation catalyst has to perform multifunctions, including dehydrogenation, removal of CO-like species, and cleavage of C−C bond at relatively low temperatures. This places the ethanol electrocatalyst to a more important position. In the case of cathode electrocatalysts, considering not only the electrocatalytic activity to oxygen reduction but also the tolerance to methanol permeated from anode to cathode, Fe, Co, Ni, and V have been used to decorate platinum [30–33] and some non-noble metal catalysts have also been prepared and used [34–37]. However, a new challenge appeared when the non-noble metals were used as the cathodes, that is, the non-noble metals would leach out in the acidic working environment.

Materials for Low-Temperature Fuel Cells, First Edition. Edited by Bradley Ladewig, San P. Jiang, and Yushan Yan.

In this chapter, a systematic research on the electrocatalysts toward oxygen reduction reaction (ORR), MOR, and ethanol oxidation reaction (EOR) at DICP in the past decade is reviewed.

10.2 Developing an Effective Method to Prepare Electrocatalysts

Particle size, morphology, and structure have strong influence on the activities of catalysts, so it is important to develop a simple but effective method to be capable of controlling the particle size and even the microstructure of nanoparticles. Several preparation methods, including impregnation–reduction method (formaldehyde was used as the reducing agent) [38], hydroperoxide oxidation decomposition method [39–41], and the modified polyol method [42–44], were attempted in our laboratory.

10.2.1 Carbon-Supported Platinum

Platinum is the most often used electrocatalyst for the ORR. To enhance the dispersion of Pt, Pt nanoparticles are usually dispersed on carbon. In this chapter, Vulcan XC 72 was used as the support. For a practical fuel cell catalyst, the Pt loading is sometimes as high as 60% in weight to decrease the thickness of the catalyst layer so as to lessen the diffusion resistance of electrodes. At such high Pt loadings, the conventional methods, such as impregnation–reduction method using gaseous hydrogen or liquid reducing agents, such as $NaBH_4$ or HCHO, failed to produce small and uniform Pt nanoparticles [45–47]. Figure 10.1a and b are transmission electron microscopy (TEM) images of 20 wt% Pt/C prepared by an aqueous impregnation method with formaldehyde as a reducing agent and a polyol process (denoted as 20% Pt/C-HCHO and 20% Pt/C-EG, respectively) [45,46]. The TEM image of the 20% Pt/C-EG reveals that the Pt nanoparticles are highly dispersed on carbon and the mean particle size is around 2 nm; in contrast, the Pt nanoparticles for the 20% Pt/C-HCHO are slightly aggregated and the mean particle size is around 5.3 nm, much larger than that of Pt/C-EG. Furthermore, we prepared a series of Pt/C catalysts with a varied Pt loading of 10–60 wt% employing the polyol method and the TEM images are shown in Figure 10.1c–g. For all the samples prepared by the polyol method, Pt nanoparticles are distributed uniformly on carbon. Figure 10.1h shows the average Pt particle sizes. It can be seen that the particle size is <5 nm even if the Pt loading is as high as 60%.

More importantly, it was found that the particle size is sensitive to the water content in the solvent for the polyol method [48]. By simply controlling the amount of water content in the solvent, particle size and distribution of electrocatalysts could be controlled finely at nanoscale. Figure 10.2 is the TEM images of 20% Pt/C with different particle sizes. The particle size of Pt/C increases from 2.0 to 3.0 nm with the increasing water content.

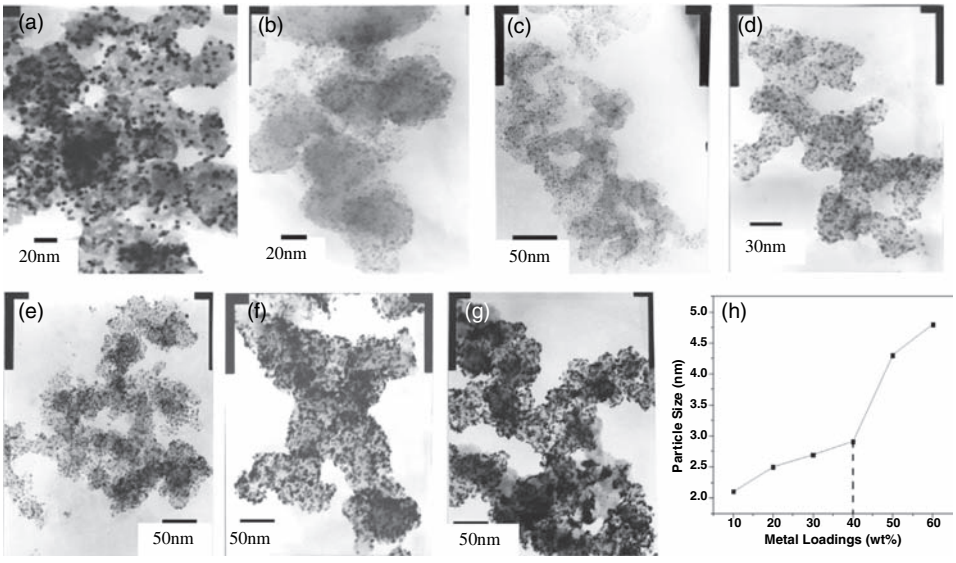

Figure 10.1 TEM images for (a) 20% Pt/C-HCHO, (b) 20% Pt/C-EG, (c) 10% Pt/C-EG, (d) 30% Pt/C-EG, (e) 40% Pt/C-EG, (f) 50% Pt/C-EG, (g) 60% Pt/C-EG, and (h) metal particle size versus metal loadings.

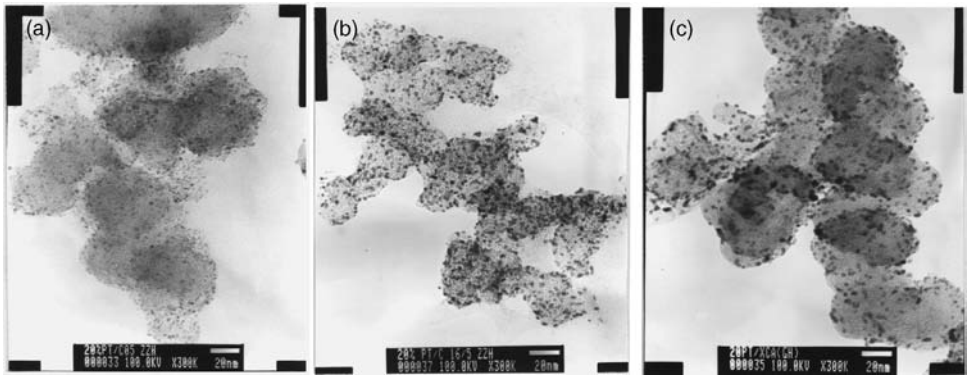

Figure 10.2 TEM images of 20% Pt/C with different particle size. (a) $d_{mean} = 2.0$ nm, (b) $d_{mean} = 2.6$ nm, (c) $d_{mean} = 3.0$ nm.

10.2.2
Carbon-Supported Platinum–Ruthenium

PtRu is the effective electrocatalyst for methanol oxidation reaction and the dispersion of the metal particles is of great importance for the utilization and activity, so we also compare several methods for the preparation of carbon-supported PtRu catalyst. Similar to the reasons mentioned in Section 10.2.1 for Pt/C, high metal loadings are required for the PtRu/C catalyst. We use 20 wt Pt% ~10 wt % Ru/C as an

Table 10.1 The XRD and TEM characterization results of PtRu/C prepared by different methods.

PtRu/C sample	XRD			TEM	
	Lattice parameter (Å)	Mean particle size (nm)	Specific surface area (S_{XRD}, $m^2 g^{-1}$)[a)]	Mean particle size (nm)	Specific surface area (S_{TEM}, $m^2 g^{-1}$)[b)]
Commercial-JM	3.890	2.4	136.1	2.7	120.9
Impregnation–reduction method	3.906	2.7	120.9	3.5	96.1
Hydroperoxide method	3.899	2.5	130.7	2.8	116.7
Polyol method	3.883	1.9	171.9	2.0	163.4

a) S_{XRD} and
b) S_{TEM} are calculated according to the average particle diameter from XRD patterns and TEM images, respectively.

example. Table 10.1 summarizes the TEM and X-ray diffraction (XRD) data of the catalysts prepared by the three preparation methods, namely, impregnation–reduction method, hydroperoxide method, and the polyol method. The data for the commercial PtRu/C (Johnson Matthey Inc.) are also included in Table 10.1 for comparison. It can be seen that PtRu/C catalyst produced by the polyol method presents a smaller mean particle size than those prepared by other methods and the lattice parameter of Pt in PtRu/C shortens compared with that of Pt (3.923 Å). The latter phenomenon suggests that a stronger interaction exists between Pt and Ru. However, in the case of PtRu/C prepared by the impregnation–reduction method, the corresponding lattice parameter is similar to that of Pt/C. This means a weak interaction exists between Pt and Ru. Furthermore, PtRu/C prepared by hydroperoxide method has the lattice parameter similar to the commercial one. It can also be found from Table 10.1 that the specific surface areas of all samples obtained from XRD are slightly higher than those from TEM. This deviation due to the different techniques is reasonable because XRD technique is more suitable for bulk crystals.

The polyol method is suitable for preparing both monometallic and bimetallic high-dispersive electrocatalysts with high metal loadings. Employing this method, bimetallic electrocatalysts including PtFe, PtRu, PtSn, and PtPd were also prepared.

10.3 Electrocatalysts for ORR

10.3.1 Highly Active PtFe Electrocatalysts for ORR

As far as the oxygen reduction is concerned, Pt-based electrocatalysts are always used as cathode catalysts in direct methanol fuel cells. We have already studied

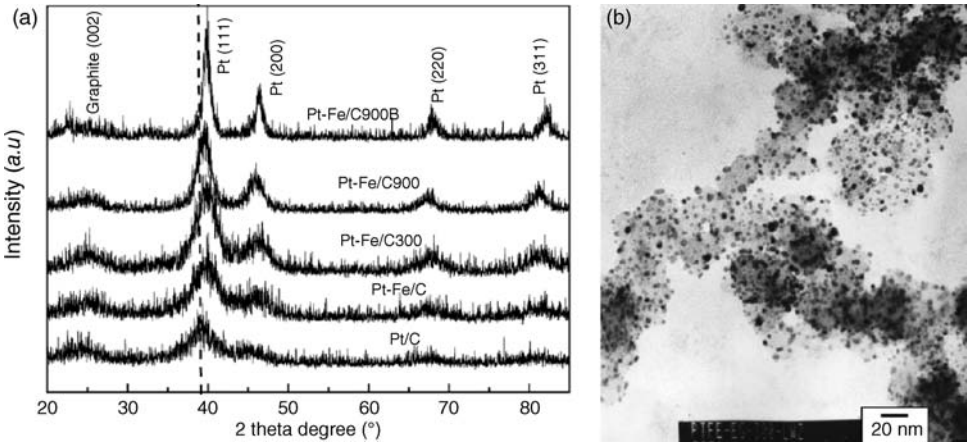

Figure 10.3 XRD patterns of the Pt–Fe/C catalysts and TEM image of Pt–Fe/C-300 [49]. Reproduced with permission from Elsevier.

the Pt–Fe/C system for the ORR [49]. PtFe/C catalysts were prepared by the modified polyol method and then were heat treated under H_2/Ar (10 vol%) at moderate temperature (300 °C, PtFe/C300) or high temperature (900 °C, PtFe/C900). As comparison, PtFe/C alloy catalyst was prepared by a two-step method (PtFe/C900B). X-ray diffraction and transmission electron microscopy images (Figure 10.3) show that the particle size of the catalyst increases with increasing treatment temperature. PtFe/C300 catalyst has a mean particle size of 2.8 nm (XRD) and 3.6 nm (TEM), and PtFe alloy was partly formed in this sample. PtFe/C900B catalyst has the biggest particle size of 6.2 nm (XRD) and the best PtFe alloy form. Cyclic voltammetry (CV) (not shown here) shows that PtFe/C300 has larger electrochemical surface area than other PtFe/C and the highest utilization ratio of 76% among these Pt-based catalysts. DMFCs with the above Pt–Fe/C as the cathode catalysts were fabricated and the results showed that PtFe/C300 exhibits higher ORR activity and better performance than other PtFe/C or Pt/C catalysts when employed for cathode in direct methanol single cell tests (Figure 10.4). The enhancement of the cell performance is logically attributed to its higher ORR activity, which might be due to more Pt^0 species existing after Fe ion corrosion from the catalyst.

10.3.2
Methanol-Tolerant PtPd Electrocatalysts for ORR

For DMFC, methanol crossover is one of the main obstacles to its development. Several efforts have been made to avoid or reduce the effect of methanol crossover on the DMFC's cathode performance [50–55], including the development of methanol-tolerant catalysts such as macrocycles or chalcogenides [34–37] and modification of Pt catalyst by adding another metal such as Fe, Co, Ni, and

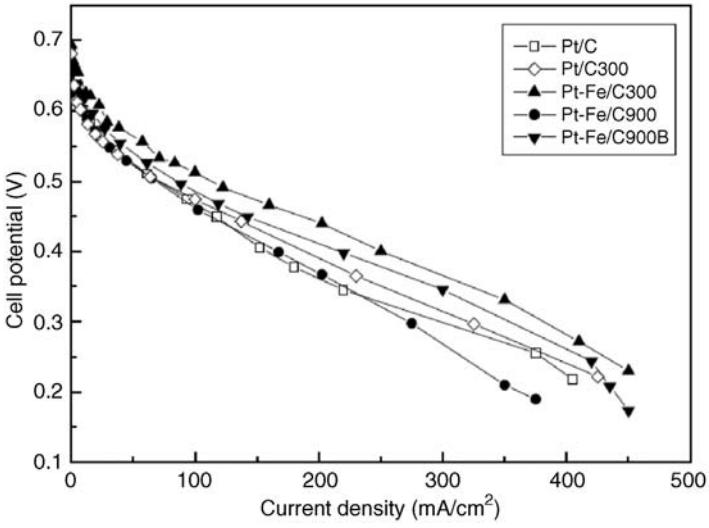

Figure 10.4 Comparison of single-cell polarization curves for the DMFC in the presence of Pt/C, PtFe/C300, PtFe/C900, PtFe/C900B cathode catalysts (1.0 mg Pt cm^{-2}); anode: PtRu/C (20 wt% Pt, 10 wt% Ru, Johnson Matthey Corp.; catalyst loading: 2.0 mg PtRu cm^{-2}); electrolyte membrane: Nafion-115® (DuPont) membranes; operation temperature: 90 °C; methanol concentration: 1.0 M CH_3OH; flow rate: 1.0 ml min^{-1}, oxygen pressure: 0.2 MPa [49]. Reproduced with permission from Elsevier.

Pd to decrease the effect of permeated methanol from the anode on the Pt cathode catalysts. In the former case, although it is known that they are good oxygen reduction electrocatalysts and inactive to methanol molecules, their unstability in acid media, especially at the operation temperatures ranging from 60 to 90 °C, limits their wide application in DMFC. PtFe seems to be a promising one as already discussed, but the issue is the loss of Fe due to the acidic operation environment in the long-term operation.

A novel carbon-supported Pd-rich Pd_3Pt_1 was developed, which showed a better direct methanol fuel cell performance than Pt/C [56]. For the ORR polarization curves in 0.5 mol l^{-1} $HClO_4$ with or without methanol (shown in Figure 10.5), judging from the half-wave potential, Pd_3Pt_1/C exhibits the ORR performance comparable with Pt/C in the absence of methanol. However, in the presence of methanol, it is interesting to find that for Pt/C, the peak for methanol oxidation is so big that its activity to ORR is decreased significantly in the potential range from 500 to 900 mV; nevertheless, the methanol oxidation peak does not appear for the Pd_3Pt_1/C in the ORR polarization curve. This suggests that Pd_3Pt_1/C exhibits a superior ORR selectivity to Pt/C in the presence of methanol. Accordingly, in the fuel cell operation mode, when Pd_3Pt_1/C was used as the cathode catalyst, the negative effect of methanol crossover on the cathode performance will be inhibited at least partially in comparison with Pt/C. The DMFC single cells with Pd_3Pt_1/C or Pt/C as the cathode catalysts were tested and compared. Figure 10.6 presents the single fuel cell test results. It can

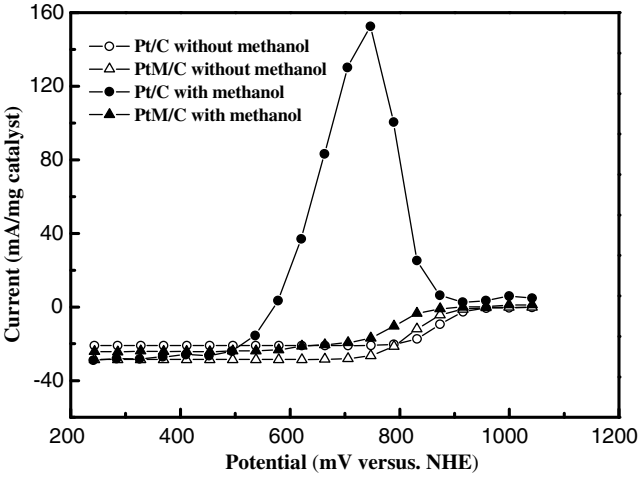

Figure 10.5 Polarization curves for oxygen reduction reaction over Pd_3Pt_1/C and Pt/C in O_2-saturated 0.5 mol l^{-1} $HClO_4$ in the presence or absence of 0.1 mol l^{-1} methanol at room temperature. Potential sweep rate: 5 mV s^{-1}. Oxygen feeding rate: 5 ml min^{-1}, rotation speed: 2500 rpm [56]. Reproduced with permission from the Royal Society of Chemistry.

be clearly seen that in all the current density range, single DMFC with Pd_3Pt_1/C shows a better performance than that with Pt/C as the cathode catalysts. The single fuel cell test results are in good agreement with the RDE results. The improved ORR activity of Pd_3Pt_1/C could be attributed to its inactivity to

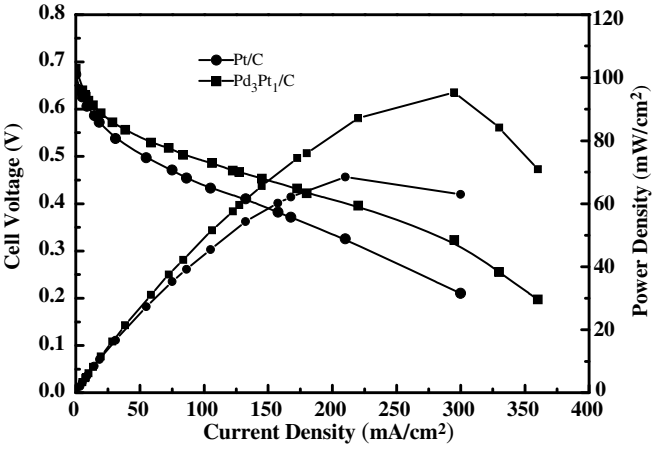

Figure 10.6 Performance of Pd_3Pt_1/C and Pt/C as DMFC cathode catalysts. $T_{cell} = 75$ °C. Anode: PtRu/C (20 Pt wt % ~10 Ru wt%, Johnson Matthey Inc.), 2.0 mg (Pt + Ru) cm^{-2}, $C_{methanol} = 1.0$ mol l^{-1}, flow rate: 1.0 ml min^{-1}. Cathode: Pt/C or Pd_3Pt_1/C (20 metal wt%), 1.0 mg metal cm^{-2}, $P_{O2} = 2.0$ atm. Electrolyte: Nafion® 115 membrane [56]. Reproduced with permission from the Royal Society of Chemistry.

methanol oxidation reaction, but similar activity to oxygen reduction reaction as Pt/C. In conclusion, palladium-rich Pd_3Pt_1/C catalyst enhanced DMFCs cathode performance for its selective ORR activity in the presence of methanol and may be an alternative methanol-tolerant cathode in DMFCs. Further theoretical calculation (density function theory (DFT)) studies on the adsorption and dissociation of O_2 on PtPd clusters indicate that, in addition to the advantage of methanol inert property, the presence of Pd atoms facilitates the dissociation of O_2 on Pt sites [57].

10.4 Electrocatalysts for MOR

10.4.1 Composition Screening for Electrocatalysts toward MOR

In the case of direct methanol fuel cells, compared with oxygen reduction, methanol oxidation accounts for the main activation loss because this process involves six-electron transfer per methanol molecule and catalyst self-poison when Pt alone was used from the adsorbed intermediate products such as CO_{ads}. From the thermodynamic point of view, methanol electrooxidation is driven due to the negative Gibbs free energy change in the fuel cell. On the other hand, in the real operation conditions, its rate is obviously limited by the sluggish reaction kinetics. In order to speed up the anode reaction rate, it is necessary to develop an effective electrocatalyst with a high activity to methanol electrooxidation. Carbon-supported (XC-72C, Cabot Corp.) PtRu, PtPd, PtW, and PtSn were prepared by the modified polyol method as already described [58]. Pt content in all the catalysts was 20 wt%.

The DMFC single cell tests with these as-prepared Pt-based catalysts as the anode catalysts are shown in Figure 10.7. For comparison, Pt/C as the anode catalyst is also shown in Figure 10.7. The cathode catalyst is Pt/C (20 wt%, Johnson Matthey Inc.). The geometric electrode area is $2.0 \times 2.0\,cm^2$. The membrane electrode assembly (MEA) preparation procedure has already been reported in detail [59].

It can be seen from Figure 10.7 that in the case of Pt/C as the anode catalyst, single DMFC exhibits the poorest performance. The open-circuit voltage (OCV) is only 0.56 V, and this value is far away from the theoretical value (1.18 V), which is mainly due to the slow reaction kinetics and methanol crossover. It can also be seen from Figure 10.7 that the maximum discharge current density is about $165\,mA\,cm^{-2}$ and the peak power density is only $17.5\,mW\,cm^{-2}$ at $120\,mA\,cm^{-2}$. From these experimental results, it can be concluded that Pt/C alone is not a suitable electrocatalyst for methanol oxidation. It is necessary to enhance the activity of Pt with other additives.

The addition of Pd, Ru, Sn, and W to Pt can overall improve the single DMFC performance. Among them, PtPd/C presents only slight improvement in the

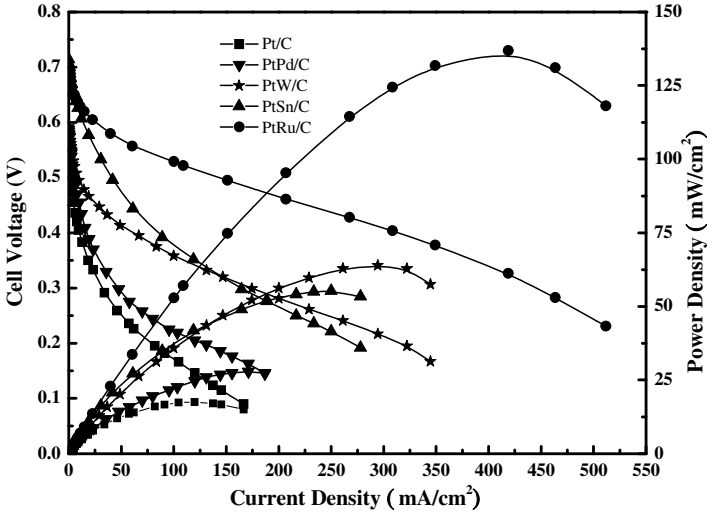

Figure 10.7 Cell performances of single DMFC with different anode catalysts. $T_{cell} = 90\,^{\circ}C$. Anode: Pt-based catalysts (Pt:M = 1 : 1, 20 Pt wt%), 1.33 mg Pt cm^{-2}, but 2.0 mg Pt cm^{-2} when Pt/C was used as the anode catalysts. $C_{methanol} = 1.0$ mol l^{-1}, flow rate: 1.0 ml min^{-1}. Cathode: Pt/C (20 Pt wt%, Johnson Matthey Inc.), 1.0 mg Pt cm^{-2}, P_{O2} = 2.0 atm. Electrolyte: Nafion 115 membrane.

DMFC performance in comparison with Pt/C. The OCV and peak power density are increased to about 0.58 V and 27.9 mW cm^{-2} at 171 mA cm^{-2}, respectively. PtSn/C gives the highest OCV in all the investigated catalysts; however, the fact is that the cell voltage with PtSn as anode decreases quickly along with the current density increment. This is probably due to the poor electronic conductivity of PtSn/C catalyst, which results from the Sn oxides in different valence in the catalyst [60]. Especially in the higher current density range, the ohmic effect becomes more serious, leading to quicker cell voltage drop. On one hand, W is considered to be able to provide abundant O-containing species and the change between its different valences can accelerate the removal of the adsorbed intermediates such as CO_{ads}. On the other hand, from the single DMFC test results, it shows inferior performance to PtRu/C. Based on these results, PtRu appears to be the most effective anode electrocatalyst for direct methanol fuel cells, which is the same result as the well-accepted idea that PtRu is the most effective electrocatalyst for methanol oxidation until now.

10.4.2
Carbon-Supported Platinum–Ruthenium for MOR

In order to clarify the relations between the microstructure of PtRu/C catalyst and the corresponding performance, HRTEM and HR-EDS experiments were carried out on particles employing the PtRu/C prepared by impregnation–reduction method (denoted as PtRu-IM) and modified polyol method (denoted

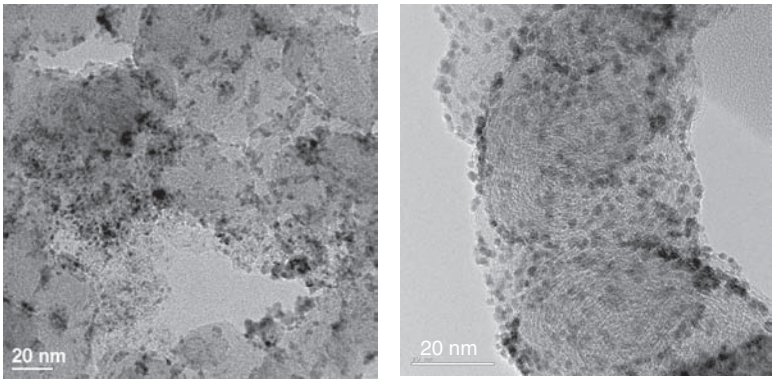

Figure 10.8 TEM images of (a) PtRu/C-IM and (b) PtRu-EG.

as PtRu-EG). Figure 10.8 shows the HRTEM images of PtRu-IM and PtRu-EG. From the HRTEM images, it can be seen that the metal particles of PtRu-IM are not uniform, and some of the small particles agglomerate into larger particles. For PtRu-EG, the particles disperse on the support uniformly. For a clear comparison, the summary data of HRTEM and HR-EDS are listed in Table 10.2. PtRu-1 and PtRu-2 have a similar mean particle size, while the particle size distribution of PtRu-IM, ~1–6 nm, is much broader than that of PtRu-EG (1.5–2.5 nm). The results of HR-EDS on particles clearly show that the distribution of Pt and Ru in the PtRu-IM sample is not uniform. For the larger particles, the atomic ratio of Pt to Ru is 8.8:1, while for the smaller particles, the corresponding value is 1:8.0. This result means that the larger particles are Pt-rich, while the smaller particles are Ru-rich. For PtRu-EG, the atomic ratio of Pt to Ru is much more uniform. For larger particles, the atomic ratio of Pt to Ru is 1.2:1 and for smaller particles the corresponding value is ~0.7:1, which is close to the nominal ratio.

To enhance the alloy degree of PtRu, the as-prepared PtRu/C-EG catalyst was heat treated in nitrogen at 200 °C [61]. TG and online MS results indicate that abundant adsorbed species exist on the electrocatalyst surface, which can be effectively removed by heat treating at 200 °C under nitrogen atmosphere for 2 h. TEM and XRD results (Figure 10.9) show that the particle size of the

Table 10.2 Summary of HRTEM and HR-EDS results.

Sample	Mean particle size (nm)	HR-EDS results (Pt/Ru atomic ratio)	
		Small particles	Large particles
PtRu/C-IM	3.5 (±2.5)	1/8.0	8.8/1
PtRu/C-EG	2.5 (±0.5)	0.7/1	1.2/1

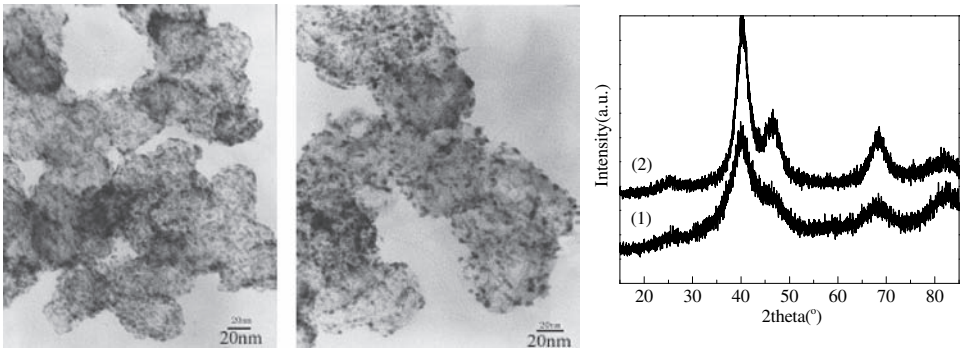

Figure 10.9 TEM images and XRD patterns of PtRu/C-EG electrocatalysts before (a) and after (b) heat treatment.

electrocatalyst increases slightly after heat treatment, but the particles retain good dispersion on the carbon support. The diffraction peak position for the PtRu/C-EG after heat treatment shifts toward higher angle and the lattice parameters for Pt shorten (Table 10.3), indicating that the interaction between Pt and Ru increases. Electrochemical and DMFC single cell testing results (Figure 10.10) indicate that the catalytic activity of PtRu/C for methanol electro-oxidation is greatly improved after the heat treatment process.

Table 10.3 XRD calculation results of PtRu/C-EG electrocatalyst.

	Before heat treatment	After heat treatment
Average particle size (nm)	2.1	2.6
(220)Peak position (°)	68.4	68.6
Lattice parameter (nm)	0.388	0.386

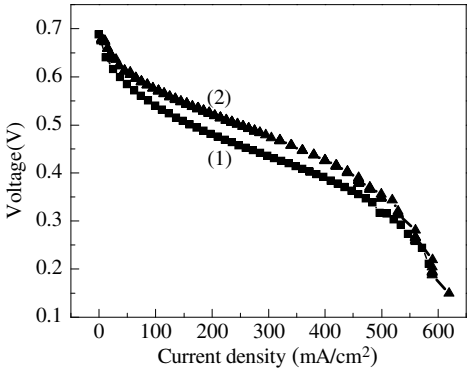

Figure 10.10 Comparison of DMFC single cell performance with PtRu/C-EG as anode electrocatalyst before (1) and after (2) heat treatment.

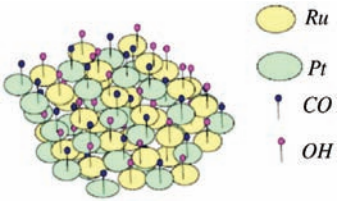

Figure 10.11 PtRu model catalyst for methanol electrooxidation.

According to bifunctional mechanism proposed by Watanabe and Motoo [62], the dehydrogenation of methanol occurs on the Pt active sites as a result of producing CO-like species. The Ru species could decompose water at a lower potential than Pt to produce −OH species, which could react with the CO-like species on Pt active sites and detoxify them. On the premise of this mechanism, the model catalyst should be described as good PtRu alloy (atomic ratio Pt/Ru = 1:1) with the two elements mixing at atomic scale (Figure 10.11).

On the basis of this model, Pt and Ru should be mixed at atomic scale in order to remove the CO-like species smoothly. From the aforementioned HRTEM and HR-EDS analyses, the PtRu-EG has uniform particle size (2.5 ± 0.5 nm) with sharp distribution and the distribution of Pt and Ru is uniform at atomic scale. This structure is favorable for removing CO-like species according to bifunctional mechanism. The PtRu-IM, which is characterized by broad particle size distribution (3.5 ± 2.5 nm) and uneven distribution of Pt and Ru at atomic scale, could not eliminate the poison smoothly. The cumulated poisons would lead to Pt active sites deactivating gradually.

10.5 Electrocatalysts for Ethanol Electrooxidation

In order to extend the practical application of low-temperature fuel cells and to facilitate their penetration into the transport market, it is also desirable to increase the number of liquid fuels that can be employed in these devices. Among all the possible fuels, ethanol is the most promising because it is a naturally available and renewable fuel, thus having positive impact on both economy and environment [63,64]. Moreover, ethanol has higher energy density in comparison with methanol (8.01 versus 6.09 kWh kg^{-1}). Therefore, ethanol is more attractive and appears to fulfill most of the requirements of the fuel for low-temperature fuel cells [65,66].

Compared with methanol electrooxidation, ethanol electrooxidation seems to be a more complicated process because it involves 12-electron transfer per ethanol molecule and cleavage of C−C bond. In order to speed up DEFC's development, it is necessary and important to develop a novel electrocatalyst with a high activity to ethanol electrooxidation.

10.5.1
Composition Screening for Electrocatalysts toward EOR

Carbon-supported PtPd, PtW, PtRu, and PtSn had been prepared by the modified polyol method and evaluated as ethanol oxidation electrocatalysts [44,67]. Figure 10.12 shows the results of CV experiments with different carbon-supported Pt and PtM catalysts. There are two oxidation peaks when the ethanol CV is carried out on the Pt/C catalyst. The first one appears at around 0.76 V (versus SCE) and the second one appears at a higher potential. Only the first oxidation peak is reported in the present work and the applied upper potential is not allowed to exceed 1.0 V versus SCE to prevent the dissolution of assistant metals. The addition of the second metal to Pt results in the negative shift of the first ethanol electrooxidation peak. The first oxidation peak on Pt_1Ru_1/C appears at the most negative potential, at ~0.53 V (versus SCE), and the peak potential is ~0.23 V lower than that on Pt/C catalyst. The first electrooxidation peak of ethanol on Pt_1Pd_1/C is ~0.65 V (versus SCE), higher than that on Pt_1Ru_1/C. The current density at the first peak of the ethanol electrooxidation on Pt_1Ru_1/C is higher than that on Pt_1Pd_1/C, but less than those on Pt_1Sn_1/C, Pt_1W_1/C, and Pt/C, respectively. The Pt_1Sn_1/C catalyst has the highest electrocatalytic activity toward ethanol oxidation in terms of the current density for the first peak, but also has a higher overpotential (0.71 versus SCE). Pt_1W_1/C catalyst also exhibits a higher current density than those of Pt/C, Pt_1Ru_1/C, and Pt_1Pd_1/C, but has a overpotential (0.75 versus SCE) similar to Pt/C. It seems that Pt_1Sn_1/C is the best electrocatalyst for ethanol oxidation from the viewpoint of current density. Pt_1Ru_1/C has the lowest overpotential to ethanol electrooxidation among the electrocatalysts already discussed, which indicates that Pt_1Ru_1/C is also a promising catalyst for ethanol electrooxidation.

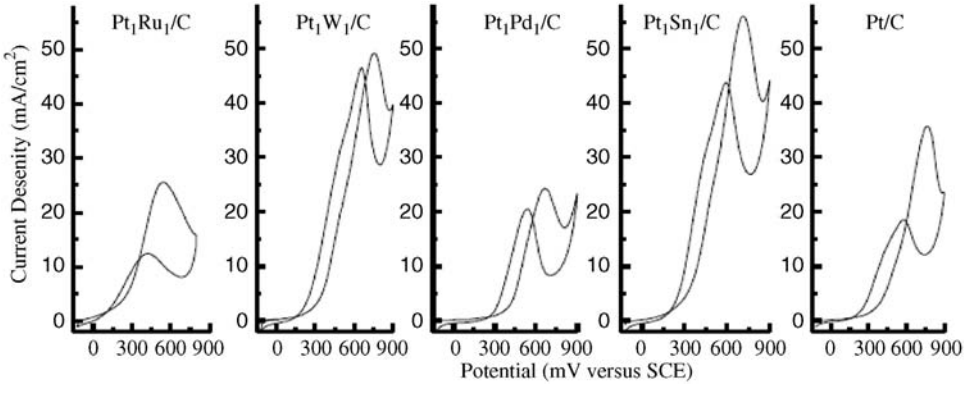

Figure 10.12 The CV results of different anode catalysts for ethanol electrooxidation. Operation temperature: 25 °C. Scan rate: 10 mV s^{-1}. Electrolyte: 1.0 M EtOH + 0.5 M H_2SO_4 [67]. Reproduced with permission from Elsevier.

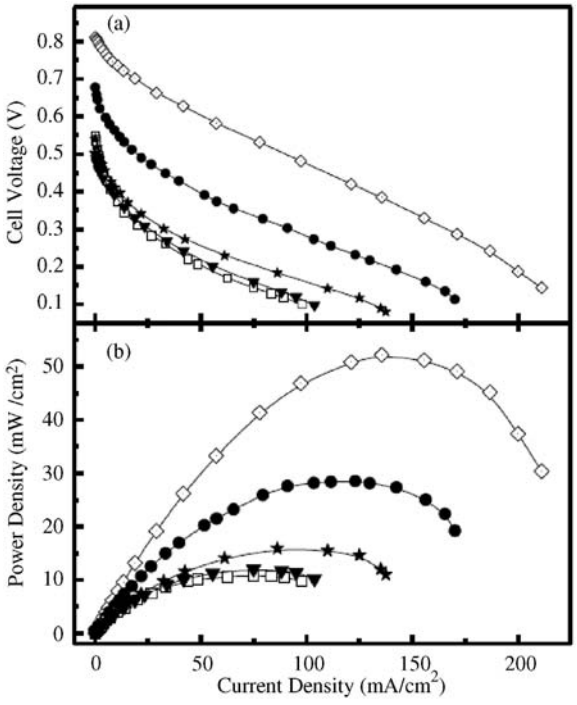

Figure 10.13 Comparison of the fuel cell characteristics of a direct ethanol fuel cell with different anode catalysts operated at 90 °C. (□) Pt/C, 2.0 mg Pt cm^{-2}; (▼) Pt_1 Pd_1/C, 1.3 mg Pt cm^{-2}; (★) Pt_1W_1/C, 2.0 mg Pt cm^{-2}; (●) Pt_1Ru_1/C, 1.3 mg Pt cm^{-2}; (◇) Pt_1Sn_1/C, 1.3 mg Pt cm^{-2}; Nafion 115 was used as electrolyte; ethanol concentration and flow rate: 1 M and 1.0 ml min^{-1}, respectively; cathode catalyst and metal loading: 1.0 mg Pt cm^{-2} (20 Pt wt%, Johnson Matthey Co.) [67]. Reproduced with permission from Elsevier.

From a practical viewpoint, every potential electrocatalyst should be ultimately investigated in fuel cells. The above five catalysts were evaluated as anode catalysts for ethanol electrooxidation by the single DEFC test. Figure 10.13 exhibits the performance differences between the single fuel cell with different anode catalysts operated at 90 °C. When Pt/C is used as anode catalyst for ethanol, the performance of the single fuel cell is poor. The OCV is only around 0.55 V, far less than the standard electromotive force (1.145 V), which is mainly attributed to the poor catalytic activity to ethanol electrooxidation and ethanol crossover from anode to cathode. The maximum output power density is only 10.8 mW cm^{-2}. The performance of the single DEFC has no obvious improvement when Pt/C is replaced with Pt_1Pd_1/C as anode catalyst, and the two single cells have similar current density–voltage (I–V) curves. The single cell with Pt_1W_1/C as anode catalyst exhibits an improved performance compared with that with Pt/C and Pt_1Pd_1/C, respectively, especially in the intrinsic resistance-controlled region and mass transfer region. The maximum output power density is close to 16.0 mW cm^{-2} at 90 °C. The single cell using either Pt_1Ru_1/C or Pt_1Sn_1/C

exhibits performance superior to those with Pt/C, Pt_1Pd_1/C, and Pt_1W_1/C. Both the OCV and the maximum power density increase when Pt_1Ru_1/C or Pt_1Sn_1/C is used. The OCV of single cell with Pt_1Ru_1/C is 0.67 V, ~0.12 V higher than that with Pt/C, and the maximum power density is 28.6 mW cm^{-2} at 90 °C. When Pt_1Sn_1/C is adopted as the anode catalyst, the OCV of single fuel cell approaches to ~0.81 V, ~0.14 mV higher than the fuel cell with Pt_1Ru_1/C as anode catalyst. The maximum power density of the cell with Pt_1Sn_1/C is 52.0 mW cm^{-2}, nearly twice as that of the single cell with Pt_1Ru_1/C catalyst. The single cell results identify evidently that Pt_1Sn_1/C is more suitable to DEFC operated at 90 °C.

Although Pt_1Ru_1/C is the best catalyst for methanol electrooxidation in DMFCs, it is not proved to be the best anode catalyst for ethanol electrooxidation. The addition of W and Mo can increase ethanol electrooxidation activity on the Pt_1Ru_1/C catalyst. The *I–V* characteristics of single direct ethanol fuel cells show clearly that the Pt_1Sn_1/C is a better anode catalyst than Pt_1Ru_1/C and other carbon-supported bimetallic Pt-based catalysts for DEFCs. From a practical point of view, Pt_1Sn_1/C is the best electrocatalyst for DEFCs among these anode catalysts investigated here.

10.5.2
PtSn/C for Ethanol Electrooxidation

Based on the fact that Pt_1Sn_1/C proved to be a very active anode catalyst for the EOR, additional work has been done to investigate the effect of Pt/Sn atomic ratio [44]. The mean particle size and lattice parameter of the PtSn/C catalyst obtained from XRD patterns and TEM images are summarized in Table 10.4. Figure 10.14 shows the performances of the single fuel cells with different PtSn/C catalysts as the anode catalyst.

In the subsequent research, great endeavor has been made to control the component of PtSn/C catalyst at atomic scale. Now we can obtain a uniform component of PtSn catalyst by modifying the preparation conditions. Figure 10.15 is the HRTEM image and HR-EDS analysis of Pt_3Sn/C nanoparticles. It can be seen

Table 10.4 XRD and TEM results of carbon-supported Pt and Pt-bimetallic catalysts [44].

Catalyst	Mean particle size (nm)		Lattice parameter (Å)
	TEM	XRD	
Pt_1Sn_1/C	2.3	2.1	3.987
Pt_3Sn_2/C	2.2	1.9	3.973
Pt_2Sn_1/C	3.0	2.6	3.956
Pt_3Sn_1/C	2.2	1.9	3.953
Pt_4Sn_1/C	2.3	1.9	3.938

Reproduced with permission from Elsevier.

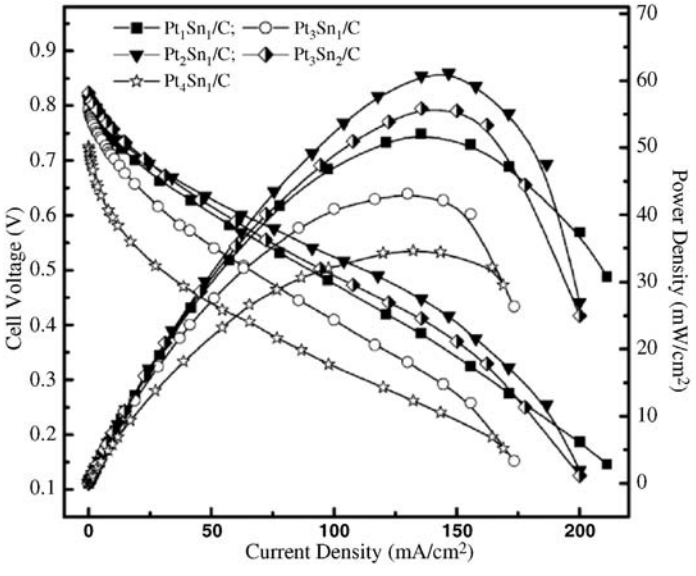

Figure 10.14 Performances of single direct ethanol fuel cells with different PtSn/C catalysts as anode catalysts at 90 °C. Anode is PtSn/C with different Pt/Sn atomic ratio (1.33 mg Pt cm^{-2}). Solid electrolyte is Nafion 115 membrane. Ethanol aqueous solution is 1.0 mol l^{-1} and its flow rate is 1.0 ml min^{-1}; cathode contains Pt/C (Johnson Matthey Co.) with 1.0 mg Pt cm^{-2} [44]. Reproduced with permission from Elsevier.

that the metal particles are uniform with a mean particle size of 3 nm. HR-EDS analysis was carried out for a random linear area and the result showed that the distribution of Pt is consistent with that of Sn. This indicates that the distribution of Pt and Sn is uniform in all of the particles.

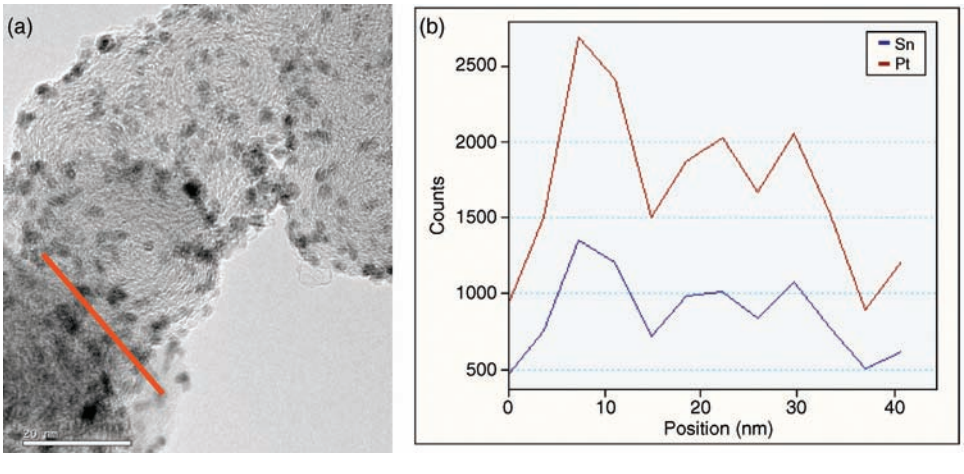

Figure 10.15 HRTEM image (a) and HR-EDS analysis (b) of Pt_3Sn/C nanoparticles.

Our primary research indicated that tin oxide could be the active component for ethanol electrooxidation [60,68–70]. Here our focus is to study the effects of the chemical state of tin and the component of PtSn/C catalysts on the performance of DEFCs. For comparison, two PtSn/C catalysts with tin oxide and PtSn alloy were prepared, respectively. For the former, tin oxide with a diameter of 1 nm was prepared first in ethylene glycol, and then platinum was reduced on the surface or near the tin oxide (denoted as PtSn-1). For the latter, first the precursor of Pt and Sn were mixed together, and then they were reduced in EG (denoted as PtSn-2).

The XRD patterns of PtSn-1 and PtSn-2 are shown in Figure 10.16. It can be seen that apart from the diffraction peaks of Pt(111), Pt(200), Pt(220), and Pt (311), there appear diffraction peaks of SnO_2(101) and SnO_2(211) at around 34° and 52° (PCPDF#411445), respectively, for PtSn-1. Both PtSn-1 and PtSn-2 have the same particle size of ~2.3 nm, calculated by Scherrer formula. The lattice parameters of PtSn-1 and PtSn-2 were 3.928 and 3.946 Å, respectively, according to Vegard's law. Compared with the lattice parameter of Pt, which is 3.923 Å, the crystalline lattice of Pt in PtSn-2 sample is dilative prominently, while that of PtSn-1 displays little dilatation. In general, the dilatation of crystalline lattice reflects the alloy degree of two metals. To clarify the microstructure of PtSn catalysts, HRTEM images of PtSn-1 and PtSn-2 are shown in Figure 10.17. In the HRTEM image of PtSn-1, SnO_2 nanoparticles were found in the vicinity of Pt particles. The nominal 0.264 nm spacing of the SnO_2(101) plane is indicated by the arrow in Figure 10.17a. The nominal 0.228 and 0.198 nm spacings of the Pt(111) and Pt(200) planes, respectively, of the fcc lattice of a typically faceted particles are also indicated by the arrows in Figure 10.17a. In Figure 10.17b, only Pt(111) plane was found with a spacing of 0.234 nm and no separate SnO_2 phase was found near the Pt particles. Based on these details, it can be concluded that

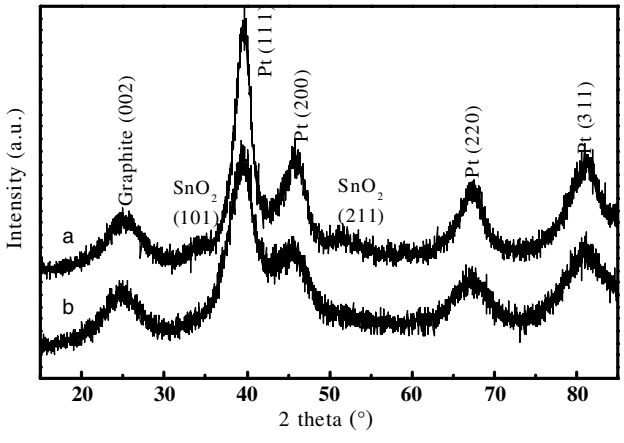

Figure 10.16 XRD patterns of (a) PtSn-1 (b) PtSn-2 [70]. Reproduced with permission from Elsevier.

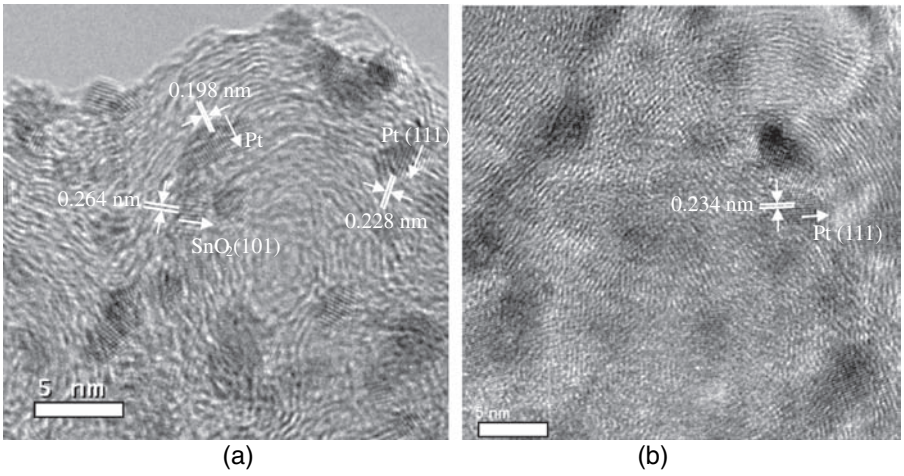

Figure 10.17 HRTEM images of (a) PtSn-1 and (b) PtSn-2 [70]. Reproduced with permission from Elsevier.

partial Sn exists in tin oxide and partial Sn alloy with Pt in the PtSn-1 sample, while most of Sn alloy with Pt in the PtSn-2 sample.

Cyclic voltammetry is a practical and simple method to characterize the electrocatalytic activity of catalysts. Figure 10.18 shows the C–V curves for PtSn electrode in 0.3 M $HClO_4$ + 1 M EtOH solution. The initial potentials of the EOR (at 0.2 mA) on PtSn-1 and PtSn-2 are 0.033 and 0.124 V, respectively. In all of the sweeping ranges, the ethanol electrooxidation current on PtSn-1 electrode is higher than that on PtSn-2 electrode. This indicates that PtSn-1 is a better catalyst for ethanol than PtSn-2.

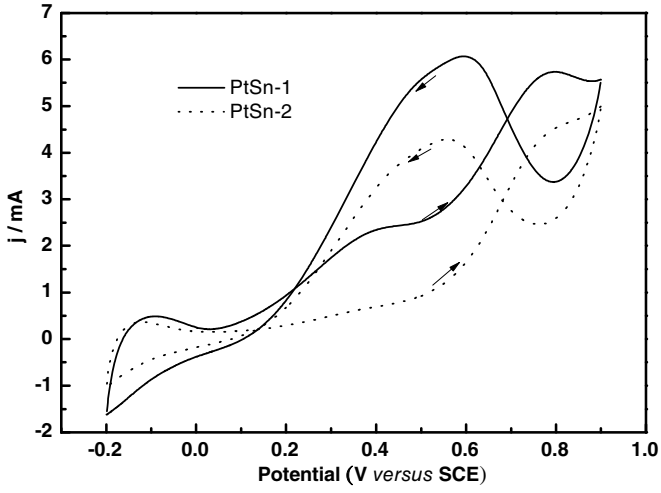

Figure 10.18 Cyclic voltammograms of PtSn electrodes in 0.3 M $HClO_4$ + 1 M EtOH solution at room temperature [70]. Reproduced with permission from Elsevier.

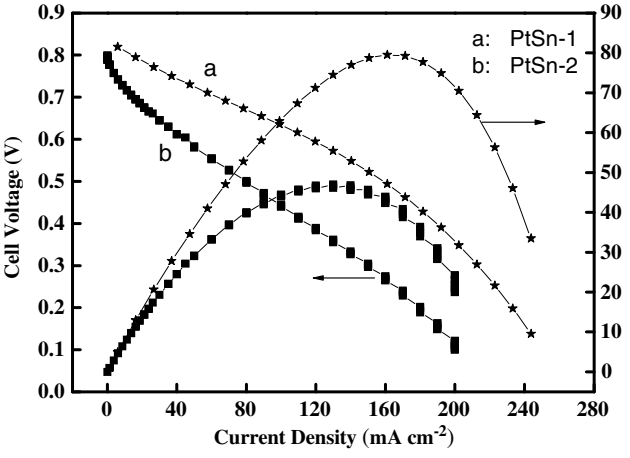

Figure 10.19 Performance of DEFCs with (a) PtSn-1 and (b) PtSn-2 as the anode catalyst [70]. Reproduced with permission from Elsevier.

Figure 10.19 shows the I–V curves of DEFCs with PtSn-1 and PtSn-2 as the anode catalysts, respectively. It can be seen that the DEFC with PtSn-1 as the anode catalyst showed much higher performance than that with PtSn-2 as anode. The maximum power density and the maximum discharge current of the DEFCs with PtSn-1 and PtSn-2 as the anode catalysts are 81 mW cm^{-2} (200 mA cm^{-2}) and 47 mW cm^{-2} (240 mA cm^{-2}), respectively. In our previous research [60], we concluded that tin oxide could offer oxygen-containing species at lower potential than platinum. The oxygen-containing species could react with the CO-like poisons resulting from the ethanol electrooxidation. Herein, according to the detailed research, PtSn-1 includes PtSn alloy and tin oxide nanoparticles, while in PtSn-2, most of tin alloys with platinum as a result of dilating the lattice parameter of Pt. In the study of MOR on PtSn catalysts, it is believed that the dilatation of lattice parameter of Pt inhibits the ability of Pt to adsorb methanol and dissociate C—H bonds [71]. Similarly, the adsorption and dissociation of ethanol may be inhibited due to the complete alloying of Pt and Sn. Our previous research indicated that suitable dilatation of Pt crystalline lattice constant is favorable for ethanol adsorption [58]. Ethanol molecules adsorbed on the active sites of Pt are dehydrogenated to produce CO-like species. For the PtSn-2 sample, the ethanol electrooxidation residues could not be removed from Pt active sites smoothly because no oxygen-containing species are around them. However, for PtSn-1, the electrooxidation residues could react with the oxygen-containing species resulting from tin oxide in the vicinity of Pt particles to free Pt active sites. On the basis of this discussion, an ideal PtSn electrocatalyst for ethanol electrooxidation may be Pt alloy with Sn to a suitable degree and partial Sn exists in oxide.

Further studies on the EOR products over PtSn-1 with different Pt/Sn atomic ratios were investigated in a three-electrode system by differential electrochemical

mass spectroscopy (DEMS) [72]. The results show that acetic acid and formaldehyde are the two main products and the CO_2 yield is lower than 5% on PtSn-1 or PtSn alloy catalyst; however, the acetic acid yield over PtSn-1 is higher than that over PtSn alloy, suggesting that the production of acetic acid requires dual-active sites – one (Pt) for dehydrogenation and another (SnOx) for providing OH species for aldehyde to form acetic acid. It is totally different when testing the PtSn-1 catalyst in a real fuel cell. It was reported that the CO_2 current efficiency of the EOR shows a strong increase with increasing catalyst loading and temperature. The CO_2 current efficiency exceeds 75% at 90 °C, 0.1 M ethanol, and 5 mg cm^{-2} Pt catalyst loading [73]. It is reasonable to consider that the CO_2 yield increases with temperature and in the thick porous catalyst layer the EOR intermediates have a large possibility to be readsorbed and reoxidized further.

10.5.3
IrSn/C for Ethanol Electrooxidation

Carbon-supported Ir_3Sn/C and Ir/C catalysts were simply prepared with $NaBH_4$ as a reducing agent under the protection of ethylene glycol at room temperature [74]. TEM and XRD data showed that the catalysts with small particle size exhibited the typical fcc structure of Ir. Their electro-catalytic activities in comparison with Pt/C and Pt_3Sn/C catalysts were characterized by linear sweep voltammetry (Figure 10.20). The results indicated that Ir-based catalysts showed superior electrocatalytic activity toward ethanol oxidation to Pt/C and Pt_3Sn/C catalysts, mainly in the low-potential region. During single cell tests at 90 °C (Figure 10.21), Ir-based catalysts as anodes performed better compared with Pt/C catalyst. The overall performance of Ir_3Sn/C comparable withPt_3Sn/C makes it a promising alternative choice of anode catalyst for DEFCs.

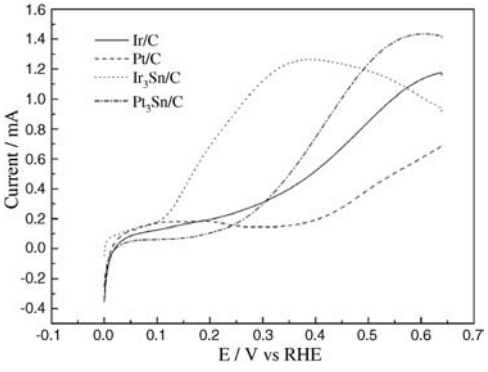

Figure 10.20 Linear sweep voltammograms of ethanol oxidation on Ir/C, Pt/C, Ir_3Sn/C, and Pt_3Sn/C catalysts in 0.5 M H_2SO_4 with 1 M ethanol at room temperature with a scan rate of 10 mV s^{-1} [74]. Reproduced with permission from Elsevier.

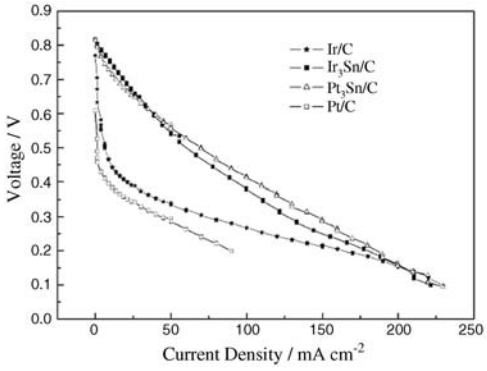

Figure 10.21 Polarization curves of a DEFC employing Ir/C, Ir_3Sn/C, Pt_3Sn/C, and Pt/C as anode catalyst, respectively. Anode: 1 M ethanol at 1 ml min^{-1}, cell temperature 90 °C, $P_{cathode}$: 2 bar, 1.5 mg cm^{-2} precious metal loading of anode catalysts, 1 mg cm^{-2} Pt cathode catalyst (Pt/C 40% from JM [74]. Reproduced with permission from Elsevier.

10.6 Conclusions

The research activities and developments in the field of electrocatalysts for direct alcohol fuel cells at DICP in the past decade are reviewed. In summary, the progress includes the following: (i) A convenient and environment-friendly polyol process was developed to prepare catalysts with controllable metal particle size, high dispersion, and uniform composition even at high metal loadings. (ii) PtFe/C and PtPd/C present promising activity toward ORR and PtPd is inert to the MOR that endows PtPd as an effective methanol-tolerant ORR catalyst. (iii) PtRu/C is identified as the most effective catalyst for the MOR, and further heat treatment can enhance the PtRu alloy degree as a result to improve the MOR activity. (iv) PtSn presents higher activity to ethanol electrooxidation than other Pt-based catalysts. Tin exists in oxides offering OH species that facilitate the formation of acetic acid, while PtSn alloy ethanol is more facile to transforming to formaldehyde.

References

1 Cheng, X., Yi, B., Han, M., Zhang, J., Qiao, Y., and Yu, J. (1999) Investigation of platinum utilization and morphology in catalyst layer of polymer electrolyte fuel cells. *Journal of Power Sources*, **79** (1), 75–81.

2 Wang, X., Hsing, I.-M., and Yue, P.L. (2001) Electrochemical characterization of binary carbon supported electrode in polymer electrolyte fuel cells. *Journal of Power Sources*, **96** (2), 282–287.

3 Schmal, D., Kluiters, C.E., and Barendregt, I.P. (1996) Testing of a De Nora polymer electrolyte fuel cell stack of 1kW for naval applications. *Journal of Power Sources*, **61** (1–2), 255–257.

4 Fournier, J., Faubert, G., Tilquin, J.Y., Côte, R., Guay, D., and Dodelet, J.P. (1997)

High-performance, low Pt content catalysts for the electroreduction of oxygen in polymer-electrolyte fuel cells. *Journal of the Electrochemistry Society*, **144**, 145–154.

5 Susai, T., Kawakami, A., Hamada, A., Miyake, Y., and Azegami, Y. (2001) Development of a 1kW PEM fuel cell power source. *Fuel Cells Bulletin*, **3**, 7–11.

6 Glaebrook, W. (1982) Efficiencies of heat engines and fuel cells: the methanol fuel cell as a competitor to otto and diesel engines. *Journal of Power Sources*, **7** (3), 215–256.

7 Ren, X., Zelenay, P., Thomas, S.C., Davey, J., and Gottesfeld, S. (2000) Recent advances in direct methanol fuel cells at Los Alamos National Laboratory. *Journal of Power Sources*, **86**, 111–116.

8 Scott, K., Argyropoulos, P., and Sundmacher, K. (1999) A model for the liquid feed direct methanol fuel cell. *Journal of Electroanalytical Chemistry*, **477**, 97–110.

9 Scott, K., Taama, W.M., Argyropoulos, P., and Sundmacher, K. (1999) The impact of mass transport and methanol crossover on the direct methanol fuel cell. *Journal of Power Sources*, **83**, 204–216.

10 Baldauf, M. and Preidel, W. (1999) Status of the development of a direct methanol fuel cell. *Journal of Power Sources*, **84**, 161–166.

11 Gao, P., Chang, S., Zhou, Z., and Weaver, M.J. (1989) Electrooxidation pathways of simple alcohols at platinum in pure nonaqueous and concentrated aqueous environments as studied by real-time FTIR spectroscopy. *Journal of Electroanalytical Chemistry*, **272**, 161–178.

12 Wang, J., Wasmus, S., and Savinell, R.F. (1995) Evaluation of ethanol, 1-propanol, and 2-propanol in a direct oxidation polymer-electrolyte fuel cell. *Journal of the Electrochemistry Society*, **142**, 4218–4224.

13 Qi, Z., Hollett, M., Atita, A., and Kaufman, A. (2002) Low temperature direct 2-propanol fuel cells. *Electrochemical Solid-State Letters*, **5**, A129–A130.

14 Peled, E., Duvdevani, T., Aharon, A., and Melman, A. (2001) New fuels as alternatives to methanol for direct oxidation fuel cells. *Electrochemical Solid-State Letters*, **4**, A38–A41.

15 Narayanan, S.R., Vamos, E., Surampudi, S., Frank, H., Halpert, G., Prakash, G.K.S., Smart, M.C., Knieler, R., Olah, G.A., Kosek, J., and Cropley, C. (1997) Direct electro-oxidation of dimethoxymethane, trimethoxymethane, and trioxane and their application in fuel cells. *Journal of the Electrochemistry Society*, **144**, 4195–4201.

16 Rice, C., Ha, S., Masel, R.I., Waszczuk, P., Wieckowski, A., and Barnard, T. (2002) Direct formic acid fuel cells. *Journal of Power Sources*, **111**, 83–89.

17 Iwasita, T., Hoster, H., John-Anacker, A., Lin, W.F., and Vielstich, W. (2000) Methanol oxidation on PtRu electrodes. Influence of surface structure and Pt–Ru atom distribution. *Langmuir*, **16**, 522–529.

18 Watanabe, M., Uchida, M., and Motoo, S. (1987) Preparation of highly dispersed Pt + Ru alloy clusters and the activity for the electrooxidation of methanol. *Journal of Electroanalytical Chemistry*, **229**, 395–406.

19 Iwasita, T., Nart, F.C., and Vielstich, W. (1990) An FTIR study of the catalytic activity of a 85:15 Pt:Ru alloy for methanol oxidation. *Physics and Chemistry*, **94**, 1030–1034.

20 Rolison, D.R., Hagans, P.L., Swider, K.E., and Long, J.W. (1999) Role of hydrous ruthenium oxide in Pt–Ru direct methanol fuel cell anode electrocatalysts: the importance of mixed electron/proton conductivity. *Langmuir*, **15**, 774–779.

21 Frelink, T. and Visscher, W. (1994) The effect of Sn on Pt/C catalysts for the methanol electro-oxidation. *Electrochimica Acta*, **39**, 1871–1875.

22 Aricò, A.S., Antonucci, V., and Giordano, N. (1994) Methanol oxidation on carbon-supported platinum-tin electrodes in sulfuric acid. *Journal of Power Sources*, **50**, 295–309.

23 Janssen, M.M.P. and Moolhuysen, J. (1976) Platinum–tin catalysts for methanol fuel cells prepared by a novel immersion technique, by electrocodeposition and by alloying. *Electrochimica Acta*, **21**, 861–868.

24 Janssen, M.M.P. and Moolhuysen, J. (1976) Binary systems of platinum and a second metal as oxidation catalysts for methanol fuel cells. *Electrochimica Acta*, **21**, 869–878.

25 Watanabe, M., Furuuchi, Y., and Motoo, S. (1985) Electrocatalysis by AD-atoms: Part XIII. Preparation of ad-electrodes with tin ad-atoms for methanol, formaldehyde and formic acid fuel cells. *Journal of Electroanalytical Chemistry*, **191**, 367–375.

26 Shukla, A.K., Ravikumar, M.K., and Aricò, A.S. (1995) Methanol electrooxidation on carbon-supported Pt-WO_{3-x} electrodes in sulphuric acid electrolyte. *Journal of Applied Electrochemistry*, **25** (6), 528–532.

27 Shen, P.K. and Tseung, A.C.C. (1994) Anodic oxidation of methanol on Pt/WO_3 in acidic media. *Journal of the Electrochemistry Society*, **141**, 3082–3090.

28 Wang, J., Nakajima, H., and Kita, H. (1990) Metal electrodes bonded on solid polymer electrolyte membrane (SPE): VI. Methanol oxidation on molybdenum modified Pt-SPE electrode. *Electrochimica Acta*, **35**, 323–328.

29 Grgur, B.N., Zhuang, G., Marvovich, M.M., Jr., and Rose, P.N. (1997) Electrooxidation of H_2/CO mixtures on a well-characterized $Pt_{75}Mo_{25}$ alloy surface. *Journal of the Physical Chemistry B*, **101**, 3910–3913.

30 Toda, T., Igarashi, H., and Watanabe, M. (1999) Enhancement of the electroreduction of oxygen on Pt alloys with Fe, Ni, and Co. *Journal of the Electrochemistry Society*, **146**, 3750–3756.

31 Toda, T., Igarashi, H., and Watanabe, M. (1999) Enhancement of the electrocatalytic O_2 reduction on Pt–Fe alloys. *Journal of Electroanalytical Chemistry*, **460**, 258–262.

32 Wan, L., Moriyama, T., Ito, M., Uchida, H., and Watanabe, M. (2002) *In situ* STM imaging of surface dissolution and rearrangement of a Pt–Fe alloy electrocatalyst in electrolyte solution. *Chemical Communications*, 58.

33 Uchiida, H., Ozuka, H., and Watanabe, M. (2002) Electrochemical quartz crystal microbalance analysis of CO-tolerance at Pt–Fe alloy electrodes. *Electrochimica Acta*, **47**, 3629–3636.

34 Jasinski, R. (1964) A new fuel cell cathode catalyst. *Nature*, **201**, 1212–1213.

35 Putten, V.D., Elzing, A., and Visscher, W. (1986) Oxygen reduction on pyrolysed carbon-supported transition metal chelates. *Journal of Electroanalytical Chemistry*, **205**, 233–244.

36 Durand, R.R., Bencosme, C.S., and Collman, J.P. (1983) Mechanistic aspects of the catalytic reduction of dioxygen by cofacial metalloporphyrins. *Journal of the American Chemical Society*, **105**, 2710.

37 Behret, H., Binder, H., and Sandstede, G. (1981) On the mechanism of electrocatalytic oxygen reduction at metal chelates: Part III. Metal phthalocyanines. *Journal of Electroanalytical Chemistry*, **117**, 29–42.

38 Tang, S., Xiong, G.X., Cai, H.L., and Wang, H.L. (1987) The metal–support interaction on the model catalysts Pt-TiO_2, Pt-Ti_2O_3 and Pt-TiO CO-sputtering film: I. TEM and HEED studies. *Chinese Journal of Catalysis*, **8**, 225–233.

39 Aricò, A.S., Créti, P., Giordano, N., Antonucci, V., Antonucci, P.L., and Chuvilin, A. (1996) Chemical and morphological characterization of a direct methanol fuel cell based on a quaternary Pt-Ru-Sn-W/C anode. *Journal of Applied Electrochemistry*, **26** (9), 959–967.

40 Chen, K.Y., Shen, P.K., and Tseung, A.C.C. (1995) Anodic oxidation of formic acid on electrodeposited Pt/WO_3 electrode at room temperature. *Journal of the Electrochemistry Society*, **142**, L54–L56.

41 Xin, Q., Zhou, W.J., Zhou, Z.H., and Li, W.Z. (2004) A preparation method for bi-/multi-metallic noble metal electrocatalysts with high loadings. Chinese Patent ZL 02106201.3.

42 Xin, Q., Zhou, W.J., Zhou, Z.H., and Wei, Z.B. (2005) A preparation method of electrocatalyst for proton-exchange-membrane fuel cell. Chinese Patent ZL 01138909.5.

43 Xin, Q., Zhou, Z.H., Jiang, L.H., Zhou, W.J., and Sun, G.Q. (2010) A highly active Pt-based electrocatalyst for fuel cell and its preparation method. Chinese Patent ZL 03143681.1.

44 Zhou, W., Zhou, Z., Song, S., Li, W., Sun, G., Tsiakaras, P., and Xin, Q. (2003) Pt based anode catalysts for direct ethanol fuel cells. *Applied Catalysis B*, **46**, 273–285.

45 Zhou, Z.H., Wang, S.L., Zhou, W.J., Wang, G.X., Jiang, L.H., Li, W.Z., Song, S.Q., Liu, J.G., Sun, G.Q., and Xin, Q. (2003) Novel synthesis of highly active Pt/C cathode electrocatalyst for direct methanol fuel cell. *Chemical Communications*, 394–395.

46 Zhou, Z.H., Zhou, W.J., Wang, S.L., Wang, G.X., Jiang, L.H., Li, H.Q., Sun, G.Q., and Xin, Q. (2004) Preparation of highly active 40wt.% Pt/C cathode electrocatalysts for DMFC via different routes. *Catalyst Today*, **93–95**, 523–528.

47 Zhou, Z.H. (2003) Direct methanol fuel cells: studies on the preparation of highly dispersed Pt based electrocatalysts with high loading. PhD thesis. Dalian Institute of Physical Chemistry.

48 Li, W.Z. (2003) Carbon supported Pt-based cathode catalysts for direct methanol fuel cells (DMFCs). Ph.D. thesis. Dalian Institute of Physical Chemistry.

49 Li, W.Z., Zhou, W., Li, H., Zhou, Z., Zhou, B., Sun, G., and Xin, Q. (2004) Nano-structured Pt–Fe/C as cathode catalyst in direct methanol fuel cell. *Electrochimica Acta*, **49**, 1045–1055.

50 Hobson, L.J., Ozu, H., Yamaguchi, M., and Hayase, S. (2001) Modified Nafion 117 as an improved polymer electrolyte membrane for direct methanol fuel cells. *Journal of the Electrochemistry Society*, **148**, A1185–A1190.

51 Uchida, H., Mizuno, Y., and Watanabe, M. (2000) Suppression of methanol crossover in Pt-dispersed polymer electrolyte membrane for direct methanol fuel cells. *Chemical Letters*, 1268–1269.

52 Ryszard, W. and Peter, N. (1996) Sulfonated polyphosphazene ion-exchange membranes. *Journal of Membrane Science*, **119**, 155–160.

53 Nolte, R., Ledjeff, K., Bauer, M., and Mülhaupt, R. (1993) Partially sulfonated poly(arylene ether sulfone): a versatile proton conducting membrane material for modern energy conversion technologies. *Journal of Membrane Science*, **83**, 211–220.

54 Peled, E., Duvdevani, T., and Melman, A. (1998) A novel proton-conducting membrane. *Electrochemical Solid-State Letters*, **1**, 210–211.

55 Argyropoulos, P., Scott, K., and Taama, W.M. (2000) Dynamic response of the direct methanol fuel cell under variable load conditions. *Journal of Power Sources*, **87**, 153–161.

56 Li, H., Xin, Q., Li, W., Zhou, Z., Jiang, L., Yang, S., and Sun, G. (2004) An improved palladium-based DMFCs cathode catalyst. *Chemical Communications*, 2776–2777.

57 Li, H., Sun, G.Q., Li, N., Sun, S.G., Su, D.S., and Xin, Q. (2007) Design and preparation of highly active Pt-Pd/C catalyst for the oxygen reduction reaction. *Journal of the Physical Chemistry C*, **111**, 5605–5617.

58 Zhou, W.J. (2003) Research on the anode catalysts for low-temperature direct alcohol fuel cells. Ph.D. thesis. Dalian Institute of Physical Chemistry.

59 Wei, Z.B., Liu, J.G., Qiao, Y.G., Zhou, W.J., Li, W.Z., Chen, L.K., Xin, Q., and Yi, B.L. (2001) Performance of a direct methanol fuel cell. *Chinese Electrochemistry*, **7** (2), 228–233.

60 Jiang, L., Zhou, Z., Li, W., Zhou, W., Song, S., Li, H., Sun, G., and Xin, Q. (2004) Effects of treatment in different atmosphere on Pt_3Sn/C electrocatalysts for ethanol electro-oxidation. *Energy & Fuel*, **18**, 866–871.

61 Yan, S.Y., Sun, G.Q., Qi, J., Gao, Y., and Xin, Q. (2009) Effect of heat-treatment on polyol-synthesized PtRu/C electrocatalyst. *Chinese Journal of Catalysis*, **30** (11), 1109–1113.

62 Watanabe, M. and Motoo, S. (1975) Electrocatalysis by ad-atoms: Part III. Enhancement of the oxidation of carbon monoxide on platinum by ruthenium ad-atoms. *Journal of Electroanalytical Chemistry*, **60**, 275–283.

63 Douvartzides, S.L., Coutelieris, F.A., Demin, A.K., and Tsiakaras, P.E. (2004) Electricity from ethanol fed SOFCs: the expectations for sustainable development and technological benefits. *International Journal of Hydrogen Energy*, **29**, 375–379.

64 Goula, M.A., Kontou, S.K., and Tsiakaras, P.E. (2004) Hydrogen production by ethanol steam reforming over a

commercial Pd/γ-Al_2O_3 catalyst. *Applied Catalysis B*, **49**, 135–144.

65 Ogden, J.M., Steinbugler, M.M., and Kreutz, T.G. (1999) A comparison of hydrogen, methanol and gasoline as fuels for fuel cell vehicles: implications for vehicle design and infrastructure development. *Journal of Power Sources*, **79**, 143–168.

66 Aricò, A.S., Cretì, P., Antonucci, P.L., and Antonucci, V. (1998) Comparison of ethanol and methanol oxidation in a liquid-feed solid polymer electrolyte fuel cell at high temperature. *Electrochemical Solid-State Letters*, **1**, 66–68.

67 Zhou, W.J., Li, W.Z., Song, S.Q., Zhou, Z.H., Jiang, L.H., Sun, G.Q., Xin, Q., Poulianitis, K., Kontou, S., and Tsiakaras, P. (2004) Bi- and tri-metallic Pt-based anode catalysts for direct ethanol fuel cells. *Journal of Power Sources*, **131**, 217–223.

68 Jiang, L.H., Sun, G.Q., Zhou, Z.H., Zhou, W.J., and Xin, Q. (2004) Preparation and characterization of PtSn/C anode electrocatalysts for direct ethanol fuel cell. *Catalysis Today*, **93–95**, 665–670.

69 Jiang, L.H., Sun, G.Q., Zhou, Z.H., Sun, S.G., Wang, Q., Yan, S.Y., Li, H.Q., Tian, J., Guo, J.S., Zhou, B., and Xin, Q. (2005) Size-controllable synthesis of monodispersed SnO_2 nanoparticles and application in electrocatalysts. *Journal of the Physical Chemistry B*, **109**, 8774–8778.

70 Jiang, L.H., Sun, G.Q., Sun, S.G., Liu, J.G., Tang, S.H., Li, H.Q., Zhou, B., and Xin, Q. (2005) Structure and chemical composition of supported Pt–Sn electrocatalysts for ethanol oxidation. *Electrochimica Acta*, **50**, 5384–5389.

71 Mukerjee, S. and McBreen, J. (1999) An *in situ* X-ray absorption spectroscopy investigation of the effect of Sn additions to carbon-supported Pt electrocatalysts. *Journal of the Electrochemistry Society*, **146**, 600–606.

72 Jiang, L.H., Colmenares, L., Jusys, Z., Sun, G.Q., and Behm, R.J. (2007) Ethanol electrooxidation on novel carbon supported Pt/SnOx/C catalysts with varied Pt:Sn ratio. *Electrochimica Acta*, **53**, 377–389.

73 Rao, V., Cremers, C., Stimming, U., Cao, L., Sun, S., Yan, S.Y., Sun, G.Q., and Xin, Q. (2007) Electro-oxidation of ethanol at gas diffusion electrodes A DEMS study. *Journal of the Electrochemical Society*, **154** (11), B1138–B1147.

74 Cao, L., Sun, G.Q., Li, H., and Xin, Q. (2007) Carbon-supported IrSn catalysts for a direct ethanol fuel cell. *Electrochemistry Communications*, **9**, 2541–2546.

Index

Materials for Low-Temperature Fuel Cells, First Edition. Edited by Bradley Ladewig, San P. Jiang, and Yushan Yan.

WILEY END USER LICENSE AGREEMENT

Go to www.wiley.com/go/eula to access Wiley's ebook EULA.